

Supramolecular Construction of Optoelectronic π -Conjugated Peptide and Peptide-Inorganic Hybrid Materials

Ph. D. Thesis

by
Manoj K. Manna



**DISCIPLINE OF CHEMISTRY
INDIAN INSTITUTE OF TECHNOLOGY INDORE
AUGUST, 2016**

Supramolecular Construction of Optoelectronic π -Conjugated Peptide and Peptide-Inorganic Hybrid Materials

A THESIS

*Submitted in partial fulfillment of the
requirements for the award of the degree
of*
DOCTOR OF PHILOSOPHY

by
Manoj K. Manna



**DISCIPLINE OF CHEMISTRY
INDIAN INSTITUTE OF TECHNOLOGY INDORE
AUGUST, 2016**



INDIAN INSTITUTE OF TECHNOLOGY INDORE

CANDIDATE'S DECLARATION

I hereby certify that the work which is being presented in the thesis entitled **Supramolecular Construction of Optoelectronic π -Conjugated Peptide and Peptide-Inorganic Hybrid Materials** in the partial fulfillment of the requirements for the award of the degree of **DOCTOR OF PHILOSOPHY** and submitted in the **DISCIPLINE OF CHEMISTRY, Indian Institute of Technology Indore**, is an authentic record of my own work carried out during the time period from July 2012 to August 2016 under the supervision of **Dr. Apurba K. Das**, Associate professor, Discipline of Chemistry.

The matter presented in this thesis has not been submitted by me for the award of any other degree of this or any other institute.

Manoj K. Manna

This is to certify that the above statement made by the candidate is correct to the best of my/our knowledge.

Dr. Apurba K. Das
(Thesis Supervisor)

Manoj K. Manna has successfully given his Ph.D. Oral Examination held on.....

Signature(s) of Thesis Supervisor(s)
Date:

Convener, DPGC
Date:

Signature of PSPC Member
Date:

Signature of PSPC Member
Date:

Signature of External Examiner
Date:

ACKNOWLEDGEMENTS

I extend my deep gratitude to Dr. Apurba K. Das, my thesis supervisor, for suggesting such an innovative and relevant research topic. His invaluable guidance, unstinting support, and expert advice from time to time, enabled me to successfully complete the Thesis.

I am deeply indebted to Dr. Pradeep Mathur (Director, IIT Indore) for his invaluable support and in providing me with all the facilities at the Institute.

I would also like to express my sincere thanks to Dr. Biswarup Pathak and Dr. Shaibal Mukherjee for their expert suggestions and guidance.

I am grateful to Dr. Vipul Singh and Dr. Syam P. Somasekharan for providing me the necessary facilities for carrying out the work.

I express my sincere gratitude to Dr. Anirban Sengupta and Ms. Monika Gupta for their constant encouragement, inspiration and useful discussions throughout my work.

My sincere thanks to Mr. Manish Kushwaha, Mr. Kinny Pandey, Ms. Sarita Batra, Mr. Nitin Upadhyay and, Mr. Ghanshyam Bhavsar for their technical help and support in Sophisticated Instrumental Centre (SIC), IIT Indore.

I am also extremely grateful to Dr. Santanu Kumar Pal (IISER Mohali) for enabling access to 2D-giSAXS measurements. My thanks are also due to SAIF, IIT Bombay, for the assistance of the EM facility.

I am greatly thankful to Mr. Sujay Patil (Metrohum Autolab) for his valuable discussions and suggestions regarding technical methods in autolab electrochemical station.

I express my sincere thanks to all the faculty, staff, and students of Indian Institute of Technology Indore for their help and advice.

In particular, special thanks are due to Dr. Indrajit Maity, Dr. Dneyeshwar B. Rasale, Dr. Bharati Agarwal, Mr. Maruti Konda, Dr. Pragya Agar Palod, Dr. Kshitij Bhargava, Dr. Shruti Verma, Dr. Sushil K. Pandey, Mr. Suresh D and Dr. Kannan Muthu for their co-operation and moral support during the various stages of my Ph. D work.

I express my sincere thanks to Dr. Lakshmi Iyengar for editing and proof reading my work.

Finally, I am very grateful to my parents for their unconditional love and blessings and for standing by me at every stage of my academic life.

Manoj K. Manna

Dedicated to My Mentor

Dr. Apurba K. Das

ABSTRACT

This dissertation investigates supramolecular construction of functional π -conjugated peptide and peptide-inorganic hybrids and their fascinating properties. Chapter 1 describes the current status regarding the assembly of π -conjugated peptides and small organic molecules used in electrochemical construction of functional organic-inorganic nanoscale hybrid materials. Chapter 2 summarizes synthetic methodology and characterization techniques used in the thesis. Chapter 3 describes the synthesis and self-assembly study of a dipeptide diphenylalanine (Phe-Phe) functionalized benzo[ghi]perylene monoimide (BPI). The solvent dependent photophysical behavior of newly synthesized compound **2** (BPI-FF-OMe) has been described in detail. Compound **2** exhibits positive solvatochromic emission as a function of solvent polarity with higher lifetimes and quantum yields. Compound **2** self-assembles into nanospheres in methanol and toluene solvents. Chapter 4 makes an attempt to describe an electrochromic hydrogel based on a self-assembled quinquethiophene functionalized peptide. In this study, hydrogel exhibits electrochromism due to the presence of a redox active quinquethiophene (5T) moiety in compound **4**. Chapter 5 describes the fabrication of peptide/Cd-doped ZnO nanohybrid for the development of a white light emitting system. White-light luminescence of peptide/Cd-doped ZnO is attributed to cadmium doping in the zinc oxide crystal and the presence of a dipeptide-functionalized BPI fluorophore in the lamellar nanohybrid. Chapter 6 attempts to describe electrochemical construction of hybrid nanostructures utilizing small peptides as an organic component with ZnO. I-V characteristics of these hybrids under dark and light illuminations indicate that the conductivity of these nanostructure materials increases owing to the presence of photon-absorbing active self-assembled peptides. Chapter 7 describes electrochemical deposition of peptide/metal hydroxide hybrids for the purpose of developing electrochemically active materials. Peptide/Co(OH)₂ nanostructured hybrid films exhibit capacitive electrochemical performance in energy storage applications. Porous nanostructure of compound **9**/Co(OH)₂ hybrid shows high capacitance of 3070 Fg⁻¹ through electron transfer mechanism in the potential range -0.2 to 0.6 V at

a discharge current of 5 mA. Porous and soft nanostructure facilitates electrochemical accessibilities of electrolyte OH⁻ ions to Co(OH)₂ thin film and fast diffusion rate within the redox phase. Chapter 8 summarizes the salient features of the work and its future prospects.

LIST OF JOURNAL PUBLICATIONS

- [1] Das A. K., Manna M. K., Agrawal B., Mukherjee S. (2016), Synergistic assembly of peptide-metal hydroxide hybrid nanostructures for electrochemical capacitors, *ChemistrySelect*, 4, 715-722 (DOI: 10.1002/slct.201600104).[†]
- [2] Manna M. K., Aaryashree, Verma S, Mukherjee S., Das A. K. (2016), Lamellar peptide-cadmium-doped zinc oxide nanohybrids that emit white light, *ChemPlusChem*, 81, 329-337 (DOI : 10.1002/cplu.201500402).[†]
- [3] Manna M. K., Rasale D. B., Das A. K. (2015), Supramolecular assembly of dipeptide functionalized benzo[ghi]perylene monoimide directs white light emission *via* donor-acceptor interactions, *RSC Adv.*, 5, 90158-90167 (DOI: 10.1039/c5ra11804b).[†]
- [4] Manna M. K., Pandey S. K., Maity I., Mukherjee S., Das A. K. (2015), Electrodeposited lamellar photoconductor nanohybrids driven by peptide self-assembly, *ChemPlusChem*, 80, 583-590 (DOI: 10.1002/cplu.201402348).[†]
- [5] Mondal S., Konda M., Kauffmann B., Manna M. K., Das A. K. (2015), Effects of donor and acceptor units attached with benzoselenadiazole: optoelectronic and self-assembling patterns, *Crystal Growth & Design*, 15, 5548-5554 (DOI: 10.1021/acs.cgd.5b01179).
- [6] Verma S., Manna M. K., Das A. K., Mukherjee S. (2014), Benzo[ghi]perylene monoimide based photosensitive lamellar Cd-doped ZnO nanohybrids, *RSC Adv.*, 4, 62603-62614 (DOI: 10.1039/c4ra13712d).
- [7] Maity I., Manna M. K., Rasale D. B., Das A. K. (2014), Peptide-nanofiber-supported palladium nanoparticles as an efficient catalyst for the removal of N-terminus protecting groups, *ChemPlusChem*, 79, 413-420 (DOI: 10.1002/cplu.201300348).
- [8] Manna M. K., Das A. K., Self-assembling peptide-quinquethiophene based electrochromic hydrogel, manuscript under review.[†]

[†] Papers pertaining to the thesis.

CONFERENCE PRESENTATION

- [1] Manna M. K., Das A. K., Peptide self-assembly directed Lamellar photoconductor hybrids, National conference on emerging areas in chemical education & research and national convention of chemistry teachers, 16-18 October 2014 held in IIS University, Jaipur, India, Oral presentation.

TABLE OF CONTENTS

Acknowledgements	i
Abstract	v
Table of Contents	ix
List of Figures	xv
List of Charts and Tables	xxvi
List of Schemes	xxvii
List of Compounds	xxviii
List of Abbreviations	xxx
Nomenclature	xxxii
Chapter 1: Introduction	1-48
1.1 Supramolecular chemistry: Supramolecular assembly of π -conjugated system	3
1.2 Non covalent interaction	4
1.2.1 Hydrogen bonding	4
1.2.2 π - π stacking	5
1.3 Supramolecular construction of optoelectronic π -conjugated biomolecules	6
1.4 π -Conjugated peptides	7
1.4.1 Peptide-oligo(<i>p</i> -phenylene vinylene)(OPV) conjugates	8
1.4.2 Peptide-oligothiophene conjugate	11
1.4.3 Peptide-perylene diimide (PDI) conjugate	17
1.4.4 Peptide-naphthalene diimide (NDI) conjugate	20
1.4.5 Other peptide small π -electron conjugates	21
1.5 Supramolecular construction of organic-inorganic hybrid Materials	23
1.6 Characterization techniques for electrochemically triggered self-assembled complex organic-inorganic hybrid nanostructures	24
1.7 Organic-inorganic hybrids	25
1.7.1 SDS-inorganic aggregates	25
1.7.2 Oligothiophene/ZnO hybrids	28
1.7.3 Organic dye/ZnO hybrids	30

1.8 References	32
Chapter 2: Materials and Methods	49-58
2.1 Introduction	51
2.2 Experimental procedure	51
2.2.1 Materials	51
2.2.2 Purification of solvents and reagents	51
2.2.3 Solution phase π -conjugated peptide synthesis	52
2.2.4 Dual ion beam sputtering deposition (DIBSD)	52
2.2.5 Electrochemical experiments	53
2.2.6 Cleaning of electrode	54
2.3 Characterization	54
2.3.1 Characterization and purification of compounds	54
2.3.2 NMR Spectroscopy	54
2.3.3 Mass Spectrometry	54
2.3.4 FTIR Spectroscopy	54
2.3.5 Circular Dichroism (CD) Spectroscopy	55
2.3.6 Rheology	55
2.3.7 UV-Vis Spectroscopy	55
2.3.8 Fluorescence Spectroscopy	55
2.3.9 Dynamic Light Scattering (DLS)	55
2.3.10 Time Correlated Single Photon Counting (TCSPC)	56
2.3.11 Field Emission Gun-Scanning Electron Microscopy	56
2.3.12 Transmission Electron Microscopy (TEM)	56
2.3.13 Energy Dispersive X-Ray Spectroscopy (EDS)	57
2.3.14 Atomic Force Microscopy (AFM)	57
2.3.15 Wide-Angle X-Ray Diffraction	57
2.3.16 2D-GISAXS	57
2.3.17 Photoluminescence (PL)	57
2.3.18 Ellipsometry (EL)	58
2.3.19 Secondary mass ion spectrometry (SIMS)	58
2.4 References	58
Chapter 3: Supramolecular Assembly of Dipeptide	
Functionalized Benzo[ghi]perylene Monoimide Directs	

White Light Emission via Donor Acceptor Interactions	59-90
3.1 Introduction	60
3.2 Experimental	63
3.2.1 Synthesis of dipeptide-benzo[<i>ghi</i>]perylene monoimide conjugates	63
3.2.2 Synthesis of leucine functionalized benzo-[<i>ghi</i>]perylene Monoimides	63
3.2.3 Synthesis of BPI-FF-OMe	65
3.3 General characterization	70
3.4 Results and Discussion	72
3.4.1 Photophysics of dipeptide functionalized benzo[<i>ghi</i>]- perylene monoimide	72
3.4.2 Theoretical calculation	75
3.4.3 Self-assembly study of BPI-FF-OMe	76
3.4.4 Morphological characterization supramolecular nanospheres	78
3.4.5 Donor-acceptor interactions lead to white light emission	80
3.5 Conclusion	81
3.6 References	82
Chapter 4: Self-assembling Peptide-Quinquethiophene based Electrochromic Hydrogel	91-122
4.1 Introduction	93
4.2 Experimental	94
4.2.1 Materials	93
4.2.2 Synthesis of quinquethiophene dicarboxylic acid (5TmDCA)	95
4.2.3 Synthesis of peptide-quinquethiophene bolaamphiphiles	99
4.3 General characterization	107
4.4 Results and Discussion	109
4.4.1 UV-Visible absorption study	110
4.4.2 Fluorescence study	110
4.4.3 Circular dichroism (CD) study	111
3.4.4 Rheological Study	112

3.4.5 FTIR Study	112
3.4.6 Microscopic study	113
3.4.7 Cyclic voltammetry	113
4.5 Conclusion	116
4.6 References	116
Chapter 5: Lamellar Peptide-Cadmium-Doped Zinc Oxide Nanohybrids That Emit White Light	123-152
5.1 Introduction	125
5.2 Experimental	127
5.3 General characterization	132
5.4 Results and Discussion	132
5.4.1 Field-Emission Scanning Electron Microscope	134
5.4.2 Energy-Dispersive X-ray Spectroscopy (EDS)	136
5.4.3 X-ray diffraction (XRD) study	136
5.4.4 Two-Dimensional Grazing-Incidence Small Angle X- ray Scattering (2D-giSAXS)	137
5.4.5 SIMS analysis	137
5.4.6 UV-Visible absorption	139
5.4.7 Photoluminescence study	140
5.4.8 CIE (Commission Internationale d'Eclairage, 1931)	143
5.5 Conclusion	144
5.6 References	145
Chapter 6: Electrodeposited Lamellar Photoconductor Nanohybrids Driven by Peptide Self-Assembly	153-182
6.1 Introduction	155
6.2 Experimental	157
6.3 General characterization	164
6.4 Results and Discussion	164
6.4.1 FTIR Study	166
6.4.2 Scanning electron microscope (SEM)	168
6.4.3 Energy-dispersive X-ray spectroscopy (EDS)	168
6.4.4 UV-Vis Study	168
6.4.5 Photoluminescence (PL) Study	171

6.4.6 X-ray diffraction (XRD) Study	171
6.4.7 Current-voltage (I-V) measurements	172
6.5 Conclusion	173
6.6 References	175
Chapter 7: The Synergistic Assembly of Peptide-Metal Hybrid Nanostructures for Electrochemical Capacitors	183-214
7.1 Introduction	185
7.2 Experimental	187
7.3 General characterization	193
7.4 Results and Discussion	194
7.4.1 Designing of peptides	194
7.4.2 Electrodeposition of peptide/M(OH) ₂	195
7.4.3 Characterization of nanoscale hybrid thin films	195
7.4.4 Electrochemical behavior of hybrid thin films	195
7.5 Conclusion	204
7.6 References	205
Chapter 8: Conclusions and Scope for Future Prospects	215-220
8.1 Conclusions	217
8.2 Future prospects	219
Annexure 1:	221-226
Table A1: List of small organic molecules reported in electrochemical self-assembly of organic/inorganic hybrids	221
Table A2: Reports on the white light emitting materials	223
Table A3: DLS characterization of BPI-FF-OMe nanospheres	227
The Lippert-Mataga Equation	228
Movie A1: Electrochromic hydrogel	228

LIST OF FIGURES

Chapter 1: Introduction

Figure 1.1. Hydrogen bonding interaction (Red dots).

Figure 1.2. Schemes describe the electrostatic view of aromatic interactions. The various modes of stacking are presented, emphasizing locations of electrostatic attraction or repulsion. (Ref: 74).

Figure 1.3. The proposed structure for the binary self-assembly of nucleotide-appended oligo-(*p*-phenylene vinylene) (OPV). (Ref: 75).

Figure 1.4. (a) The molecular structures of an antiparallel β -sheet conformation of a peptide-OPV conjugate **1** monolayer, (b) STEM images of **1** at the 1-octanoic acid-HOPG interface with a superimposed molecular model, (c) AFM images of nano-fibrillar aggregates of **1**. (Ref: 57).

Figure 1.5. (a) Energy-minimized model of a 1-D nanostructure expected after self-assembly and (b) representative UV-vis/PL and (c) CD spectra of a peptide-OPV conjugate in basic, molecularly dissolved (---) and acidic, assembled solutions (—). (Ref: 77).

Figure 1.6. (a) CD (b) fluorescence of **3** in basic (dissolved, black traces) and acidic (assembled, red traces) solutions. The inset of panel B depicts a concentrated solution (left) and a gel (right) irradiated at 365 nm. Tapping-mode AFM images and height profiles of the indicated line trace of (c) large area and (d) isolated structures formed after assembly and deposition on freshly cleaved mica surfaces, (e) Supramolecular assembly of oligothiophene-oligopeptide conjugate **3**. (Ref: 78).

Figure 1.7. AFM image of 0.1 mg/mL drop-cast film of assembled EAA-4T peptide, (a) height and (b) phase profiles; (c) TEM image of 1 mg/mL solution of acidified EAA-4T solution (width = 8.9 (2.4 nm); (d) surface profile of a 10 mg/mL drop-cast film of EAA-4T under a laser microscope. (Ref: 79).

- Figure 1.8.** Self-assembly of PTP and TPT in different organic solvents. (Ref: 82).
- Figure 1.9.** Self-assembly and electron transfer of a donor-acceptor π -peptide hybrid (left). Spectral dynamics following photoexcitation of (a) unassembled and (b) assembled **10** at 400 nm (right). (Ref: 83).
- Figure 1.10.** Self-assembly of PBI-[GY]₂ and PBI-[GD]₂ to chiral fibrous and spherical structures in different polar solvents :PBI-[GY]₂ forms fibers in buffer solution (pH 10.8), DMSO, DMF, THF, and acetone. PBI-[GD]₂ forms fibers in DMF and spheres in water and DMSO. Inset photographs are PBI-[GY]₂ gels in buffer solution (pH 10.8) and DMF, solutions in DMSO, acetone, and THF, PBI-[GD]₂ gels in DMF and DMSO, and solution in buffer solution (pH 10.8). (Ref: 86).
- Figure 1.11.** Structure of the peptide-PDIs explored in the study (top). Self-assembly strategy of PDI-Peptides (Bottom). (Ref: 87).
- Figure 1.12.** AFM images of (a) bisimide **15A** microspheres and (b) bisimide **15B** nanofibers. (Ref: 90).
- Figure 1.13.** Lamellar hybrid nanostructure: (a) SEM (top-down) image of deposited platelets using PyBA, magnified in the inset. (b) SEM (cross-sectional view) image of deposited platelets using PyBA. (c) TEM image of lamellar sheets within platelets deposited using PyBA, magnified in the inset. (d) Schematic diagram of lamellar ordering composed of inorganic Zn-rich regions and bilayers of PyBA. (Ref: 103).
- Figure 1.14.** (a) Schematic representations of possible surfactant assemblies at the solid-liquid interface, (b) Lamellar structured ZnO films templated bilayer assembly of surfactants, (c) An interfacial amphiphilic assembly composed of hexagonally close-packed spherical micelles is used as a template in this scheme. (Ref: 111, 112).
- Figure 1.15** Cooperative templating model for the electrochemical synthesis of hexagonal mesoporous Ni(OH)₂ thin films on the

surface of working electrode. (Ref: 113).

Figure 1.16. Schematic representation of electrochemical interfacial surfactant templating (Ref: 114).

Figure 1.17. Mechanism for the directed growth of different nanoscale lamellar morphologies grew with decanoic acid on different surfaces. (a) A hydrophilic surface such as ITO interacts more favorably with the polar headgroups, resulting in two-dimensional bilayer assemblies at the surface that promotes Zn(OH)_2 nucleation parallel to the substrate. (b) A more hydrophobic surface such as PEDOT:PSS interacts more favorably with the alkyl tails, leading to lower-dimensional assemblies such as hemimicelles, which template the growth of Zn(OH)_2 perpendicular to the substrate. (Ref: 104).

Figure 1.18. Electrochemical self-assembly of the ZnO/TSPcM thin films. (Ref: 105).

Chapter 3: Supramolecular Assembly of Dipeptide Functionalized Benzo[ghi]perylene Monoimide Directs White Light Emission via Donor Acceptor Interactions.

Figure 3.1. Schematic represents white light emission upon energy transfer between donor and acceptor (PyBA: BPI-FF-OMe). BPI-FF-OMe molecules show efficient solvatochromic effects in protic polar solvent methanol and aprotic solvent toluene. BPI-FF-OMe self-assembled to form spherical nanosphere in solution phase.

Figure 3.2. ^1H NMR spectrum (400 MHz, $\text{DMSO-}d_6$) for *N,N'*-maleyl-L-Phe(1)-L-Phe(2)-OMe (**15a**).

Figure 3.3. Mass spectrum of *N,N'*-maleyl-L-Phe(1)-L-Phe(2)-OMe with sodium ion adduct.

Figure 3.4. ^1H NMR spectrum (400 MHz, CDCl_3) for *N,N'*-maleoyl-L-Phe(1)-L-Phe(2)-OMe (**16a**).

Figure 3.5. Mass spectrum of *N,N'*-maleoyl-L-Phe(1)-L-Phe(2)-OMe with sodium ion adduct.

Figure 3.6. ^1H NMR spectrum (400 MHz, CDCl_3) for benzo[ghi]perylene-

1,2-dicarboxylic(L-Phe-L-Phe-OMe)imide (**2**).

Figure 3.7. Mass spectrum of benzo[*ghi*]perylene-1,2-dicarboxylic(L-Phe-L-Phe-OMe)imide (**2**).

Figure 3.8. ^1H NMR spectrum (400 MHz, $\text{DMSO-}d_6$) for *N,N'*-Maleyl-Leu-OMe (**15b**).

Figure 3.9. ^1H NMR spectrum (400 MHz, CDCl_3) for *N,N'*-Maleoyl-L-Leu-OMe (**16b**).

Figure 3.10. ^1H NMR spectrum (400 MHz, CDCl_3) for benzo[*ghi*]perylene-1,2-dicarboxylic(L-Leu-OMe)imide (**3**).

Figure 3.11 (a) UV-Vis absorption spectra of compound **2** (BPI-FF-OMe) in various solvents. (b) Normalized UV-Vis absorption and fluorescence spectra in polar and non polar solvents. Optical images of compound **2** show green emission in toluene and yellow emission in methanol under 365 nm UV light. (c) Emission spectra of compound **2** in solvents listed in Table 3.1. (d) Emission spectra of compound **2** normalized with respect to absorption peak at 483 nm. (e) UV-Vis of compound **2** in solvents from listed Table 3.1. (f) Lippart-Mataga plot.

Figure 3.12. (a) Fluorescence excitation spectra of donor BPI-FF-OMe **2** in methanol (emission wavelength 564 nm), (b) Time correlated single photon counting decay traces of BPI-FF-OMe ($9 \times 10^{-5} \text{ mol L}^{-1}$) in toluene $\lambda_{\text{em}} = 508 \text{ nm}$ (red) and methanol $\lambda_{\text{em}} = 566 \text{ nm}$ (blue).

Figure 3.13. HOMO and LUMO frontier orbital of BPI-FF-OMe at the B3LYP/6-31G (d) level. ^[a]Optical band gap of BPI-FF-OMe in methanol was calculated from UV-Vis spectroscopy.

Figure 3.14. Size distribution histogram of nanospheres from DLS measurement. The mean hydrodynamic diameter of nanospheres in (a) methanol and (b) toluene. (c) Temperature dependent ^1H NMR spectra of BPI-FF-OMe (20 mmol L^{-1}) in $\text{DMSO-}d_6$.

Figure 3.15. Microscopic images of compound **2**. (a) SEM image of

compound **2** in toluene, (b) SEM image of compound **2** in methanol, (c) TEM image of BPI-FF-OMe in toluene and (d) TEM image of compound **2** in methanol show nanospheres. AFM images show the nanospherical morphology of compound **2** (e) in toluene and (f) in methanol.

Figure 3.16. (a) UV-Vis and (b) fluorescence spectra of (1×10^{-6} mol L⁻¹) of PyBA **1**, BPI-FF-OMe **2** and mixture of different equivalents of PyBA and BPI-FF-OMe in methanol respectively. (c) Spectral overlaps region of emission spectrum of donor PyBA and absorption spectrum of acceptor BPI-FF-OMe. (d) Light emission of PyBA, BPI-FF-OMe and mixture of PyBA and BPI-FF-OMe (10:1) under 365 nm UV light.

Chapter 4: Self-assembling Peptide-Quinquethiophene based Electrochromic Hydrogel

Figure 4.1. ¹H NMR spectrum (400 MHz, CDCl₃) of Tributyl(2-thienyl)stannane (**17**).

Figure 4.2. ¹H NMR spectrum (400 MHz, CDCl₃) of 3-methyl-2,5-di(thiophen-2-yl)thiophene (**18**).

Figure 4.3. ¹H NMR spectrum (400 MHz, CDCl₃) of tert-butyl 5-bromothiophene-2-carboxylate.

Figure 4.4. ¹H NMR spectrum (400 MHz, CDCl₃) of ditertbutyl ester 3-methyl-Quinquethiophene (**20**).

Figure 4.5. ¹H NMR spectrum (400 MHz, DMSO-*d*₆) of dicarboxylic acid 3-methyl-quinquethiophene (5TmDCA) (**21**).

Figure 4.6. ¹H NMR spectrum (400 MHz, CDCl₃) of MeO-Leu-5T-Leu-OMe (**22a**)

Figure 4.7. ¹H NMR spectrum (400 MHz, DMSO-*d*₆) of MeO-Tyr-5T-Tyr-OMe (**22b**).

Figure 4.8. ¹H NMR spectrum (400 MHz, DMSO-*d*₆) of HO-Leu-5T-Leu-OH (**23a**).

Figure 4.9. ¹H NMR spectrum (400 MHz, DMSO-*d*₆) of HO-Tyr-5T-Tyr-OH (**23b**).

- Figure 4.10.** ^1H NMR spectrum (400 MHz, $\text{DMSO-}d_6$) of MeO-Leu-Leu-5T-Leu-Leu-OMe (**24a**).
- Figure 4.11.** ^1H NMR spectrum (400 MHz, $\text{DMSO-}d_6$) of MeO-Tyr-Tyr-5T-Tyr-Tyr-OMe (**24b**).
- Figure 4.12.** ^1H NMR spectrum (400 MHz, $\text{DMSO-}d_6$) of HO-Leu-Leu-5T-Leu-Leu-OH (**4**).
- Figure 4.13.** ^{13}C NMR spectrum (100 MHz, $\text{DMSO-}d_6$) of HO-Leu-Leu-5T-Leu-Leu-OH (**4**).
- Figure 4.14.** ^1H NMR spectrum (400 MHz, $\text{DMSO-}d_6$) of HO-Tyr-Tyr-5T-Tyr-Tyr-OH (**5**).
- Figure 4.15.** ^{13}C NMR spectrum (100 MHz, $\text{DMSO-}d_6$) of HO-Tyr-Tyr-5T-Tyr-Tyr-OH (**5**).
- Figure 4.16.** (a) Molecular structures of the peptide-quinquethiophene conjugates **4** (LL5TLL) and, **5** (YY5TYYY); (b) Digital images of solution of compounds **4** and **5** at basic pH and (c) hydrogel **1** and **2**.
- Figure 4.17.** (a) UV-vis absorbance, (b) fluorescence spectra compound **4**. Excitation wavelength ($\lambda_{\text{max}} = 430 \text{ nm}$) in aqueous medium. Temperature dependent CD spectra in water (c) upon heating, and (d) upon cooling. CD Spectra recorded at $200 \mu\text{M}$.
- Figure 4.18.** (a) Dynamic rheology (frequency sweep) of hydrogel **1** ($c = 20 \text{ mmol L}^{-1}$), and (b) ATR-FTIR spectra of compound **4** in powder form (red curve) and gel state (blue curve).
- Figure 4.19.** (a)-(b) TEM micrograph of compound **4** showing nanostructures in high and low magnification.
- Figure 4.20.** Cyclic voltammogram of compound **4** in $0.10 \text{ M Bu}_4\text{NClO}_4/\text{CH}_2\text{Cl}_2$ electrolyte with (a) scan rate of 25, 50, 100 and 200 mVs^{-1} and (b) at continuous scanning. (c) Reversible colour change in hydrogel **1** coated ITO glass at operating voltage 0 V (bright yellow) and 1.21 V (deep blue).
- Figure 4.21.** The redox mechanism of compound **4** (LL5TLL) ($\text{R}_1 = \text{R}_2 = \text{Leu}$) during electrochemical reaction.

Chapter 5: Lamellar Peptide-Cadmium-Doped Zinc Oxide

Nanohybrids That Emit White Light

- Figure 5.1.** (a) Molecular structure of compound **6** (BPI-FF-OH). Electrochemical synthesis of (b) unannealed cadmium-doped ZnO NSs and (c) unannealed BPI-FF-OH/cadmium-doped ZnO NFs at a constant applied potential of -700 mV at 80 °C bath temperature. Synthesis of annealed (d) cadmium-doped ZnO NSs and e) BPI-FF-OH/cadmium-doped ZnO NFs upon heating at 150 °C. Insets are digital photographs of whitish light emission from the corresponding hybrids.
- Figure 5.2.** ^1H NMR spectrum (400 MHz, $\text{DMSO-}d_6$) of BPI-FF-OH (**6**).
- Figure 5.3.** ^{13}C NMR spectrum (100 MHz, $\text{DMSO-}d_6$) of BPI-FF-OH (**6**).
- Figure 5.4.** ESI-MS spectrum of BPI-FF-OH (**6**).
- Figure 5.5.** FE-SEM images of (a) unannealed cadmium-doped ZnO, (b) annealed cadmium-doped ZnO NS, (c) unannealed BPI-FF-OH/cadmium-doped ZnO, and (d) annealed BPI-FF-OH/cadmium-doped ZnO NF architectures.
- Figure 5.6.** EDS spectra of annealed (a) cadmium-doped ZnO and (b) BPI-FFOH/ cadmium-doped ZnO films.
- Figure 5.7.** XRD patterns of GZO and annealed, and unannealed cadmium-doped ZnO (a) and (b) and GZO, annealed and unannealed BPI-FF-OH/cadmium-doped ZnO films (c) and (d). The peaks marked with asterisks are associated with silicon.
- Figure 5.8.** (a) SAXS of lamellar BPI-FF-OH/cadmium-doped ZnO hybrid films. Insets show the corresponding 2D giSAXS images of annealed BPI-FF-OH/cadmium-doped ZnO and unannealed BPI-FF-OH/cadmium-doped ZnO nanohybrids, (b) SIMS profile of Cd-doped ZnO and hybrid thin films deposited from 0.01 M $\text{Cd}(\text{OAc})_2 \cdot 6\text{H}_2\text{O}$; 0.04 M $\text{Zn}(\text{NO}_3)_2 \cdot 6\text{H}_2\text{O}$, BPI-FF-OH.
- Figure 5.9.** Optical absorption spectra of (a) Cd-doped ZnO and (b) lamellar BPI-FF-OH/ cadmium-doped ZnO films. Insets show the corresponding Tauc's plots to evaluate the band gap

energy. Room-temperature PL spectra of (c) cadmium-doped ZnO before and after annealing. The inset shows the whitish luminescence from unannealed and annealed cadmium-doped ZnO NSs. (d) PL spectra of the organic dye BPI-FF-OH and the lamellar BPI-FF-OH/cadmium-doped ZnO nanohybrid. The inset shows white-light emission from unannealed and annealed BPI-FFOH/cadmium-doped ZnO nanohybrids.

Figure 5.10. Tauc's plots to evaluate band gap energy of (a) Cd-doped ZnO and (b) BPI-FFOH/ Cd-doped ZnO hybrid deposited from different Cd precursor bath concentration. Bath compositions are (A) 0.04 M Cd(OAc)₂.6H₂O; 0.04 M Zn(NO₃)₂.6H₂O, (B) 0.02 M Cd(OAc)₂.6H₂O; 0.04 M Zn(NO₃)₂.6H₂O and (C) 0.01 M Cd(OAc)₂.6H₂O; 0.04 M Zn(NO₃)₂.6H₂O.

Figure 5.11. PL spectra of (a) Cd-doped ZnO and (b) BPI-FF-OH/Cd-doped ZnO hybrids. Bath compositions are (A) 0.01 M Cd(OAc)₂.6H₂O; 0.04 M Zn(NO₃)₂.6H₂O, (B) 0.02 M Cd(OAc)₂.6H₂O; 0.04 M Zn(NO₃)₂.6H₂O and (C) 0.04 M Cd(OAc)₂.6H₂O; 0.04 M Zn(NO₃)₂.6H₂O.

Figure 5.12. The CIE (1931) chromaticity diagram for white-light-emitting (1) unannealed cadmium-doped ZnO, (2) annealed cadmium-doped ZnO, (3) unannealed BPI-FF-OH/cadmium-doped ZnO, and (4) annealed BPI-FF-OH/cadmium-doped ZnO. The plot was obtained by using the gocie.exe program.

Chapter 6: Electrodeposited Lamellar Photoconductor Nanohybrids Driven by Peptide Self-Assembly

Figure 6.1. ¹H NMR spectrum (400 MHz, DMSO-*d*₆) of Nm-FF-OH (7).

Figure 6.2. ¹³C NMR spectrum (100 MHz, DMSO-*d*₆) of Nm-FF-OH (7).

Figure 6.3. ESI-MS spectrum of Nm-FF-OH (7).

Figure 6.4. ¹H NMR spectrum (400 MHz, DMSO-*d*₆) of Nm-YF-OH (8).

Figure 6.5. ¹³C NMR spectrum (100 MHz, DMSO-*d*₆) of Nm-YF-OH (8).

Figure 6.6. ESI-MS spectrum of Nm-YF-OH (8).

Figure 6.7. (a) The molecular structures of the designed peptide amphiphiles and Zn(NO₃)₂ precursor used for electrochemical

deposition. (b) Digital photograph of the electrodeposited annealed hybrid thin film on an indium tin oxide (ITO)-coated quartz glass substrate. (c) Field-emission scanning electron microscopy (FESEM) image of the electrodeposited hybrid film with peptide 2. (d) Schematic illustration of alternate ZnO and peptide layers in the lamellar network structures. (e) Schematic presentation of the peptide assembly within the ZnO inorganic phases. The aromatic π - π stacking interactions among the aromatic Nmoc moieties and hydrogen bonding of the peptide amphiphiles are the driving force for the evolution of lamellar nanostructures. Upon excitation with light, excited electrons move through the aromatic Nmoc groups of the peptide amphiphiles into inorganic ZnO lattices and the flow of current produces a photocurrent.

Figure 6.8. FTIR spectra of (a) annealed hybrid **1** and peptide **7**, and (b) annealed hybrid **2** with peptide **8**. Absorption spectra of unannealed and annealed hybrids.

Figure 6.9. FESEM images of the top view of annealed hybrids **1** (a) and **2** (b), as well as cross-sectional images of hybrids **1** (c) and **2** (d).

Figure 6.10. Energy-dispersive X-ray spectroscopy (EDS) of electrodeposited hybrid films in the presence of (a) peptide Nmoc-FF-OH **7**, (b) peptide Nmoc-YF-OH **8**.

Figure 6.11. (a) FESEM image showing the wurtzite hexagonal ZnO grown without any peptide Amphiphile. (b) PL spectra of annealed electrodeposited ZnO thin film. (c) Powder XRD of annealed electrodeposited ZnO thin film.

Figure 6.12. PL spectra of hybrids **1** (a) and **2** (b) before and after annealing recorded with $\lambda = 325$ nm laser excitation. Powder XRD patterns of hybrid thin films a) ZnO/**7** and b) ZnO/**8**. Powder XRD peak patterns (001) and (001)* refer to lamellar ordering in the hybrid material; (100), (002), (101) indicate lattice planes of the wurtzite ZnO crystal.

Chapter 7: The Synergistic Assembly of Peptide-Metal Hydroxide Hybrid Nanostructures for Electrochemical Capacitors

- Figure 7.1.** ^1H NMR spectrum (400 MHz, $\text{DMSO-}d_6$) of NmYW (**9**).
- Figure 7.2.** ^{13}C NMR spectrum (100 MHz, $\text{DMSO-}d_6$) of NmYW (**9**).
- Figure 7.3.** ESI-MS spectrum of NmYW (**9**).
- Figure 7.4.** ^1H NMR spectrum (400 MHz, $\text{DMSO-}d_6$) of NmFW (**10**).
- Figure 7.5.** ^{13}C NMR spectrum (100 MHz, $\text{DMSO-}d_6$) of NmFW (**10**).
- Figure 7.6.** ESI-MS spectrum of NmFW (**10**).
- Figure 7.7.** ^1H NMR spectrum (400 MHz, $\text{DMSO-}d_6$) for NmFY (**11**).
- Figure 7.8.** ^{13}C NMR spectrum (100 MHz, $\text{DMSO-}d_6$) of NmFY (**11**).
- Figure 7.9.** ESI-MS spectrum of NmFY (**11**).
- Figure 7.10.** FE-SEM images of peptide/ $\text{M}(\text{OH})_2$: $\text{Co}(\text{OH})_2$ nanostructure hybrid films with three peptides (top row), (a) hybrid **3**: Compound **9**/ $\text{Co}(\text{OH})_2$, (b) hybrid **4**: Compound **10**/ $\text{Co}(\text{OH})_2$ and (c) hybrid **5**: Compound **11**/ $\text{Co}(\text{OH})_2$; $\text{Ni}(\text{OH})_2$ nanostructure hybrid films with three different peptides (middle row), (d) hybrid **6**: Compound **9**/ $\text{Ni}(\text{OH})_2$, (e) hybrid **7**: Compound **10**/ $\text{Ni}(\text{OH})_2$ and (f) hybrid **8**: Compound **11**/ $\text{Ni}(\text{OH})_2$; $\text{Zn}(\text{OH})_2$ nanostructure hybrids films with three different peptides (bottom row), (g) hybrid **9**: Compound **9**/ $\text{Zn}(\text{OH})_2$, (h) hybrid **10**: Compound **10**/ $\text{Zn}(\text{OH})_2$ and (i) hybrid **11**: Compound **11**/ $\text{Zn}(\text{OH})_2$.
- Figure 7.11.** EDS spectra of peptide/metal hydroxide hybrid films; (a) hybrid **3**: NmYW/ $\text{Co}(\text{OH})_2$, (b) hybrid **6**: NmYW/ $\text{Ni}(\text{OH})_2$ and (c) hybrid **9**: NmYW/ $\text{Zn}(\text{OH})_2$.
- Figure 7.12.** EDS spectra of peptide/ $\text{M}(\text{OH})_2$: (a) hybrid **4**: NmFW/ $\text{Co}(\text{OH})_2$, (b) hybrid **5**: NmFY/ $\text{Co}(\text{OH})_2$, (c) hybrid **7**: NmFW/ $\text{Ni}(\text{OH})_2$, (d) hybrid **8**: NmFY/ $\text{Ni}(\text{OH})_2$, (e) hybrid **10**: NmFW/ $\text{Zn}(\text{OH})_2$ and (f) hybrid **11**: NmFY/ $\text{Zn}(\text{OH})_2$.
- Figure 7.13.** FTIR and XRD spectra of NmYW (peptide **9**), NmYW/ $\text{Co}(\text{OH})_2$ (hybrid **3**), NmYW/ $\text{Ni}(\text{OH})_2$ (hybrid **6**) and NmYW/ $\text{Zn}(\text{OH})_2$ (hybrid **9**).
- Figure 7.14.** FTIR spectra of (a) NmFW (peptide **10**), NmFW/ $\text{Co}(\text{OH})_2$

(hybrid **4**), NmFW/Ni(OH)₂ (hybrid **7**), NmFW/Zn(OH)₂ (hybrid **10**) and (b) NmFY (peptide **11**), NmFY/Co(OH)₂ (hybrid **5**), NmFY/Ni(OH)₂ (hybrid **8**) and NmFY/Zn(OH)₂ (hybrid **11**).

Figure 7.15. XRD spectra of (a) NmFW (peptide **10**), NmFW/Co(OH)₂ (hybrid **4**), NmFW/Ni(OH)₂ (hybrid **7**), NmFW/Zn(OH)₂ (hybrid **10**) and (b) NmFY (peptide **11**), NmFY/Co(OH)₂ (hybrid **5**), NmFY/Ni(OH)₂ (hybrid **8**) and NmFY/Zn(OH)₂ (hybrid **11**).

Figure 7.16. (a) Cyclic voltammograms of NmYW and NmYW/Co(OH)₂ recorded by scanning the potential from -0.3 to 0.5 V at scan rate of 20 mV s⁻¹, (b) charging–discharging curve of NmYW/Co(OH)₂ in 4 m KOH with a potential window of -0.2 to 0.6 V vs. Ag/AgCl, discharging curve obtained at 5 mA. (c) Cyclic voltammograms of NmYW and NmYW/Ni(OH)₂ recorded by scanning the potential from -0.3 to 0.6 V at a scan rate of 20 mV s⁻¹ and (d) charging–discharging curve of NmYW/Ni(OH)₂ in 4 m KOH with a potential window of -0.2 to 0.6 V vs. Ag/AgCl, discharging curve obtained at 6 mA.

Figure 7.17. (a)-(b) Cyclic voltammogram of NmYW/Co(OH)₂ at different scan rates and repetitive 5 cycles at scan rate of 20 mVs⁻¹ respectively. (c)-(d) Cyclic voltammogram of NmYW/Ni(OH)₂ at different scan rates and repetitive 5 cycles at scan rate of 20 mVs⁻¹ respectively. Experiments performed in 4 M aqueous KOH solution.

LIST OF CHARTS AND TABLES

- Chart 1.** Chemical structure of few bio motifs.
- Chart 2.** Molecular structures of peptide-oligo(p-phenylene vinylene)(OPV) conjugates.
- Chart 3.** Molecular structures of oligothiophene-peptide conjugates.
- Chart 4.** Molecular structures of PDI-peptide conjugates.
- Chart 5.** Molecular structures of NDI-peptide conjugates.
- Chart 6.** Molecular structures of different small aromatic dye-peptide conjugates.
- Table 3.1.** Spectroscopic and photophysical properties of BPI-FF-OMe (2) in different solvents of increasing polarity.
- Table 5.1.** Parameters obtained from spectroscopic ellipsometry and PL measurements.
- Table 5.2.** Lattice parameters and FWHM parameters of Cd-doped ZnO, BPI-FF-OH/Cd-doped ZnO hybrids.

LIST OF SCHEMES

- Scheme 3.1.** Synthesis of N-dipeptide functionalized benzo[*ghi*]perylene-1,2-dicarboxylic monoimide.
- Scheme 3.2.** Schematic presentation shows a possible mechanism of BPI-FF-OMe **2** for nanosphere formation.
- Scheme 4.1.** Reaction steps for the synthesis of quinquethiophene dicarboxylic acid (5TmDCA).
- Scheme 4.2.** Reaction steps for the synthesis of peptide-quinquethiophene conjugates.
- Scheme 4.3.** Self-assembly model for peptide-quinquethiophenes in aqueous medium.
- Scheme 5.1.** Synthesis of N-dipeptide functionalized benzo[*ghi*]perylene-1,2-dicarboxylic monoimide.
- Scheme 5.2.** Schematic of possible growth mechanisms for cadmium-doped ZnO and BPI-FF OH/cadmium-doped ZnO nanostructures on the Ga-doped ZnO (GZO)/n-Si(100) electrode.
- Scheme 6.1.** Solution-phase synthetic procedure of preparation for peptides Nmoc-FF-OH (**7**) and Nmoc-YF-OH (**8**).
- Scheme 6.2.** Peptide design for the fabrication of photoconductor nanohybrids.
- Scheme 7.1.** Synthetic route for peptides **9** (NmYW), **10** (NmFW) and, **11** (NmFY).
- Scheme 7.2.** Molecular structures of peptides **9** (NmYW), **10** (NmFW) and, **11** (NmFY)

LIST OF COMPOUNDS

Naphthalene-2-methyloxichloroformate (**31**)
Nmoc-Phe-OMe (**32**)
Nmoc-Tyr-OMe (**33**)
Nmoc-Phe-Phe-OMe (**34a**)
Nmoc-Phe-Phe-OH (**7**)
Nmoc-Tyr-Phe-OMe (**34b**)
Nmoc-Tyr-Phe-OH (**8**)
Nmoc-Tyr-Trp-OMe (**34c**)
Nmoc-Tyr-Trp-OH (**9**)
Nmoc-Phe-Trp-OMe (**34d**)
Nmoc-Phe-Trp-OH (**10**)
Nmoc-Phe-Tyr-OMe (**34e**)
Nmoc-Phe-Tyr-OH (**11**)
Boc-L-Phe-OH (**12**)
Boc-L-Phe-L-Phe-OMe (**13**)
H₂N-L-Phe-L-Phe-OMe (**14**)
N,N'-maleyl-L-Phe(1)-L-Phe(2)-OMe (**15a**)
N,N'-maleoyl-L-Phe(1)-L-Phe(2)-OMe (**16a**)
Benzo[*ghi*]perylene-1,2-dicarboxylic(L-Phe-L-Phe-OMe)imide (**2**)
Boc-D-Phe-OH (**25**)
Boc-D-Phe-D-Phe-OMe (**26**)
H₂N-D-Phe-D-Phe-OMe (**27**)
N,N'-maleyl-D-Phe(1)-D-Phe(2)-OMe (**28**)
N,N'-maleoyl-D-Phe(1)-D-Phe(2)-OMe (**29**)
Benzo[*ghi*]perylene-1,2-dicarboxylic(D-Phe-D-Phe-OMe)imide (**30**)
Benzo[*ghi*]perylene-1,2-dicarboxylic(D-Phe-D-Phe-OH)imide (**6**)
N,N'-Maleyl-Leu-OMe (**15b**)
N,N'-Maleoyl-Leu-OMe (**16b**)
Benzo[*ghi*]perylene-1,2-dicarboxylic(L-Leu-OMe)imide (**3**)
Tributyl(2-thienyl)stannane (**17**)
3-methyl-2,5-di(thiophen-2-yl)thiophene (**18**)
tert-butyl 5-bromothiophene-2-carboxylate (**19**)

diterbutyl ester 3-methyl-quintthiophene (**20**)
dicarboxylic acid 3-methyl-quintthiophene (5TmDCA) (**21**)
MeO-Leu-5T-Leu-OMe (**22a**)
MeO-Tyr-5T-Tyr-OMe (**22b**)
HO-Leu-5T-Leu-OH (**23a**)
HO-Tyr-5T-Tyr-OH (**23b**)
MeO-Leu-Leu-5T-Leu-Leu-OMe (**24a**)
MeO-Tyr-Tyr-5T-Tyr-Tyr-OMe (**24b**)
HO-Leu-Leu-5T-Leu-Leu-OH (**4**)
HO-Tyr-Tyr-5T-Tyr-Tyr-OH (**5**)

LIST OF ABBREVIATIONS

AFM	Atomic Force Microscope
2D-GISAXS	2D-Grazing Incidence Small Angle X-ray Scattering
3TCA	terthiophene carboxylic acid
3TDCA	terthiophene dicarboxylic acid
3TBA	terthiophene butyric acid
3TDBA	terthiophene dibutyric acid
5TmDCA	dicarboxylic acid 3-methyl-quinquethiophene
a.u.	arbitrary units
Boc	tert-butyloxycarbonyl
CD	Circular Dichroism
CDCl ₃	Chloroform-d
cmc	critical micelle concentration
cps	counts per second
DCC	Dicyclohexylcarbodiimide
DCU	Dicyclohexyl Urea
DIPC	Diisopropylcarbodiimide
DIU	Diisopropyl Urea
DMSO	Dimethyl Sulfoxide
DMF	Dimethyl Formamide
ESI-MS	Electrospray Ionization Mass Spectrometry
FWHM	Full Width at Half Maximum
FTIR	Fourier Transform Infrared Spectroscopy
HOBt	1-Hydroxybenzotriazole
HCl	Hydrochloric Acid
ITO	Indium-Doped Tin Oxide
Leu (L)	Leucine
MeOH	Methanol
Me	Methyl
M	Molar
Nmoc	Naphthalene-2-methoxycarbonyl
NaCl	Sodium Chloride

NaOH	Sodium Hydroxide
NaHCO ₃	Sodium Bicarbonate
NMR	Nuclear Magnetic Resonance
Ph	Phenyl
pH	- log ₁₀ [H ⁺]
Phe (F)	Phenylalanine
PyBA	1-pyrenebutyric acid
SAXS	Small Angle X-Ray Sattering
SEM	Scanning Electron Microscopy
TEM	Transmission Electron Microscopy
TFA	Trifluoroacetic Acid
TLC	Thin Layer Chromatography
TCSPC	Time Correlated Single Photon Counting
Tyr (Y)	Tyrosine
Trp (W)	Tryptophan
UV-Vis	Ultraviolet-Visible Spectroscopy
XRD	X-ray Diffraction

NOMENCLATURE

θ	(Theta) Angle
λ (Lambda)	Wavelength
\AA	Angstrom
s	Singlet
d	Doublet
t	Triplet
st	Strong
nm	Nanometer
ω	Angular Frequency
τ	Life Time
δ	Chemical Shift
μM	Micrometer (Length)
μL	Microliter (Volume)
γ	Gamma
G'	Storage Modulus

Chapter 1

Introduction

1.1 Supramolecular chemistry: Supramolecular assembly of π -conjugated system

Nature exhibits various self-assembled supramolecular nanoarchitectures including DNA double helices, micelles, liposomes and biological membranes. The chemistry of self-assembled molecules was first defined by Lehn in 'Chemistry Beyond Molecules' and termed as 'Supramolecular Chemistry.'^[1-3] The supramolecular chemistry exploits noncovalent interactions between molecules to form 1D, 2D and 3D architectures. The noncovalent interactions are the driving force for supramolecular assembly which are hydrogen bonding,^[4-8] metal coordination,^[9-13] host-guest,^[14-17] aromatic,^[18-20] charge-transfer,^[21-23] and dipolar interactions.^[9] The subareas of supramolecular chemistry include self-assembled π -conjugated chromophores,^[19,24-29] supramolecular polymers^[30,31] and crystal engineering.^[32] Self-assembly of the π -conjugated system achieves supramolecular nano-architectures which are the most promising functional materials in flexible electronic devices as they are not so expensive. Applications of supramolecular materials are found in field-effect transistors (FET)s,^[29] light-emitting diodes (LED)s,^[33] and photovoltaic cells.^[34] The performance of such organic devices is mainly associated with chemical structure, purity, and morphology of the self-assembled π -conjugated material.

Supramolecular organization of such π -conjugated systems is mainly driven by π - π stacking and H-bonding interactions. In the supramolecular assembly of the π -conjugated system, noncovalent interaction offers precise control in intermolecular π - π contacts with self-correcting and defect free structure which exhibit effective charge transfer through overlapping π -orbitals. Keeping this view in mind, researchers worldwide have developed a variety of molecular building blocks. Recent examples include: tetrathiafulvalene (TTF),^[35-39] discotic molecules such as hexabenzocoronene (HBC),^[40] phthalocyanine (Pcs)^[41] or porphyrin (Pp),^[42-44] fused aromatics like pyrene,^[45] perylene bisimide (PBI),^[46-50] triphenylenes,^[51,52] or azatriphenylenes^[53-55] and conjugated oligomers like oligophenylene vinylene (OPV),^[50,56-61] oligofluorene (OF)^[62] or oligothiophene (OT),^[63,64] among others. The structural diversity of supramolecular building blocks modulates

intermolecular interactions for a self-assembled system and hence produces engineered nanostructures with distinct morphologies which give alteration in photophysical, electrical and mechanical properties. The mechanism of self-assembly of small functional molecules into supramolecular polymers in solution or in the solid state is also exploited. Three mechanisms for supramolecular polymerization have been envisaged, that is, ring-chain, isodesmic and cooperative self-assembly.^[65–70] In isodesmic assembly, there is a gradual increase in the number and length of the aggregated species, and it is only at high concentrations or for high association constants that long, nanometer-sized objects are formed. In the case of cooperative self-assembly, there is a bimodal distribution of monomers and elongated objects.

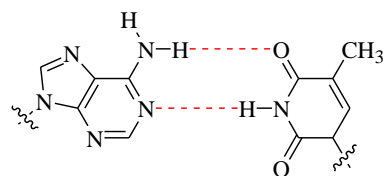
1.2 Noncovalent interaction

One of the most important aspects of supramolecular chemistry is the understanding and the ability to exploit non-covalent interactions for the controlled and reversible assembly of functional entities. These intermolecular interactions include (a) electrostatic interactions (ion-ion, ion-dipole and dipole-dipole interactions) and coordinative bonding (metal-ligand) (b) hydrogen bonding (c) π - π stacking and (d) Van der Waals forces. Among the non-covalent interactions, the hydrogen bonds and, π - π stacking interactions play a crucial role in the supramolecular organization of π -conjugated systems. A brief account of hydrogen (H) bonding and π - π stacking interactions is described below.

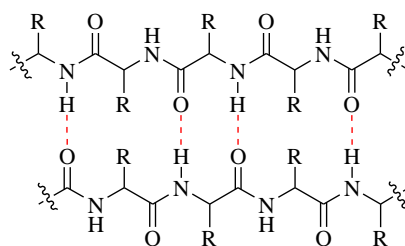
1.2.1 Hydrogen bonding

Hydrogen bonds (H-bonds) are ideal noncovalent interactions to construct supramolecular architectures since they are highly selective and directional.^[71,72] H-bonds are formed when a donor (D) with an available acidic hydrogen atom is interacting with an acceptor (A) carrying available nonbonding electron lone pairs. The strength depends mainly on the solvent and number and sequence of the H-bond donors and acceptors.^[73] In order to construct a significant amount of desired H-bonded assemblies, high association constants are required. In many cases, however, relatively weak hydrogen bond interactions are used so that additional supramolecular

interactions are required to obtain nanosized assemblies. Figure 1.1 shows hydrogen bonding interaction in biomolecules.



H-bonding between nucleobases



H-bonding in peptides

Figure 1.1. Hydrogen bonding interaction (Red dots)

1.2.2 π - π stacking:

The interaction between two aromatic rings is commonly defined as π - π interactions or π stacking. This aromatic interaction is nothing but an electrostatic interaction between π clouds/orbitals of differential polarization of a pair of aromatic molecules. A face-centered stacking is possible if an aromatic pair possesses strongly electron withdrawing groups that polarize pi electron density away from the aromatic core relative to an underivatized aromatic, such as benzene or naphthalene. In such cases, face centered stacking is accompanied by close contact between π orbitals of adjacent molecules, resulting in varying π -orbital mixing. The π -stacking is significant when the interaction originated from alternating stacking between an electron deficient aromatic and electron rich aromatic. This is also referred as “aromatic donor-acceptor interaction”. The various modes of stacking interaction are described in Figure 1.2.^[74]

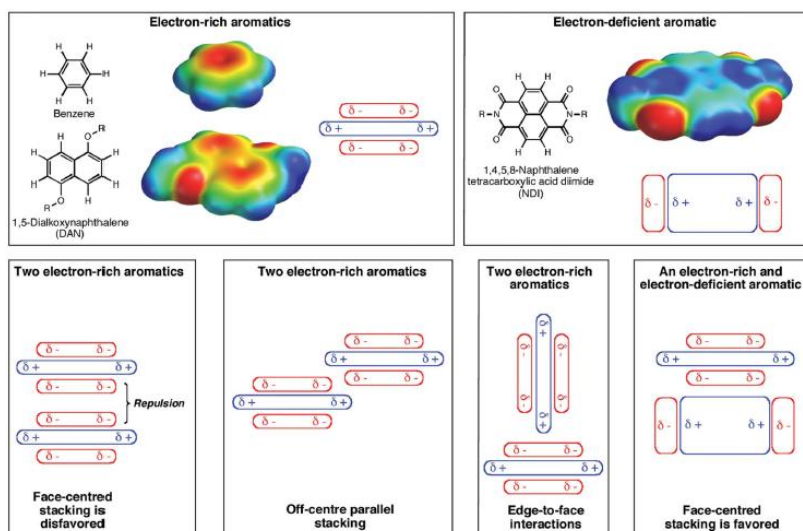
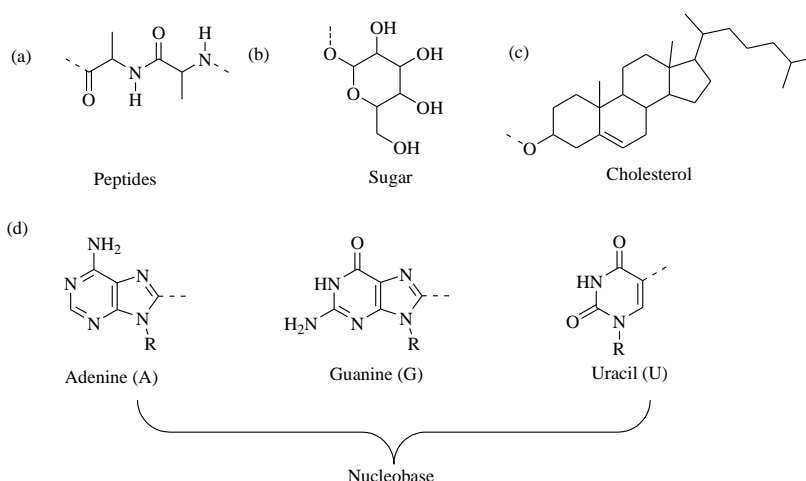


Figure 1.2. Schemes describe the electrostatic view of aromatic interactions. The various modes of stacking are presented, emphasizing locations of electrostatic attraction or repulsion. (Ref: 74).

1.3 Supramolecular construction of optoelectronic π -conjugated biomolecules

Chart 1. Chemical structure of a few bio motifs



Molecules with structural motifs amino acids, peptides, sugar, nucleobases, and cholesterol (Chart 1) have been found to facilitate assembly of the π -conjugated system. In the majority of cases, the presence of functional groups such as hydroxyl, amides, carboxylic acid in bio motifs are capable of

forming several intermolecular noncovalent bonding interactions. For instance, a group of Meijer has demonstrated bi-functionalized nucleotide-appended oligo-(*p*-phenylene vinylene) (OPV) which undergoes programmed assembly right-handed helical stacks to nanofibre (Figure 1.3).^[75] Carbohydrates are also attractive biomolecule to facilitate assembly of the π -conjugated system. Carbohydrate contains a significant number of hydrogen bonding sites ($-OH$ groups) which participate in hydrogen bonding interaction and triggers the self-assembly process. An example of such carbohydrate functionalised π system includes peptide-tetra(*p*-phenylene).^[76]

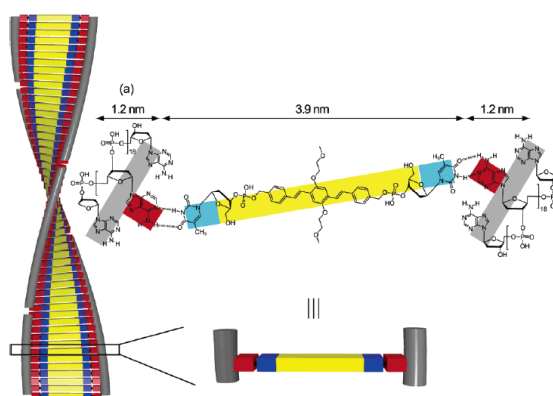


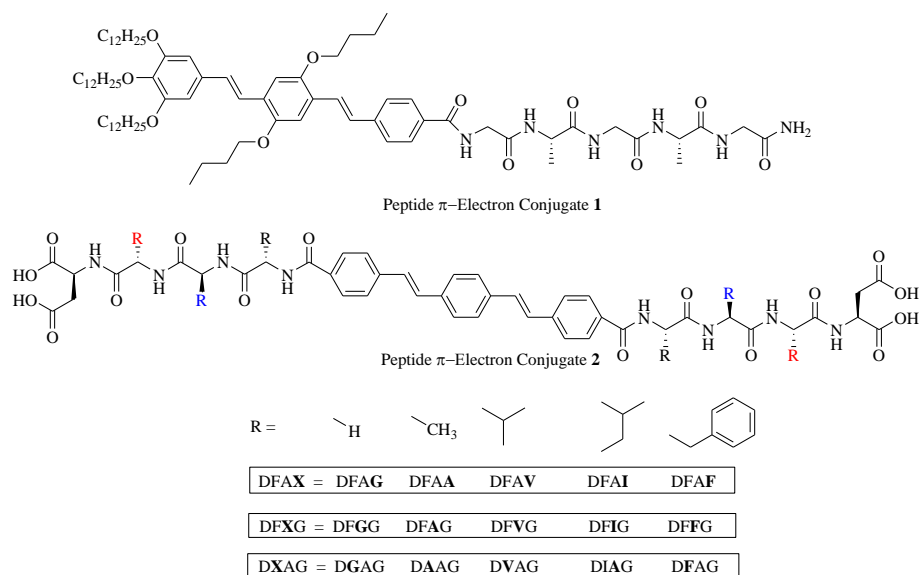
Figure 1.3. The proposed structure for the binary self-assembly of nucleotide-appended oligo-(*p*-phenylene vinylene) (OPV). (Ref: 75).

1.4 π -Conjugated peptide

Peptides are mostly studied as bio motifs for the biomolecule assisted supramolecular assembly of the π -conjugated system. Due to the intrinsic ability of peptides to self-assemble, several types of conjugated π -systems have been functionalized with peptides to further control specific intermolecular interactions that give rise to distinct assembly architectures and electronic delocalization. Herein, current examples of oligopeptide- π conjugated system such as (a) oligopeptide-oligo(*p*-phenylenevinylene) (OPV), (b) oligopeptide-oligothiophene, (c) oligopeptide-perylene diimide (PDI), (d) oligopeptide-naphthalene diimide (NDI) have been described in brief.

1.4.1 Peptide-oligo(*p*-phenylene vinylene)(OPV) conjugates

Chart 2. Molecular structures of peptide-oligo(*p*-phenylene vinylene)(OPV) conjugates:^[57,77]



Among the different classes of organic π -electron system, self-assembly of linear π -systems is at center stage due to favorable optical and electronic properties, useful to the design of organic electronic devices. The self-assembly of *p*-phenylene vinylenes, a linear π -system, has been extensively studied by several research groups over the years due to both its fundamental and technological importance. Meijer *et al.* reported GAGAG-OPV conjugate **1** (Chart 1) which consist of π -conjugated oligo(*p*-phenylene vinylene) trimer and glycylalanyl-glycylalanyl-glycine (GAGAG) pentapeptide. GAGAG pentapeptide sequence was especially adopted for β -sheet domains. The self-assembly of GAGAG-OPV has been studied in liquid-solid interfaces as well as in aqueous solution. In liquid-solid interfaces, STM images of GAGAG-OPV show the formation of bilayerlike supramolecular structures (Figure 1.4b). These structures consist of GAGAG-OPV molecules that are stacked antiparallel next to each other. Each bilayer contains three rows in which the bright rods correspond to the OPV part (highest tunneling efficiency) of GAGAG-OPV, whereas the darker line in between is related to the peptide part. The peptide backbone is fully extended on the graphite-forming a β strand of which successive strands are formed in an antiparallel β sheet held together by six hydrogen bonds (Figure 1.4a). In aqueous solution,

the supramolecular aggregates of GAGAG-OPV produce a network of bundled fibers of micrometer length and having a width up to 0.2 μm on a mica surface (Figure 1.4c).^[57]

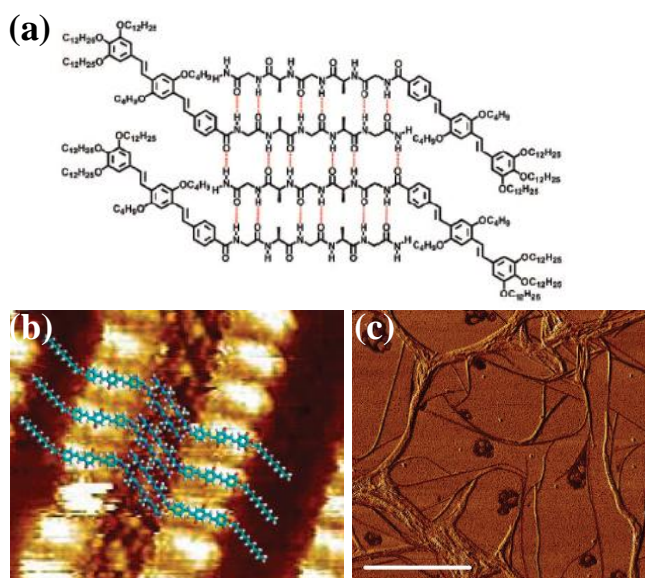


Figure 1.4. (a) The molecular structures of an antiparallel β -sheet conformation of a peptide-OPV conjugate **1** monolayer, (b) STEM images of **1** at the 1-octanoic acid-HOPG interface with a superimposed molecular model, (c) AFM images of nano-fibrillar aggregates of **1**. (Ref: 57).

In the case of oligopeptide-OPV conjugate **2**, three families of π -conjugated peptide nanomaterials with primary amino acid sequences that differ in their size and their “hydrophobicity” were synthesized from a common OPV core structure. The spectroscopic study and molecular stimulation suggested that variations introduced into the amino acid side chains at specific residue locations along the molecular peptide backbone lead to pronounced changes in the photophysical behavior of the fibrillar structures (Figure 1.5). These substitutions vary both in their relative size and in their hydrophobic nature, which impact the intermolecular interactions and influence hierarchical fibrillization processes. Chart 2 shows the three different series of peptides referred to as DFAX, DFXG, and DXAG, where the aspartic acid residue (D) remains unchanged and serves as a pH trigger for assembly, X denotes the location and identity of the amino acid substitution (Gly/G, Ala/A, etc.), and R indicates the specific side chain variation (H, Me, Ph, etc.). The sequence variations with glycine (G, R = H), alanine (A, R =

CH₃), valine (V, R = CH(CH₃)₂), isoleucine (I, R = CH(CH₃)(CH₂CH₃)), and phenylalanine (F, R = CH₂Ph) to perturb the internal structure of the assemblies and nature of the associated electronic delocalization. A systematic increase in the size of the residue leads to progressively less π -electron overlap due to increased OPV spacing resulting from steric crowding imposed within 1-D tapelike assemblies. The progressively more hydrophobic residues also encourage more intermolecular van der Waals-type attractions among the larger hydrophobic groups in lieu of aqueous environment, a well-established factor in the formation and stabilization of amyloid-based materials, leading to decreased OPV spacing and strengthened electronic coupling. In the three families of peptide variations, the placement of the residues with respect to the OPV core and the large and aromatic phenylalanine (F) residue of the parent DFAG structure. This allows for a survey of the optoelectronic influences of situation demanding residues on the same face of the formed nanotapes as the constant phenylalanine (DFAX series) and on the opposite face (DFXG series). The third class (DXAG series) is presented that assesses aliphatic steric bulk well removed from the chromophore unit. With these three families, the complicated interplay of steric and hydrophobic influences that elicits dramatic variation in the electronic coupling of the OPV cores within the peptidic nanostructures is described.^[77]

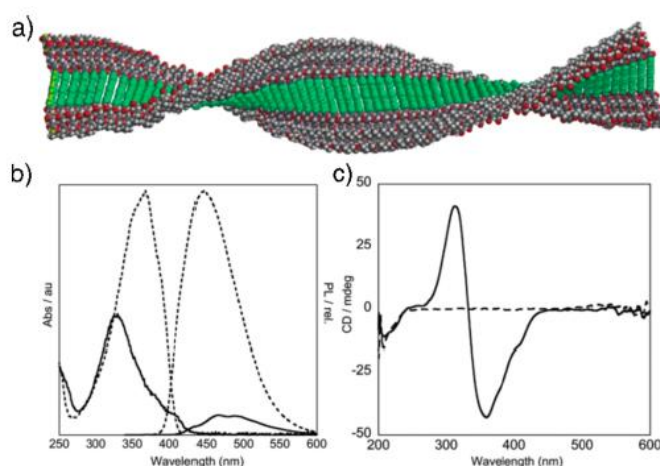
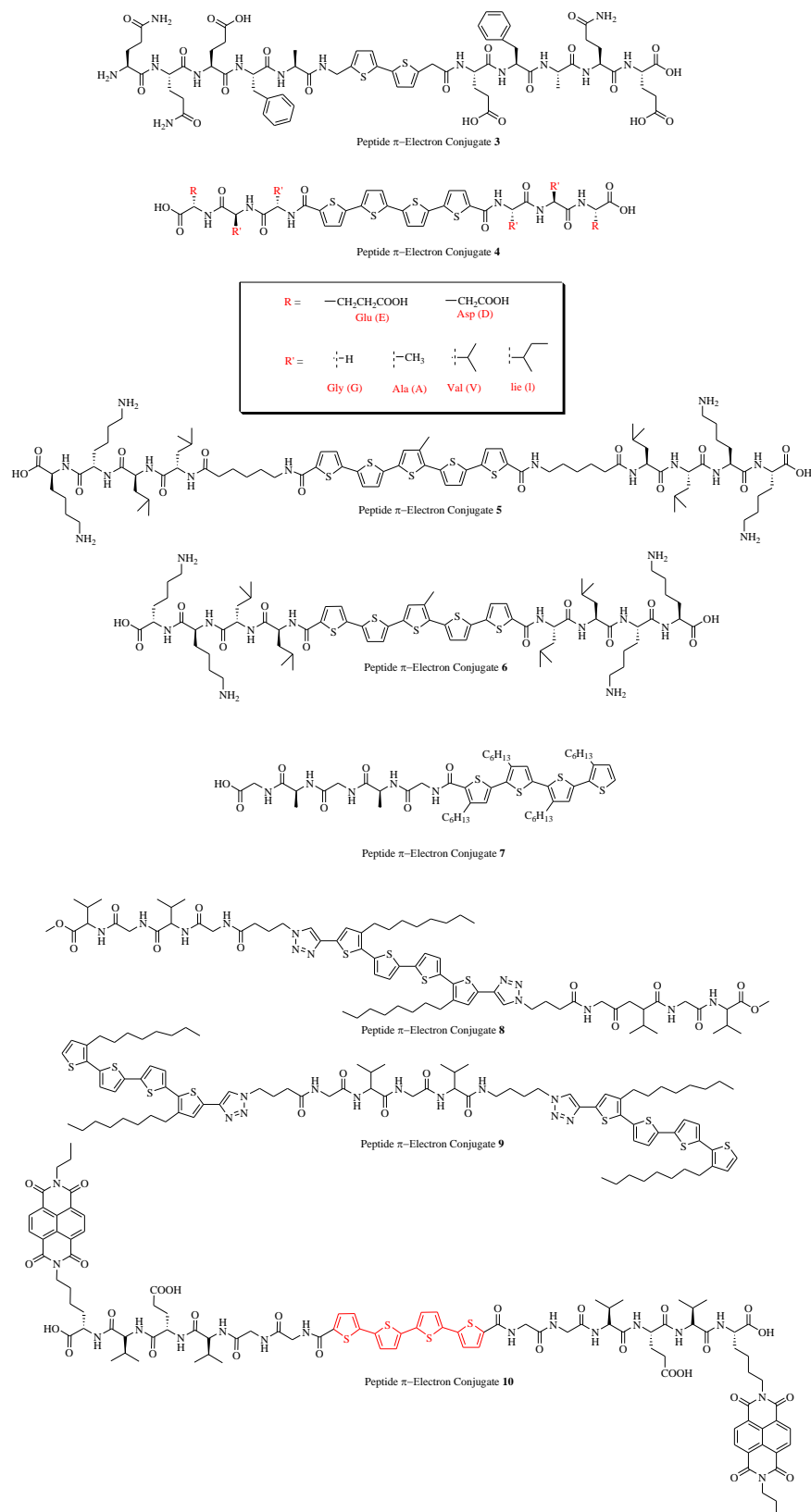


Figure 1.5. (a) Energy-minimized model of a 1-D nanostructure expected after self-assembly and (b) representative UV-vis/PL and (c) CD spectra of a peptide-OPV conjugate in basic, molecularly dissolved (---) and acidic, assembled solutions (—). (Ref: 77).

1.4.2 Peptide-oligothiophene conjugates

Chart 3. Molecular structures of oligothiophene-peptide conjugates:^[78–83]



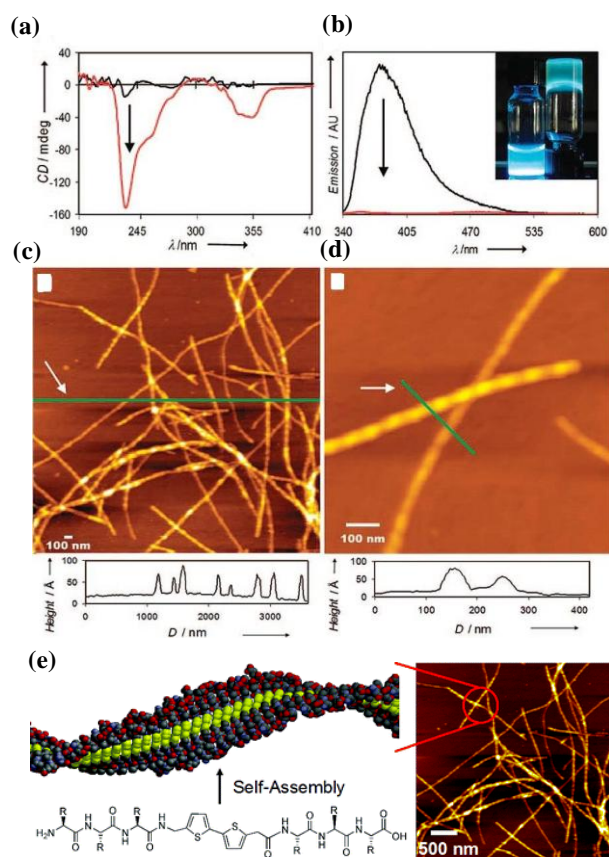


Figure 1.6. (a) CD (b) fluorescence of **3** in basic (dissolved, black traces) and acidic (assembled, red traces) solutions. The inset of panel B depicts a concentrated solution (left) and a gel (right) irradiated at 365 nm. Tapping-mode AFM images and height profiles of the indicated line trace of (c) large area and (d) isolated structures formed after assembly and deposition on freshly cleaved mica surfaces. (e) Supramolecular assembly of oligothiophene-oligopeptide conjugate **3** (Ref: 78).

Oligothiophenes are another attractive linear π -conjugated system useful in numerous applications in optoelectronic devices. Peptide-oligothiophenes are also studied extensively. The first example of an oligothiophene-peptide conjugate is **3**, presented in chart 3. The peptide embedded bithiophene π -conjugated oligomer undergoes self-assembly into 1-D nanostructures with the strong π - π intermolecular electronic communication under completely aqueous and physiologically relevant conditions. Circular dichroism (CD) of assembled **3** shows intense absorptions only associated with the π -conjugated unit (Figure 1.6a). Molecularly dissolved **3** exhibited a low-energy absorption λ_{max} at 320 nm. Excitation at 320 nm triggered strong photoluminescence at 380 nm (Figure 1.6b). Upon assembly, the absorption profile remained comparable but the emission was dramatically quenched. The

bisignate CD response crossing over at 320 nm (coincident with the absorption λ_{max}) is a classic signature for exciton-coupled chromophores in chiral environments. Atomic force microscopy (AFM) of gel samples deposited on mica revealed 1-D nanostructures with heights ranging from 2 to 6 nm (Figure 1.6c,d).^[78]

In oligothiophene-oligopeptide conjugate **4**, a set of oligothiophene-oligopeptide conjugate were designed by varying the amino acid residue with a common 4T core to investigate both the current and voltage transmission activities of one-dimensional π -conjugated peptide nanostructures. Tripeptide- π -tripeptide triblock system consisting of quaterthiophene (4T), a hole-transporting organic semiconductor, as the central π -system and the tripeptide segment, a negatively charged amino acid (aspartic acid, D, or glutamic acid, E) at the distal termini and aliphatic dipeptides (glycine, G; alanine, A; valine, V; isoleucine, I) near the π -core. Eight 4T bis(tripeptide) (chart 3) observed to have pH-triggered assembly behavior under acidic conditions and formation of 1D nanostructures. All peptide sequences show well-connected nanostructures in the gel form, as found in the transmission electron microscopy (TEM) images. Alanine-containing peptides exhibit the largest nanostructure in widths (Figure 1.7). The nanostructure assembly and macroscopic film morphology both are crucial features for determining electronic signal transmission. A remarkable change in photophysics of 4T is observed with the variation of amino acid residue at terminal tripeptides of both ends of 4T core. This is because of the differences in local packing order and contact of π -electron units within each assembled nanostructure. All eight peptides studied form 1D nanostructures that are microns in length, 3-12 nm in width, varied network connectivities in gel and solution state, and varied surface roughness in the microscale (for drop-cast films). The semiconducting behavior of the 4T cores are bound within peptide environments with different hydrophobicities, the deposited thin films of peptide nanomaterials as semiconducting layers in bottom-gate OFET configurations. All of the peptide 4T nanowires exhibit semiconductor characteristics, but the mobility values differ by 3 orders of magnitude upon varying amino acids adjacent to the 4T semiconductor. To reveal impacts of molecular variation on nanostructure-dependent transport

properties, one-dimensional peptide nanostructure analogue of peptide-4T-peptide was chosen as a control sample. When the controls were used as the semiconducting layer, no apparent gating effects were observed. This supports the premise that the 4T-containing nanostructures in the film provide charge-transport pathways that do not merely rely on ionic effects and in fact require the presence of hole-transporting 4T subunits.^[79]

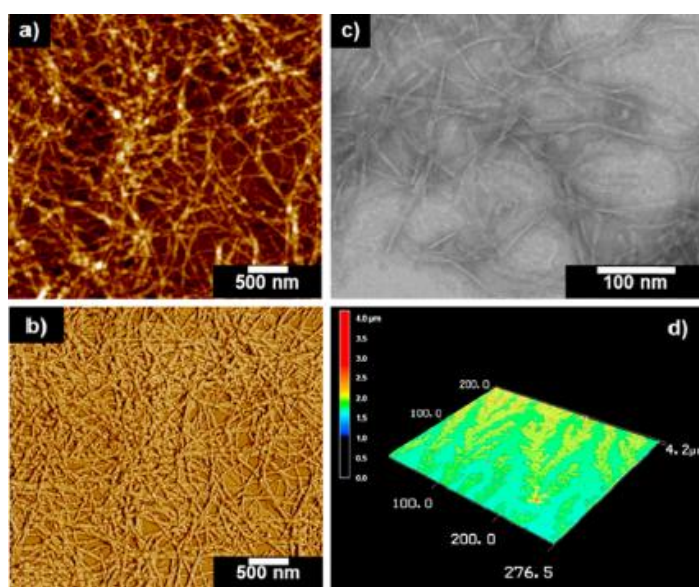


Figure 1.7. AFM image of 0.1 mg/mL drop-cast film of assembled EAA-4T peptide, (a) height and (b) phase profiles; (c) TEM image of 1 mg/mL solution of acidified EAA-4T solution (width = 8.9 (2.4 nm); (d) surface profile of a 10 mg/mL drop-cast film of EAA-4T under a laser microscope. (Ref: 79).

In the third example, oligopeptide-oligothiophene conjugates **5** and **6** consist of a symmetric bolaamphiphile that has three segments: an outer region of polar amino acids for solubility, β -sheet forming amino acids for self-assembly, and an oligothiophene core for conductivity (chart 3). Lysine residues have been included giving the molecule a net positive charge to impart solubility. Leucine has been used for its high propensity to form β -sheets. Quinquethiophene has been chosen as the central segment of the molecule due to its π - π stacking and conductive properties. The basic difference between **5** and **6** is that **5** includes an alkyl spacer between the amino acid segment and the thiophene core added for molecular flexibility where as **6** does not contain alkyl chain. Hydrogen bonding occurs over longer length scales than π - π stacking, so a flexible linker facilitates β -sheets

formation and π - π stacking within a supramolecular nanostructure. Both **5** and **6** were found to form self-supporting gels in water at low concentrations (1 wt %) and corresponding 1 D nanostructure present within the gel as revealed by TEM. Peptide segments (LLKK) in 5T-peptide is capable of forming β sheet domain whereas **6** does not for β sheet due to lack of molecular flexibility in absence of alkyl spacer between the amino acid segment and the thiophene core of 5T-peptide **6**. Therefore, this study shows that addition of an alkyl spacer between extended π -conjugated core and the peptide residue allows both π - π stacking and β -sheet formation to coexist. Without an alkyl spacer, π - π stacking has been found to dominate the aggregation and suppress β -sheet formation.^[80]

In this example, oligopeptide-oligothiophene conjugates **7** (chart 3) is a diblock-oligomer, combining a regioregular head to tail oligo(3-alkylthiophene) (HT-O3AT) and an oligopeptide sequence. The conjugated oligomer part is a tetramer, head-to-tail coupled tetra(3-hexylthiophene) (4T), which is functionalized by the pentapeptide sequence glycine-(L-alanine)-glycine-(L-alanine)-glycine (GlyAlaGlyAlaGly, GAGAG) inspired by Bombyx mori (silkworm) silk.^[81] AlaGly has been identified as the most important repeat sequence in the crystalline β -sheet domains that is dominated by multiple hydrogen bonding and provides the strength of the silk fiber. On the other hand, on substrates such as graphite, β -alkylated oligothiophenes typically form highly organized, lamellar-type 2D-assemblies. This process is driven by relatively weak and unspecific van der Waals interactions of the alkyl side chains.^[84,85] The significant difference between GAGAG-4T and 4T-COOH was noted with respect to their 2D-ordering which might be due to the tendency of the peptide sequence in GAGAG-4T to form β -sheets via multiple hydrogen bonding. Scanning tunnelling microscopy (STM) investigations on the hybrid molecule at the solid/liquid interface reveal completely novel features and superstructures, which explicitly differ from those of the parent compound 4TCOOH.

In the oligothiophene-oligopeptide system **8-9** (Chart 3), the hybrid composed of quaterthiophene and tetrapeptide (Gly-Val-Gly-Val) were designed, namely peptide-thiophene-peptide (PTP) and thiophene-peptide-thiophene (TPT), to investigate the influence of peptide content ratio and its

location in the molecular structures on the nanostructures and properties of the assemblies. Both conjugates formed organogels consisting of left-handed twisted nanostructures; however, anti-parallel β -sheets were observed in PTP while parallel β -sheets were obtained for TPT, although in both cases oligothiophenes adopted an H-like stacking mode. The self-assembly of oligopeptide–oligothiophene conjugates **8-9**, the competition of H-bonds and π – π stacking plays a major role. PTP and TPT display different assembly behaviors in organic solvents (Figure 1.8). For PTP assemblies, every PTP molecule could form anti-parallel β -sheet via 16 pairs of H-bonds with other PTPs, although hydrogen bond interaction belongs to weak non-covalent interactions. However, for TPT assemblies, only six pairs of H-bonds were formed per TPT. The resultant intermolecular noncovalent interaction (H-bonds and π – π stacking) in TPT assemblies is weaker as compared to PTP assemblies.^[82]

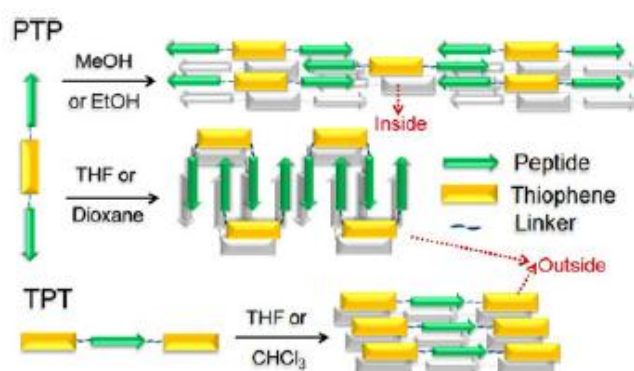


Figure 1.8. Self-assembly mode of PTP and TPT in different organic solvents. (Ref: 82).

One of the current reports in such peptide-chromophore conjugate system is photoinduced electron transfer within supramolecular donor-acceptor peptide nanostructures under aqueous conditions (Figure 1.9). In the peptide-oligothiophene conjugate system **10** (chart 3), modified peptides contain π -conjugated oligothiophene electron donor cores that are peripherally substituted with naphthalene diimide electron acceptors installed via imidation of site-specific lysine residues. These molecules self-assemble into one-dimensional nanostructures in aqueous media, as shown through steady-state absorption, photoluminescence, and circular dichroism spectra, as well as

transmission electron microscopy. Excitation of the oligothiophene donor moieties results in electron transfer to the acceptor units, ultimately creating polar, charge-separated states that persist for over a nanosecond as observed with transient absorption spectroscopy.^[83]

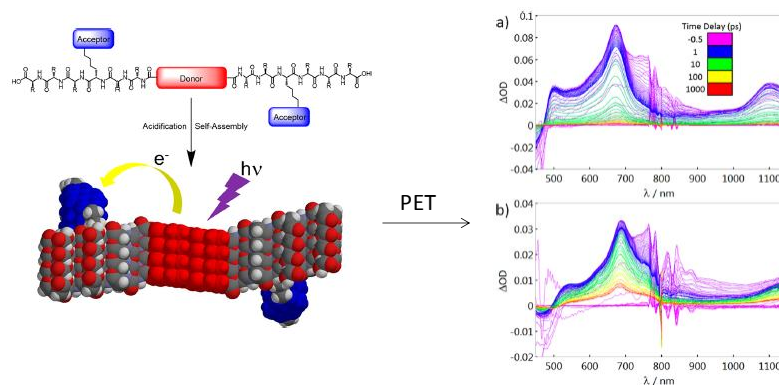
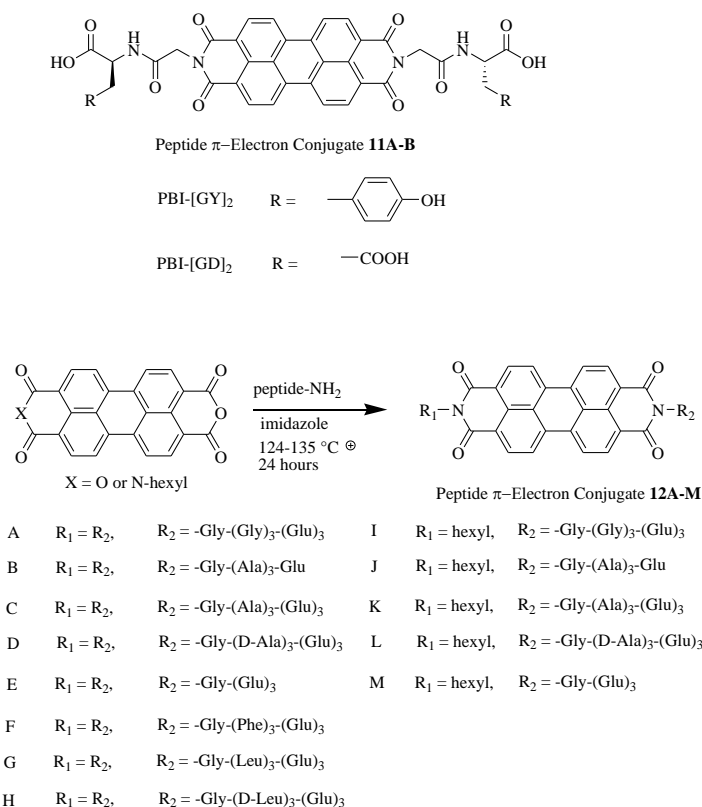


Figure 1.9. Self-assembly and electron transfer of a donor-acceptor π -peptide hybrid (left). Spectral dynamics following photoexcitation of (a) unassembled and (b) assembled **10** at 400 nm (right). (Ref: 83).

1.4.3 Peptide-perylenediimide (PDI) conjugates

Chart 4. Molecular structure of PDI-peptide-conjugates:^[86,87]



The peptide-PDI conjugates 11A-B (Chart 4) bearing two hydrophilic peptide side groups possessing chiral self-assembly (Figure 1.10). Among the different peptide substitutions, chiral nanofibers can only be formed from 11A through self-assembly in an aqueous buffer or organo-gelation method.^[86]

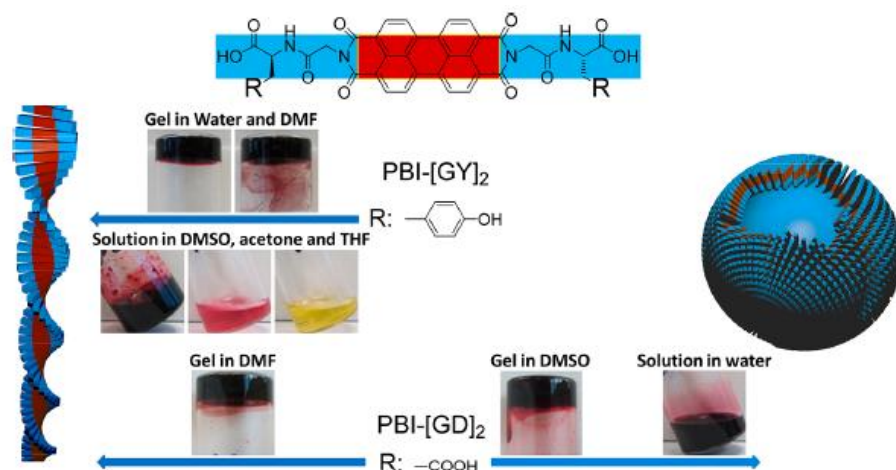


Figure 1.10. Self-assembly of PBI-[GY]₂ and PBI-[GD]₂ to chiral fibrous and spherical structures in different polar solvents :PBI-[GY]₂ forms fibers in buffer solution (pH 10.8), DMSO, DMF, THF, and acetone. PBI-[GD]₂ forms fibers in DMF and spheres in water and DMSO. Inset photographs are PBI-[GY]₂ gels in buffer solution (pH 10.8) and DMF, solutions in DMSO, acetone, and THF, PBI-[GD]₂ gels in DMF and DMSO, and solution in buffer solution (pH 10.8). (Ref: 86).

In peptide-PDI conjugates **12**, a detailed account of the role of peptide on the assembly of perylene diimide is described in terms of thermodynamic parameter by Hodgkiss *et al.* To investigate the effect of peptide sequence on the self-assembly of peptide-PDI conjugates, a set of conjugates with widely varied structural features was synthesized consisting of the following three strategic peptide regions highlighted in : (i) a glycine unit presents a reactive terminal amine and low steric demand efficiently condensing with perylene anhydride; (ii) a central sequence of three amino acids; and (iii) a terminal glutamic acid region introduces charge that engenders solubility and hydrophilic character. Based on this strategy, the specific peptide sequences shown in Figure 1.11 were synthesized in order to probe the effects of incremental structural variations on the multifaceted interactions that govern peptide-driven PDI assembly. With dipeptide-PDI series 12A-H, conjugates

12I-M featured PDIs with a hydrophobic hexyl chain in place of one of the peptides to engender pronounced amphiphilic character.

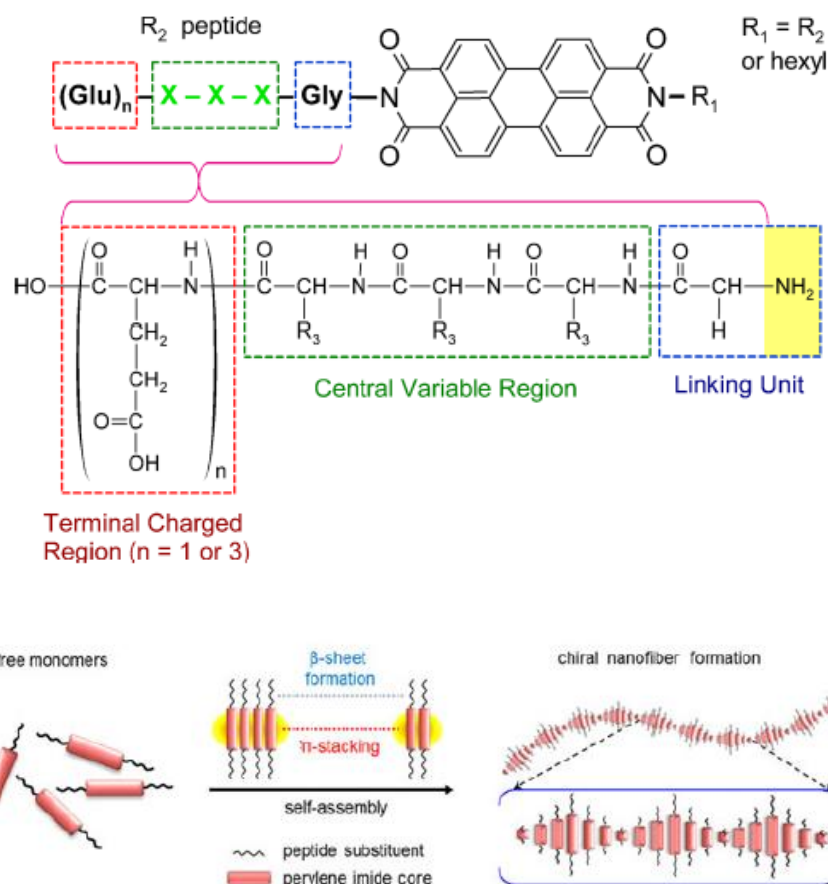


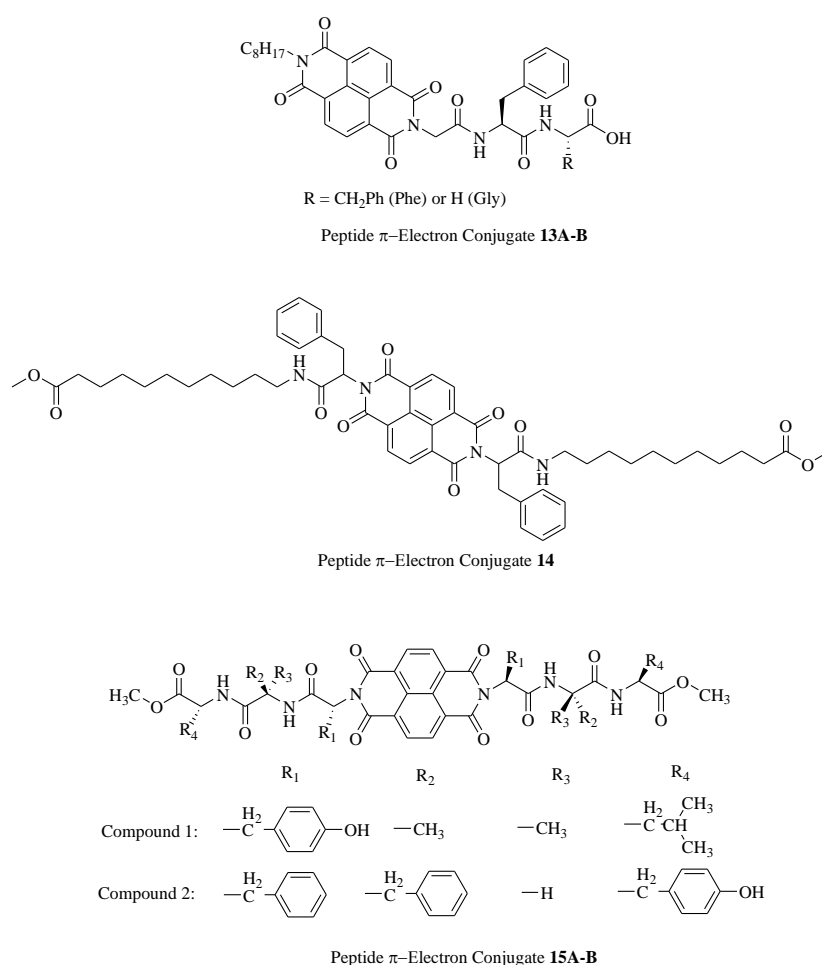
Figure 1.11. Structure of the peptide-PDIs explored in the study (top). Chiral self-assembly in PDI-peptides (bottom). (Ref: 87).

The effect of different amino acids may be considered relative to glycine rich references PDI A (for dipeptide-PDIs A-H) and PDI I (for hexyl-PDIs 12I-M). The impact of increasing the peptide hydrophobicity and the steric demand can be evaluated by comparing PDIs 12A-H, while the effect of replacing one peptide with a hexyl chain is revealed by comparing dipeptide-PDIs 12A-E with their hexyl-PDI counterparts' 12I-M. The effect of charge density can be examined by comparing PDI pairs B/C and J/K, and the effect of peptide length is probed by comparison of A and E. In addition, the diastereomer pairs C/D, G/H, and K/L provide an opportunity to examine the role of stereocenters and specific structure within the peptides. Among the structural variations that have been examined, hydrophobicity and the inclusion of an imide hexyl substituent produce the greatest changes in the

thermodynamic properties. Comparatively smaller influences are seen from changing stereocenter chirality, varying the number of ionizable amino acid residues or the length of the central peptide sequence. This relative importance of the effects that have been examined through comparison of thermodynamic aggregation parameters for various sets of compounds is summarized in Figure 1.11.^[87]

1.4.4 Peptide-naphthalene diimide (NDI) conjugates

Chart 5. Molecular structures of NDI-peptide conjugates:^[88–90]



For asymmetric peptide-NDI conjugate **13**, dipeptide Phe-Phe or Phe-Gly conjugated NDI promotes self-assembly into 1-D nanostructures at physiological conditions whereas Gly-Phe or Gly-Gly conjugated NDI remain silent. These one-dimensional (1-D) nanostructures are stabilized through intermolecular π - π interactions of the conjugated NDI systems and extended hydrogen bonding of the dipeptide units. This study suggested that self-

assembly of the peptide-functionalized NDI is strongly dependent on the nature of peptide and amino acid sequence.^[88] In the case of peptide-NDI **14**, three-dimensional nanofibres are found in CHCl₃ and MCH mixture by H-aggregation mode. A dramatic variation in morphology of self-assembled peptide-NDI conjugate is observed based on amino acid variation in the terminal peptide chain.^[89] The bisimide **15A** containing a core of adjacent aromatic rings and two termini of folded tripeptide moieties (-Tyr-Aib-Leu-OMe) adopts a dumbbell shape conformation, and it self-assembles through noncovalent interactions to promote microspheres. In contrast, the bisimide **15B** containing two termini of extended tripeptide moieties (-Phe-Phe-Tyr-OMe) adopt a wrist band shape structure, and it self-assembles to produce elongated fibrils.^[90]

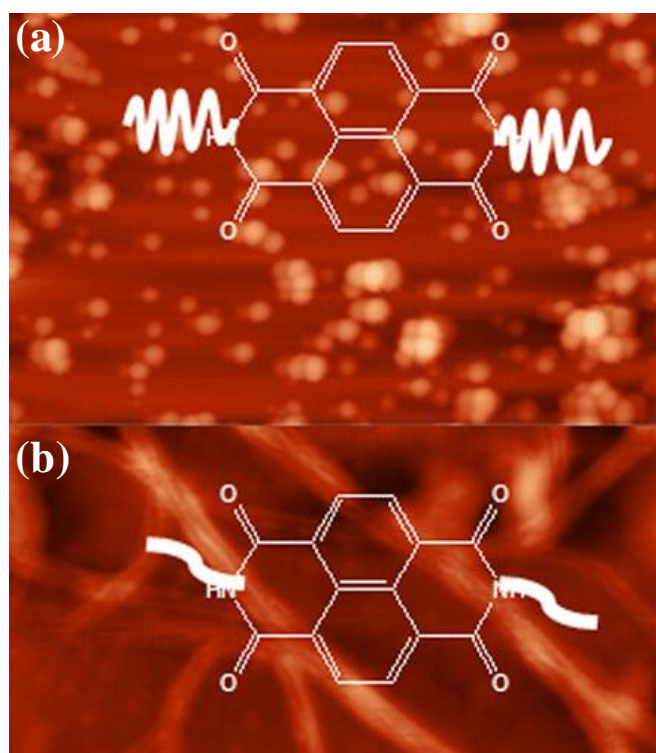


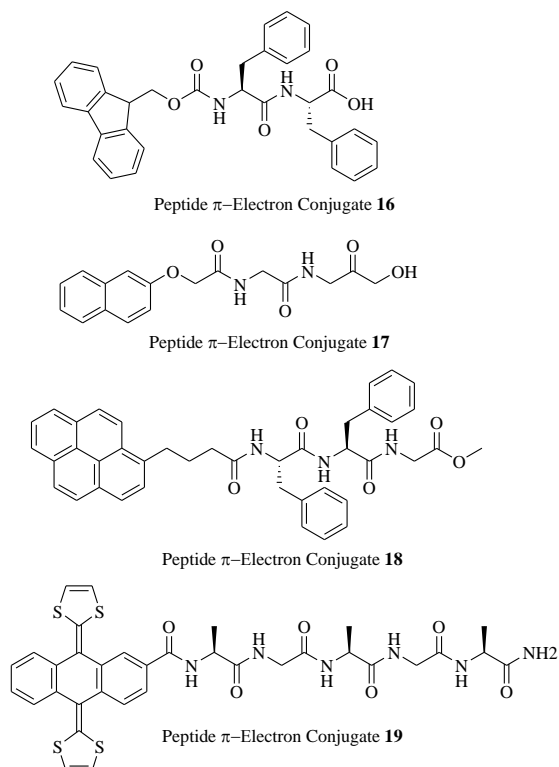
Figure 1.12. AFM images of (a) bisimide **15A** microspheres and (b) bisimide **15B** nanofibers. (Ref: 90).

1.4.5 Other peptide small π -electron conjugates

Self-assembling peptides coupled with the small aromatic unit such as fluorenyl-9-methoxycarbonyl (Fmoc) group, pyrene, naphthalene, TTF and/or with multiple phenylalanine units offer additional π - π interactions that can

guide supramolecular interactions, inspiring a lot of π -conjugated peptides with optoelectronic activity. Chart 6 shows examples of Fmoc-peptide, pyrene-peptide, peptide-naphthalene, and peptide-TTF conjugates.

Chart 6. Molecular structures of different small aromatic dye-peptide conjugate.^[91-94]



Fmoc-diphenylalanine (**16**) self-assemble to form nanocylindrical nanoarchitecture. Nanocylinders are formed by anti-parallel β -sheets interlocked by π - π stacking interactions of fluorenyl groups and phenyl rings. Naphthalene conjugated peptide (**17**) shows ability to form chiral nanostructure *via* self-assembly. Pyrene conjugated peptide (**18**) forms transparent, stable supramolecular fluorescent organogel in various organic solvents. Supramolecular electroactive fibrous aggregates have observed in the case of planer tetrathiafulvalene (TTF) conjugated oligopeptide **19**. This is the first example of hydrogen-bonded one-dimensional aggregates. Hydrogen bonding, π - π stacking, and solvophobic interactions made possible the efficient generation of electroactive helical fibers.

1.5. Supramolecular construction of organic-inorganic hybrid materials

The synergistic assembly of organic/inorganic hybrids offers chemical tunability, novel functionalities and enhanced performance over their individual component. The reason behind this is hybrid materials made up of organic and inorganic components combine the advantages of both the materials while overcoming their respective disadvantages. The major issue in developing such organic-/inorganic hybrids is the choice of cost-effective fabrication technique. To date, a number of fabrication techniques have been used to construct such nanoscale hybrid materials. Examples include gas phase method, sol-gel chemistry,^[95] immiscible liquid-liquid biphasic system,^[96] chemical methods^[97,98] and electrochemical methods.^[99,100] Among these methods, electrochemical self-assembly strategy is found to be a simple, economically cheap and bottom-up approach to a growing desire well-ordered nanoscale organic-inorganic hybrid nanomaterials. In the strategy of electrochemical self-assembly, electrochemistry is coupled with the molecular self-assembly, where self-assembly of organic system holds great prospects to develop nanoscale materials with novel properties. Several small organic molecules have been designed to develop hybrids where chemical structure of the molecule plays several significant roles in determining the structure and the morphology of hybrid films (Table A1). These molecules play three major roles in the hybrid: First, organic molecules behave as a structure directing agent and control the morphology of inorganic component. Secondly, self-assembled organic phase stabilizes the hybrid nanoarchitectures through covalent bonding with the inorganic component. Lastly, it becomes a functional component of organic/inorganic hybrid. The structural diversity of organic component makes it unique among all the other materials. A few research groups have developed such hybrids with varying organic and inorganic components. For instance, Choi *et al.* extensively used only SDS for the fabrication of such hybrids altering the inorganic component.^[101,102] A group of Stupp has developed hybrids composed of π -conjugated organic semiconductor and inorganic ZnO photoconductive materials using electrochemical self-assembly (Figure 1.13).^[103] In another report, Stupp *et al.*

have investigated the internal assembly pattern of organic and inorganic components depending on the chemical structure of the organic molecule and the selection of working electrode substrate.^[104] Maura and co-workers used a number of different organic dyes with ZnO to develop photovoltaics cells.^[105]

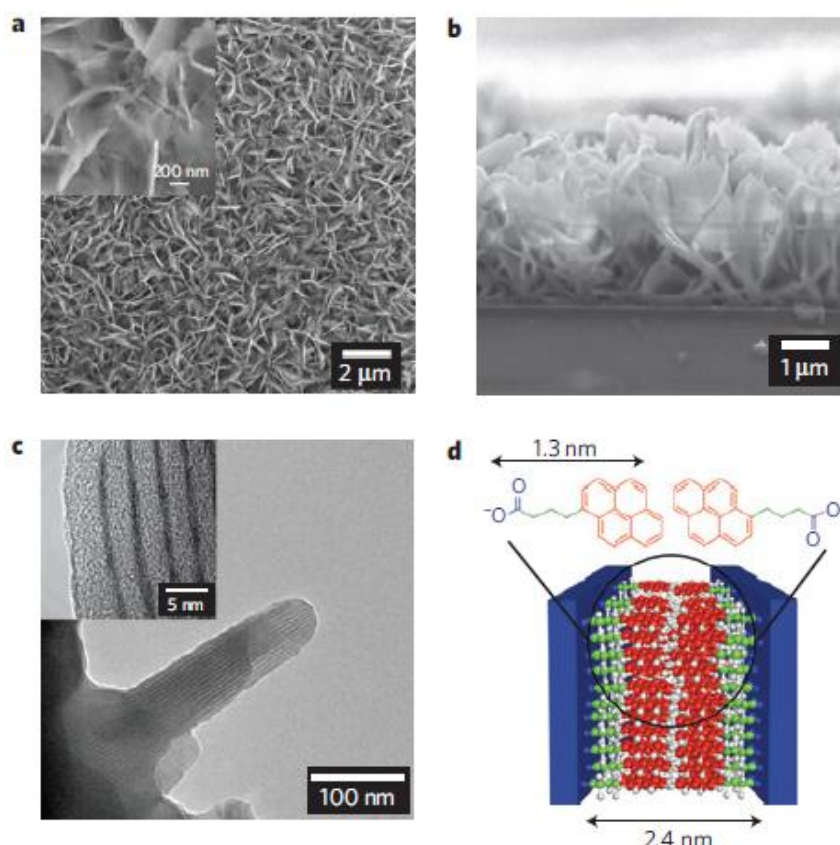


Figure 1.13. Lamellar hybrid nanostructure. (a) SEM (top-down) image of deposited platelets using PyBA, magnified in the inset. (b) SEM (cross-sectional view) image of deposited platelets using PyBA. (c) TEM image of lamellar sheets within platelets deposited using PyBA, magnified in the inset. (d) Schematic diagram of lamellar ordering composed of inorganic Zn-rich regions and bilayers of PyBA. (Ref: 103).

1.6. Characterization techniques for electrochemically triggered self-assembled complex organic-inorganic hybrid nanostructures

To date, a range of experimental methods has been used to study the mechanism of complex hybrid film growth and internal ordering of organic and inorganic components in the hybrid films. In this strategy, mostly a

lamellar hybrid structure is formed. For instance, some basic techniques essential to characterize the lamellar film morphology are Two-dimensional grazing-incidence small-angle X-ray scattering (2D-giSAXS), Transmission electron microscopy (TEM), Scanning electron microscopy (SEM), Fourier-transform infrared spectroscopy (FTIR), High-resolution TEM and TEM electron diffraction. 2D-giSAXS is an excellent technique to characterize hybrid film, which gives information about lamellar orientation on the substrate and interlayer spacing (organic domain) and the thickness of the inorganic wall in the lamellar nanostructure. TEM also gives an idea on the formation of an organic monolayer or bilayer in the hybrid. Furthermore, it helps to understand the growth mechanism of the lamellar structure. TEM gives information about both the organic and inorganic components present in the lamellar structure. While, TEM electron diffraction pattern identifies the nature of inorganic crystals. SEM visualizes morphologies of electrodeposited lamellar hybrid structure. FTIR analyses the binding site of the organic component with the inorganic crystals.

1.7 Organic-inorganic hybrids

1.7.1 SDS-inorganic hybrids

The potential-controlled surfactant assemblies at the interface can be utilized as templates for the production of thin semiconducting and metallic nanostructured films when they are combined with an electrodeposition process. In this aspect, Sodium dodecyl sulfate (SDS) is one of the extensively used organic surfactants in the electrochemical deposition of metal oxides. Surfactants in solution spontaneously aggregate at solid-liquid interfaces due to surface forces (i.e., electrostatic interaction between the surfactant head group and a surface charge).^[106] The assembly patterns of the surface aggregates are frequently different from those formed in free solution.^[107] Among the factors that affect the organization of surfactants on the surface (i.e., the hydrophilicity of the substrate, surfactant types, types of counter ions, and ionic strength), surface charge density are unique in that it can be controlled externally using a bias voltage applied to the substrate. This makes it possible to selectively induce and stabilize phases of surfactant aggregates

by deliberate control of the electrochemical potential.^[108] Potential-controlled surface assembly with an electrodeposition process to fabricate nanostructured films.^[101] In this approach, the surface of the working electrode serves as a solid-liquid interface in a plating solution containing surfactants. When there exists a common potential that can simultaneously induce the desired phase of surfactant-inorganic aggregates and reduce the metal ions, a nanostructured metallic film will be deposited patterned by the surfactant-inorganic aggregates. Figure 1.14a shows a different kind of surface assemblies of surfactants. Phases composed of hemisphere/sphere micelles and hemicylinder/cylinder micelles are suitable to fabricate mesoporous films (i.e., hexagonal, cubic, and disordered porous structures). Few examples of SDS-inorganic hybrids are described in the next section.

SDS/ZnO

In many cases, SDS is used as a surfactant in electrodeposition of nanostructured ZnO films on indium tin oxide (ITO) electrode. In the deposited film with SDS, dramatic changes in shapes and crystallinity of the ZnO deposits happen after a certain concentration of SDS added. The desired X-ray diffraction pattern of ZnO gets lost and the results indicate that the anionic head groups of SDS cooperatively interact with the inorganic species under the deposition condition to form effective in situ templates on the electrode for the production of nanostructure films. The small-angle X-ray diffraction and Transmission Electron Microscopic (TEM) results suggest the presence of lamellar structure in the deposited films (Figure 1.14b). The diffraction pattern indicates the presence of two different phases, one with $d_{001} = 31.7 \text{ \AA}$ and the other with $d_{001}^* = 27.5 \text{ \AA}$, implying two slightly different pathways to form stable surfactant bilayers under our deposition condition. The presence of high-order $00l$ peaks for both phases is indicative of well-defined nanostructures with long-range order. The interlayer spacing and the inorganic wall thickness was estimated to be 15 and 15 \AA respectively. TEM analysis also suggests that 0.1% of SDS, which is below the cmc of pure SDS solution, can fully cover the electrode surface under the deposition condition and effectively templates nanostructures in the ZnO films. Increasing or decreasing the content of SDS in the solution (0.1- 20 wt %) does not influence the surface morphology of the resulting films, suggesting that the

interfacial structure is not significantly affected by bulk surfactant concentration when the surfactant concentration is above surface micelle concentration.^[109,110]

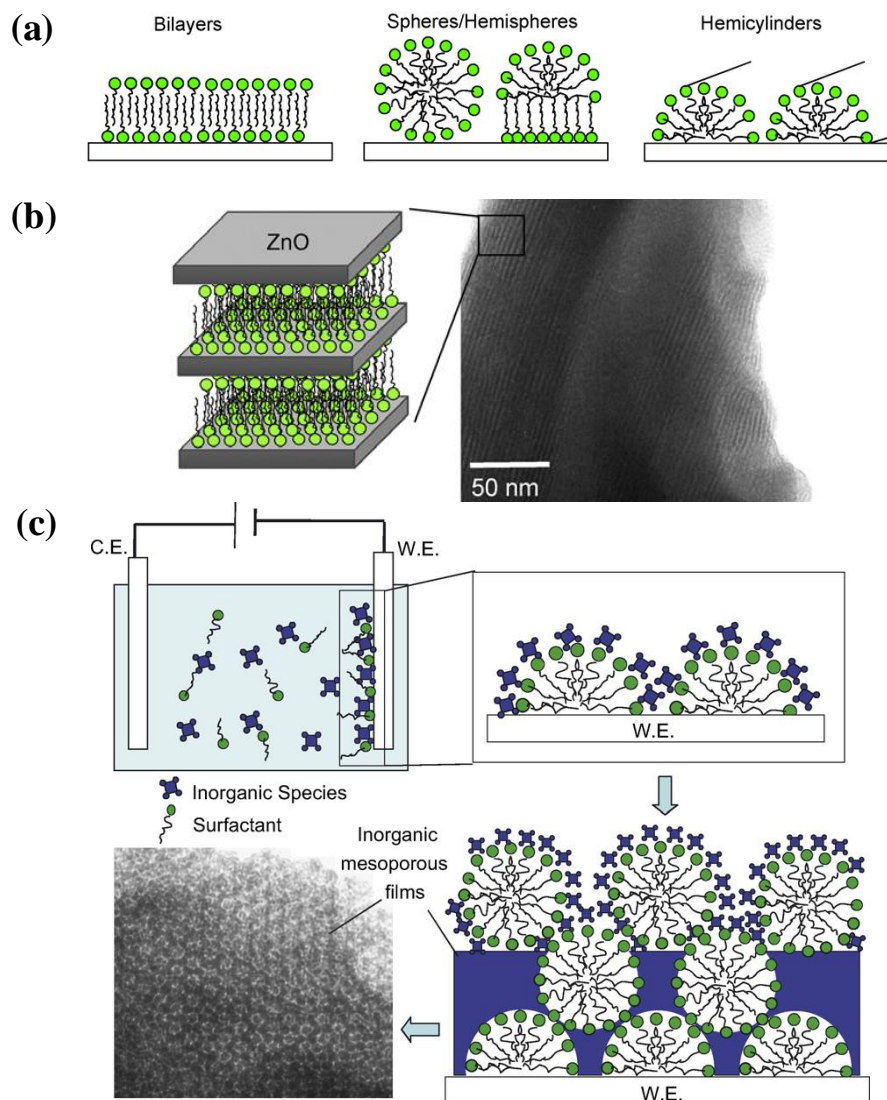


Figure 1.14. (a) Schematic representations of possible surfactant assemblies at the solid-liquid interface.^[111] (b) Lamellar structured ZnO films templated bilayer assembly of surfactants.^[112] (c) An interfacial amphiphilic assembly composed of hexagonally close-packed spherical micelles is used as a template in this scheme.^[112]

SDS/Pt

In another example, mesoporous platinum films produce by coupling potential-controlled self-assembly of surfactant-inorganic aggregates and electrodeposition processes. This method uses extremely dilute surfactant solutions ($< \text{cmc}$) to generate films with accessible pores and thermally stable

frameworks. The resulting films possess high surface areas that lead to enhanced electrocatalytic properties towards methanol oxidation compared to those of non-mesoporous platinum films.^[111]

SDS/Ni(OH)₂

SDS is found to be a useful template in electrodeposition of mesoporous Ni(OH)₂ thin films (Figure 1.15).^[113]

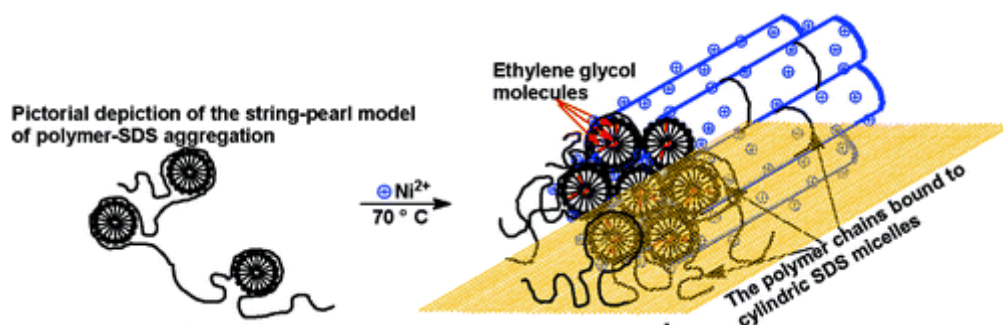


Figure 1.15. Cooperative templating model for the electrochemical synthesis of hexagonal mesoporous Ni(OH)₂ thin films on the surface of working electrode. (Ref: 113).

SDS/SnO₂

Electrochemical synthesis of SnO₂ films containing three-dimensionally organized uniform mesopores via interfacial surfactant templating (Figure 1.16).^[114]

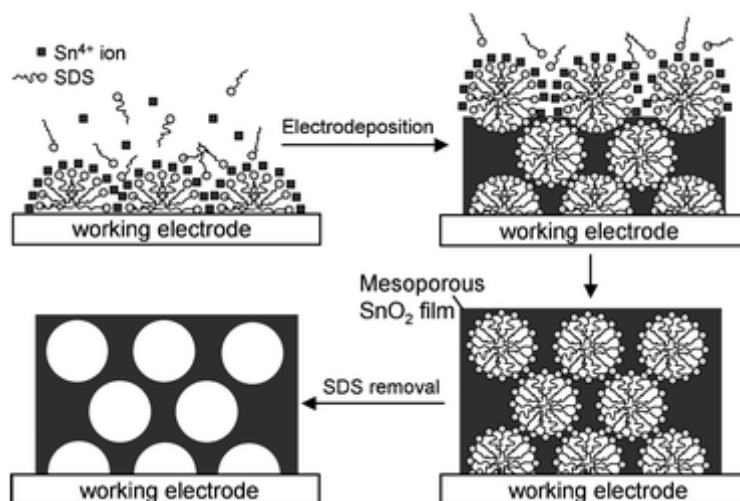


Figure 1.16. Schematic representation of electrochemical interfacial surfactant templating (Ref: 114).

1.7.2 Oligothiophene/ZnO hybrids^[104]

In the electrochemical self-assembly of oligothiophene/ZnO hybrid, Stupp and co-workers have designed and synthesized a family of carboxylated terthiophene-based surfactants with systematic modifications to molecular geometry, valency, and flexibility to investigate how these features affect the synthesis of the p-type/n-type semiconducting hybrid materials (Table A1). Based on the experimental outcomes, it is found that the molecular geometry has a strong influence on the lamellar growth of hybrid film with either bare ITO (hydrophilic surface) or PEDOT:PSS (hydrophobic surface) coated ITO substrates as the working electrode. On investigations, it is revealed that molecules with linear geometry 3TCA and 3TBA each successfully deposit lamellar films on both ITO and PEDOT:PSS substrates, Zn(OH)_2 lamellae were never observed on either substrate when using the T-shaped homologues TAA(T)₂ and TBA(T)₂. The reason is those T-shaped molecules are too wide to allow them to pack with sufficient density to stabilize the inorganic phase by coordinating all the exposed Zn^{2+} sites. 3TDCA and 3TDBA are the divalent homologues of the monovalent 3TCA and 3TBA compounds. 3TDCA and 3TDBA forms monolayered organic phase because divalent molecules can bind two Zn atoms (one at each terminus of the molecule) and are incorporated into the LDH as monolayers instead of bilayers. On the other hand, 3TCA and 3TBA form bilayered organic phase to give rise to lamellar domains. The 3TCA-3TBA and 3TDCA-3TDBA pairs were designed to investigate the effect of installing a flexible linker in the 3T surfactants. The molecules within each pair share the same geometry and valency, but differ in the connection that separates their 3T core from the carboxylic acid. 3TBA and 3TDBA have a hydrocarbon linker that separates these two groups, whereas the carboxylic acid is directly conjugated to the 3T core in 3TCA and 3TDCA. A comparison between films deposited from solutions with surfactants that have different linkers reveals that both morphology and orientation have a high dependency on surfactant flexibility. The flexible surfactants reveal a much greater orientational dependence on surface chemistry than their rigid homologues. Whereas the rigid surfactants 3TCA and 3TDCA always deposit isotropic films, the flexible surfactants deposit

anisotropic films in all cases except for 3TDBA on PEDOT: PSS. Therefore, monovalent, flexible surfactant design is ideal for achieving substrate-dependent anisotropic lamellar growth to maximize the density, persistence length, and anisotropy of the lamellar films. 5TmDCA/ZnO hybrid is useful material for photoconductor as well as photovoltaics. In comparison, decanoic acid with greater flexibility and aspect ratio greatly enhance the anisotropy of the lamellae film (Figure 1.17).

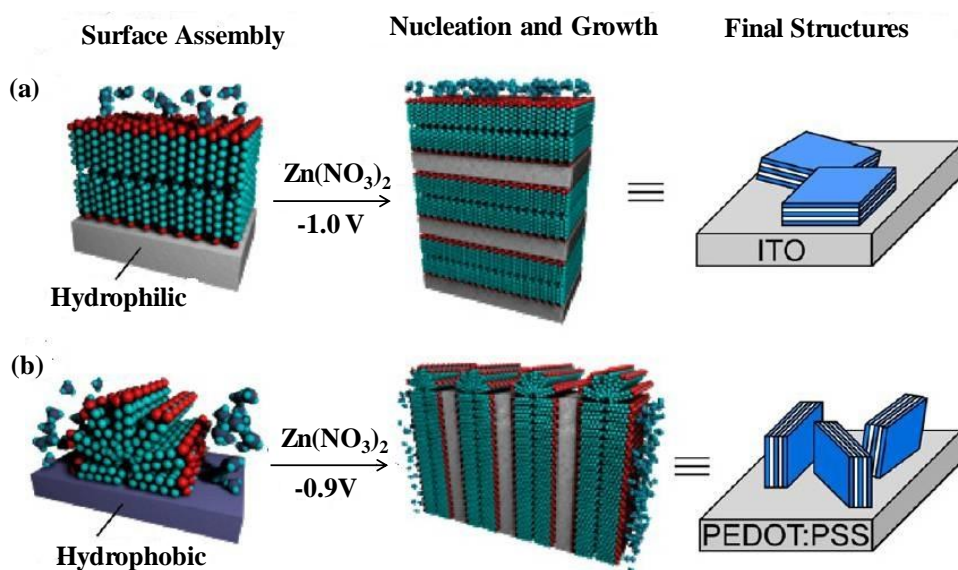


Figure 1.17. Mechanism for the directed growth of different nanoscale lamellar morphologies grew with decanoic acid on different surfaces. (a) A hydrophilic surface such as ITO interacts more favorably with the polar headgroups, resulting in two-dimensional bilayer assemblies at the surface that promotes Zn(OH)_2 nucleation parallel to the substrate. (b) A more hydrophobic surface such as PEDOT:PSS interacts more favorably with the alkyl tails, leading to lower-dimensional assemblies such as hemimicelles, which template the growth of Zn(OH)_2 perpendicular to the substrate. (Ref: 104).

1.7.3 Organic dye/ZnO hybrids

A number of water-soluble organic dyes have been used as an organic component in electrochemical self-assembly of various organic/inorganic hybrid thin films for applications in the field of dye-sensitized solar cells/photoelectrochemical cells. Such organic dyes include Rhodamine B, tetrasulfonated metallophthalocyanines (TSPcMs), eosin Y, $\text{Ru(dcbpy)}_2(\text{NCS})_2$, riboflavin 5'-phosphate, N,N'-bis(ethylenesulfate)-

3,4,9,10-perylene tetracarboxylic acid diimide (Table A1).^[105,115–121] In most of the cases, ZnO has been selected as an inorganic component for the growth of hybrids. All of these dyes contain acidic functional group such as sulphonic, phosphonic, and carboxylic acid which not only makes the molecule soluble but also act as “anchors” to bind to ZnO surface. Anchoring groups have a significant effect on electrochemical self-assembly (ESA) of hybrid thin films.^[122] The adsorption of a dye on ZnO surface is caused by coulombic and van der Waals forces between ZnO and dye molecules. The coulombic force is assumed to arise from the localized electrostatic interaction between Zn^{2+} on the surface of ZnO and the carbonyl groups of the dye molecule.^[123] FTIR studies suggest that characteristic changes were observed for the bands from stretching of the carboxylate group and were attributed to the formation of a chemical bond between the carboxylic acid group of dye and the Zn^{2+} site of the ZnO surface. Investigation shows that chemical stability of dye adsorption and their structure on the ZnO surface can vary from dye to dye to affect the film growth. In the ZnO/dye hybrid thin films, relevant chemical analysis was done by employing three xanthene dyes with different anchoring groups, namely, 2',4',5',7'-tetrabromofluorescein (eosin Y, hereafter abbreviated as EY) as the reference, 5(6)carboxy eosin (dicarboxy-eosin Y, hereafter abbreviated as CEY) having an extra carboxylic acid group at the phenyl group attached to the xanthene frame work and 2',4',5',7'-tetrabromosulfofluorescein (sulfonated eosin Y, hereafter abbreviated as SEY) having sulfonic acid as the anchoring group instead of carboxylic acid. Doubly carboxylated CEY exhibited a much higher stability compared to EY, while sulfonated SEY was weakly adsorptive, when they are compared to their oxidized state.^[124] The concentration of dissolved dye molecules in electrochemical bath affect the growth rate and film properties, while all other parameters remained constant (concentrations of zinc salt and supporting electrolyte, applied potential, temperature, electrode. For instance, in the absence of eosin dye molecule, zinc oxide films are made of individual hexagonal crystallites with flat surfaces. With the introduction of eosin into the solution, the shape of the grain changes dramatically. The morphology of ZnO/dye hybrids appears as a cauliflower-like morphology on its top. The most significant changes occur in the shape and size of grains. For the highest

concentration of eosin, the grains are cylindrical with an almost perfect hemispherical outer surface whose diameter is much larger than at the lowest concentrations.^[121] Electrochemically, self-assembled nanoporous ZnO/eosinY hybrid thin films lead to a large improvement in the dye-sensitized photoelectrochemical performance, achieving an incident photon to current conversion efficiency up to 90 %. The as-deposited R5-P/ZnO thin film electrode exhibited anodic photocurrent upon visible light irradiation, indicating the sensitization of ZnO by incorporated R5-P molecules. A model of electrochemical self-assembly of the ZnO/TSPcM hybrid is shown in Figure 1.18.

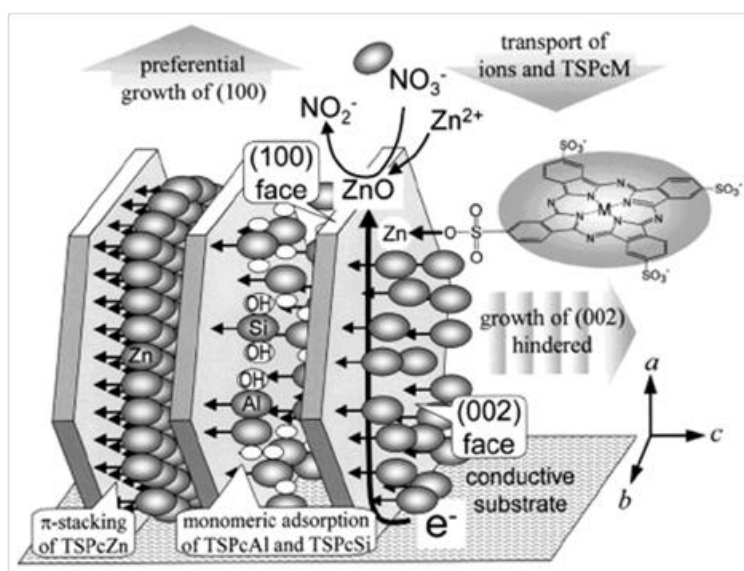


Figure 1.18. Electrochemical self-assembly of the ZnO/TSPcM thin films. (Ref: 105).

1.8 References

- [1] Lehn J.-M. (1985), Supramolecular Chemistry: Receptors, Catalysts, and Carriers, *Science*, 227, 849-856 (DOI:10.1126/science.227.4689.849).
- [2] Lehn J.-M. (1995), Supramolecular chemistry: Concepts and perspectives, Wiley-VCH: Weinheim, Germany.
- [3] Lehn J.-M. (1999) Supramolecular Science: Where It Is and Where It Is Going, (DOI: 10.1007/978-94-011-4554-1).

- [4] Castellano R. K., Rudkevich D. M., Rebek J. (1997), Polycaps: Reversibly formed polymeric capsules, *Proc. Natl. Acad. Sci.*, 94, 7132–7137. (DOI:10.1073/pnas.94.14.7132).
- [5] Sijbesma R. P., Beijer F. H., Brunsveld L., Folmer B. J. B., Hirschberg J. H. K. Ky, Lange R. F. M., Lowe J. K. L., Meijer E. W. (1997), Reversible polymers formed from self-complementary monomers using quadruple hydrogen bonding, *Science*, 278, 1601-1604 (DOI: 10.1126/science.278.5343.1601).
- [6] Sijbesma R. P., Meijer E. W. (2002), Quadruple hydrogen bonded systems, *Chem. Commun.*, 5-16 (DOI: 10.1039/b205873c).
- [7] Keizer H. M., Sijbesma R. P. (2005), Hierarchical self-assembly of columnar aggregates, *Chem. Soc. Rev.*, 34, 226-234 (DOI: 10.1039/b312177C).
- [8] Sivakova S., Rowan S. J. (2005), Nucleobases as supramolecular motifs, *Chem. Soc. Rev.* 34, 9-21(DOI: 10.1039/b304608g).
- [9] Lohr A., Würthner F. (2011), Chiral amplification, kinetic pathways, and morphogenesis of helical nanorods upon self-assembly of dipolar merocyanine dyes, *Isr. J. Chem.*, 51, 1052-1066 (DOI: 10.1002/ijch.201100023).
- [10] Dobrawa R., Würthner F. (2005), Metallosupramolecular approach toward functional coordination polymers, *J. Polym. Sci. A Polym. Chem.*, 43, 4981–4995 (DOI: 10.1002/pola.20997).
- [11] Bellas V., Rehahn M. (2007), Polyferrocenylsilane-based polymer systems, *Angew. Chemie Int. Ed.*, 46, 5082–5104 (DOI: 10.1002/anie.200604420).
- [12] Elhabiri M., Albrecht-Gary A.-M. (2008), Supramolecular edifices and switches based on metals, *Coord. Chem. Rev.*, 252, 1079–1092 (DOI: 10.1016/j.ccr.2007.09.014).
- [13] Friese V. A., Kurth D. G. (2008), Soluble dynamic coordination polymers as a paradigm for materials science, *Coord. Chem. Rev.*, 252, 199–211 (DOI: 10.1016/j.ccr.2007.06.001).
- [14] Yebeutchou R. M., Tancini F., Demitri N., Geremia S., Mendichi R., Dalcanale E. (2008), Host–guest driven self-assembly of linear and star

- supramolecular polymers, *Angew. Chemie Int. Ed.*, 47, 4504-4508 (DOI: 10.1002/anie.200801002).
- [15] Harada A., Takashima Y., Yamaguchi H. (2009), Cyclodextrin-based supramolecular polymers, *Chem. Soc. Rev.*, 38, 875-882 (DOI: 10.1039/b705458k).
- [16] Harada A., Hashidzume A., Yamaguchi H., Takashima Y. (2009), Polymeric Rotaxanes, *Chem. Rev.*, 109, 5974-6023 (DOI: 10.1021/cr9000622).
- [17] Zheng B., Wang F., Dong S., Huang F. (2012), Supramolecular polymers constructed by crown ether-based molecular recognition, *Chem. Soc. Rev.*, 41, 1621-1636 (DOI: 10.1039/c1cs15220c).
- [18] Hunter C. A., Lecture M. (1994), The role of aromatic interactions in molecular recognition, *Chem. Soc. Rev.*, 23, 101-109 (DOI: 10.1039/cs9942300101).
- [19] Chen Z., Lohr A., Saha-Möller C. R., Würthner F. (2009), Self-assembled π -stacks of functional dyes in solution: structural and thermodynamic features, *Chem. Soc. Rev.*, 38, 564-584 (DOI: 10.1039/b809359h).
- [20] Hasegawa M., Iyoda M. (2010), Conducting supramolecular nanofibers and nanorods, *Chem. Soc. Rev.*, 39, 2420-2427 (DOI: 10.1039/b909347h).
- [21] Reczek J. J., Villazor K. R., Lynch V., Swager T. M., Iverson B. L. (2006), Tunable columnar mesophases utilizing C_2 symmetric aromatic donor-acceptor complexes, *J. Am. Chem. Soc.*, 128, 7995-8002 (DOI: 10.1021/ja061649s).
- [22] Pérez E. M., Martín N. (2008), Curves ahead: molecular receptors for fullerenes based on concave-convex complementarity, *Chem. Soc. Rev.*, 37, 1512-1519 (DOI: 10.1039/b802589b).
- [23] Liu Y., Yu Y., Gao J., Wang Z., Zhang X. (2010), Water-soluble supramolecular polymerization driven by multiple host-stabilized charge-transfer interactions, *Angew. Chemie.*, 122, 6726-6729 (DOI: 10.1002/ange.201002415).

- [24] Würthner F. (2004), Perylene bisimide dyes as versatile building blocks for functional supramolecular architectures, *Chem. Commun.*, 1564-1579 (DOI: 10.1039/b401630k).
- [25] Sakai N., Mareda J., Vauthey E., Matile S. (2010), Core-substituted naphthalenediimides, *Chem. Commun.*, 46, 4225-4237 (DOI: 10.1039/c0cc00078g).
- [26] Ajayaghosh A., Praveen V. K. (2007), π -Organogels of self-assembled p-phenylenevinyls: soft materials with distinct size, shape, and functions, *Acc. Chem. Res.*, 40, 644-656 (DOI: 10.1021/ar7000364).
- [27] Mishra A., Ma C.-Q., Bäuerle P. (2009), Functional oligothiophenes: molecular design for multidimensional nanoarchitectures and their applications, *Chem. Rev.*, 109, 1141-1276 (DOI: 10.1021/cr8004229).
- [28] Rao M. R., Sun S.-S. (2013), Supramolecular assemblies of amide-derived organogels featuring rigid π -conjugated phenylethynyl frameworks, *Langmuir*, 29, 15146-15158 (DOI: 10.1021/la402449e).
- [29] Hoeben F. J. M., Jonkheijm P., Meijer E.W., Schenning A. P. H. J. (2005), About supramolecular assemblies of π -conjugated systems, *Chem. Rev.*, 105, 1491-1546 (DOI: 10.1021/cr030070z).
- [30] De Greef T. F. A., Smulders M. M. J., Wolfs M., Schenning A. P. H. J., Sijbesma R.P., Meijer E.W. (2009), Supramolecular polymerization, *Chem. Rev.*, 109, 5687-5754 (DOI: 10.1021/cr900181u).
- [31] Huang F., Scherman O. A. (2012), Supramolecular polymers, *Chem. Soc. Rev.*, 41, 5879-5880 (DOI: 10.1039/c2cs90071h).
- [32] Sarma J. A. R. P., Desiraju G. R. (1999), Polymorphism and pseudopolymorphism in organic crystals, *Cryst. Eng. Des. Appl. Funct. Solids.*, 325-356 (DOI: 10.1007/978-94-015-9105-8-15).
- [33] Friend R. H., Gymer R. W., Holmes A. B., Burroughes J. H., Marks R. N., Taliani C., Bradley D. D. C., Dos Santos D. A., Brédas J. L., Lögdlund M., Salaneck W. R. (1999), Electroluminescence in conjugated polymers, *Nature.*, 397, 121-128 (DOI: 10.1038/16393).
- [34] Organic Photovoltaics, (2003). (DOI:10.1007/978-3-662-05187-0).
- [35] Kitahara T., Shirakawa M., Kawano S., Beginn U., Fujita N., Shinkai S. (2005), Creation of a mixed-valence state from one-dimensionally aligned TTF utilizing the self-assembling nature of a low molecular-

- weight gel, *J. Am. Chem. Soc.*, 127, 14980-14981 (DOI: 10.1021/ja0552038).
- [36] Puigmartí-Luis J., Laukhin V., Pérez del Pino Á., Vidal-Gancedo J., Rovira C., Laukhina E., Amabilino D. B. (2007), Supramolecular conducting nanowires from organogels, *Angew. Chemie Int. Ed.*, 46, 238–241(DOI: 10.1002/anie.200602483).
- [37] Puigmartí-Luis J., Pérez del Pino Á., Laukhina E., Esquena J., Laukhin V., Rovira C., Vidal-Gancedo J., Kanaras A. G., Nichols R. J., Brust M., Amabilino D. B. (2008), Shaping supramolecular nanofibers with nanoparticles forming complementary hydrogen bonds, *Angew. Chemie Int. Ed.*, 47, 1861-1865 (DOI: 10.1002/anie.200704864).
- [38] López J. L., Pérez E. M., Viruela P. M., Viruela R., Ortí E., Martín N.(2009), Controlled self-assembly of electron donor nanotubes, *Org. Lett.*, 11, 4524-4527 (DOI: 10.1021/ol901695m).
- [39] Puigmartí-Luis J., Pérez del Pino Á., Laukhin V., Feldborg L. N., Rovira C., Laukhina E., Amabilino D. B. (2010), Solvent effect on the morphology and function of novel gel-derived molecular materials, *J. Mater. Chem.*, 20, 466-474 (DOI: 10.1039/b917751e).
- [40] Dou X., Pisula W., Wu J., Bodwell G. J., Müllen K. (2007), Reinforced self-assembly of hexa- peri -hexabenzocoronenes by hydrogen bonds: From microscopic aggregates to macroscopic fluorescent organogels, *Chem. - A Eur. J.*, 14, 240-249 (DOI: 10.1002/chem.200700921).
- [41] Kumaran N., Veneman P.A., Minch B.A., Mudalige A., Pemberton J. E., O'Brien D. F., Armstrong N. R. (2010), Self-organized thin films of hydrogen-bonded phthalocyanines: characterization of structure and electrical properties on nanometer length scales, *Chem. Mater.*, 22, 2491-2501 (DOI: 10.1021/cm903127w).
- [42] Shirakawa M., Kawano S., Fujita N., Sada K., Shinkai S. (2003), Hydrogen-bond-assisted control of H versus J aggregation mode of porphyrins stacks in an organogel system, *J. Org. Chem.*, 68, 5037–5044 (DOI: 10.1021/jo0341822).
- [43] Helmich F., Lee C. C., Nieuwenhuizen M. M .L., Gielen J. C., Christianen P. C. M., Larsen A., Fytas G., Leclère P. E. L. G.,

- Schenning A. P. H. J., Meijer E. W. (2010), Dilution-induced self-assembly of porphyrin aggregates: a consequence of coupled equilibria, *Angew. Chemie Int. Ed.*, 49, 3939-3942 (DOI: 10.1002/anie.201000162).
- [44] Iavicoli P., Xu H., Feldborg L. N., Linares M., Paradinas M., Stafström S., Ocal C., Nieto-Ortega B., Casado J., López Navarrete J. T., Lazzaroni R., De Feyter S., Amabilino D. B. (2010), Tuning the supramolecular chirality of one- and two-dimensional aggregates with the number of stereogenic centers in the component porphyrins, *J. Am. Chem. Soc.*, 132, 9350-9362 (DOI: 10.1021/ja101533j).
- [45] Kimura M., Miki N., Suzuki D., Adachi N., Tatewaki Y., Shirai H. (2009), Wrapping of self-organized fluorescent nanofibers with a silica wall, *Langmuir*, 25, 776-780 (DOI: 10.1021/la802991g).
- [46] Würthner F., Hanke B., Lysetska M., Lambright G., Harms G. S. (2005), Gelation of a highly fluorescent urea-functionalized perylene bisimide dye, *Org. Lett.*, 7, 967-970 (DOI: 10.1021/ol0475820).
- [47] Syamakumari A., Schenning A. P. H. J., Meijer E. W. (2002), Synthesis, optical properties, and aggregation behavior of a triad system based on perylene and oligo(p-phenylene vinylene) units, *Chem. -A Eur. J.*, 8, 3353-3361 (DOI: 10.1002/1521-3765(20020802)8:15<3353::aid-chem3353>3.0.co;2-x).
- [48] Li X.-Q., Stepanenko V., Chen Z., Prins P., Siebbeles L. D. A., Würthner F. (2006), Functional organogels from highly efficient organogelator based on perylene bisimide semiconductor, *Chem. Commun.*, 3871-3873 (DOI: 10.1039/b611422a).
- [49] Yagai S., Seki T., Karatsu T., Kitamura A., Würthner F. (2008), Transformation from H- to J-aggregated perylene bisimide dyes by complexation with cyanurates, *Angew. Chemie Int. Ed.*, 47, 3367-3371. (DOI: 10.1002/anie.200705385).
- [50] Yagai S., Kubota S., Iwashima T., Kishikawa K., Nakanishi T., Karatsu T., Kitamura A. (2008), Supramolecular polymerization and polymorphs of oligo(p-phenylene vinylene)-functionalized bis- and monoureas, *Chem. -A Eur. J.*, 14, 5246-5257 (DOI: 10.1002/chem.200701782).

- [51] Paraschiv I., Giesbers M., van Lagen B., Grozema F. C., Abellon R. D., Siebbeles L. D. A., Marcelis A. T. M., Zuilhof H., Sudhölter E. J. R. (2006), H-Bond-stabilized triphenylene-based columnar discotic liquid crystals, *Chem. Mater.*, 18, 968-974 (DOI: 10.1021/cm052221f).
- [52] Paraschiv I., Tomkinson A., Giesbers M., Sudhölter E. J. R., Zuilhof H., Marcelis A.T. M. (2007), Amide, urea and thiourea-containing triphenylene derivatives: influence of H-bonding on mesomorphic properties, *Liq. Cryst.*, 34, 1029-1038 (DOI: 10.1080/02678290701609640).
- [53] Gearba R. I., Lehmann M., Levin J., Ivanov D. A., Koch M. H. J., Barberá J., Debije M. G., Piris J., Geerts Y. H. (2003), Tailoring discotic mesophases: columnar order enforced with hydrogen bonds, *Adv. Mater.*, 15, 1614-1618 (DOI: 10.1002/adma.200305137).
- [54] Yip H.-L., Zou J., Ma H., Tian Y., Tucker N. M., Jen A. K.-Y. (2006), Patterning of robust self-assembled n-type hexaazatrinaphthylene-based nanorods and nanowires by microcontact printing, *J. Am. Chem. Soc.*, 128, 13042-13043 (DOI: 10.1021/ja064934k).
- [55] Palma M., Levin J., Debever O., Geerts Y., Lehmann M., Samorì P. (2008), Self-assembly of hydrogen-bond assisted supramolecular azatriphenylene architectures, *Soft Matter.*, 4, 303-310 (DOI: 10.1039/b713570j).
- [56] van Herrikhuyzen J., Jonkheijm P., Schenning A. P. H. J., Meijer E. W. (2006), The influence of hydrogen bonding and π - π stacking interactions on the self-assembly properties of C_3 -symmetrical oligo(p-phenylenevinylene) discs, *Org. Biomol. Chem.*, 4, 1539-1545 (DOI: 10.1039/b517993a).
- [57] Matmour R., De Cat I., George S. J., Adriaens W., Leclère P., Bomans P. H. H., Sommerdijk N. A. J. M., Gielen J. C., Christianen P. C. M., J.T. Heldens, J.C.M. van Hest, D.W.P.M. Löwik, S. De Feyter, E.W. Meijer, Schenning A. P. H. J. (2008), Oligo(p-phenylenevinylene)-peptide conjugates: synthesis and self-assembly in solution and at the solid-liquid interface, *J. Am. Chem. Soc.*, 130, 14576-14583 (DOI: 10.1021/ja803026j).

- [58] Fang F.-C., Chu C.-C., Huang C.-H., Raffy G., Del Guerzo A., Wong K.-T., Bassani D. M. (2008), Versatile one-step introduction of multiple hydrogen-bonding sites onto extended π -conjugated systems, *Chem. Commun.*, 6369-6371 (DOI: 10.1039/b813704h).
- [59] Babu S. S., Mahesh S., Kartha K. K., Ajayaghosh A. (2009), Solvent-directed self-assembly of π gelators to hierarchical macroporous structures and aligned fiber bundles, *Chem. Asian J.*, 4, 824-829 (DOI: 10.1002/asia.200900145).
- [60] Xue P., Lu R., Yang X., Zhao L., Xu D., Liu Y., Zhang H., Nomoto H., Takafuji M., Ihara H. (2009), Self-assembly of a chiral lipid gelator controlled by solvent and speed of gelation, *Chem.-A Eur. J.*, 15, 9824-9835 (DOI: 10.1002/chem.200900732).
- [61] Xue P., Lu R., Zhao L., Xu D., Zhang X., Li K., Song Z., Yang X., Takafuji M., Ihara H. (2010), Hybrid self-assembly of a π gelator and fullerene derivative with photoinduced electron transfer for photocurrent generation, *Langmuir*, 26, 6669-6675 (DOI: 10.1021/la903990m).
- [62] Abbel R., van der Weegen R., Pisula W., Surin M., Leclère P., Lazzaroni R., Meijer E. W., Schenning A. P. H. J. (2009), Multicolour self-assembled fluorene co-oligomers: from molecules to the solid state via white-light-emitting organogels, *Chem - A Eur. J.*, 15, 9737-9746 (DOI: 10.1002/chem.200900620).
- [63] Brustolin F., Surin M., Lemaire V., Romanazzi G., Sun Q., Cornil J., Lazzaroni R., Sommerdijk N. A. J. M., Leclère P., Meijer E. W. (2007), The self-assembly of amphiphilic oligothiophenes: hydrogen bonding and poly(glutamate) complexation, *Bull. Chem. Soc. Jpn.* 80, 1703-1715 (DOI: 10.1246/bcsj.80.1703).
- [64] Prasanthkumar S., Saeki A., Seki S., Ajayaghosh A. (2010), Solution phase epitaxial self-assembly and high charge-carrier mobility nanofibers of semiconducting molecular gelators, *J. Am. Chem. Soc.*, 132, 8866-8867 (DOI: 10.1021/ja103685j).
- [65] Rest C., Kandanellia R., Fernández G. (2015), Strategies to create hierarchical self-assembled structures via cooperative non-covalent

- interactions, *Chem Soc Rev*, 44, 2543-2572 (DOI:10.1039/c4cs00497c).
- [66] Smulders M. M. J., Nieuwenhuizen M. M. L., de Greef T. F. A., Van Der Schoot P., Schenning A. P. H. J., Meijer E. W. (2009), How to distinguish isodesmic from cooperative supramolecular polymerisation, *Chem - A Eur. J.*, 16, 362-367 (DOI: 10.1002/chem.200902415).
- [67] Brunsveld L., Folmer B. J. B., E. W. Meijer, R. P. Sijbesma (2001), Supramolecular polymers, *Chem. Rev.*, 101, 4071-4098 (DOI: 10.1021/cr990125q)
- [68] Ciferri A. (2002), Supramolecular Polymerizations, *Macromolecular Rapid Communications* 23, 511-529 (DOI: 10.1002/1521-3927(20020601)23:9<511::AID-MARC511>3.0.CO;2-F).
- [69] Gershberg J., Fennel F., Rehm T. H., Lochbrunner S., Würthner F. (2015), Anti-cooperative supramolecular polymerization: a new K_2 -K model applied to the self-assembly of perylene bisimide dye proceeding via well-defined hydrogen-bonded dimmers, *Chemical Science*, 7, 1729-1737 (DOI:10.1039/C5SC03759J).
- [70] Zhao D., Moore S. (2003), Nucleation-elongation : a mechanism for cooperative supramolecular polymerization, *Org. Biomol. Chem.*, 1, 3471-3491 (DOI: 10.1039/B308788C).
- [71] Steiner T. (2002), The Hydrogen Bond in the Solid State, *Angew. Chemie Int. Ed.*, 41, 48-76 (DOI: 10.1002/1521-3773(20020104)41:1<48::aid-anie48>3.0.co;2-u).
- [72] Prins L. J., Reinhoudt D. N., Timmerman P. (2001), Noncovalent synthesis using hydrogen bonding, *Angew. Chemie Int. Ed.*, 40, 2382-2426 (DOI: 10.1002/1521-3773(20010702)40:13<2382::aid-anie2382>3.0.co;2-g).
- [73] Sijbesma R. P., Meijer E.W. (2003), Quadruple hydrogen bonded systems, *Chem. Commun.*, 0, 5-16 (DOI: 10.1039/b205873c).
- [74] Martinez C. R., Iverson B. L. (2012), Rethinking the term “pi-stacking”, *Chem. Sci.*, 3, 2191-2201 (DOI: 10.1039/c2sc20045g).
- [75] Iwaura R., Hoebe F., Masuda M., Schenning A. P. H. J., Meijer E. W., Shimizu T. (2006), Molecular-level helical stack of a nucleotide-

- appended oligo(p-phenylenevinylene) directed by supramolecular self-assembly with a complementary oligonucleotide as a template, *J. Am. Chem. Soc.*, 128, 13298-13304 (DOI: 10.1021/ja064560v).
- [76] Kim B.-S., Hong D.-J., Bae J., Lee M. (2005), Controlled self-assembly of carbohydrate conjugate rod-coil amphiphiles for supramolecular multivalent ligands, *J. Am. Chem. Soc.*, 127, 16333-16337 (DOI: 10.1021/ja055999a).
- [77] Wall B. D., Zacca A. E., Sanders A. M., Wilson W. L., Ferguson A. L., Tovar J. D. (2014), Supramolecular polymorphism: tunable electronic interactions within π -conjugated peptide nanostructures dictated by primary amino acid sequence, *Langmuir*, 30, 5946-5956 (DOI: 10.1021/la500222y)
- [78] Diegelmann S. R., Gorham J. M., Tovar J. D. (2008), One-dimensional optoelectronic nanostructures derived from the aqueous self-assembly of π -conjugated oligopeptides, *J. Am. Chem. Soc.*, 130, 13840-13841 (DOI: 10.1021/ja805491d).
- [79] Besar K., Ardoña H. A. M., Tovar J. D., Katz H. E. (2015), Demonstration of hole transport and voltage equilibration in self-assembled π -conjugated peptide nanostructures using field-effect transistor architectures, *ACS Nano.*, 9, 12401-12409 (DOI: 10.1021/acsnano.5b05752).
- [80] Stone D. A., Hsu L., Stupp S. I. (2009), Self-assembling quinquethiophene-oligopeptide hydrogelators, *Soft Matter*, 5, 1990-1993 (DOI: 10.1039/b904326h).
- [81] Klok H.-A., Rosler A., Gotz G., Osteritzc E. M., Bauerle P. (2004), Synthesis of a silk-inspired peptide-oligothiophene conjugate, *Org. Biomol. Chem.*, 2, 3541-3544 (DOI: 10.1039/b415454a).
- [82] Guo Z., Song Y., Gong R., Mu Y., Jiang Y., Li M., Wan X. (2014), Assembly of peptide-thiophene conjugates: the influence of peptide content and location, *Supramol. Chem.*, 26, 383-391 (DOI: 10.1080/10610278.2013.844810).
- [83] Sanders A. M., Magnanelli T. J., Bragg A. E., Tovar J. D. (2016), Photoinduced electron transfer within supramolecular donor-acceptor

- peptide nanostructures under aqueous conditions, *J. Am. Chem. Soc.*, 138, 3362-3370 (DOI: 10.1021/jacs.5b12001).
- [84] Kirschbaum T., Azumi R., Mena-Osteritz E., Bäuerle P. (1999), Synthesis and characterization of structurally defined head-to-tail coupled oligo(3-alkylthiophenes), *New J. Chem.*, 23, 241-250 (DOI: 10.1039/a808026g).
- [85] Azumi R., Götz G., Debaerdemaeker T., Bäuerle P. (2000), Coincidence of the molecular organization of β -substituted oligothiophenes in two-dimensional layers and three-dimensional crystals, *Chem.-A Eur. J.*, 6, 735-744 (DOI: 10.1002/(SICI)1521-3765(20000218)6:4<735::AID-CHEM735>3.0.CO;2-A).
- [86] Bai S., Debnath S., Javid N., Frederix Pim W. J. M., Fleming S., Pappas C., Ulijn R. V.(2014), Differential self-assembly and tunable emission of aromatic peptide bola-amphiphiles containing perylene bisimide in polar solvents including water, *Langmuir*, 30, 7576-7584 (DOI: 10.1021/la501335e).
- [87] Eakins G. L., Gallaher J. K., Keyzers R. A., Falber A., Webb J. E. A., Laos A., Tidhar Y., Weissman H., Rybtchinski B., Thordarson P., Hodgkiss J. M. (2014), Thermodynamic factors impacting the peptide-driven self-assembly of perylene diimide nanofibers, *J. Phys. Chem. B*, 118, 8642-8651 (DOI: 10.1021/jp504564s).
- [88] Liu Y.-H., Hsu S.-M., Wu F.-Y., Cheng H., Yeh M.-Y., Lin H.-C. (2014), Electroactive organic dye incorporating dipeptides in the formation of self-assembled nanofibrous hydrogels, *Bioconjugate Chem.*, 25, 1794-1800 (DOI: 10.1021/bc500299c).
- [89] Basak S., Nandi N., Bhattacharyya K., Datta A., Banerjee A. (2015), Fluorescence from an H-aggregated naphthalenediimide based peptide: photophysical and computational investigation of this rare phenomenon, *Phys. Chem. Chem. Phys.* 17, 30398-30403 (DOI: 10.1039/C5CP05236J).
- [90] Jana P., Bera S., Paikar A., Haldar D. (2014), Terminal peptide directed assembly of naphthalene-bisimides, *Cryst. Growth Des.*, 14, 3918-3922 (DOI:10.1021/cg500501r).

- [91] Smith A. M., Williams R. J., Tang C., Coppo P., Collins R. F., Turner M. L., Saiani A., Ulijn R. V. (2008), Fmoc-diphenylalanine self assembles to a hydrogel via a novel architecture based on π - π interlocked β -sheets, *Adv. Mater.*, 20, 37-41 (DOI: 10.1002/adma.200701221).
- [92] Yang Z., Liang G., Ma M., Gao Y., Xu B. (2007), Conjugates of naphthalene and dipeptides produce molecular hydrogelators with high efficiency of hydrogelation and superhelical nanofibers, *J. Mater. Chem.*, 17, 850-854 (DOI: 10.1039/b611255b).
- [93] Adhikari B., Nanda J., Banerjee A. (2011), Pyrene-containing peptide-based fluorescent organogels: inclusion of graphene into the organogel, *Chem.-A Eur. J.*, 17, 11488–11496 (DOI: 10.1002/chem.201101360).
- [94] López J. L., Atienza C., Insuasty A., López-Andarias J., Romero-Nieto C., Guldi D. M., Martín N. (2012), Concave versus Planar Geometries for the Hierarchical Organization of Mesoscopic 3D Helical Fibers, *Angew. Chemie Int. Ed.*, 51, 3857-3861 (DOI: 10.1002/anie.201109162).
- [95] Sanchez C., Soler-Illia G. J. D. A. A., Ribot F., Grosso D. (2003), Design of functional nano-structured materials through the use of controlled hybrid organic-inorganic interfaces, *C. R. Chimie*, 6, 1131-1151 (DOI: 10.1016/j.crci.2003.06.001).
- [96] Inoue S., Fujihara S. (2010), Synthesis of inorganic-organic layered compounds using immiscible liquid-liquid systems under the distribution law. *Langmuir*, 26, 15938-15944 (DOI: 10.1021/la1028542).
- [97] Briseno A. L., Holcombe T. W., Boukai A. I., Garnett E. C., Shelton S. W., Frechet J. J. M., Yang P. (2010), Oligo- and polythiophene/ZnO hybrid nanowire solar cells, *Nano Lett.*, 10, 334-340 (DOI: 10.1021/nl9036752).
- [98] Li L.-L., Fu X.-F., Ren Z., Zhao Y.-G., Feng W., Yan C.-H. (2010), Hierarchical self-assembly of superlattice hybrids consisting of periodic and alternating cores of porphyrin molecules separated by nanoscale silica walls, *Langmuir*, 26, 15730-15733 (DOI: 10.1039/C4CC05192K).

- [99] Raeburn J., Alston B., Kroeger J., McDonald T. O., Howse J. R., Cameron P. J., Adams D. J. (2014), Electrochemically-triggered spatially and temporally resolved multi-component gels, *Mater. Horiz.*, 1, 241-246 (DOI: 10.1021/la1034036).
- [100] Li M., Ishihara S., Akada M., Liao M., Sang L., Hill J. P., Krishnan V., Ma Y., Ariga K. (2011), Electrochemical-coupling layer-by-layer (ECCLbL) assembly, *J. Am. Chem. Soc.*, 133, 7348-7351 (DOI: 10.1021/ja202768k).
- [101] Choi K.-S., Lichtenegger H. C., Stucky G. D. (2002), Electrochemical synthesis of nanostructured ZnO films utilizing self assembly of surfactant molecules at solid-liquid interfaces, *J. Am. Chem. Soc.*, 124, 12402-12403 (DOI:10.1021/ja0275562).
- [102] Yarger S. M., Steinmillar E. M. P., Choi K.-S. (2007), Electrochemical synthesis of cobalt hydroxide films with tunable interlayer spacing, *Chem. Commun*, 159-161 (DOI: 10.1039/B609621B).
- [103] Sofos M., Goldberger J., Stone D. A., Allen J. E., Ma Q., Herman D. J., Tsai W.-W., Lauhon L. J., Stupp S. I. (2009), A synergistic assembly of nanoscale lamellar photoconductor hybrids, *Nat. Mater.*, 8, 68-75 (DOI: 10.1038/NMAT2336).
- [104] Bruns C. J., Herman D. J., Minuzzo J. B., Lehrman J. A., Stupp S. I. (2013), Rationalizing molecular design in the electrodeposition of anisotropic lamellar nanostructures, *Chem. Mater.* 25, 4330-4339 (DOI: 10.1021/cm402505p).
- [105] Yoshida T., Minoura H. (2000), Electrochemical self-assembly of dye-modified zinc oxide thin films, *Adv. Mater.*, 12, 1219-1222 (DOI: 10.1002/1521-4095(200008)12:16<1219::aid-adma1219>3.0.co;2-5).
- [106] Manne S., Cleveland J. P., Gaub H. E., Stucky G. D., Hansma P. K. (1994), Direct visualization of surfactant hemimicelles by force microscopy of the electrical double layer, *Langmuir*, 10, 4409-4413 (DOI: 10.1021/la00024a003).
- [107] Hu K., Bard A. J. (1997), Characterization of adsorption of sodium dodecyl sulfate on charge-regulated substrates by atomic force microscopy force measurements, *Langmuir*, 13, 5418-5425 (DOI: 10.1021/la970483t).

- [108] Burgess I, Jeffrey C. A., Cai X., Szymanski G., Galus Z., Lipkowski J. (1999), Direct visualization of the potential-controlled transformation of hemimicellar aggregates of dodecyl sulfate into a condensed monolayer at the Au(111) electrode surface, *Langmuir*, 15, 2607–2616 (DOI: 10.1021/la981023i)
- [109] Steinmiller E. M. P., Choi K.-S. (2007), Anodic construction of lamellar structured ZnO films using basic media, *Langmuir*, 23, 12710–12715 (DOI: 10.1021/la702066w).
- [110] Choi K.-S., Steinmiller E. M. P. (2008), Electrochemical synthesis of lamellar structured ZnO films via electrochemical interfacial surfactant templating, *Electrochim. Acta*, 53, 6953–6960 (DOI: 10.1016/j.electacta.2007.12.058).
- [111] Choi K.-S., McFarland E. W., Stucky G. D. (2003), Electrocatalytic properties of thin mesoporous platinum films synthesized utilizing potential-controlled surfactant assembly, *Adv. Mater.*, 15, 2018–2021. (DOI:10.1002/adma.200304557).
- [112] Tan Y., Steinmiller E. M. P., Choi K.-S. (2005), Electrochemical tailoring of lamellar structured ZnO films by interfacial surfactant templating, *Langmuir*, 21, 9618–9624. (DOI: 10.1021/la050789x).
- [113] Tan Y., Srinivasan S., Choi K.-S. (2005), Electrochemical deposition of mesoporous nickel hydroxide films from dilute surfactant solutions, *J. Am. Chem. Soc.*, 127, 3596–3604 (DOI: 10.1021/ja0434329).
- [114] Spray R. L., Choi K.-S. (2007), Electrochemical synthesis of SnO₂ films containing three-dimensionally organized uniform mesopores via interfacial surfactant templating, *Chem. Commun.*, 3655–3657 (DOI: 10.1039/B704428C).
- [115] Yoshida T., Tochimoto M., Schlettwein D., Wöhrle D., Sugiura T., Minoura H. (1999), Self-assembly of zinc oxide thin films modified with tetrasulfonated metallophthalocyanines by one-step electrodeposition, *Chem. Mater.*, 11, 2657–2667 (DOI: 10.1021/cm980619o).
- [116] Karuppuchamy S., Yoshida T., Sugiura T., Minoura H. (2001), Self-assembly of ZnO/riboflavin 5'-phosphate thin films by one-step

- electrodeposition and its characterization, *Thin Solid Films*, 397, 63-69 (DOI: 10.1016/S0040-6090(01)01356-6).
- [117] Yoshida T., Terada K., Schlettwein D., Oekermann T., Sugiura T., Minoura H. (2002), Electrochemical self-assembly of nanoporous ZnO/Eosin Y thin films and their sensitized photoelectrochemical performance, *Adv. Mater.*, 12, 1214-1217 (DOI: 10.1002/1521-4095(200008)12:16<1214::aid-adma1214>3.0.co;2-z).
- [118] Oekermann T., Karuppuchamy S., Yoshida T., Schlettwein D., Woehrl D., Minoura H. (2004), Electrochemical self-assembly of ZnO/SO₃EtPTCDI hybrid photoelectrodes, *J. Electrochem. Soc.*, 151, 62-68 (DOI: 10.1149/1.1630596).
- [119] Karuppuchamy S. (2002), Cathodic electrodeposition of oxide semiconductor thin films and their application to dye-sensitized solar cells, *Solid State Ionics*. 151, 19-27 (DOI: 10.1016/s0167-2738(02)00599-4).
- [120] Nonomura K., Yoshida T., Schlettwein D., Minoura H. (2003), One-step electrochemical synthesis of ZnO/Ru(dcbpy)₂(NCS)₂ hybrid thin films and their photoelectrochemical properties, *Electrochim. Acta*, 48, 3071-3078 (DOI: 10.1016/S0013-4686(03)00381-5).
- [121] Iwamoto T., Ogawa Y., Sun L., White M. S., Glowacki E. D., Scharber M. C., Sariciftci N. S., Manseki K., Sugiura T., Yoshida T. (2014), Electrochemical self-assembly of nanostructured CuSCN/Rhodamine B hybrid thin film and its dye-sensitized photocathodic properties, *J. Phys. Chem. C*, 118, 16581-16590 (DOI: 10.1021/jp412463v).
- [122] Zhang J., Sun L., Ichinose K., Funabiki K., Yoshida T. (2010), Effect of anchoring groups on electrochemical self-assembly of ZnO/xanthene dye hybrid thin films, *Phys. Chem. Chem. Phys.*, 12, 10494-10502 (DOI: 10.1039/c002831b).
- [123] Tani T., Kikuchi S., Hosoya K. (1967), Respiration during Germination in Uredospores of Puccinia coronata *Bull. Soc. Sci. Photography Jpn.*, 17, 24-34 (DOI: 10.3186/jjphytopath.33.17).
- [124] Goux A., Pauporte T., Yoshida T., Lincot D. (2006), Mechanistic study of the electrodeposition of nanoporous self-assembled ZnO/eosin

Y hybrid thin films: effect of eosin concentration, *Langmuir*, 22, 10545-10553 (DOI: 10.1021/la061199h).

Chapter 2

Materials and Methods

2.1 Introduction

This chapter describes the synthesis of π -conjugated peptide molecules and electrochemical synthesis of peptide-inorganic hybrid nanostructure materials. This chapter is also a detailed account of several characterizations such as spectroscopic, microscopic and electrochemical techniques.

2.2 Experimental procedure

2.2.1 Materials

All the raw starting materials listed here were purchased from Sigma-Aldrich, U.S.A.; E-Merck, Germany, and SRL, India. They include phenylalanine (F), tyrosine (Y), tryptophan (W), leucine (L) dicyclohexylcarbodiimide (DCC), N,N'-Diisopropylcarbodiimide (DIPC), 1-hydroxybenzotriazole (HOBt) Maleic anhydride, ZnCl_2 , 1,1,1,3,3,3-hexamethyldisilazane (HMDS), benzene, Perylene, *p*-chloranil Boc-anhydride, thiophene, *n*-butyl lithium (1.6 M in hexane), Tributyltin chloride, 2,5-dibromo-3-methylthiophene, 5-bromo-2-thiophenecarboxylic acid, Citric acid, Tetrakis(triphenyl)phosphine palladium(0), 1-Ethyl-3-(3-dimethylaminopropyl)carbodiimide (EDC), 4-(N,N-dimethylamino)pyridine, tert-butyl alcohol, Trifluoroacetic acid (TFA), 1-hydroxybenzotriazole (HOBt), Acetonitrile, Tetrabutylammonium perchlorate (Bu_4NClO_4), naphthalene methanol, phosgene, $\text{Zn}(\text{NO}_3)_2 \cdot 6\text{H}_2\text{O}$ and $\text{Cd}(\text{CH}_3\text{COO})_2 \cdot 6\text{H}_2\text{O}$, $\text{Co}(\text{NO}_3)_2 \cdot 6\text{H}_2\text{O}$, $\text{Ni}(\text{NO}_3)_2 \cdot 6\text{H}_2\text{O}$. Deuterated solvents CDCl_3 , $\text{DMSO}-d_6$ for NMR characterization were obtained from Sigma-Aldrich, U.S.A. Silica gel (100-200 mesh) for column chromatography was obtained from SRL and TLC pre-coated silica gel plates (Kieselgel 60F254, Merck. All the other local chemicals were purchased from local manufacturers like SD Fine Chemicals Pvt. Ltd., SRL India, and E-Merck India etc.

2.2.2 Purification of solvents and reagents

The solvents used during the course of synthesis were distilled accordingly.^[1-2] Chloroform and ethyl acetate were dried with P_2O_5 and distilled. Dioxane was passed through basic alumina before use. Methanol was fractionally distilled with CaO and used.^[3] Thionyl chloride was distilled from boiled linseed oil (20 mL/50 g SOCl_2). Dimethylformamide (DMF) was

fractionally distilled using CaH_2 under reduced pressure. Tetrahydrofuran (THF) was dried over Na/benzophenone ketyl and freshly distilled prior to use. ITO coated quartz glass substrates ($10\text{ mm} \times 10\text{ mm}$) having a thickness of about 150 nm were purchased from J. K. Impex, Mumbai.

2.2.3 Solution phase π -conjugated peptide synthesis

The solution phase π -conjugated peptide synthesis is a classical and more powerful approach in peptide chemistry. All the π -conjugated peptide and peptide derivatives used in this study were synthesized by conventional solution phase methodology. For the synthesis of π -conjugated peptide **2-3**, benzo[ghi]perylene monoimide unit was functionalized with peptide DPA and leucine amino acid. For π -conjugated peptide compound **4-6**, quinquethiophene was functionalized with different peptide symmetrically at the both the ends. The first step for the synthesis of compound **7-11**, the N-terminal amino group of one amino acid was protected by naphthalene-2-methoxy carbonyl (Nmoc) and C-terminal acid group of another amino acid was protected by methyl ester. Then, the coupling reactions were successively performed by using conventional coupling agent (EDC/ HOBt) or (DIPC/HOBt) by solution phase peptide synthesis. All the coupling reactions were done at room temperature ($25\text{ }^\circ\text{C}$). To prevent the racemization problem during the coupling reactions, HOBt was used in the coupling reactions. This reacts with acyl urea and forms less reactive ester which is less labile toward racemization. The possibility of formation of diastereomers due to racemization effect was checked by NMR. Generally, no diastereomers or very little 1-5% diastereomers were found. For the synthesis of peptide derivatives, tert-butyloxycarbonyl (Boc-) group was also used for N-terminus protection of amino acids. The C-terminus deprotections were performed by saponification for ester groups in alkaline methanolic solutions at room temperature ($25\text{ }^\circ\text{C}$).

2.2.4 Dual ion beam sputtering deposition (DIBSD)

Dual ion beam sputtering deposition (DIBSD) The Elettrovava DIBSD system was deployed to deposit ITO thin films (200 nm) on quartz glass substrates. The angle between the sputtering beam and sputtering target was fixed at 45° off-normal, while the angle between the assist ion beam and the

substrate was maintained at 60°. Before being inserted into the DIBSD growth chamber, quartz glass substrates were rinsed thoroughly with trichloroethylene, acetone, isopropanol, and deionized (DI) water and subsequently purged with nitrogen gas (purity 99.999%) to remove dust particles and various organic contaminants. Prior to actual film deposition, the assist source was turned on for 10 min to perform substrate precleaning by argon ion bombardment. During material growth, the assist ion beam, consisting of plasma of argon ions, helped in the reduction of columnar growth, and thereby, enhanced growth uniformity and film adhesion to the substrate. The discharge voltage and current of the assist ion source was kept constant at 70 V and 600 mA, respectively, during ITO thin-film deposition by using a 4N (99.99%) pure 4-in-diameter ITO target mounted on a water-cooled target holder inside the DIBSD system chamber. The background pressure inside the process chamber was maintained at approximately 1×10^{-8} mbar, whereas the working pressure during film growth was kept at 3.26×10^{-4} mbar.

2.2.5 Electrochemical experiments

Electrochemical station (Autolab PGSTAT 302N) from Metrohm was used to conduct all electrochemical experiments including electrochemical synthesis of all the peptide-inorganic hybrids. Electrochemical deposition was carried out in 24 mL solution (1:1 v/v) DMSO/water of 0.04 M of each $\text{Co}(\text{NO}_3)_2 \cdot 6\text{H}_2\text{O}$, $\text{Ni}(\text{NO}_3)_2 \cdot 6\text{H}_2\text{O}$ and $\text{Zn}(\text{NO}_3)_2 \cdot 6\text{H}_2\text{O}$ with 6.0-12.0 mg of each peptide (**6-11**). Working electrode (ITO) was placed upright in cell and deposition was performed potentiodynamically at -0.7 to -0.9 V for 1-24 hours depending on the growth time under constant stirring at 80°C in water bath. After deposition, films were rinsed with de-ionized water and dried under a flow of nitrogen gas. For cyclic voltammograms and chronopotentiometry measurements, a conventional three-electrode cell assembly consisting of Ag/AgCl electrode (KCl Autolab Model 6.0726.107) as a reference electrode, platinum or zinc wire as a counter electrode and peptide/metal hydroxide deposited ITO as working electrode, was used for carrying out electrochemical measurements. For cyclic voltammetry (CV) of compound **4**, the supporting electrolyte was $\text{Bu}_4\text{NClO}_4/\text{CH}_2\text{Cl}_2$ (0.1 M). For the electrochromic test, a thin

film of peptide-quinquethiophene hydrogel was prepared onto an ITO coated glass and used as working electrode. Pt and Ag/AgCl were used as counter electrode and reference electrode respectively.

2.2.6 Cleaning of electrode

Working electrode ITO was cleaned with soap water under sonication for 15 minute. Then with methanol and acetone for 10 minute each. Finally it was washed with distilled water and dried with N₂ gas.

2.3 Characterization

2.3.1 Characterization and purification of compounds

All the reactions were routinely monitored by thin layer chromatography (TLC) on pre-coated silica gel plates (Kieselgel 60F254, Merck) using ethyl acetate/toluene (1:1) as eluents before work up. The crude products were purified by column chromatography using silica gel (100-200 mesh size) as a stationary phase and ethyl acetate/toluene (1:1) as an eluents. Detailed characterization was performed at every stage by the analysis of 300 MHz and 400 MHz ¹H NMR and mass spectrometry.

2.3.2 NMR Spectroscopy

All NMR studies were carried out on a Bruker AV 300 MHz spectrometer at 300 K and a Bruker AV 400 MHz NMR. TMS was used as internal reference and the deuterated solvents (CDCl₃, DMSO-*d*₆) were used. The compound concentrations were generally used in the range of 1-10 mmol L⁻¹.

2.3.3 Mass Spectrometry

Mass spectra of some compounds were recorded on a Waters HPLCMS system (Column Symmetry C18, 7mm) by negative mode electrospray ionization. The other compounds were recorded on a Bruker micrOTOF-Q II instrument in positive- and negative-mode electrospray ionizations using methanol/water, acetonitrile/water and chloroform as a liquid carrier.

2.3.4 FT-IR Spectroscopy

FT-IR spectra were taken using a Bruker (Tensor 27) FT-IR spectrophotometer. The solid-state measurements were performed using the

KBr pellet technique with a scan range of 400 to 4000 cm^{-1} over 64 scans at a resolution of 4 cm^{-1} and at an interval of 1 cm^{-1} . The gel sample was prepared in mili-Q water, placed between crystal Zn-Se windows and scanned between 900 to 4000 cm^{-1} over 64 scans at a resolution of 4 cm^{-1} and at an interval of 1 cm^{-1} .

2.3.5 Circular Dichroism (CD) Spectroscopy

Secondary structures of peptide bolaamphiphiles **4** were analyzed with Jasco J-815 circular dichroism spectrometer. In all the case, peptide hydrogel were diluted to final concentration of 10 mM to 500 mM in milli-Q water and measured from 300 nm to 190 nm with 0.1 data pitch, 20 nm/min scanning speed, 1 nm band width and 4 s D.I.T.

2.3.6 Rheology Analysis

Oscillating rheology was used to quantify the final mechanical properties of the peptide bolaamphiphile **4**. For each case 2 mL of peptide bolaamphiphile hydrogel (8-25 mmol L^{-1}) was prepared. The experiment was done on a Paar Physica Modular Compact Rheometer (MCR 301, Austria). 50 and 25 mm cone plate with a 1° angle configuration were used and the temperature was set constant at 25 °C. Storage (G') and loss (G'') moduli were measured at a strain range of 0.05-0.1% with a true gap ranging from 0.05 to 0.097 mm.

2.3.7 UV-Vis Spectroscopy

UV-Vis absorption spectra of the compounds were recorded using a Varian Cary100 Bio UV-Vis spectrophotometer.

2.3.8 Fluorescence Spectroscopy

Fluorescence emission spectra of the peptide solutions and hydrogels were recorded on a Horiba Scientific Fluoromax-4 spectrophotometer with a 1 cm path length quartz cell at room temperature. The slit width for the emission was set at 2-5 nm and a 1 nm data pitch. The excitation spectra of these samples were also done with the same instrument and under the same conditions.

2.3.9 Dynamic light scattering (DLS)

Dynamic light scattering (DLS) and zeta potential measurements were made with a NanoPlus-3 zeta/nano particle analyzer (Micromeritics

Instrument). The errors for d_h and ξ values were ± 2 nm and $\pm 10\%$, respectively.

2.3.10 Time Correlated Single Photon Counting (TCSPC)

A 2 mL of solution sample was prepared in a quartz cuvette (1 cm \times 1 cm) and time-correlated single photon counting (TCSPC) experiment was performed on Horiba Yovin (Model: Fluorocube-01-NL) instrument. The sample was excited at 376 nm using a picosecond diode laser (Model: Pico Brite-375L). The signals were collected at magic angle (54.70) polarization using a photomultiplier tube (TBX-07C) as a detector, with a dark count less than 20 cps. The instrument response function (IRF, FWHM~140 ps) was recorded using a dilute scattering solution. The data analysis was performed using IBH DAS (version 6, HORIBA Scientific, Edison, NJ) decay analysis software. The amplitude-weighted lifetime was estimated by

$$\langle \tau \rangle = \sum_{i=1}^n a_i \tau_i$$

where τ_i was the fluorescence lifetime of various fluorescent species, a_i are the normalized pre-exponential factors. The goodness of the fit is judged by the reduced chi-square (χ^2) value.

2.3.11 Field Emission Gun-Scanning Electron Microscopy (FEG-SEM) Study

For SEM study, electrodeposited hybrid films were coated with gold. Then the micrographs were recorded in a SEM apparatus (Jeol Scanning Microscope-JSM-7600F). The solution samples were dried on a glass slide and coated with platinum. Then the micrographs were recorded on a SEM apparatus (Jeol Scanning Microscope-JSM-6700F).

2.3.12 Transmission Electron Microscopy (TEM) Study

High resolution transmission electron microscopic images were taken using PHILIPS electron microscope (model: CM 200), JEM 2010 electron microscope and JEM-2100 HRTEM, operated at an accelerating voltage of 200 kV. Solutions of the peptide (BPI-FF-OMe) were dried on carbon-coated copper grids (300 mesh) by slow evaporation in air, then allowed to dry

separately in a vacuum at room temperature. The average size of the nanospheres was determined from the TEM images.

2.3.13 Energy Dispersive X-Ray Spectroscopy (EDS)

Energy-dispersive X-ray spectroscopy (Oxford Instruments: Aztec) was used for elemental composition analysis of electrodeposited hybrid materials.

2.3.14 Atomic Force Microscopy (AFM) Study

The morphology of the self-assembled π -conjugated peptide (BPI-FF-OMe) was investigated by AFM. The peptide solutions were placed on a microscopic glass coverslip. Then, it was dried by slow evaporation. Images were taken using an AIST-NT instrument, model no. smartSPM 1000 in soft tapping-mode.

2.3.15 Wide-Angle X-Ray Diffraction Study

Some data were collected for the peptide powder and its corresponding electrodeposited hybrid thin films on a Rigaku Smart Lab X-ray diffractometer at a wavelength of 1.5406 Å. X-rays were produced using a sealed tube and were detected using a linear counting detector based on silicon strip technology (Scintillator NaI photomultiplier detector). The XRD measurements of rest of the samples were carried out using a Bruker D8 Advance X-ray diffractometer. The X-rays were produced using a sealed tube and the wavelength of the X-ray was 0.154 nm (Cu K-alpha). The X-rays were detected by using a fast counting detector based on Silicon strip technology (Bruker LynxEye detector).

2.3.16 Two-dimensional grazing-incidence small-angle X-ray scattering (2D-giSAXS).

SAXS experiments were performed on electrodeposited thin films by using CuK α ($\lambda = 1.54$) radiation from a source (GeniX 3D, Xenocs) operating at 50 kV and 0.6 mA. The diffraction patterns were collected on a two-module Pilatus detector.

2.3.17 PL measurements

A DongWoo Optron PL setup, affixed with a 20 mW continuous wave He-Cd laser (excitation wavelength = 325 nm, TEM00 mode), 320 mm and 150 mm focal length monochromators, chopper, lock-in amplifier, and a

photomultiplier tube (PMT) detector, were deployed to conduct optical studies of annealed and unannealed hybrid thin films. The UV light He-Cd laser (excitation wavelength = 325 nm, TEM00 mode) was used to measure the photosensitivity of the hybrid materials.

2.3.18 Ellipsometry

The absorption coefficient (α) was measured by using an M-2000 J. A. Woollam spectroscopic ellipsometer. Spectroscopic ellipsometry is a non-destructive and sensitive technique to study the optical response of various materials. The change in polarization state, i.e., psi (ψ) and delta (Δ) of the reflected light from the surface of a film by utilization of an appropriate model enables precise extraction of the optical constants and accurate thickness of the material under study. The spectra of psi (ψ) and delta (Δ) for GZO, Cd-doped ZnO and BPI-FF-OH/Cd-doped ZnO hybrid was measured at 70 °C as an optical incident angle. The fitting consistency of the calculated data with the GenOsc model could be seen as a result of low mean square error (MSE) observed for all samples, which eventually resulted in the accurate and precise determination of optical constants.

2.3.19 Secondary mass ion spectrometry (SIMS)

SIMS (Hiden) equipped with an oxygen ion gun with an energy up to 3.5 keV was used to characterize the depth profile of the cadmium-doped ZnO films.

2.4 References

- [1] Perrin D. D., Armarego W. L. F., Perrin D. R. (1980), Purification of laboratory chemicals, Oxford, Pergamon.
- [2] Vogel A. I., Text book of practical organic chemistry, 4th edition, ELBS, Longmans, 1978.
- [3] Marcus Y., Glikberg S. (1985), Recommended method for the purification of solvent and tests for impurities: Methanol and ethanol, Pure & Appl. Chem., 57, 855-864 (DOI: 10.1351/pac 198557060855).

Chapter 3

Supramolecular Assembly of Dipeptide Functionalized Benzo[*ghi*]perylene Monoimide Directs White Light Emission *via* Donor Acceptor Interactions

3.1 Introduction

Chapter 3 focuses on the study of self-assembled π -conjugated perylene based amphiphiles have attracted considerable interest in recent years.^[1-3] Self-assembled perylene based amphiphiles have been used in the fabrication of supramolecular 1D, 2D, and 3D based micro and nanoarchitectures for the applications in biology and supramolecular electronics.^[4-6] A variety of perylene based molecules have been designed for the development of perylene dye chemistry through extension of perylene core via functionalizing the bay position of perylene.^[7-13] Extensive work has been done on perylene diimides (PDI).^[14] The stable supramolecular architectures are achieved by designing the molecular structure of self-assembled materials as well as optimizing the response of suitable stimuli.^[15-19] Various stimuli have been used to drive the self-assembly of organic moieties *via* hydrogen bonding, π - π stacking and hydrophobic interactions. Zang *et al.* reported several examples of PDI based self-assembly.^[20-22] Self-assembly of amino acid functionalized perylene bisimides is also reported in literature.^[23-25] Recently, self-assembly of peptides functionalized perylene bisimides has been reported.^[26,27] In general, low molecular weight hydrophobic peptides have been used for the evolution of self-assembled architectures.^[28-32] Schenning *et al.* reported mixed fluorescent co-oligomer systems for the creation of white-light-emitting gels.^[33] Ajayaghosh *et al.* reported supramolecular organogel composed of intertwined twisted helical fibrillar assemblies made of OPV decorated with cholesterol units.^[34] Meijer and co-worker have also described a supramolecular copolymer resulting from the self-assembly in films of blue, green, and red π -conjugated oligomers.^[35] Zhang and co-workers described photo-facilitated aggregation and stable white-light emission in solution.^[36] Zhang *et al.* also reported bright white-light emission from a novel donor-acceptor small organic molecule in the solid state via intermolecular charge transfer.^[37] Number of strategies have been used to fabricate white light emitting materials. These include metal mediated white light emission,^[38] combination of three primary colors (red, green and blue), polymers^[39] and self-assembly of organic molecules.^[40] Development of low molecular weight white light emitting material is particularly interesting

due to their good solubility in distinct solvents. They can easily be applied on solid surface or can be soaked on solid materials. There are various reports but none of the examples show acceptor perylene monoimide functionalized small organic molecules based white light emission upon donor–acceptor interactions Table A2 (Annexure 1). Thus, keeping all these aspects in view, an attempt has been made to explore an aromatic benzo[*ghi*]perylene monoimide (BPI) functionalized diphenylalanine methyl ester BPI-FF-OMe (F: L-Phenylalanine) and BPI-L-OMe (L: L-Leucine) for the evolution of white light emission. The BPI-FF-OMe is highly soluble in various organic solvents and shows solvochromic behavior in different solvents. Herein, the objective is to explore self-assembly of benzo[*ghi*]perylene monoimide (BPI) functionalized dipeptide for the evolution of white light emission *via* donor-acceptor interactions. White light emitting materials have become an area of interest because of their opto-electronic applications. Till date, several research groups have emphasized the development of white light emitting materials. Acceptors benzo[*ghi*]perylene monoimides (BPIs) and donor pyrenebutyric acid have lead to white light emission *via* donor-acceptor interactions. Benzo[*ghi*]-perylene monoimide functionalized dipeptide (BPI-FF-OMe) and amino acid (BPI-L-OMe) are a new class of acceptor molecules that show white light emission with pyrene *via* energy transfer from donor to acceptor molecular interactions (Figure 3.1).

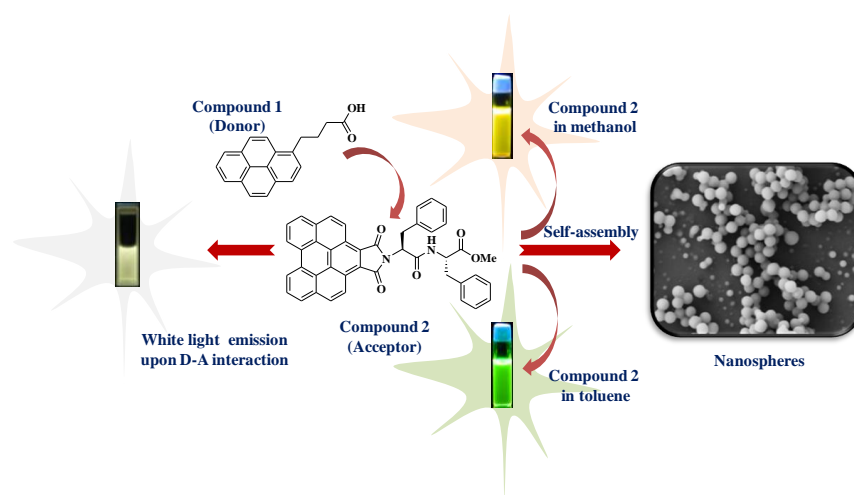


Figure 3.1. Schematic represents white light emission upon energy transfer between donor and acceptor (PyBA: BPI-FF-OMe). BPI-FF-OMe molecules show efficient solvatochromic effects in protic polar solvent methanol and aprotic solvent toluene. BPI-FF-OMe self-assembled to form spherical nanosphere in solution phase.

3.2 Experimental

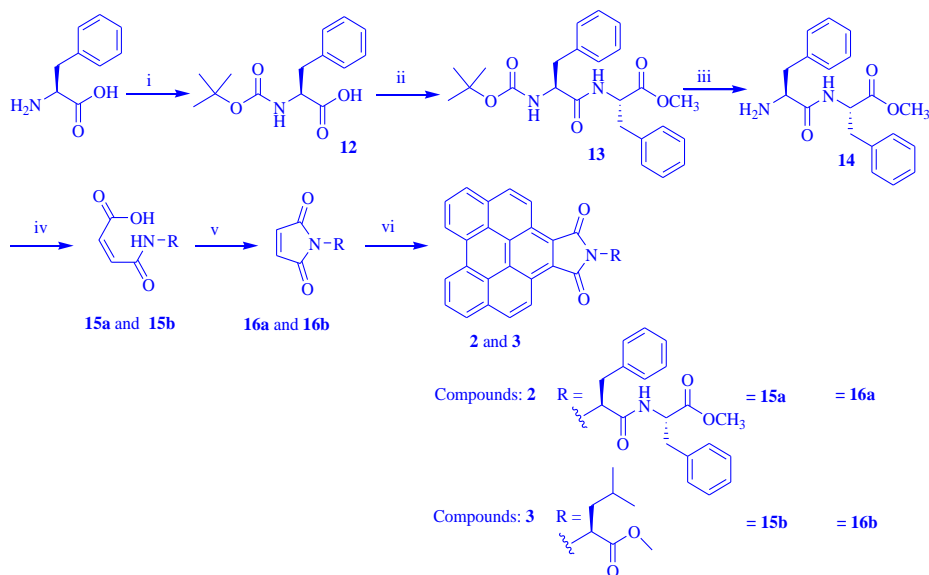
3.2.1 Synthesis of dipeptide-benzo[ghi]perylene monoimide conjugate

In general, the widely followed pathway to synthesize benzo[ghi]perylene monoimide is a Diels-Alder reaction of perylene with maleic anhydride and subsequent condensation reaction^[41-44] with primary aliphatic amines.^[45-48] Herein, an alternative method has been considered to synthesize benzo[ghi]perylene monoimide so as to obtain the product with a high yield in respect of bulky hindered substitute. The dienophile imide derivative has been synthesized by reaction of maleic anhydride with a dipeptide diphenylalanine. Crucial steps involved in the synthesis of the dienophile are (i) the reaction of H₂N-L-Phe-L-Phe-OMe with maleic anhydride for the formation of *N,N'*-maleyl-L-Phe-L-Phe-OMe and (ii) subsequent cyclization of *N,N'*-maleyl-L-Phe-L-Phe-OMe to form *N,N'*-maleoyl-L-Phe-L-Phe-OMe using 1 equiv. of ZnCl₂ and 1.5 equiv. of HMDS in benzene solvent.^[49,50] Finally, a dipeptide Phe-Phe-OMe appended benzo[ghi]perylene monoimide **2** is obtained by using Diels-Alder reaction of perylene with *N,N'*-maleoyl-Phe-Phe-OMe as orange color solid powder with 96% yield. Synthetic methodology of N-dipeptide functionalized benzo[ghi]perylene-1,2-dicarboxylic monoimide (**2**) and other derivatives have been shown in Scheme 3.1. Dipeptide attached with BPI core helps to increase the solubility of compound BPI-FF-OMe in a range of organic solvents, which acts as an alternative to the mostly used 'swallow' alkyl chains directly attached to the main perylene or PDI moieties.

3.2.2 Synthesis of leucine methyl ester functionalized benzo-[ghi]perylene monoimides

Similarly, BPI-Leu-OMe **3** has been synthesized by (i) the reaction of H₂N-L-Leu-OMe with maleic anhydride for the formation of *N,N'*-maleyl-L-Leu-OMe **15b** and (ii) subsequent cyclization of *N,N'*-maleyl-L-Leu-OMe to form *N,N'*-maleoyl-L-Leu-OMe **16b** using 1 equiv. of ZnCl₂ and 1.5 equiv. of HMDS in benzene solvent.^[50,51] Finally, a Leu-OMe appended benzo[ghi]perylene monoimide **3** is obtained by using Diels-Alder reaction of

perylene with *N,N'*-maleoyl-L-Leu-OMe **16b** as a red solid powder with 76% yield.



Scheme 3.1. Synthesis of N-dipeptide functionalized benzo[ghi]perylene-1,2-dicarboxylic monoimide. (i) Boc-anhydride, 1,4 dioxane, Na_2CO_3 ; (ii) phenylalanine methyl ester, HOBt/DIPC, DMF; (iii) TFA; (iv) maleic anhydride, EtOAc; (v) $\text{ZnCl}_2/\text{HMDS}$, benzene, 80°C ; (vi) perylene, *p*-chloranil, 240°C , 3h.

Synthesis of Boc-L-Phe-OH (12):

A solution of L-phenylalanine (3.3 g, 20 mmol) in a mixture of 1, 4 dioxane (40 mL), 1 N sodium hydroxide (20 mL) was stirred and cooled in an ice-water bath. Boc anhydride (4.8 mL, 21 mmol) was added and stirring was continued at room temperature for 12 hrs. Reaction mixture was diluted with 200 mL of water and dioxane was evaporated under vacuum. The aqueous layer was washed with diethyl ether and the pH of aqueous layer was adjusted to 2 with 2 M HCl. The aqueous phase was extracted with ethyl acetate (3 x 50 mL) and dried over Na_2SO_4 and concentrated in vacuo to obtain product **12** as a colorless oil. Yield= 5.105 g (19.2 mmol, 96 %) ^1H NMR (400 MHz, $\text{DMSO}-d_6$): δ = 7.28 (m, 5H), 7.11 (d, 1H, NH), 4.09 (q, 1H, C^αH of Phe), 3.00 (d, 2H, C^βH of Phe), 1.32 (s, 9H, CH_3), 12.66 (s, 1H) ppm. HRMS (ESI) m/z for $\text{C}_{14}\text{H}_{19}\text{NO}_4$ ($M+\text{Na}$) $^+$ calcd.: 288.1212, found: 288.1223.

Synthesis of Boc-L-Phe(1)-L-Phe(2)-OMe (13):

A solution of Boc-L-Phe-OH (1.32 g, 5 mmol) and HOBt (5 mmol, 0.677 g) was stirred in 2 mL of DMF. A neutralized solution of phenylalanine

methyl ester was extracted from its corresponding hydrochloride salt and concentrated on adding to the reaction mixture followed by DCC (5.1 mmol, 1.052 g) at 0 °C. The mixture is allowed to stir at room temperature for 12 hrs. The mixture was diluted with ethyl acetate and the organic layer was washed with 1 M HCl (2 x 30 ml), brine solution, 1 M Na₂CO₃ (3 x 30 ml) and brine solution. The ethyl acetate layer was dried over Na₂SO₄ and evaporated under vacuum to yield white solid product **13**. Purification was done by silica gel column (100-200 mesh) using ethyl acetate-toluene as eluent. Yield= 1.85g, (4.6 mmol, 92 %). ¹H NMR (400 MHz, CDCl₃): δ = 7.54 (m, 10H), 7.00 (d, 1H, NH of Phe(1), 6.28 (d, 1H, NH of Phe(2), 4.81(q, 1H, C^αH of Phe(1), 4.34 (q, 1H, C^αH of Phe(2), 3.12 (d, 4H, CH₂), 1.47 (s, 9H, CH₃) ppm. HRMS (ESI) *m/z* for C₂₄H₃₀N₂O₅ (*M*+Na)⁺ calcd.: 449.2052, found: 449.2086.

Synthesis of NH₂-L-Phe(1)-L-Phe(2)-OMe (**14**):

A solution of Boc-L-Phe(1)-L-Phe(2)-OMe (**13**) (1.6 g, 3.7 mmol) in TFA was stirred for 12 hrs under argon at room temperature. The excess TFA removed under vacuum oily residue was taken in 100 ml of water and washed with diethyl ether (2 × 20 ml) a white product **14** was obtained after lypholization and used further for the reactions. Yield = 1.18 g (3.6 mmol, 97.29 %). ¹H NMR (400 MHz, DMSO-*d*₆): δ = 9.03 (d, 1H, NH of Phe(2), 7.35 (m, 10H), 4.60 (q, 1H, C^αH of Phe(2), 4.03 (q, 1H, C^αH of Phe(1), 3.66 (s, 3H, OCH₃), 3.12 (d, 2H, C^βH of Phe(2), 3.05 (d, 2H, C^βH of Phe(1) ppm. HRMS (ESI) *m/z* for C₁₉H₂₃N₂O₃ (*M*+H)⁺ calcd.: 327.1709, found: 327.1717.

3.2.3 Synthesis of BPI-FF-OMe

1.63 g (5 mmol) of H₂N-L-Phe-L-Phe-OMe **14** was taken in 8 mL ethyl acetate. Maleic anhydride (0.735 g, 7.5 mmol) was dissolved into the ethyl acetate and added to the reaction mixture at room temperature. After stirring for over 24 hrs, the mixture was fully washed with H₂O, saturated brine and dried over Na₂SO₄. The above solution was concentrated by rotary evaporator to obtain the product *N,N'*-maleyl-L-Phe-L-Phe-OMe **15a** as white powder. 1.50 g (3.5 mmol) of *N,N'*-maleyl-L-Phe-L-Phe-OMe **15a** was dissolved in benzene and put into a double-neck flask. The solution was heated to 50 °C and 0.48 g (3.5 mmol) ZnCl₂ was added. Then, the solution of 0.85 g (5.25 mmol) 1,1,1,3,3,3-hexamethyldisilazane (HMDS) in benzene was added drop

by drop into the reaction mixture at 80 °C, and stirred for 12 hrs. Then, the mixture was poured into 600 mL 0.5 (N) HCl and stirred until a clear solution was obtained. The organic layer was separated; the aqueous phase was extracted with 300 mL EtOAc. The combined organic layer was washed with 3 × 100 mL NaHCO₃ and brine solution and dried over Na₂SO₄. The organic layer was evaporated under vacuum to obtain the product *N,N'*-maleoyl-L-Phe-L-Phe-OMe **16a**. Perylene (0.504 g, 2 mmol), *N,N'*-maleoyl-L-Phe-L-Phe-OMe **16a** (1.2192 g, 3 mmol) and *p*-chloranil (1.0326 g, 4.2 mmol) were thoroughly mixed and heated at 240 °C stirring for 3 hrs. The mixture solidified after cooling at room temperature. Chloroform was added to dissolve the solidified mass. The mixture was purified using a silica gel column with chloroform/ether (1:1) as eluent. The compound benzo[*ghi*]perylene-1,2-dicarboxylic(L-Phe-L-Phe-OMe)imide **2** was collected as orange solid.

***N,N'*-maleyl-L-Phe(1)-L-Phe(2)-OMe (15a):**

Yield = 3.0 g (7.07 mmol, 94.33%) ¹H NMR (400 MHz, DMSO-*d*₆): δ = 9.65 (d, 1H, *J* = 8.82 Hz), 9.09 (d, 1H, *J* = 7.76 Hz), 7.60-7.69 (m, 10H, aromatic protons), 6.76 (d, 1H, *J* = 12.52 Hz), 6.66 (d, 1H, *J* = 12.56 Hz), 5.05 (m, 1H, C^αH of Phe (2)), 4.91 (m, 1H, C^αH of Phe (1)), 3.99 (s, 3H, -OCH₃), 3.44 (m, 2H, C^βHs of Phe), 3.35 (m, 1H, C^βH of Phe), 3.16 (m, 1H, C^βH of Phe). MS (ESI) *m/z* for C₂₃H₂₄N₂O₆Na (*M* + Na)⁺ calcd: 447.1532, found: 447.1577.

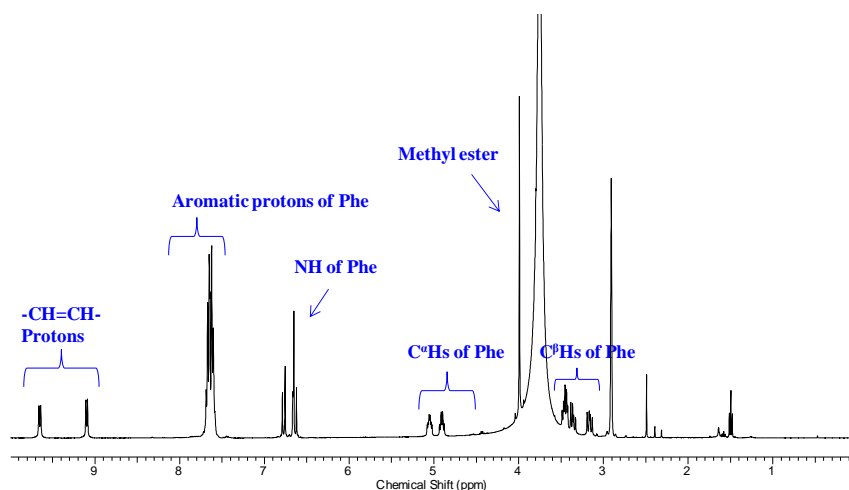


Figure 3.2. ¹H NMR spectrum (400 MHz, DMSO-*d*₆) of *N,N'*-maleyl-L-Phe(1)-L-Phe(2)-OMe (**15a**).

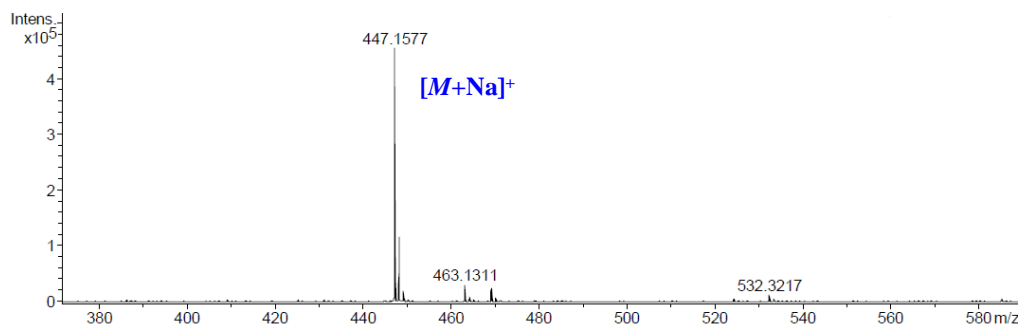


Figure 3.3. Mass spectrum of *N,N'*-maleoyl-L-Phe(1)-L-Phe(2)-OMe with sodium ion adduct. The peak m/z $(M + Na)^+ = 447.1577$ corresponds to synthesis of *N*-maleoyl-L-Phe(1)-L-Phe(2)-OMe **15a**.

***N,N'*-maleoyl-L-Phe(1)-L-Phe(2)-OMe (16a):**

Yield = 1.3912 g (3.42 mmol, 96.86%). ^1H NMR (400 MHz, CDCl_3): δ = 6.98–7.21 (m, 10H, aromatic protons), 6.48 (s, 2H), 6.35 (d, 1H, J = 7.24 Hz, NH), 4.76–4.82 (m, 2H, C^αH s of Phe (1) and Phe (2)), 3.65 (s, 3H, -OMe), 3.28–3.30 (m, 2H, C^βH s), 3.07–3.12 (m, 1H, C^βH), 2.97–3.02 (m, 1H, C^βH). MS (ESI) m/z for $\text{C}_{23}\text{H}_{22}\text{N}_2\text{O}_5\text{Na}$ $(M + Na)^+$ calcd: 429.1426, found: 429.1470.

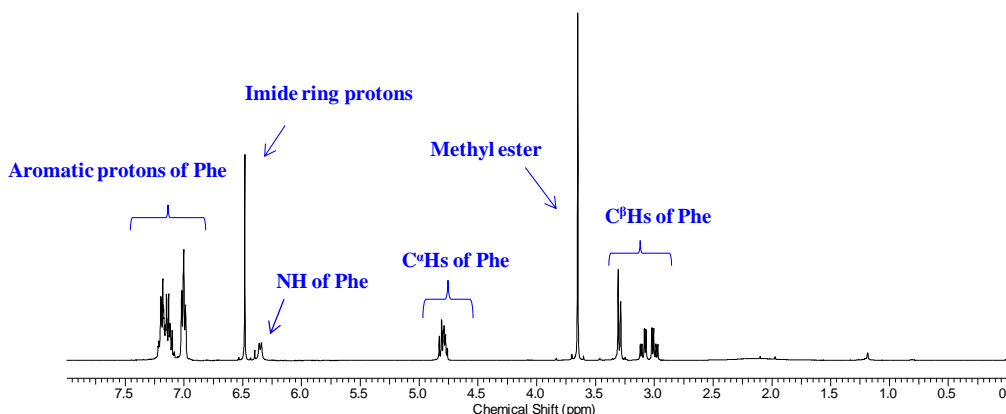


Figure 3.4. ^1H NMR spectrum (400 MHz, CDCl_3) of *N,N'*-maleoyl-L-Phe(1)-L-Phe(2)-OMe (**16a**).

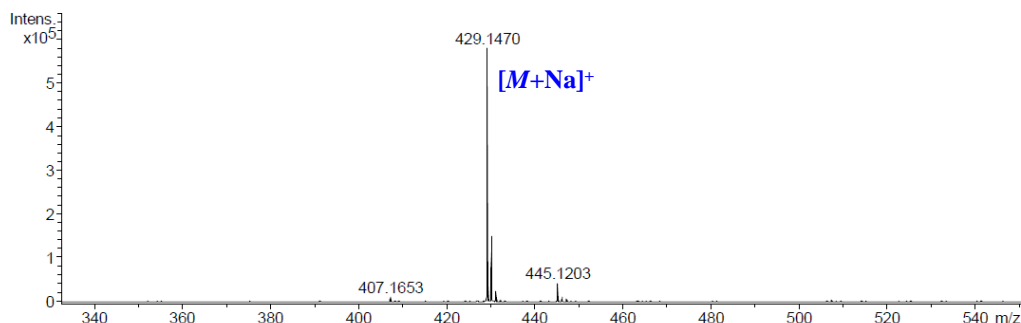


Figure 3.5. Mass spectrum of *N,N'*-maleoyl-L-Phe(1)-L-Phe(2)-OMe with sodium ion adduct. The peak m/z $(M + Na)^+ = 429.1470$ corresponds to synthesis of *N*-maleoyl-L-Phe(1)-L-Phe(2)-OMe (**16a**).

Benzo[ghi]perylene-1,2-dicarboxylic(L-Phe-L-Phe-OMe)imide (2):

Yield = 1.26 g (1.93 mmol, 96.92%). ^1H NMR (400 MHz, CDCl_3) δ = 8.60 (d, 2H, J = 8 Hz), 8.39 (d, 2H, J = 8 Hz), 7.65–7.73 (m, 6H), 7.23 (d, 2H, J = 8 Hz), 7.04 (d, 2H, J = 4 Hz), 7.12 (t, 2H), 7.01 (t, 2H), 6.93 (t, 2H), 6.85 (d, 1H, NH), 5.28 (m, 1H, C^αH of Phe (1)), 4.97 (m, 1H, C^αH of Phe (2)), 3.68 (s, 3H, $-\text{OCH}_3$), 3.23 (d, C^βH of Phe (1)), 3.18 (d, C^βH of Phe (1)), 3.07 (d, C^βH of Phe (2)), 3.03 (d, C^βH of Phe (2)). MS (ESI) m/z for $\text{C}_{43}\text{H}_{30}\text{N}_2\text{O}_5\text{Na}$ ($M + \text{Na}$) $^+$ calcd: 677.2052, found: 677.2096.

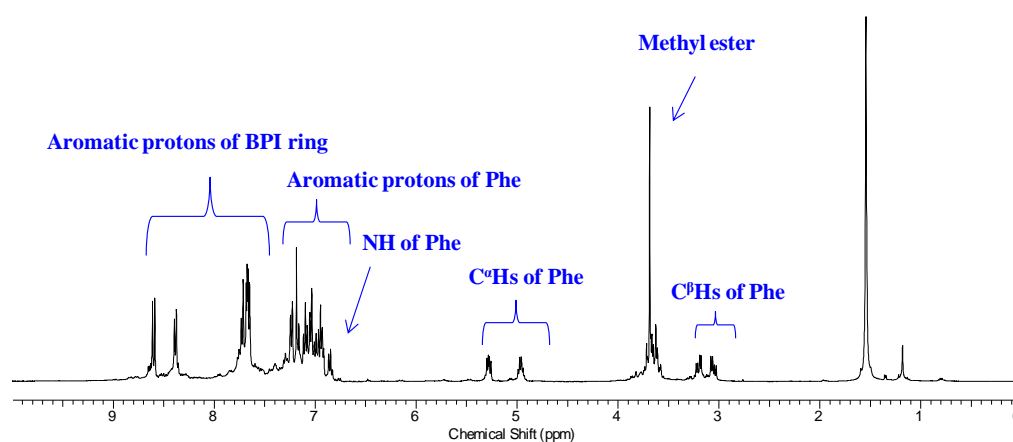


Figure 3.6. ^1H NMR spectrum (400 MHz, CDCl_3) for benzo[ghi]perylene-1,2-dicarboxylic(L-Phe-L-Phe-OMe)imide (2).

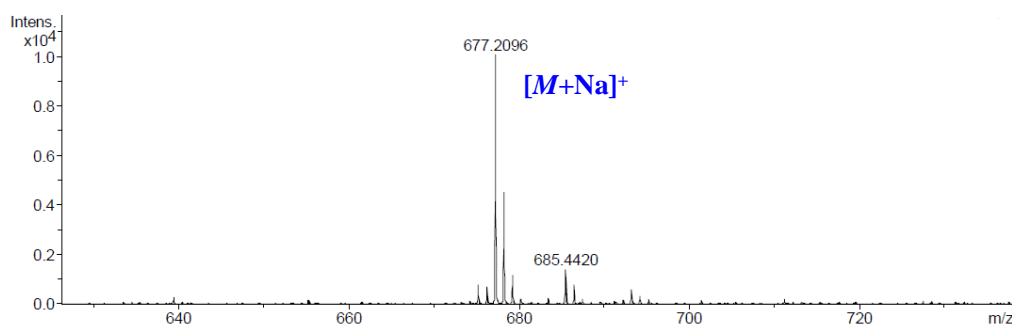


Figure 3.7. Mass spectrum of benzo[ghi]perylene-1,2-dicarboxylic(L-Phe-L-Phe-OMe)imide 2. The peak m/z ($M + \text{Na}$) $^+$ = 677.2096 corresponds to the synthesis of benzo[ghi]perylene-1,2-dicarboxylic(L-Phe-L-Phe-OMe)imide (2).

***N,N'*-Maleyl-L-Leu-OMe (15b):**

Yield = 0.78 g (3.46 mmol, 98.99%). ^1H NMR (400 MHz, $\text{DMSO } d_6$): δ = 13.76 (s, 1H), 9.06 (d, 1H, $-\text{NH}-$), 6.35 (d, 1H), 6.28 (d, 1H), 4.36 (m, 1H, C^αH

of Leu), 3.63 (s, 3H), 1.57 (m, 2H, C^βH of Leu), 1.19 (m, 1H, C^γH of Leu), 0.88 (d, 3H, C^δH of Leu, $J = 6.24$ Hz), 0.85 (d, 3H, C^δH of Leu, $J = 6.28$ Hz).

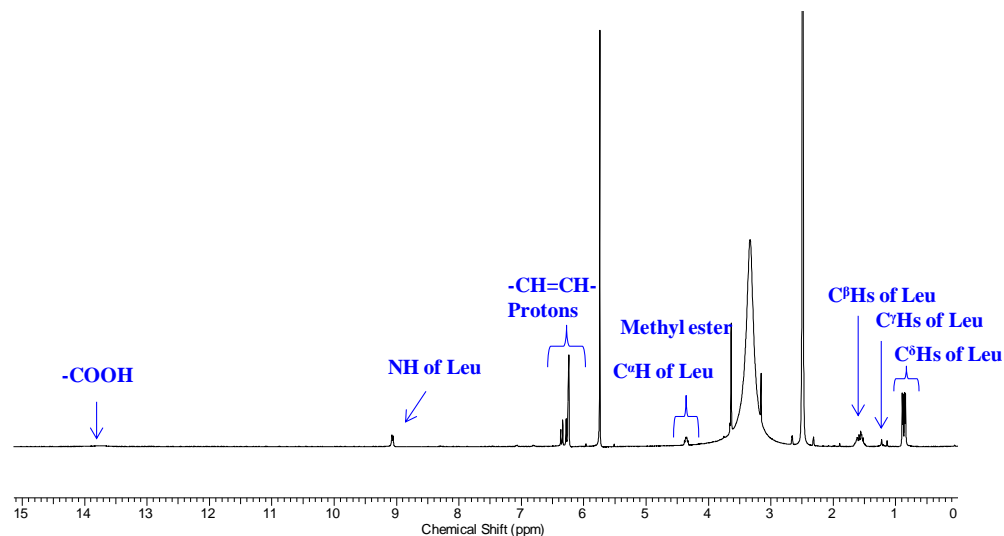


Figure 3.8. ¹H NMR spectrum (400 MHz, DMSO-*d*₆) for *N,N'*-Maleyl-L-Leu-OMe (**15b**).

***N,N'*-Maleoyl-L-Leu-OMe (**16b**):**

Yield = 1.62 g (6.65 mmol, 90.07%). ¹H NMR (400 MHz, CDCl₃): δ = 6.74 (s, 2H), 4.75 (m, 1H, C^αH of Leu), 3.72 (s, 3H), 2.23 (m, 1H, C^βH of Leu), 1.87 (m, 1H, C^βH of Leu), 1.14 (m, 1H, C^γH of Leu), 0.92 (d, 3H, C^δH of Leu, $J = 3.24$ Hz), 0.90 (d, 3H, C^δH of Leu, $J = 3$ Hz).

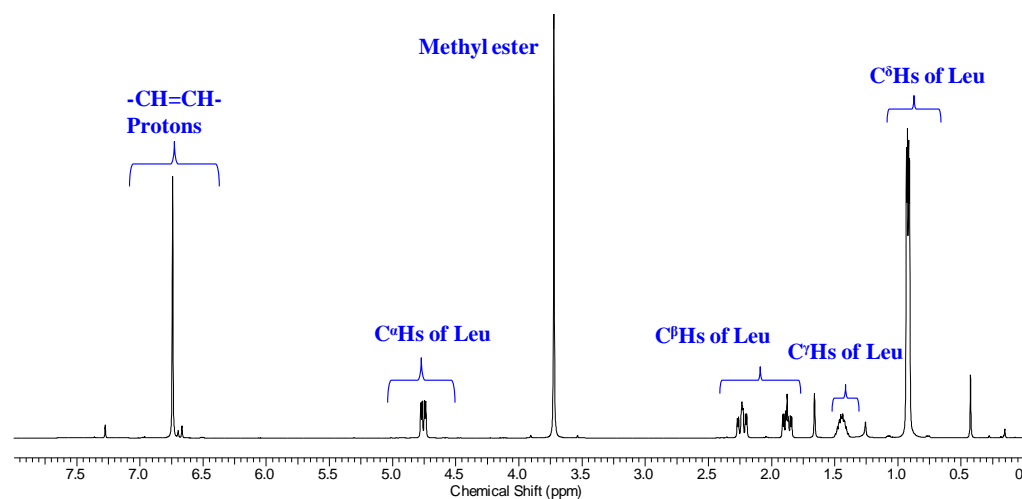


Figure 3.9. ¹H NMR spectrum (400 MHz, CDCl₃) for *N*-Maleoyl-L-Leu-OMe **16b**.

Benzo[ghi]perylene-1,2-dicarboxylic(L-Leu-OMe)imide (3**):**

Yield = 0.7259 g (1.99 mmol, 76.74%). ¹H NMR (400 MHz, CDCl₃): δ = 9.14 (d, 2H, $J = 9.04$ Hz), 8.98 (d, 2H, $J = 7.76$ Hz), 8.19 (d, 2H, $J = 7.8$ Hz), 8.15

(d, 2H, $J = 9$ Hz), 8.08 (t, 2H), 5.18 (m, 1H, C $^{\alpha}$ H of Leu), 3.84 (s, 3H), 2.52 (m, 1H, C $^{\beta}$ H of Leu), 2.13 (m, 1H, C $^{\beta}$ H of Leu), 1.72 (m, 1H, C $^{\gamma}$ H of Leu), 1.08 (d, 3H, C $^{\delta}$ H of Leu, $J = 6.52$ Hz), 1.02 (d, 3H, C $^{\delta}$ H of Leu, $J = 6.8$ Hz).

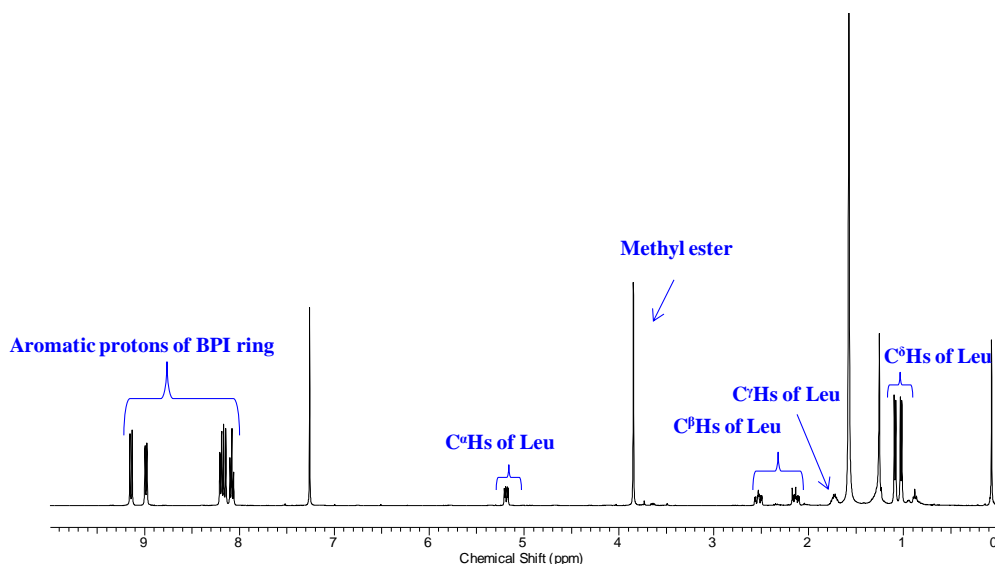


Figure 3.10. ^1H NMR spectrum (400 MHz, CDCl_3) for benzo[*ghi*]perylene-1,2-dicarboxylic(L-Leu-OMe)imide (**3**).

3.3 General characterization

All NMR characterizations were carried out on a Bruker AV 400 MHz spectrometer at 300 K. Compound concentrations in the range of 5-10 mmol L^{-1} in $(\text{CD}_3)_2\text{SO}$. Mass spectra were recorded on a Bruker microTOF-Q II by positive mode electrospray ionisation. Field Emission Scanning Electron Micrographs were recorded in a Carl Zeiss supra 55 and field-emission JSM-7001F (JEOL) was operated at an accelerating voltage 200 kV. For SEM study, BPI-FF-OMe (6 mmol L^{-1}) solutions were dried on a glass slide from respective solvents toluene and methanol and coated with gold. TEM measurements were performed on a PHILIPS electron microscope (model: CM 200), operated at 200 kV. Samples were prepared by placing a drop of the solution on carbon coated copper grids followed by drying under xenon lamp. AFM measurements were performed on a scanning probe microscope AIST-NT instrument (model no. smartSPM-1000). The samples were prepared by drop casting on glass substrate and dried under vacuum. Compound **2** was

dissolved in respective solvents. The samples were allowed to stand for 48 hours at room temperature. Then the solutions were drop casted on to the glass substrate and allowed to dry for scanning electron microscopic study. UV-Vis absorption spectra of samples were recorded using a Varian Cary100 Bio UV-Vis spectrophotometer. Fluorescence spectra of samples were recorded on a Horiba Scientific Fluoromax-4 spectrophotometer with a 1 cm path length quartz cell at room temperature. The slit width for the excitation and emission was set at 2 nm and 1 nm data pitch. Excitations of samples were performed at 338 nm and the data range was in between 348 to 666 nm. The fluorescence quantum yields in various solvents were calculated using steady-state comparative method using fluorescein as a standard ($\phi_{std} = 0.79$).^[53-54]

$$\phi_{un} = \phi_{std} \times \frac{S_{un}}{S_{std}} \times \frac{A_{std}}{A_{un}} \times \frac{n^2 D_{un}}{n^2 D_{std}} \quad (1)$$

ϕ_{un} is the quantum yield of the unknown sample and ϕ_{std} is the emission quantum yield of the standard compound. A_{std} and A_{un} represent the absorbance of the standard and the sample at the excitation wavelength, while S_{std} and S_{un} are the integrated emission band areas of the standard and the sample respectively. nD_{std} and nD_{un} are the solvent refractive index of the standard and the sample respectively. Here, “un” stands for unknown sample and “std” stands for standard sample. The values are quite similar to those previously studied structurally similar fluorophores.^[55] Time resolved studies were performed using a time correlated single photon counting (TCSPC) system from Horiba–Yovin (model: Fluorocube-01-NL). Samples were excited at 376 nm using a picosecond diode laser (model: Pico Brite-375L). The amplitude-weighted lifetime is estimated by

$$\langle \tau \rangle = \sum_{i=1}^n a_i \tau_i \quad (2)$$

where τ_i is the fluorescence lifetime of various fluorescent species, a_i is the normalized pre-exponential factors. The goodness of the fit is judged by the reduced chi-square (χ^2) value. The excited state lifetime (τ) of BPI-FF-OMe **2** decays as a single exponential and decreases with increasing solvent polarity from 8.4 ns in toluene to 5.7 ns in methanol (Figure 3.12b).

3.4 Results and Discussion

3.4.1 Photophysics of dipeptide functionalized benzo[ghi]-perylene monoimide

UV-vis absorption study was performed to determine the optical and electronic properties of synthesized BPI-FF-OMe **2**. UV-vis absorption spectra of BPI-FF-OMe were recorded in various solvents of different polarity (Figure 3.11a). UV-vis absorption spectra shows characteristics absorption bands between 325-500 nm in an aprotic solvent toluene. The strongest absorption peak at 341 nm with molar absorptivity $51000 \text{ M}^{-1}\text{cm}^{-1}$ is attributed to $\pi \rightarrow \pi^*$ transition of benzo[ghi]perylene monoimide system. The lowest energy transition at 483 nm with a shoulder at 455 nm corresponds to $S_0 \rightarrow S_1$ transition. The absorbance at 455 nm is attributed to the transition at highest excited vibrational level. The minimal blue shift was observed in the UV-vis absorbance spectra of BPI-FF-OMe when changing the solvent from aprotic non-polar toluene to protic polar solvent methanol. In general, polar solvents play an important role in stabilization of molecules in ground state and excited state which lead to either hypsochromic or bathochromic shift in the absorption maxima.^[51] The λ_{max} of BPI-FF-OMe in ten different solvents are listed in Table 3.1.

Table 3.1. Spectroscopic and photophysical properties of BPI-FF-OMe (**2**) in different solvents of increasing polarity.

S. No.	Solvent	λ_{abs} (nm)	ϵ_{max} ($\text{M}^{-1}\text{cm}^{-1}$)	λ_{em} (nm) ^a	$\Delta\bar{\nu}$ (cm^{-1}) ^b	Δf	$\tau(\text{ns})$	ϕ_f^c
1	Toluene	341/391/484	51000	508	976	0.013	8.4	0.55
2	<i>o</i> -xylene	341/391/483	53750	508	1018	0.029	8.4	0.51
3	Benzene	341/390/483	52500	508	1018	0.001	7.5	0.56
4	Tetrahydrofuran	337/389/475	80875	517	1710	0.209	7.9	0.43
5	Chloroform	341/390/487	53125	528	1594	0.149	6.0	0.42
6	Dimethylformamide	338/390/479	50875	535	2185	0.274	7.4	0.51
7	Dimethyl sulfoxide	340/391/480	72875	540	2314	0.263	7.2	0.43
8	Acetonitrile	337/387/479	63000	543	2460	0.305	6.7	0.39
9	Ethanol	337/387/477	47500	557	3011	0.288	6.2	0.38
10	Methanol	337/386/476	42500	566	3340	0.309	5.7	0.39

^aEmission data obtained at λ_{max} for each solvent. ^bStokes shift was calculated based on the absorption at lower energy. ^cQuantum yields measured using fluorescein standard in 0.1 (N) NaOH.

Later, we tried to evaluate the fluorescence properties of the fluorophore BPI-FF-OMe. The emission of BPI-FF-OMe strongly depends on solvent polarity. Herein, we observed that effect of solvent polarity on the emission maxima was more pronounced than the absorption maxima (Figure 3.11b and 3.11c). The emission maxima of BPI-FF-OMe in various aprotic protic solvents are listed in Table 3.1.

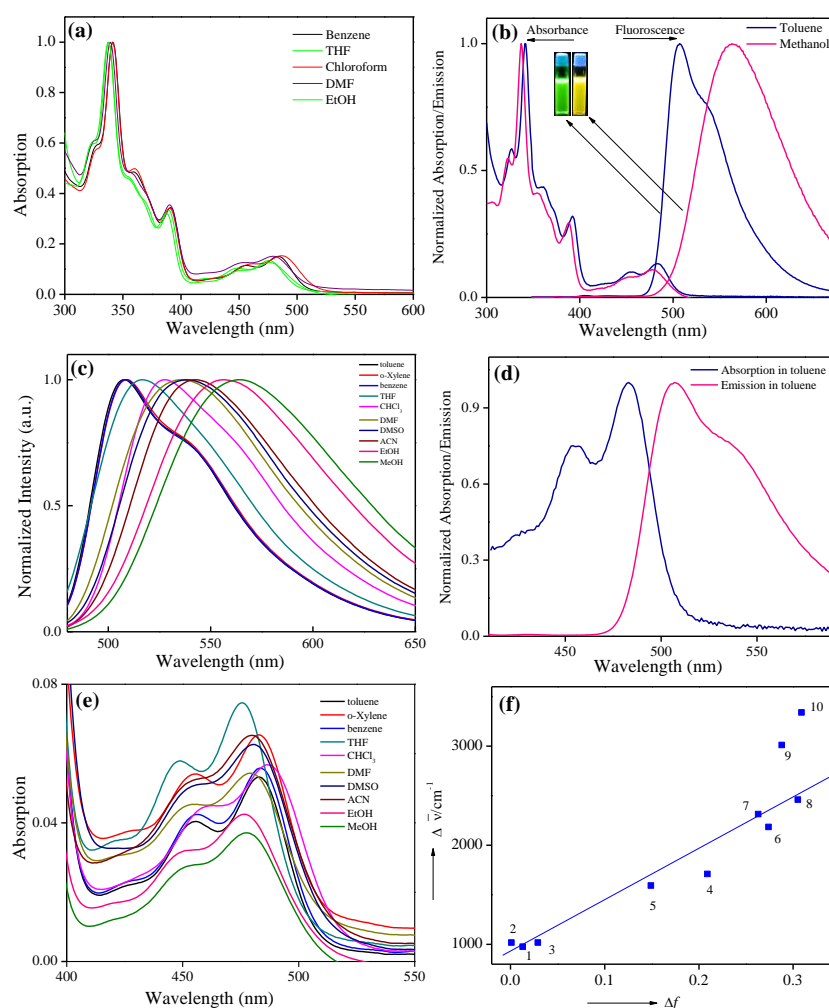


Figure 3.11 (a) UV-Vis absorption spectra of compound **2** (BPI-FF-OMe) in various solvents. (b) Normalized UV-Vis absorption and fluorescence spectra in polar and non polar solvents. Optical images of compound **2** show green emission in toluene and yellow emission in methanol under 365 nm UV light. (c) Emission spectra of compound **2** in solvents listed in Table 3.1. (d) Emission spectra of compound **2** normalized with respect to absorption peak at 483 nm. (e) UV-Vis of compound **2** in solvents from listed Table 3.1. (f) Lippert–Mataga plot.

Excitation wavelength at 337 nm was used to collect the emission spectra of compound BPI-FF-OMe. The emission of BPI-FF-OMe shifts from green emission to yellow emission in the visible region as a function of increasing solvent polarity (Figure 3.11c). BPI-FF-OMe exhibits emission maxima at 508 nm in aprotic toluene solvent whereas the emission was shifted to 566 nm in polar protic methanol solvent. The strong red shift of about 58 nm was observed with decrease in both the fluorescence intensity as well as the quantum yield (Table 3.1) upon increase in solvent polarity.

The peak broadening was also observed with increase in solvent polarity. The shift in fluorescence maximum was attributed due to the solvent polarizability factors (Δf) of different solvents. The excited state dipole moment (μ_e) of a molecule is different in toluene and methanol which leads to the variation of change in dipole moment $\Delta\mu$ ($\Delta\mu = \mu_e - \mu_g$). The dipole moment ($\Delta\mu$) directs the excited state energy levels of a molecule in a solvent.^[45] The excited state energy level is lower in methanol than toluene. Therefore, energy gap difference is lower in methanol than toluene and corresponding fluorescence emission is shifted to longer wavelength (red shift). Similarly, BPI-Leu-OMe is also synthesized to determine the role of dipeptide in emissions. Spectroscopic analysis of BPI-Leu-OMe exhibits similar emission to BPI-FF-OMe. Thus, benzo[ghi]perylene moiety plays an important role in the emission as well as chromic effects for two synthesized compounds. The excitation spectrum for the 564 nm emission band of BPI-FF-OMe in methanol solvent shows the peaks at 315 nm, 327 nm, 369 nm, 384 nm, 453 nm and 476 nm which are similar to the absorption spectrum with a 30 nm red shift (Figure 3.12a). The fluorescence quantum yields of BPI-FF-OMe in ten different solvents are listed in Table 3.1. The fluorescence quantum yield of BPI-FF-OMe was found to be in between 0.39 in methanol and 0.55 in toluene. The nature of solvents plays an important role in emission of BPI-FF-OMe. Similar observation was reflected from the optical images of BPI-FF-OMe in different solvents under UV light at a wavelength of 365 nm. The compound BPI-FF-OMe showed green fluorescence in aprotic non-polar solvent toluene while yellow fluorescence was observed in polar protic methanol solvent (Figure 3.1). A mirror image relationship between the

electronic transitions of $S_0 \rightarrow S_1$ (absorption) and $S_1 \rightarrow S_0$ (emission) of BPI-FF-OMe in aprotic nonpolar toluene solvent is clearly observed at the wavelength of 410-590 nm (Figure 3.11d).^[45,46] Solvent dependent Stokes shifts for BPI-FF-OMe was interpreted in terms of the Lippert-Mataga equation. Stoke shifts calculated from lower energy transition of BPI-FF-OMe molecule (Figure 3.11e). Figure 3.11f represents the Lippert-Mataga plot of $S_1 \rightarrow S_0$ Stokes' shift $\Delta\bar{\nu}$ versus Δf for compound **2** in the solvents listed in Table 3.1. The plot depicts a good linear relationship of $\Delta\bar{\nu}$ and Δf . Time Correlated Single Photon Counting (TCSPC) experiment was performed to determine the average fluorescence lifetime of BPI-FF-OMe. To measure the average fluorescence decay traces of BPI-FF-OMe, the samples were excited at 376 nm and the emissions were monitored at 508 nm for toluene and 566 nm for methanol. The excited state lifetime of BPI-FF-OMe decreases with increasing in solvent polarity from 8.4 ns in toluene to 5.7 ns in methanol (Figure 3.12b).

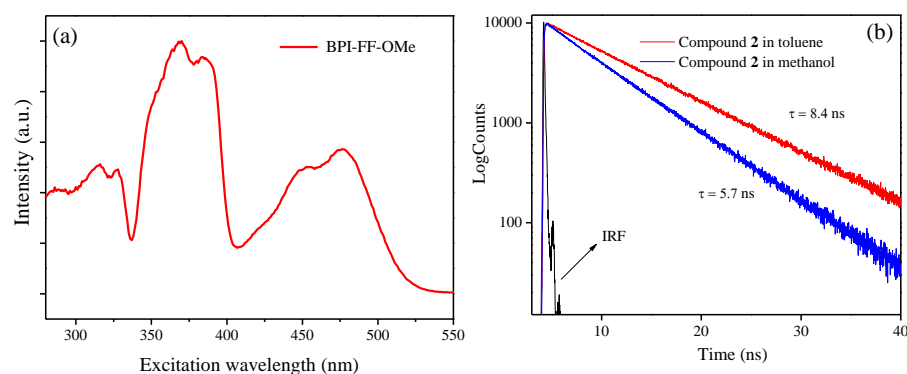


Figure 3.12. (a) Fluorescence excitation spectra of donor BPI-FF-OMe **2** in methanol (emission wavelength 564 nm); (b) Time correlated single photon counting decay traces of BPI-FF-OMe (9×10^{-5} mol L⁻¹) in toluene $\lambda_{em} = 508$ nm (red) and methanol $\lambda_{em} = 566$ nm (blue).

3.4.2 Theoretical calculation

DFT calculation was performed to determine the energy minimized geometry of BPI-FF-OMe in ground state. Theoretical calculation of highest occupied molecular orbital (HOMO) and lowest unoccupied molecular orbital

(LUMO) of synthesized compound BPI-FF-OMe were calculated using the B3LYP/6-31G* basis set of Gaussian 09 program. The highest occupied molecular orbital (HOMO) and lowest unoccupied molecular orbital (LUMO) levels of BPI-FF-OMe **2** molecule are 5.57 eV and -2.50 eV respectively. HOMO of the molecule is mostly found on conjugated BPI core and the LUMO mostly exists at imide nitrogen of BPI core (Figure 3.13). HOMO/LUMO calculation determines the band gap energy of molecules.^[56] The calculated band gap energy of BPI-FF-OMe is 3.06 eV. The optical band gap 2.6 eV was calculated from the experiment performed on UV-Visible spectroscopy in methanol. It is found that N-capped dipeptide appended BPI molecule has no effect on the HOMO and LUMO distribution of BPI core.

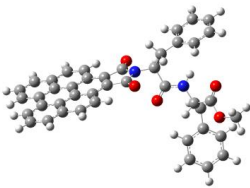
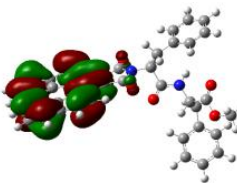
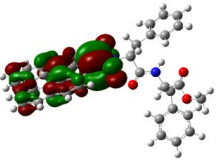
BPI-FF-OMe	HOMO	LUMO	Calculated Band gap (eV)	Optical band gap (eV) ^[a]
	 -5.57 eV	 -2.50 eV	3.06 eV	2.6 eV

Figure 3.13. HOMO and LUMO frontier orbital of BPI-FF-OMe at the B3LYP/6-31G (d) level. ^[a]Optical band gap of BPI-FF-OMe in methanol was calculated from UV-Vis spectroscopy.

3.4.3 Self-assembly study of BPI-FF-OMe

Variable temperature dependent ¹H NMR was performed in DMSO-*d*₆ to understand the various non-covalent interactions responsible for the self-assembly nature of aromatic dipeptide Phe-Phe-OMe functionalized benzo[*ghi*]perylene monoimide **2**. The change in chemical shift (δ) of aromatic BPI ring protons and peptide NH proton with different temperatures suggests the presence of intermolecular H-bonding and π - π stacking interactions of BPI-FF-OMe molecules. A significant change in chemical shift (δ) was observed for NH proton of dipeptide backbone. The chemical shift of NH proton was shifted to up-field (8.86 ppm to 8.60 ppm) with increase in

temperature from 303 K to 343 K (Figure 3.14c). The up-field shifting is due to the weaker in H-bonding between BPI molecules and corresponding disassembly on warming.^[57-60] Moreover, the down-field δ shift of BPI protons with increasing temperature is the evidence in favor of π - π stacking interactions. ¹H NMR signals of all benzo[*ghi*]perylene ring protons shifted to down-field because the aromatic ring protons of benzo[*ghi*]perylene moieties experience de-shielding effect from the ring current at high temperature where the interacting π clouds of aromatic protons are loosely associated to each other than the lower temperature.^[61-62] Therefore, H-bonding and π - π stacking interactions play the crucial role in the stabilization of self-assembly structure of BPI-FF-OMe molecule where the amide functionality of peptide backbone provides hydrogen-bonding interaction and benzo[*ghi*]perylene monoinide protons contributes in π - π stacking interactions. The amphiphile BPI-FF-OMe form self-assembled nanospherical structures in different solvents.

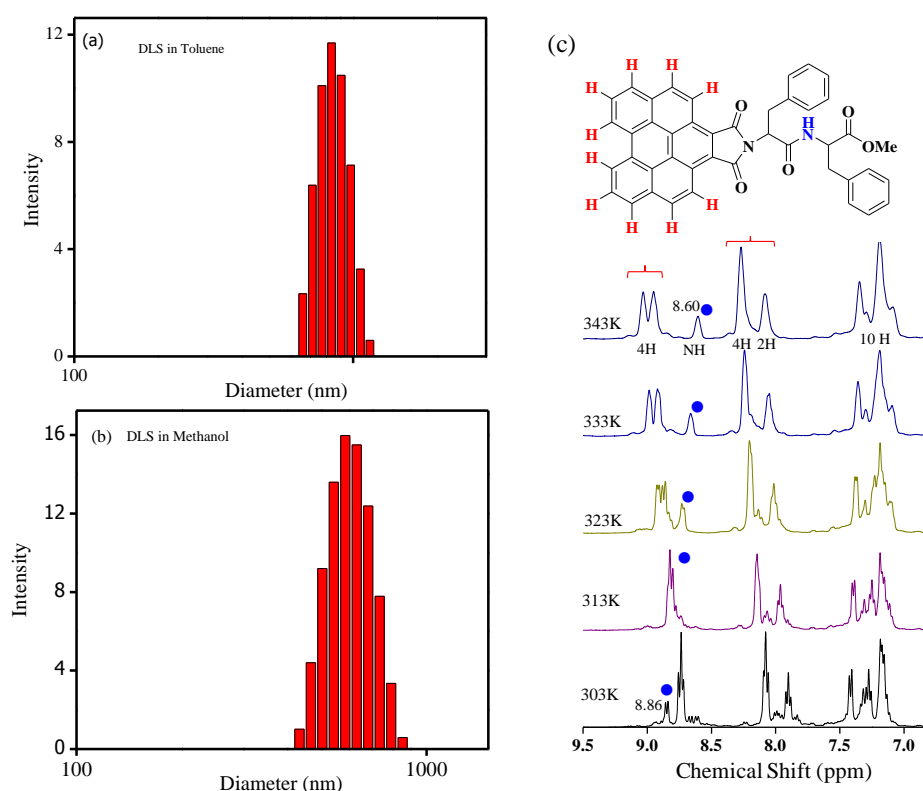


Figure 3.14. Size distribution histogram of nanospheres from DLS measurement. The mean hydrodynamic diameter of nanospheres in (a) methanol and (b) toluene. (c) Temperature dependent ¹H NMR spectra of BPI-FF-OMe (20 mmol L⁻¹) in DMSO-*d*₆.

To further investigate the formation, stability and equilibrium state of nanospheres, the particle size distribution was analyzed by dynamic light scattering (DLS) experiments in methanol and toluene at 25 °C (Figure 3.14a,b). The hydrodynamic diameters of nanospheres 857 nm and 613 nm were observed in DLS analysis. Polydispersity index was calculated as 0.47 in toluene and 0.30 in methanol solutions. These results suggest that nanospheres are polydispersed both in toluene and methanol solutions. The estimated zeta-potential of formed nanospheres of BPI-FF-OMe were -25.89 mV and -17.97 mV in toluene and methanol respectively. These zeta potential determine the surface charge of nanospheres.

3.4.5 Morphological characterization: supramolecular nanospheres

Scanning electron microscope (SEM), transmission electron microscope (TEM) was used to explore the morphology of BPI-FF-OMe **2** in an aprotic solvent toluene and protic solvent methanol. The solution of BPI-FF-OMe in toluene and methanol showed well organized uniform nanosphere architectures (Figures 3.15a and b). The possible mechanism for nanosphere formation could lead via miceller formation in the initial stage followed by higher order self-assembly into the nanosphere architectures (Scheme 3.2). An aromatic dipeptide Phe-Phe-OMe functionalized benzo[*ghi*]perylene-monoimide (BPI-FF-OMe) self-organized into nanospheres *via* intermolecular hydrogen bonding and π - π stacking interactions in toluene and methanol. SEM results are consistent with the results obtained from TEM analysis (Figure 3.15c and d). Atomic force microscopic images were recorded for BPI-FF-OMe solution upon drop casted on glass substrate. The AFM images showed the similar characteristics features of nanosphere architectures which were observed for the SEM and TEM analysis. The average heights of nanosphere architectures are 176 nm in methanol and 203 nm in toluene (Figures 3.15e and 3.15f). Scheme 3.2 depicts the possible self-assembly process of BPI-FF-OMe into nanospherical architectures.

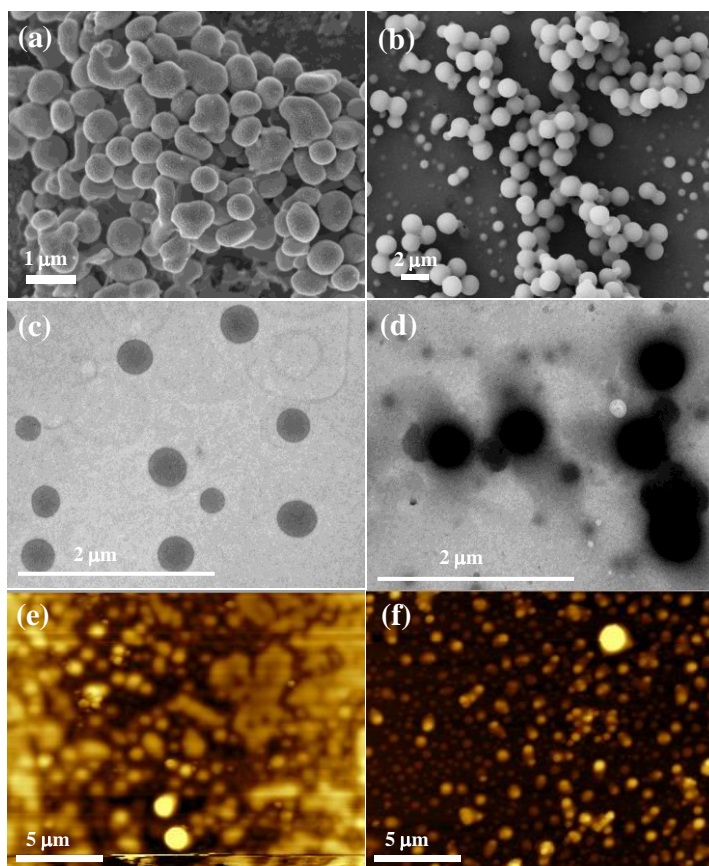
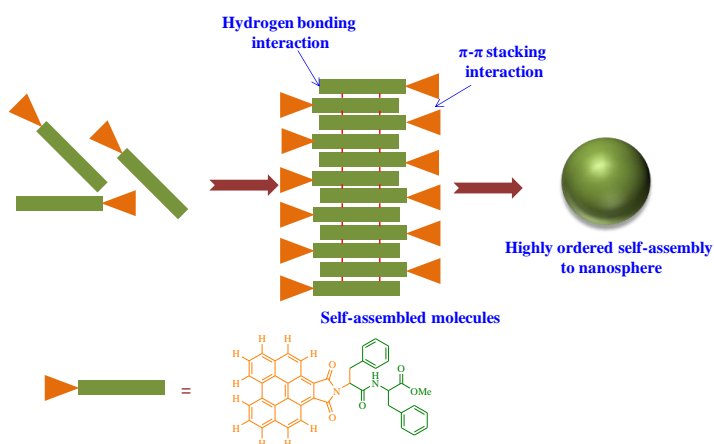


Figure 3.15. Microscopic images of compound **2**. (a) SEM image of compound **2** in toluene, (b) SEM image of compound **2** in methanol, (c) TEM image of BPI-FF-OMe in toluene and (d) TEM image of compound **2** in methanol show nanospheres. AFM images show the nanospherical morphology of compound **2** (e) in toluene and (f) in methanol.



Scheme 3.2. Schematic presentation shows a possible mechanism of BPI-FF-OMe **2** for nanosphere formation.

3.4.6 Donor-acceptor Interactions Lead to White Light Emission

The aromatic π - π stacking interaction of BPI-FF-OMe was utilized in white light emission through the co-assembly with 1-pyrenebutyric acid (PyBA). PyBA (compound **1**) was selected because it contains π -conjugated aromatic moiety. Both the aromatic donor and acceptor molecules can participate in aromatic π - π stacking interaction and lead to energy transfer. Solution of donor PyBA **1** to acceptor BPI-FF-OMe **2** in methanol show white light emission upon exposure to a UV lamp at 365 nm (Figure 3.1). UV-Vis spectroscopic studies were performed to examine spectral characteristic features of different molar ratios of donor and acceptor molecules (Figure 3.16a). Emission spectra were also collected to establish the mechanism of energy transfer from donor PyBA to acceptor BPI-FF-OMe **2** molecules. Titrating PyBA with BPI-FF-OMe, emission spectra were recorded at an excitation wavelength of 341 nm. The gradual addition of BPI-FF-OMe **2** to PyBA **1**, a steady decrease in fluorescence intensity at 375 nm, 395 nm, 415 nm and a concomitant increase of a new peak at 568 nm (Figure 3.16b) was observed. The energy transfer from donor PyBA to acceptor BPI-FF-OMe is well noticeable from the spectral overlap region of emission spectra of donor PyBA and absorption spectra of acceptor BPI-FF-OMe (Figure 3.16d). In general, white light is constituted by many wavelengths. The emission spectra of equimolar mixture of donor PyBA and acceptor BPI-FF-OMe show various emission peaks in the range of 350 nm to 650 nm. The individual emission of BPI-FF-OMe and PyBA in a protic solvent methanol was analyzed. BPI-FF-OMe emits yellow fluorescence upon exposure to UV lamp at 365 nm. However, a solution of PyBA shows blue emission under UV lamp at 365 nm (Figure 3.16c). The combination of donor-acceptor pair at different molar ratio shows remarkable changes in the emission. A white light emission was observed when a pair of donor (PyBA)-acceptor (BPI-FF-OMe) (10:1) was exposed to UV lamp at 365 nm in methanol. The white light emission was observed due to the energy transfer between donor and acceptor. The white light emitting solution of PyBA:BPI-FF-OMe coated over the silica plate

shows excellent white light emission. Thus, the solution PyBA:BPI-FF-OMe can be used for the coating purpose in various materials.

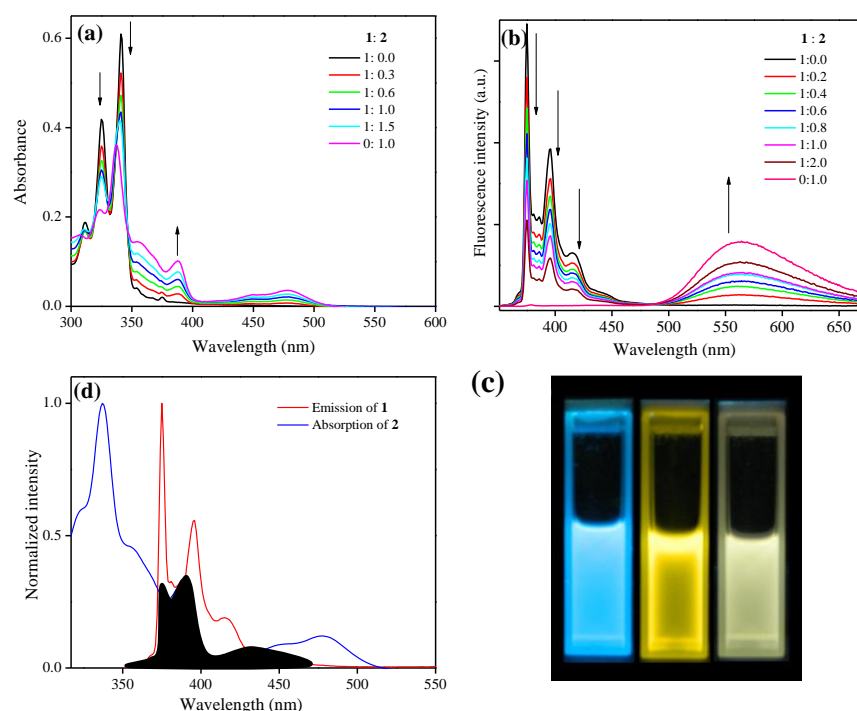


Figure 3.16. (a) UV-Vis and (b) fluorescence spectra of (1×10^{-6} mol L $^{-1}$) of PyBA **1**, BPI-FF-OMe **2** and mixture of different equivalents of PyBA and BPI-FF-OMe in methanol respectively. (c) Spectral overlaps region of emission spectrum of donor PyBA and absorption spectrum of acceptor BPI-FF-OMe. (d) Light emission of PyBA, BPI-FF-OMe and mixture of PyBA and BPI-FF-OMe (10:1) under 365 nm UV light.

3.5 Conclusion

In this work, we have synthesized an aromatic benzo[*ghi*]-perylene monoimide capped derivatives BPI-FF-OMe and BPI-LOMe. The optical behavior of BPI-FF-OMe was studied in a wide range of organic solvents. BPI-FF-OMe preferably forms nanospherical architecture both in protic polar and aprotic solvents like methanol and toluene. Intermolecular hydrogen bonding and aromatic π - π stacking interactions play important role in the formation of nanospherical architecture of dipeptide functionalized benzo[*ghi*]perylene monoimide (BPI-FF-OMe). Temperature dependent ^1H -NMR studies support the intermolecular interactions in solution phase self-

assembly of BPI-FFOMe. The microscopic techniques including SEM, TEM and AFM elucidate the nanostructural morphology of BPI-FF-OMe. The theoretical studies also support the experimental results. The acceptor benzo[ghi]perylene monoimide BPI-L-OMe molecule also shows white light emission through efficient energy transfer between donor and acceptor pairs where pyrenebutyric acid was used as an efficient donor molecule. These results could be an efficient approach for the construction of new organic light emitting devices.

3.6 References

- [1] Würthner F., Sautter A., Thalacker C. (2000), Substituted diazadibenzoperylenes: new functional building blocks for supramolecular chemistry, *Angew. Chem. Int. Ed.*, 39, 1243-1245 (DOI: 10.1002/(SICI)1521-3773(20000403)39:7).
- [2] Zang L., Che Y., Moore J. S. (2008), One-dimensional self-assembly of planar π -conjugated molecules: adaptable building blocks for organic nanodevices, *Acc. Chem. Res.*, 41, 1596-1608 (DOI: 10.1021/ar800030w).
- [3] Tovar J. D. (2013), Supramolecular construction of optoelectronic biomaterials, *Acc. Chem. Res.*, 46, 1527–1537 (DOI: 10.1021/ar3002969).
- [4] Schenning, A. P. H. J., Meijer E. W. (2005), Supramolecular electronics; nanowires from self-assembled π -conjugated Systems, *Chem. Commun.*, 3245–3258 (DOI: 10.1039/b501804h).
- [5] Hoeben F. J. M., Jonkheijm P., Meijer E. W., Schenning A. P. H. J. (2005) About supramolecular assemblies of π -conjugated systems. *Chem. Rev.*, 105, 1491-1546 (DOI: 10.1021/cr030070z).
- [6] Ide J., Mereau R., Ducasse L., Castet F. (2011), Supramolecular organization and charge transport properties of self-assembled π - π stacks of perylene diimide dyes, *J. Phys. Chem. B*, 115, 5593-5603 (DOI: 10.1021/jp111422v).
- [7] Avlasevich Y., Li C., Mullen K. (2010), Synthesis and applications of core-enlarged perylene dyes. *J. Mater. Chem.*, 20, 3814-3826 (DOI: 10.1039/c000137f).

- [8] Langhals H., Kirner S. (2000), Novel fluorescent dyes by the extension of the core of perylenetetracarboxylic bisimides, *Eur. J. Org. Chem.*, 365-380 (DOI: 10.1002/(SICI)1099-0690(200001)2000:2).
- [9] Zagranski Y., Chen L., Jansch D., Gessner T., Li C., Müllen K. (2014), Toward perylene dyes by the hunsdiecker reaction, *Org. Lett.*, 16, 2814-2817 (DOI: 10.1021/ol5008586).
- [10] Jana A., Nguyen K. T., Li X., Zhu P., Tan N. S., Ågren H., Zhao Y. (2014), Perylene-derived single-component organic nanoparticles with tunable emission: efficient anticancer drug carriers with real-time monitoring of drug release, *ACS Nano*, 8, 5939-5952 (DOI: 10.1021/nn501073x).
- [11] Würthner F. (2004) Perylene bisimide dyes as versatile building blocks for functional supramolecular architectures, *Chem. Commun.*, 1564-1579 (DOI: 10.1039/b401630k).
- [12] Vajiravelu S., Ramunas L., Vidas G. J., Valentas G., Vygintasc J., Valiyaveetil S. (2009), Effect of substituents on the electron transport properties of bay substituted perylene diimide derivatives, *J. Mater. Chem.*, 19, 4268-4275 (DOI: 10.1039/b901847f).
- [13] Mizoshita N., Tani T., Shinokubo H., Inagaki S. (2012), Mesoporous organosilica hybrids consisting of silica-wrapped π - π stacking columns, *Angew. Chem., Int. Ed.*, 51, 1156-1160 (DOI: 10.1002/anie.201105394).
- [14] Segura J. L., Herrera H., Bauerle P. (2012), Oligothiophene-functionalized naphthalimides and perylene imides: design, synthesis and applications, *J. Mater. Chem.*, 22, 8717-8733 (DOI: 10.1039/C2JM16690A).
- [15] Jeong W., Choi S., Choi J. S., Lim Y.-B. (2013), Chameleon-like self-assembling peptides for adaptable biorecognition nanohybrids, *ACS Nano*, 7, 6850-6857 (DOI: 10.1021/nn402025r).
- [16] Fleming S., Ulijn R. V. (2014), Design of nanostructures based on aromatic peptide amphiphiles, *Chem. Soc. Rev.*, 43, 8150-8177 (DOI: 10.1039/C4CS00247D).

- [17] Segarra-Maset M. D., Nebot V. J., Miravet J. F., Escuder B. (2013), Control of molecular gelation by chemical stimuli, *Chem. Soc. Rev.*, 42, 7086-7098 (DOI: 10.1039/C2CS35436E).
- [18] Yang Z., Liang G., Xu B. (2008), Enzymatic hydrogelation of small molecules, *Acc. Chem. Res.*, 41, 315-326 (DOI: 10.1021/ar7001914).
- [19] Draper E. R., Walsh J. J., McDonald T. O., Zwijnenburg M. A., Cameron P. J., Cowan A. J., Adams D. J. (2014), Air-stable photoconductive films formed from perylene bisimide gelators, *J. Mater. Chem. C*, 2, 5570-5575 (DOI: 10.1039/C4TC00744A).
- [20] Che Y., Datar A., Balakrishnan K., Zang L. (2007), Ultralong nanobelts self-assembled from an asymmetric perylene tetracarboxylic diimide, *J. Am. Chem. Soc.* 129, 7234-7235 (DOI: 10.1021/ja071903w).
- [21] Balakrishnan K., Datar A., Oitker R., Chen H., Zuo J., Zang L. (2005), Nanobelt self-assembly from an organic n-type semiconductor: propoxyethyl-PTCDI, *J. Am. Chem. Soc.*, 127, 10496-10497 (DOI: 10.1021/ja052940v).
- [22] Balakrishnan K., Datar A., Naddo T., Huang J., Oitker R., Yen M., Zhao J., Zang L. (2006), Effect of side-chain substituents on self-assembly of perylene diimide molecules morphology control, *J. Am. Chem. Soc.*, 128, 7390-7398 (DOI: 10.1021/ja061810z).
- [23] Zhong L., Xing F., Shi W., Yan L., Xie L., Zhu S. (2013), Synthesis, spectra, and electron-transfer reaction of aspartic acid-functionalized water-soluble perylene bisimide in aqueous solution, *ACS Appl. Mater. Interfaces*, 5, 3401-3407 (DOI: 10.1021/am4004446).
- [24] Feng X., An Y., Yao Z., Li C., Shi G. (2012), A turn-on fluorescent sensor for pyrophosphate based on the disassembly of Cu²⁺-mediated perylene diimide aggregates, *ACS Appl. Mater. Interfaces*, 4, 614-618 (DOI: 10.1021/am201616r).
- [25] Roy S., Maiti D. K., Panigrahi S., Basak D., Banerjee A. (2012), A new hydrogel from an amino acid-based perylene bisimide and its semiconducting, photo-switching behaviour, *RSC Adv.*, 2, 11053-11060 (DOI: 10.1039/C2RA21319B).

- [26] Bai S., Debnath S., Javid N., Frederix Pim W. J. M., Fleming S., Pappas C., Ulijn R. V. (2014), Differential self-assembly and tunable emission of aromatic peptide bola-amphiphiles containing perylene bisimide in polar solvents including water, *Langmuir*, 30, 7576–7584 (DOI:10.1021/la501335e).
- [27] Eakins G. L., Gallaher J. K., Keyzers R. A., Falber A., Webb J. E. A., Laos A., Tidhar Y., Weissman H., Rybtchinski B., Thordarson P., Hodgkiss, J. M. (2014), Thermodynamic factors impacting the peptide-driven self-assembly of perylene diimide nanofibers, *J. Phys. Chem. B*, 118, 8642-865 (DOI: 10.1021/jp504564s).
- [28] Briggs B. D., Knecht M. R. (2012), Nanotechnology meets biology: peptide-based methods for the fabrication of functional materials, *J. Phys. Chem. Lett.*, 3, 405-418 (DOI: 10.1021/jz2016473).
- [29] Yan X., Cui Y., He Q., Wang K., Li J. (2008), Organogels based on self-assembly of diphenylalanine peptide and their application to immobilize quantum dots, *Chem. Mater.*, 20, 1522-1526 (DOI: 10.1021/cm702931b).
- [30] Na N., Mu X., Liu Q., Wen J., Wanga F., Ouyang J. (2013), Self-assembly of diphenylalanine peptides into microtubes with “turn On” fluorescence using an aggregation-induced emission molecule, *Chem. Commun*, 49, 10076-10078 (DOI: 10.1039/C3CC45320K).
- [31] Gazit E. (2007), Self-assembled peptide nanostructures: the design of molecular building blocks and their technological utilization, *Chem. Soc. Rev.*, 36, 1263-1269 (DOI: 10.1039/b605536m).
- [32] Gan Z., Wu X., Zhu X., Shen J. (2013), Light-induced ferroelectricity in bioinspired self-assembled diphenylalanine nanotubes/microtubes, *Angew. Chem. Int. Ed*, 52, 2055-2059 (DOI: 10.1002/anie.201207992).
- [33] Abbel R., Weegen R., Pisula W., Surin M., Leclere P., Lazzaroni R., Meijer E. W., Schenning A. P. H. J. (2009), Multicolour self-assembled Fluorene co-oligomers: from molecules to the solid state via white-light-emitting organogels, *Chem.–Eur. J.*, 15, 9737–9746 (DOI: 10.1002/chem.200900620).
- [34] Vijayakumar C., Praveen V. K., Ajayaghosh A. (2009), RGB emission through controlled donor self-assembly and modulation of excitation

- energy transfer: a novel strategy to white-light-emitting organogels, *Adv. Mater.*, 21, 2059–2063 (DOI: 10.1002/adma.200802932).
- [35] Abbel R., Grenier C., Pouderoijen M. J., Stouwdam J. W., Leclerc P. E. L. G, Sijbesma R. P., Meijer E. W., Schenning A. P. H. J. (2009), White-light emitting hydrogel-bonded supramolecular copolymers based on π -conjugated oligomers, *J. Am. Chem. Soc.*, 131, 833–843 (DOI: 10.1021/ja807996y).
- [36] Chen C., Jin X.-H., Zhou X.-J., Cai L.-X., Zhang Y.-J., Zhang J. (2015), Photo-facilitated aggregation and correlated color temperature adjustment of single component organic solid state white-light emitting materials, *J. Mater. Chem. C*, 3, 4563–4569 (DOI: 10.1039/C4TC02771J).
- [37] Jin X.-H., Chen C., Ren C.-X., Cai L.-X., Zhang J. (2014), Bright white-light emission from a novel donor–acceptor organic molecule in the solid state via intermolecular charge transfer, *Chem. Commun.*, 50, 15878–15881 (DOI: 10.1039/C4CC07063A).
- [38] Huyal I. O., Koldemir U., Ozel T., Demir H. V., Tuncel D. (2008), On the origin of high quality white light emission from a hybrid organic/inorganic light emitting diode using azide functionalized polyfluorene, *J. Mater. Chem.*, 18, 3568–3574 (DOI: 10.1039/B802910E).
- [39] Liu J., Guo X., Bu L., Xie Z., Cheng Y., Geng Y., Wang L., Jing X., Wang F. (2007), White electroluminescence from a single-polymer system with simultaneous two-color emission: polyfluorene blue host and side-chain-located orange dopant, *Adv. Funct. Mater.*, 17, 1917–1925 (DOI: 10.1002/adfm.200600988).
- [40] Giansante C., Raffy G., Schaefer C., Rahma H., Kao M.-T., Olive A. G. L., Guenzo A. D. (2011), White-light-emitting self-assembled nanofibers and their evidence by microspectroscopy of individual objects, *J. Am. Chem. Soc.*, 133, 316–325 (DOI: 10.1021/ja106807u).
- [41] Langhals H., Bock B., Schmid T., Marchuk A. (2012), Angular Benzoperylenetetracarboxylic bisimides, *Chem. Eur. J.*, 18, 13188–13194 (DOI: 10.1002/chem.201103221).

- [42] Langhals H., Poxleitner S., Krotz O., Pust T., Walter A. (2008), FRET in orthogonally arranged chromophores, *Eur. J. Org. Chem.*, 4559-4562 (DOI: 10.1002/ejoc.200800451).
- [43] Langhals H., Speckbacher M. (2001), Intramolecular effects in covalently connected units-ring-type oriented chromophores and their interactions, *Eur. J. Org. Chem.* 2481-2485 (DOI: 10.1002/1099-0690(200107)2001:13).
- [44] Clar E., Zander M. (1957), Syntheses of coronene and 1 : 2-7 : 8-dibenzocoronene. *J. Chem. Soc.*, 4616-4619 (DOI: 10.1039/JR9570004616).
- [45] Manning S. J., Bogen W., Kellyreference L. A. (2011), Synthesis, characterization, and photophysical study of fluorescent N-substituted benzo[ghi]perylene “swallow tail” monoimides, *J. Org. Chem.*, 76, 6007-6013 (DOI: 10.1021/jo200529p).
- [46] Rao K. V., George S. J. (2010), Synthesis and controllable self-assembly of a novel coronene bisimide amphiphile, *Org. Lett.* 12, 2656-2659 (DOI: 10.1021/ol100864e).
- [47] Alibert-Fouet S., Seguy I., Bobo J.-F., Destruel P., Bock H. (2007) Liquid-crystalline and electron-deficient coronene oligocarboxylic esters and imides by twofold benzogenic Diels-Alder reactions on perylenes, *Chem. Eur. J.*, 13, 1746-1753 (DOI: 10.1002/chem.200601416).
- [48] Langhals H. (1995), Cyclic carboxylic imide structures as structure elements of high stability. novel developments in perylene dye chemistry, *Heterocycles*, 40, 477-500 (DOI: 10.3987/REV-94-SR2).
- [49] Reddy P. Y., Kondo, S., Toru T., Ueno Y. (1997), Lewis acid and hexamethyldisilazane-promoted efficient synthesis of N-alkyl- and N-arylimide derivatives, *J. Org. Chem.*, 62, 2652-2654 (DOI: 10.1021/jo962202c).
- [50] Oishi T., Gao H., Nakamura T., Isobe Y., Onimura K. (2007), Synthesis and properties of new organosoluble alkoxylated naphthalene-based novolacs prepared by addition-condensation of mono- or di-alkoxynaphthalene with formaldehyde, *Polym. J.*, 39, 1047-1059.

- [51] Bag S. S., Pradhan M. K., Kundu R., Jana S. (2013), Highly solvatochromic fluorescent naphthalimides: design, synthesis, photophysical properties and fluorescence switch-on sensing of ct-DNA, *Bioorg. Med. Chem. Lett.*, 23, 96–101 (DOI:10.1016/j.bmcl.2012.11.003).
- [52] Rasale D. B., Maity I., Das A. K. (2012), Emerging π -stacked dynamic nanostructured library, *RSC Adv.*, 2, 9791–9794 (DOI: 10.1039/C2RA21334F).
- [53] Umberger J. Q., LaMer V. K. (1945), The kinetics of diffusion controlled molecular and ionic reactions in solution as determined by measurements of the quenching of fluorescence, *J. Am. Chem. Soc.*, 67, 1099–1109 (DOI: 10.1021/ja01223a023).
- [54] Kim E., Koh M., Lim B. J., Park S. B. (2011), Emission wavelength prediction of a full-color-tunable fluorescent core skeleton, 9-aryl-1,2-dihydropyrrolo[3,4-b]indolizin-3-one, *J. Am. Chem. Soc.*, 133, 6642–6649 (DOI: 10.1021/ja110766a).
- [55] Schmidt R., Oh J. H., Sun Y.-S., Deppisch M., Krause A.-M., Radacki K., Braunschweig H., Konemann M., Erk P., Bao Z., Wurthner F. (2009), High-performance air-stable n-channel organic thin film transistors based on halogenated perylene bisimide semiconductors, *J. Am. Chem. Soc.*, 131, 6215–6228 (DOI: 10.1021/ja901077a).
- [56] Z. Zhang, H. Huang, X. Yang and L. Zang, (2011), Tailoring electronic properties of graphene by π - π stacking with aromatic molecules, *J. Phys. Chem. Lett.*, 2, 2897–2905 (DOI: 10.1021/jz201273r).
- [57] Syamakumari A., Schenning A. P. H. J., Meijer E. W. (2002), Synthesis, optical properties, and aggregation behavior of a triad system based on perylene and oligo(*p*-phenylene vinylene) units, *Chem.-Eur. J.*, 8, 3353–3361 (DOI: 10.1002/1521-3765(20020802)8:15).
- [58] Yu H., Lu Y., Chen X., Liu K., Fang Y. (2014), Functionality-oriented molecular gels: synthesis and properties of nitrobenzoxadiazole (NBD)-containing low-molecular mass gelators, *Soft Matter*, 10, 9159–9166 (DOI: 10.1039/C4SM01869A).

- [59] Allix F., Curcio P., Pham Q. N., Pickaert G., Jamart- Gregoire B. (2010), Evidence of intercolumnar π - π stacking interactions in amino-acid-based low-molecular-weight organogels, *Langmuir*, 26, 16818–16827 (DOI: 10.1021/la102864y).
- [60] Debnath S., Shome A., Dutta S., Das P. K. (2008), Dipeptide-based low-molecular-weight efficient organogelators and their application in water purification, *Chem.–Eur. J.*, 14, 6870–6881 (DOI: 10.1002/chem.200800731).
- [61] Jain A., Rao K. V., Kulkarni C., George A., George S. J. (2012), Fluorescent coronene monoimide gels via H-bonding induced frustrated dipolar assembly, *Chem. Commun.*, 48, 1467–1469 (DOI: 10.1039/C1CC14990C).
- [62] Brunsveld L., Zhang H., Glasbeek M., Vekemans J. A. J. M., Meijer E. W. (2000), Hierarchical growth of chiral self-Assembled structures in protic media, *J. Am. Chem. Soc.*, 122, 6175–6182, (DOI: 10.1021/ja0005237).

Chapter 4

**Self-assembling Peptide-Quinquethiophene based
Electrochromic Hydrogel**

4.1 Introduction

A variety of biomolecules such as peptide,^[1-2] carbohydrate,^[3-4] nucleobases^[5-6] and nucleotide^[7] have been functionalized with the semiconducting organic π -conjugated system for the synthesis of self-assembled nanostructure and their application in supramolecular electronics.^[8-12] Among these biomolecules, peptides are one of the most attractive bio-segments to assist the self-assembly of π -conjugated oligomers because of its structure variability and the tendency to participate in noncovalent interactions such as π - π stacking and H-bonding. For instance, oligothiophene,^[13-17] oligo(*p*-phenylene vinylene) (OPV),^[18] diacetylenes (DA),^[19] benzo[*ghi*]perylene monoimide (BPI),^[20] naphthalene diimide (NDI)^[21] and perylene diimide (PDI)^[22-23] have been conjugated with various kind of peptide motifs. Ubiquitously, the main objective is to assemble π -conjugated units into a highly ordered superstructure for effective charge-carrier mobility. Among a large number of extended π -conjugated systems, oligothiophenes are one of the most studied oligomer owing to their relatively high conductivity, chemical stability, solubility, and processability. To date, a number of self-assembled peptide-oligothiophene conjugate systems have been reported. For instance, Bauerle *et al.* are the first to described a peptide-oligothiophene conjugate composed of a head-to-tail coupled tetra(3-hexylthiophene) and a silk-inspired GlyAlaGlyAlaGly (GAGAG) pentapeptide sequence.^[24] The oligothiophene conjugate pentapeptide participates in hydrogen bonding interactions and self-organization which lead to novel two-dimensional (2D) and three-dimensional (3D) nanostructures. Tovar *et al.* have shown peptide bearing internal π -conjugated segment (bithiophene) that self-assembled into one-dimensional (1D) nanostructures in completely aqueous and physiologically relevant environments.^[25] Stupp *et al.* have reported self-assembly of quinquethiophenes functionalized with the β -sheet forming amino acid residues lysine and leucine into 1D nanostructure in aqueous solution.^[26]

In the above reports, synthesis and the self-assembling process of oligothiophene conjugated peptides have been mainly investigated, but the existence of electrochromism in such self-assembled system has not yet been explored. Electrochromism (the reversible change in optical properties when a

material is electrochemically oxidized or reduced) enables the electrochromic device (ECD)^[27-31] to be used for applications such as smart sunglasses,^[32-34] smart-window,^[35-36] stretchable electronic skin,^[37] and electrochromic display^[38] devices. Among the variety of molecular and polymeric organic electrochromes reported up to date, oligothiophene as well as polythiophene derivatives are an important class of π -conjugated organic materials for applications in electrochromic devices. Thiophene-based oligomers and polymers possess intrinsic contrasting colors between the neutral and oxidized forms concomitant with forming stable intermediates.^[39-40] Moreover, these exhibit several additional advantages including well defined molecular structure, solution processability and higher molecular ordering and crystallites for superior charge transfer. The molecular structure is a key factor for molecular packing induced by several noncovalent interactions which influence the morphology of materials. Morphology strongly influences the material properties and performance of devices. Hence, the molecular structure of electrochromes and packing capability are a crucial factor for the fabrication of good functional material. In this chapter, our objective is to develop self-assembled peptide conjugated oligothiophenes for electrochromic device application.

Herein, we have reported design, synthesis, and self-assembly study of peptide-quinquethiophene based hydrogel, which exhibits electrochromic property. Functionalization of peptide segment into oligothiophene unit provide two interesting effects, (i) π -conjugated peptide capable of forming hydrogelation, (ii) oligothiophene unit that does not suffer from solution processability, unlike polymeric electrochromes. Several spectroscopic techniques are utilized to describe the self-assembly of peptide-quinquethiophene bolaamphiphiles. TEM is used to identify the nanostructures present within the gel.

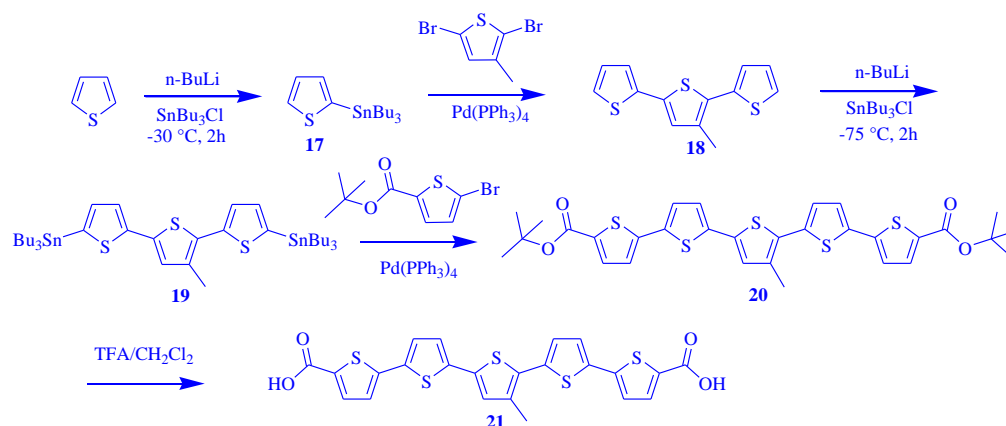
4.2 Experimental

4.2.1 Materials

All raw materials such as amino acids, thiophene, *n*-butyl lithium (1.6 M in hexane), Tributyltin chloride, 2,5-dibromo-3-methylthiophene, 5-bromo-2-thiophenecarboxylic acid, Tetrakis(triphenylphosphine) palladium(0), 1-

Ethyl-3-(3-dimethylaminopropyl)carbodiimide (EDC), Citric acid, 4-(N,N-dimethylamino)pyridine, tert-butyl alcohol, Trifluoroacetic acid, 1-hydroxybenzotriazole (HOBt), Acetonitrile, Tetrabutylammonium perchlorate (Bu_4NClO_4) have been purchased from commercial sources (Sigma-Aldrich, Alfa-aesar, Marck, SD Fine, SRL). Tetrahydrofuran (THF) was dried over Na/benzophenone ketyl and freshly distilled prior to use. ITO coated quartz glass substrate ($10\text{ mm} \times 10\text{ mm}$) having a thickness of about 150 nm was purchased from J. K. Impex, Mumbai.

4.2.2 Synthesis of Quinquethiophene Dicarboxylic Acid (5TmDCA): Quinquethiophene dicarboxylic Acid (5TmDCA) was synthesized according to the following procedure.



Scheme 4.1. Reaction steps for the synthesis of quinquethiophene dicarboxylic acid (5TmDCA).

2-(tributylstannyl)thiophene (17):

n-Butyl lithium in hexane (1.6 M, 41.22 mL, 33 mmol) was added to thiophene (5.54 g, 66 mmol) in anhydrous tetrahydrofuran (70 mL) at $-78\text{ }^{\circ}\text{C}$ and the mixture was stirred at this temperature under nitrogen for 2 hrs. Tributyltin chloride (17.92 mL, 33 mmol) was added and the mixture was stirred at $-30\text{ }^{\circ}\text{C}$ for another 30 minutes. Saturated aqueous sodium hydrogen carbonate (100 ml) was added, and the organic phase was separated and washed with saturated aqueous sodium hydrogen carbonate (50 mL) and brine (30 mL). The solvent was evaporated from the dried (Na_2SO_4) extract, and the residue was chromatographed on a column of neutral alumina (light petroleum) to

give the title compound (**17**) (15.19 g, 62.87 %) as a colorless oil. ^1H NMR (400 MHz, CDCl_3 , δ_{ppm}): δ = 7.72 (d, 1H, J = 4.76 Hz), 7.33 (dd, 1H, J = 3.28, 3 Hz), 7.27 (d, 1H, J = 3 Hz), 1.64 (m, 6H), 1.42 (m, 6H), 1.18 (m, 6H), 0.96 (t, 9H).

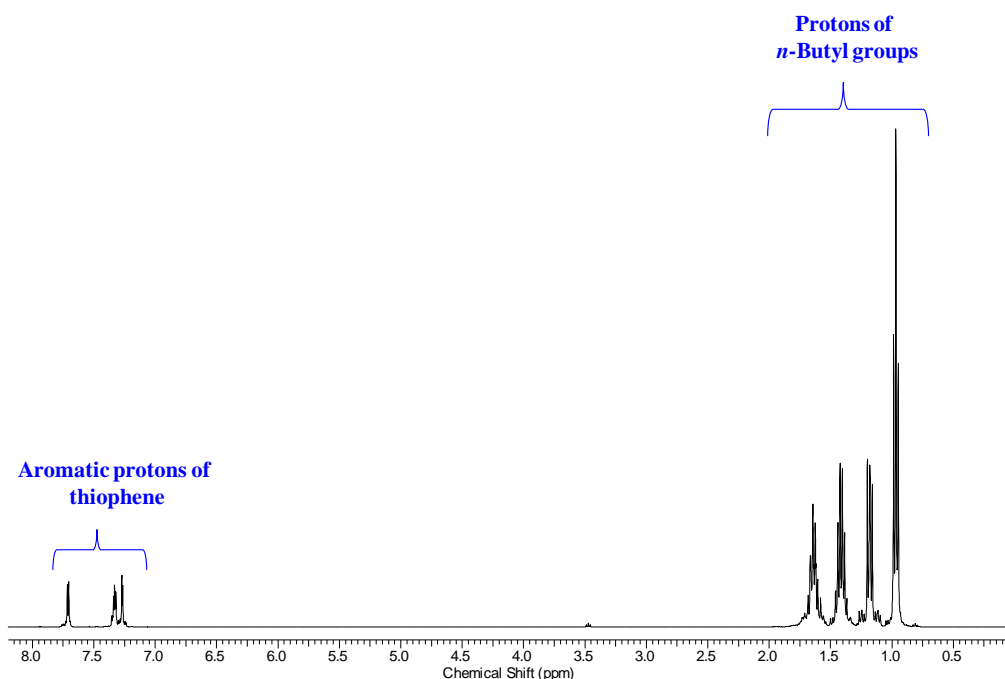


Figure 4.1. ^1H NMR spectrum (400 MHz, CDCl_3) of Tributyl(2-thienyl)stannane (**17**).

3-methyl-2,5-di(thiophen-2-yl)thiophene (**18**):

In a dry and degassed flask, a solution of 2,5-dibromo-3-methylthiophene (3.07g, 12 mmol) in DMF (40 mL) was added 2-(tributylstannyl)thiophene (8.95 g, 24 mmol). The solution was sparged with N_2 gas for 20 minutes. Following the N_2 sparge, tetrakis(triphenylphosphine) palladium(0) (138 mg) was added to the solution. After stirring it to 100 $^\circ\text{C}$ for 16 hrs, the reaction was cooled to room temperature. The reaction mixture was diluted with chloroform and extracted three times with 5% citric acid (aq). The organic layer was dried over Na_2SO_4 and the solvent was removed in vacuo. The crude product was purified by column chromatography (silica gel; chloroform/hexanes, 10:90) to yield (2.86 g, 90.73 %) of the compound **18** as a yellow oil. ^1H NMR (400 MHz, CDCl_3 , δ_{ppm}): δ = 7.34 (d, 1H, J = 4Hz), 7.24 (d, 1H, J = 5.24 Hz), 7.18 (m, 2H), 7.10 (t, 1H), 7.04 (t, 1H), 7.01 (s, 1H), 2.41 (s, 3H).

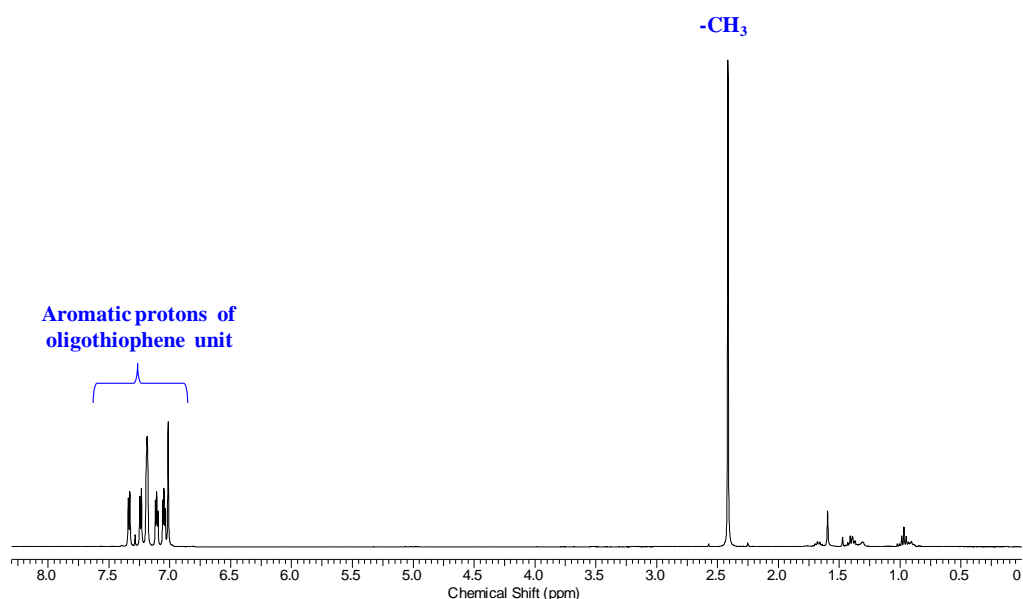


Figure 4.2. ^1H NMR spectrum (400 MHz, CDCl_3) of 3-methyl-2,5-di(thiophen-2-yl)thiophene (**18**).

2,5-bis(5-(tributylstannyl)thiophen-2-yl)-3-methylthiophene (19**):**

A solution of **18** (2.64 g, 10 mmol) in anhydrous THF (60 mL) was cooled to $-78\text{ }^\circ\text{C}$. *n*-Butyl lithium in a 1.6 M solution of hexane (13.12 mL) was added and the reaction was stirred for 1 hr while warming to room temperature. Tributyltin chloride (6.83 g, 21 mmol) was added and the reaction stirred for 16 hrs at room temperature. The reaction was diluted with hexanes and extracted 3 times with sat. NaHCO_3 (aq), then dried over Na_2SO_4 , concentrated and was used directly for the next step.

tert-butyl 5-bromothiophene-2-carboxylate.

To the solution of 4-(*N,N*-dimethylamino)pyridine (4.28 g, 35 mmol), 1-Ethyl-3-(3-dimethylaminopropyl)carbodiimide (EDC) (5.43g, 35 mmol), tert-Butyl alcohol (50 mL, 525 mmol) in dichloromethane (100 mL), 5-bromo-2-thiophenecarboxylic acid (4.96 g, 24 mmol) was added. After stirring for 16 hr at room temperature, the solvent was removed. The mixture was then dissolved in dichloromethane and extracted 3 times with 2 M HCl (aq) followed by 3 times with sat. NaHCO_3 . The organic layer was dried with Na_2SO_4 and concentrated to yield 5.11 g (28.11 %) of the desired product as a

clear oil. ^1H NMR (400 MHz, CDCl_3 , δ_{ppm}): $\delta = 7.48$ (d, 1H, $J = 3.76$ Hz), 7.05(d, 1H, $J = 3.76$ Hz), 1.57 (s, 9H).

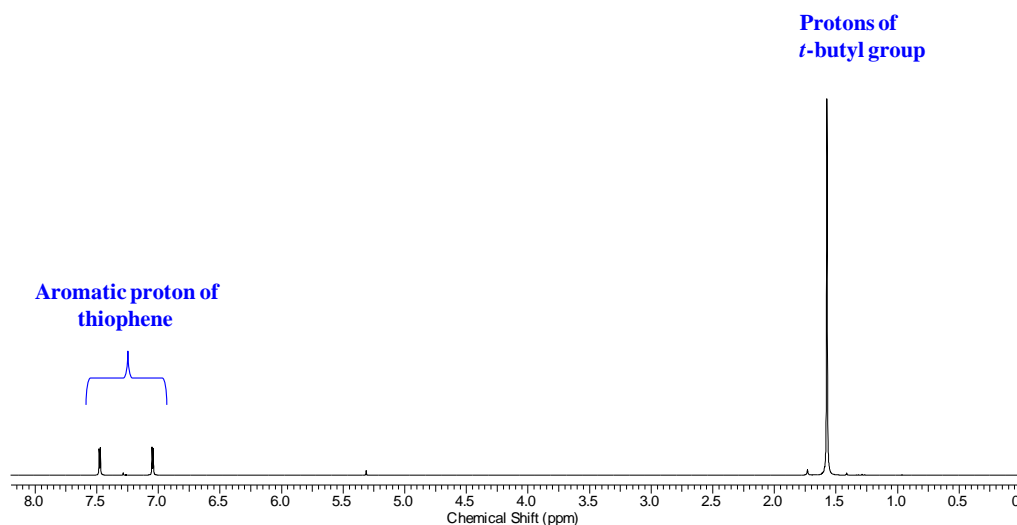


Figure 4.3. ^1H NMR spectrum (400 MHz, CDCl_3) of tert-butyl 5-bromothiophene-2-carboxylate.

diterbutyl ester 3-methyl-Quinquethiophene (20):

In an N_2 atmosphere, tert-butyl 5-bromothiophene-2-carboxylate (1.11 g, 4.2 mmol), a solution of **19** (1.32 g, 2.1 mmol) in DMF (50 mL) was added. The solution was sparged with nitrogen gas for 20 min and tetrakis(triphenylphosphine) palladium(0) (242 mg) was added. The reaction stirred at 100 $^\circ\text{C}$ for 16 hrs. The reaction mixture was cooled to room temperature, diluted with chloroform, and extracted 3x with 5% citric acid (aq) to remove the DMF. After drying the organic layer over Na_2SO_4 , the product was purified by column chromatography (silica gel; chloroform/hexanes, 65:35) to yield 0.85 g (86.73 %) to obtain desired product as a red-orange powder. ^1H NMR (400 MHz, CDCl_3 , δ_{ppm}): $\delta = 7.55$ (d, 2H), 7.16 (d, 1H, $J = 3.76$ Hz), 7.11 (d, 1H, $J = 3.76$ Hz), 7.06 (d, 1H, $J = 4$ Hz), 7.04 (d, 1H, $J = 4$ Hz), 7.02 (d, 2H, $J = 3.76$ Hz), 6.93 (s, 1H), 2.35 (s, 3H), 1.52 (s, 18 H).

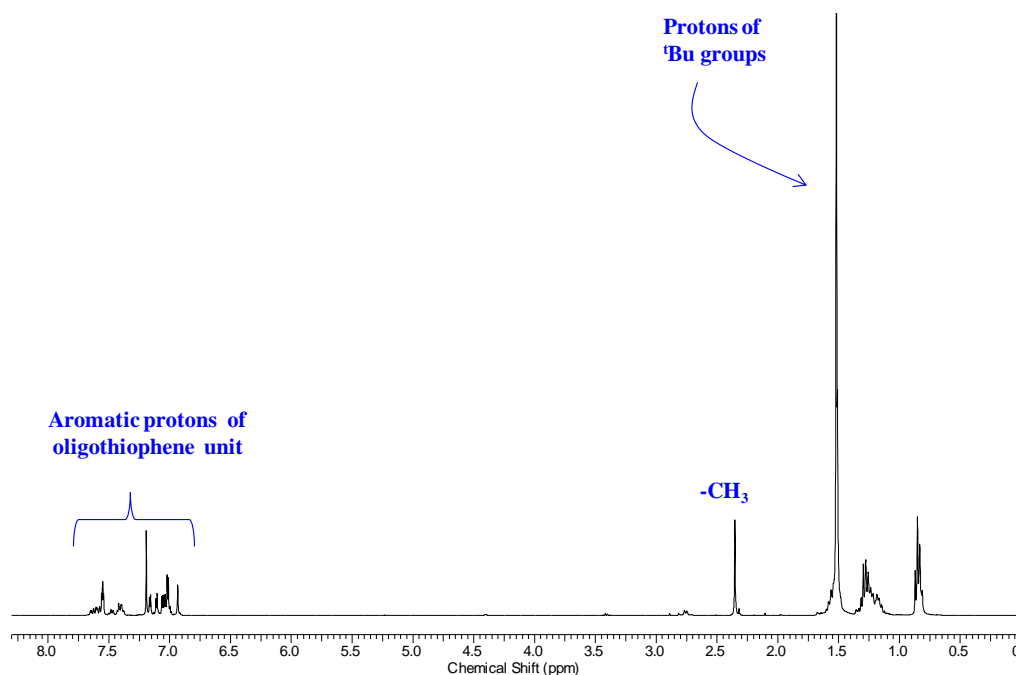


Figure 4.4. ^1H NMR spectrum (400 MHz, CDCl_3) of ditertbutyl ester 3-methylquinquethiophene (**20**).

Dicarboxylic acid 3-methyl-Quinquethiophene (5TmDCA) (**21**):

In a 160 mL solution of Dichloromethane and TFA (5:1) **20** (0.63 g, 1mmol) was stirred at room temperature for 2 h. The solvent was removed and the product was triturated 3 times with methanol and dried to yield 0.50g (96. 61 %) desired product as a red solid. ^1H NMR (400 MHz, $\text{DMSO}-d_6$, δ_{ppm}): δ = 13.31 (s, 1H), 7.67 (d, 2H, J = 3.04 Hz), 7.53 (d, 1H, J = 3.76Hz), 7.49 (d, 1H, J = 3.76Hz), 7.42 (d, 1H, J = 3.76Hz), 7.40 (d, 1H, J = 3.76Hz), 7.37 (d, 1H, J = 3.76Hz), 7.33 (s, 1H), 7.30 (d, 1H, J = 3.76Hz), 2.40 (s, 3H). ESI-MS (m/z): $[M-H]^+$ calcd for $\text{C}_{23}\text{H}_{14}\text{O}_4\text{S}_5$, 512.9418; found, 512..9412.

4.2.3 Synthesis of Peptide-Quinquethiophene Bolaamphiphiles:

The general procedure was used for the synthesis of peptide-Quinquethiophene which is described below: The amino acids were coupled with chromophore Quinquethiophene by the general peptide coupling process and the methyl esters of the coupling product were deprotected by alkali hydrolysis prior to another amino acid coupling symmetrically in both the sides.

The coupling between 5T diacids and amino acid was performed according to the following procedure: A solution of diacid (0.51 g, 1.0 mmol)

and HOBt (0.31 g, 2.3 mmol) was stirred in DMF (2 mL). A neutralized solution of H₂N-Leu-OMe was extracted from its corresponding hydrochloride salt and concentrated to add to the reaction mixture followed by EDC (0.36 g, 2.3 mmol) and DMAP (0.28 g, 2.3 mmol) at 0 °C. The mixture was allowed to stir at room temperature for 12 hrs. The reaction mixture was diluted with ethyl acetate and the organic layer was washed with 1M HCl (2 × 30 mL), brine, 1 M Na₂CO₃ (3 × 30 mL), and again with brine. The organic layer was dried over Na₂SO₄ and evaporated under vacuum to yield a white solid. Purification of **22a** was performed by column chromatography on silica gel (100–200 mesh) with ethyl acetate/ toluene (1:1) as the eluent.

The methyl ester deprotection reaction was performed according to the following procedure: A solution of **22a** (0.6 g, 0.8 mmol) in dry MeOH (10 mL) was allowed to react with a 2 M solution of NaOH. The progress of the reaction was monitored by TLC. The reaction mixture was stirred up to 6 hrs. Then, methanol was removed under vacuum. The residue was dissolved in water (100 mL) and washed with diethyl ether (2 × 20 mL). Then, the pH of the aqueous layer was adjusted to 2 by using 2 M HCl and extracted with ethyl acetate (3 × 30 mL). The ethyl acetate layer was dried over anhydrous sodium sulfate and evaporated under vacuum to yield **23a** as orange solid.

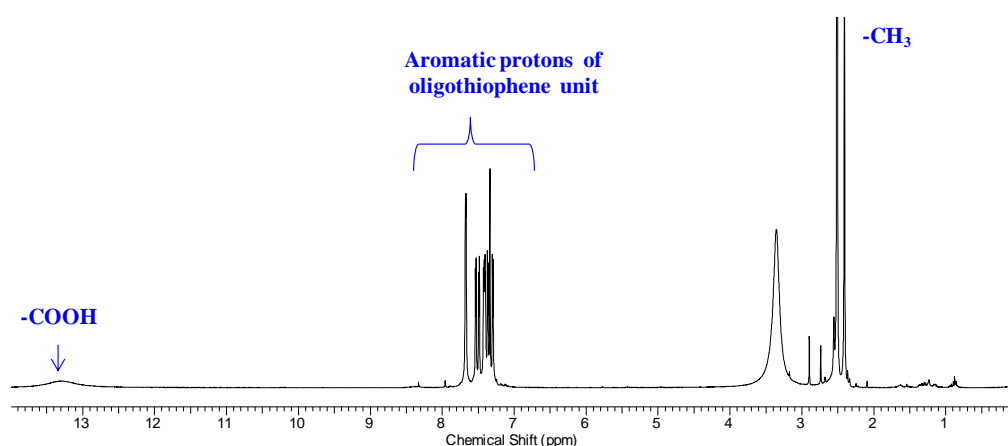


Figure 4.5. ¹H NMR spectrum (400 MHz, DMSO-*d*₆) of dicarboxylic acid 3-methyl-Quinquethiophene (5TmDCA) (**21**).

MeO-Leu-5T-Leu-OMe (22a): yield (0.67 g, 88.81%); ¹H NMR (400 MHz, CDCl₃, δ_{ppm}): 7.30 (d, 2H, -NH-), 7.19 (s, 2H, ring protons of 5T), 7.02 (d, 1H,

ring proton of 5T), 6.09 (m, 5H, ring protons of 5T), 6.80 (s, 1H, ring proton of 5T), 4.76 (m, 2H, C^αHs of Leu), 3.73 (s, 6H, -OCH₃), 2.29 (s, 3H, -CH₃), 1.66 (m, 4H, C^βHs of Leu), 1.18 (s, 2H, C^γHs of Leu), 1.08 (d, 6H, C^δHs of Leu), 0.91 (d, 6H, C^δHs of Leu). MS (ESI) m/z : (M+Na)⁺ Calcd. for C₃₇H₄₀N₂O₆S₅Na: 791.1388; found: 791.1483.

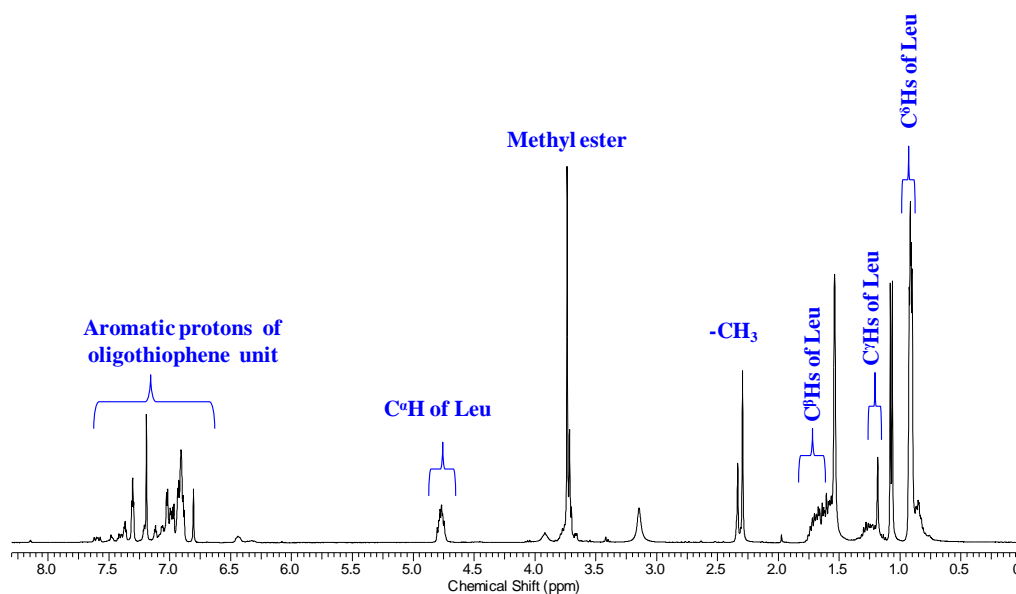


Figure 4.6. ¹H NMR spectrum (400 MHz, CDCl₃) of MeO-Leu-5T-Leu-OMe (**22a**).

MeO-Tyr-5T-Tyr-OMe (22b): ¹H NMR (400 MHz, DMSO-*d*₆, δ_{ppm}): 9.29 (s, 2H, -NH-), 8.92 (t, 2H, ring protons of 5T), 7.82 (d, 2H, ring protons of 5T), 7.46-7.26 (m, 5H, ring protons of 5T), 7.07 (d, 4H, ring protons of Tyr), 6.65 (d, 4H, ring protons of Tyr), 4.55 (m, 2H, C^αHs of Tyr), 3.64 (s, 6H, -OCH₃), 3.06-2.92 (m, 4H, C^βHs of Tyr), 2.50 (s, 3H, -CH₃).

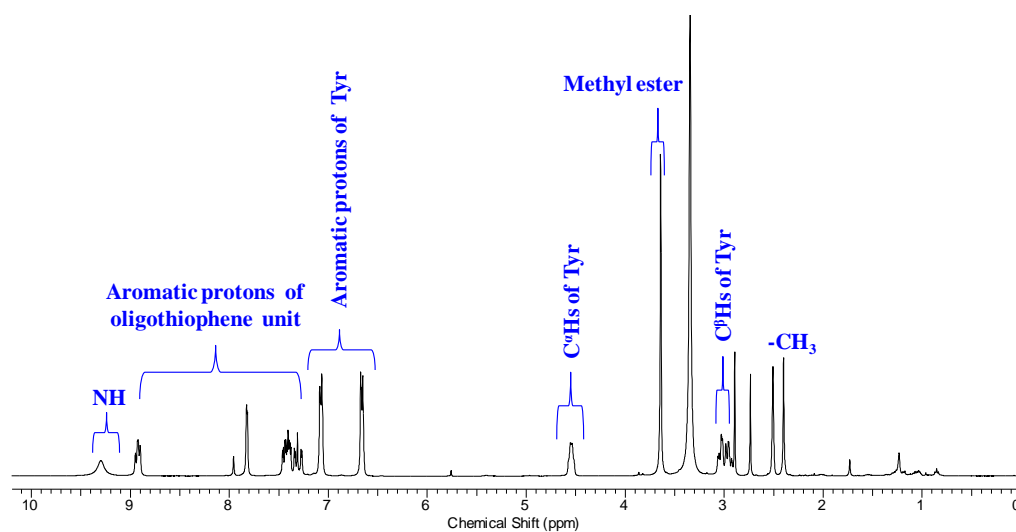
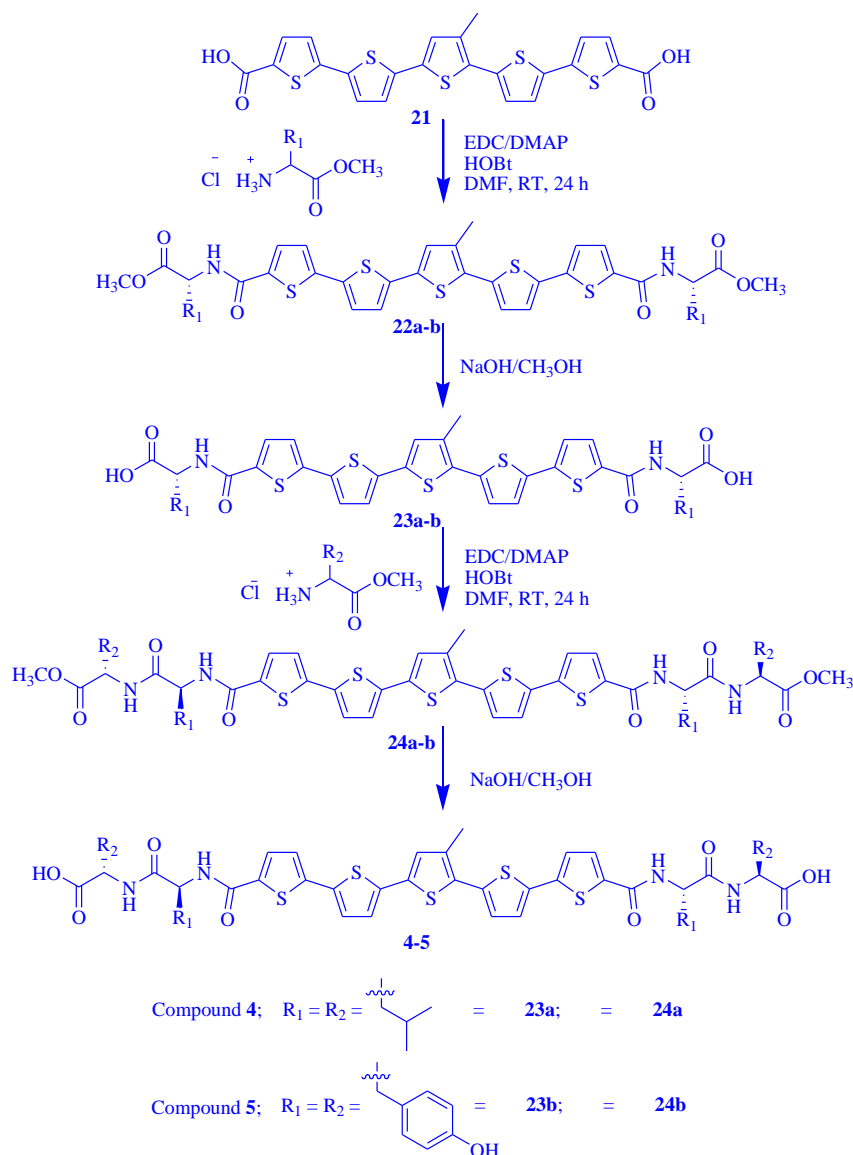


Figure 4.7. ^1H NMR spectrum (400 MHz, $\text{DMSO-}d_6$) of MeO-Tyr-5T-Tyr-OMe (**22b**).



Scheme 4.2. Reaction steps for the synthesis of peptide-quinquethiophene bolaamphiphiles.

HO-Leu-5T-Leu-OH (23a): yield (0.50 g, 87.71%); ^1H NMR (400 MHz, $\text{DMSO-}d_6$, δ_{ppm}): δ = 12.69 (s, 2H, $-\text{COOH}$), 8.72 (d, 2H, $-\text{NH-}$), 7.87 (d, 2H, ring protons of 5T), 7.48 (d, 1H, ring proton of 5T), 7.44-7.40 (m, 3H, ring protons of 5T), 7.36 (d, 1H, ring proton of 5T), 7.32 (s, 1H, ring proton of 5T), 7.29 (s, 1H, ring proton of 5T), 4.40 (m, 2H, C^αHs of Leu), 2.51 (s, 2H, C^γHs of Leu), 2.41 (s, 3H, $-\text{CH}_3$), 1.71 (m, 2H, C^βHs of Leu), 1.63 (m, 2H, C^βHs of Leu), 0.94 (d, 6H, J = 5.8 Hz, C^δHs of Leu), 0.89 (d, 6H, J = 5.76 Hz, C^δHs of Leu)

Leu). MS (ESI) m/z : $(M-H)^+$ Calcd. for $C_{35}H_{36}N_2O_6S_5$: 739.1099; found: 739.1093.

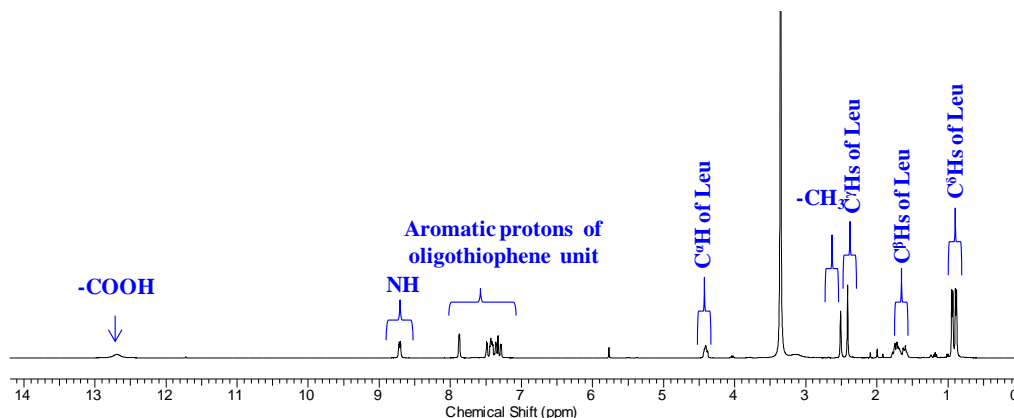


Figure 4.8. ^1H NMR spectrum (400 MHz, $\text{DMSO-}d_6$) of HO-Leu-5T-Leu-OH (**23a**).

HO-Tyr-5T-Tyr-OH (23b): ^1H NMR (400 MHz, $\text{DMSO-}d_6$, δ_{ppm}): 12.76 (s, 2H, $-\text{COOH}$), 9.19 (s, 1H, $-\text{NH-}$), 8.76 (1H, $-\text{NH-}$), 7.81 (d, 2H, ring protons of 5T), 7.45 (d, 1H, $J = 3.76$ Hz, ring proton of 5T), 7.42- 7.36 (m, 3H, ring protons of 5T), 7.34 (d, 1H, $J = 3.76$, ring proton of 5T), 7.30 (s, 1H, ring proton of 5T), 7.27 (d, 1H, $J = 4$ Hz, ring proton of 5T), 7.10 (d, 4H, $J = 8.28$ Hz, ring protons of Tyr), 6.67 (d, 4H, $J = 8.04$ Hz, ring protons of Tyr), 4.50 (m, 2H, C^αHs of Tyr), 3.07 (m, 2H, C^βHs of Tyr), 2.91 (m, 2H, C^βHs of Tyr), 2.40 (s, 3H, $-\text{CH}_3$).

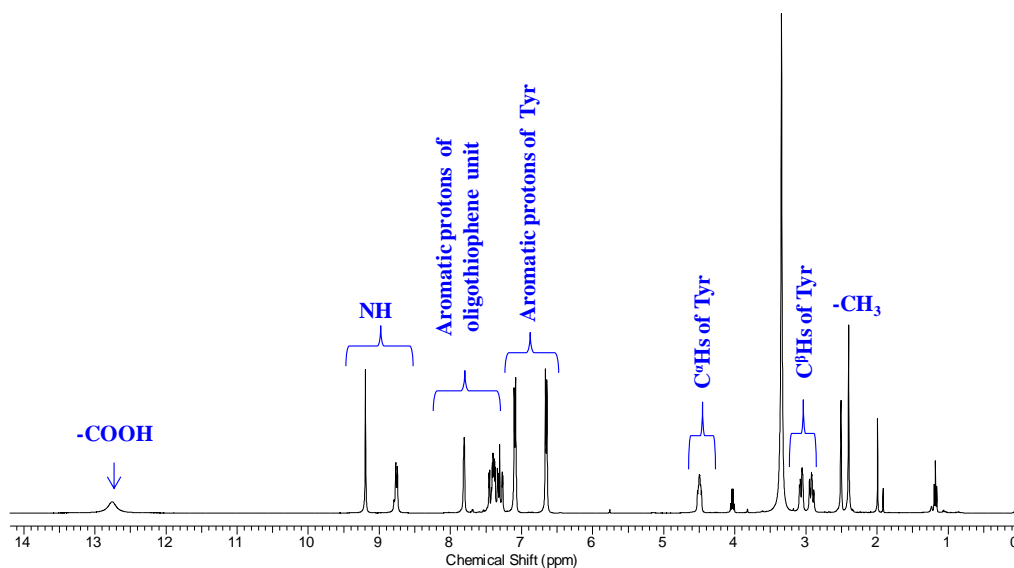


Figure 4.9. ^1H NMR spectrum (400 MHz, $\text{DMSO-}d_6$) of HO-Tyr-5T-Tyr-OH (**23b**).

MeO-Leu-Leu-5T-Leu-Leu-OMe (24a): yield (0.37 g, 80.48%); ^1H NMR (400 MHz, $\text{DMSO-}d_6$, δ_{ppm}): δ = 8.18 (d, 2H, -NH-), 7.44 (d, 2H, -NH-), 6.97 (d, 2H, ring protons of 5T), 6.87 (m, 6H, ring protons of 5T), 6.72 (s, 1H, ring protons of 5T), 4.62 (m, 4H, C^αHs of Leu), 3.68 (s, 6H, $-\text{OCH}_3$), 2.20 (s, 3H, $-\text{CH}_3$), 1.73 (m, 8H, C^βHs of Leu), 1.18 (s, 4H, C^γHs of Leu), 0.86 (d, 24H, C^δHs of Leu); MS (ESI) m/z : $(M+\text{Na})^+$ Calcd. for $\text{C}_{49}\text{H}_{62}\text{N}_4\text{O}_8\text{S}_5\text{Na}$: 1017.3069; found: 1017.3123.

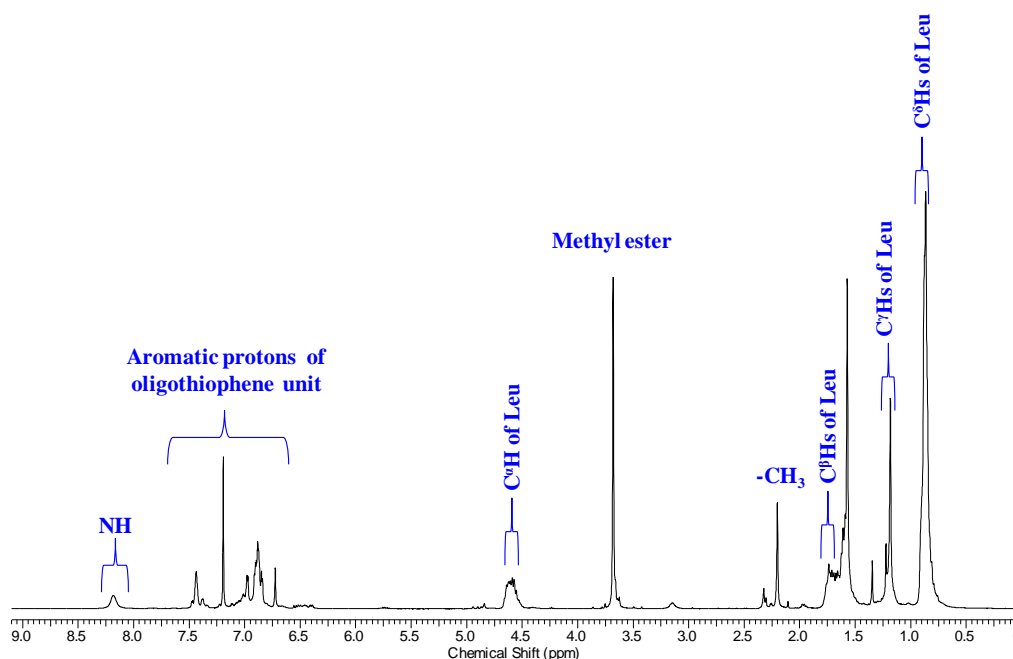


Figure 4.10. ^1H NMR spectrum (400 MHz, $\text{DMSO-}d_6$) of MeO-Leu-Leu-5T-Leu-Leu-OMe (**24a**).

MeO-Tyr-Tyr-5T-Tyr-Tyr-OMe (24b): ^1H NMR (400 MHz, $\text{DMSO-}d_6$, δ_{ppm}): δ = 9.21 (s, 2H, -NH-), 9.14 (s, 2H, -NH-), 8.63 (d, 2H, ring protons of 5T), 8.46 (d, 2H, ring protons of 5T), 7.79 (d, 2H, ring protons of 5T), 7.43-7.24 (m, 3H, ring protons of 5T), 7.09 (d, 4H, ring protons of Tyr), 7.00 (d, 4H, ring protons of Tyr), 6.62 (d, 8H, ring protons of Tyr), 4.60 (m, 2H, C^αHs of Tyr), 4.39 (m, 2H, C^αHs of Tyr), 3.56 (s, 6H, $-\text{OCH}_3$), 2.94-2.75 (m, C^βHs of Tyr 8H), 2.49 (s, 3H, $-\text{CH}_3$).

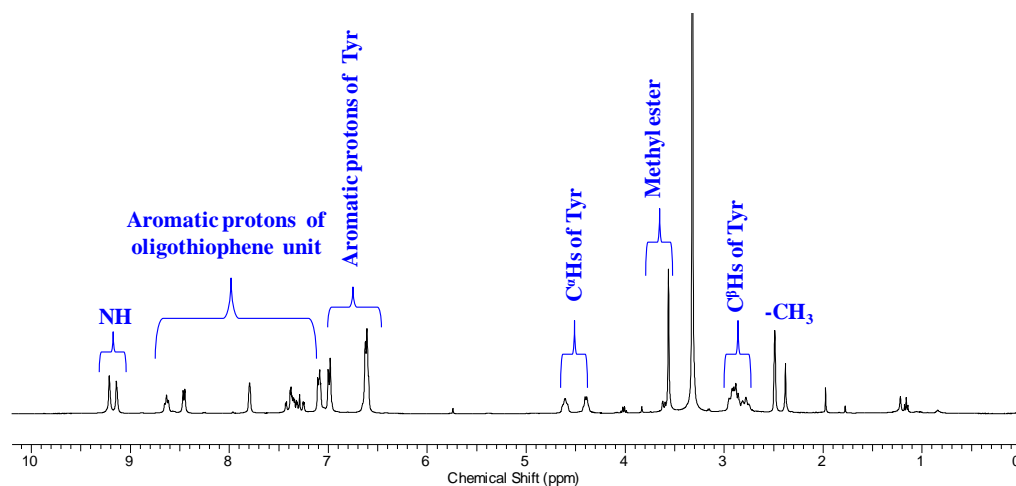


Figure 4.11. ^1H NMR spectrum (400 MHz, $\text{DMSO}-d_6$) of MeO-Tyr-Tyr-5T-Tyr-Tyr-OMe (**24b**).

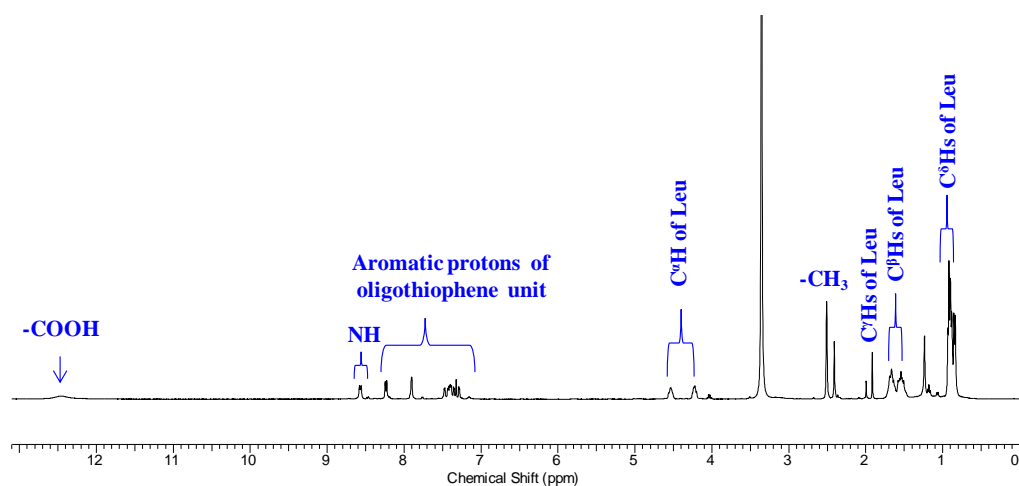


Figure 4.12. ^1H NMR spectrum (400 MHz, $\text{DMSO}-d_6$) of HO-Leu-Leu-5T-Leu-Leu-OH (**4**).

HO-Leu-Leu-5T-Leu-Leu-OH (4): yield (0.25 g, 86.20 %); ^1H NMR (400 MHz, $\text{DMSO}-d_6$, δ_{ppm}): δ = 12.48 (s, 2H, $-\text{COOH}$), 8.55 (d, 2H, J = 7.76 Hz, -NH-), 8.21 (d, 2H, J = 7.8 Hz, -NH-), 7.89 (d, 2H, J = 3.28, ring protons of 5T), 7.63 (d, 1H, ring protons of 5T), 7.54 (d, 1H, J = 4.8 Hz, ring protons of 5T), 7.45 (d, 1H, J = 3.52, ring protons of 5T), 7.37 (d, 2H, J = 3.76 Hz, c ring protons of 5T), 7.31 (d, 1H, J = 3.76 Hz, ring protons of 5T), 7.16 (d, 1H, ring protons of 5T), 4.54 (m, 2H, C^αHs of Leu), 4.23 (m, 2H, C^αHs of Leu), 2.50 (s, 2H, C^γHs of Leu), 2.36 (s, 3H, $-\text{CH}_3$), 1.67 (m, 4H, C^βHs of Leu), 1.54 (m, 4H, C^βHs of Leu), 0.89 (d, 12 H, C^δHs of Leu), 0.83 (d, 12 H, C^δHs of Leu); ^{13}C NMR (100 MHz, $\text{DMSO}-d_6$, δ_{ppm}): δ = 179.14, 177.34, 165.80, 145.25, 143.60, 143.56, 140.97, 140.86, 140.73, 140.42, 140.14, 138.56, 134.89,

134.41, 134.33, 132.03, 131.68, 131.30, 130.67, 129.93, 56.62, 55.44, 29.53, 29.46, 28.33, 28.09, 26.64, 26.55, 20.67; MS (ESI) m/z : $(M-H)^+$ Calcd. for $C_{47}H_{58}N_4O_8S_5$: 965.2780; found: 965.2774.

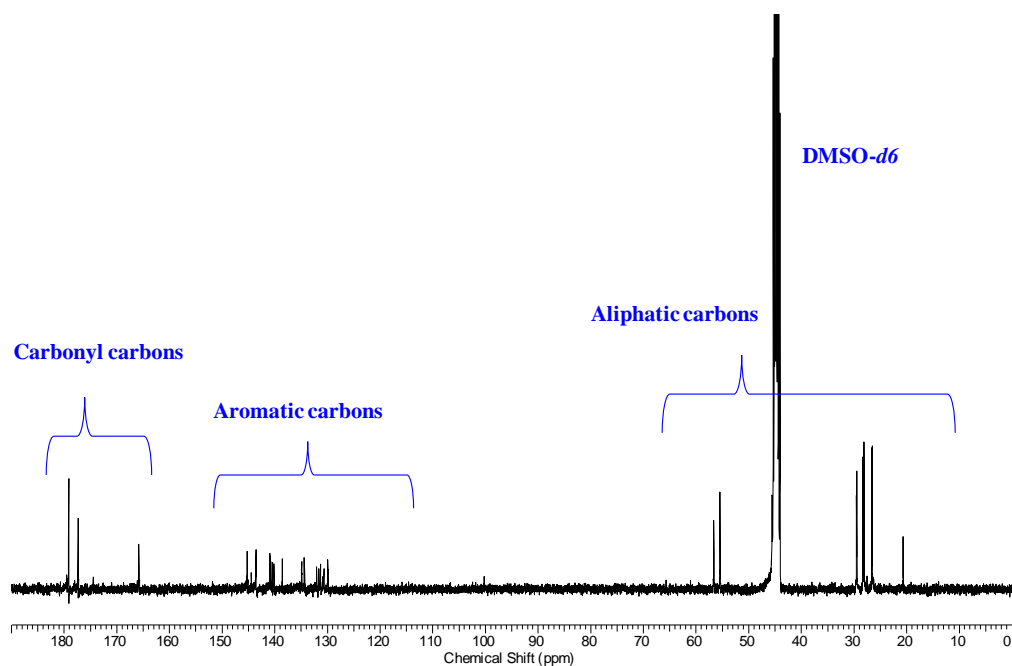


Figure 4.13. ^{13}C NMR spectrum (100 MHz, $DMSO-d_6$) of HO-Leu-Leu-5T-Leu-Leu-OH (4).

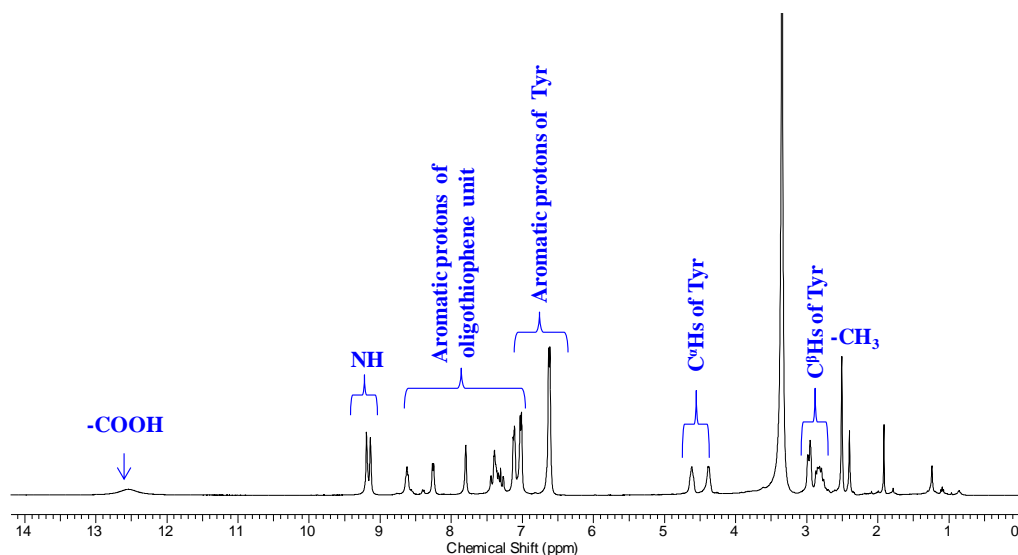


Figure 4.14. 1H NMR spectrum (400 MHz, $DMSO-d_6$) of HO-Tyr-Tyr-5T-Tyr-Tyr-OH (5).

HO-Tyr-Tyr-5T-Tyr-Tyr-OH (5): ^1H NMR (400 MHz, $\text{DMSO-}d_6$, δ_{ppm}), δ = 12.55(s, 2H, $-\text{COOH}$), 9.19 (s, 2H, $-\text{NH}-$), 9.14 (s, 2H, $-\text{NH}-$), 8.62 (d, 1H, J = 6.76 Hz, ring protons of 5T), 8.26 (d, 1H, J = 7.28 Hz, ring protons of 5T), 7.79 (s, 2H, ring protons of 5T), 7.43-7.26 (m, 5H, ring protons of 5T), 7.13 (d, 4H, J = 7.52 Hz, ring protons of Tyr), 7.03 (d, 4H, J = 7.52 Hz, ring protons of Tyr), 6.63 (d, 8H, J = 7.52 Hz, ring protons of Tyr), 4.61 (m, 2H, C^αHs of Tyr), 4.38 (m, 2H, C^αHs of Tyr), 2.95 (m, 4H, C^βHs of Tyr), 2.83 (m, 4H, C^βHs of Tyr), 2.50 (s, 3H, $-\text{CH}_3$); ^{13}C NMR (100 MHz, $\text{DMSO-}d_6$, δ_{ppm}): δ = 173.28, 170.59, 160.52, 155.72, 155.64, 139.98, 138.11, 138.08, 135.71, 135.48, 135.41, 135.21, 134.86, 133.28, 130.29, 130.00, 129.52, 129.17, 128.98, 128.39, 128.24, 126.66, 126.27, 125.96, 125.28, 124.54, 114.89, 114.73, 55.59, 55.03, 36.26, 36.16, 15.42.

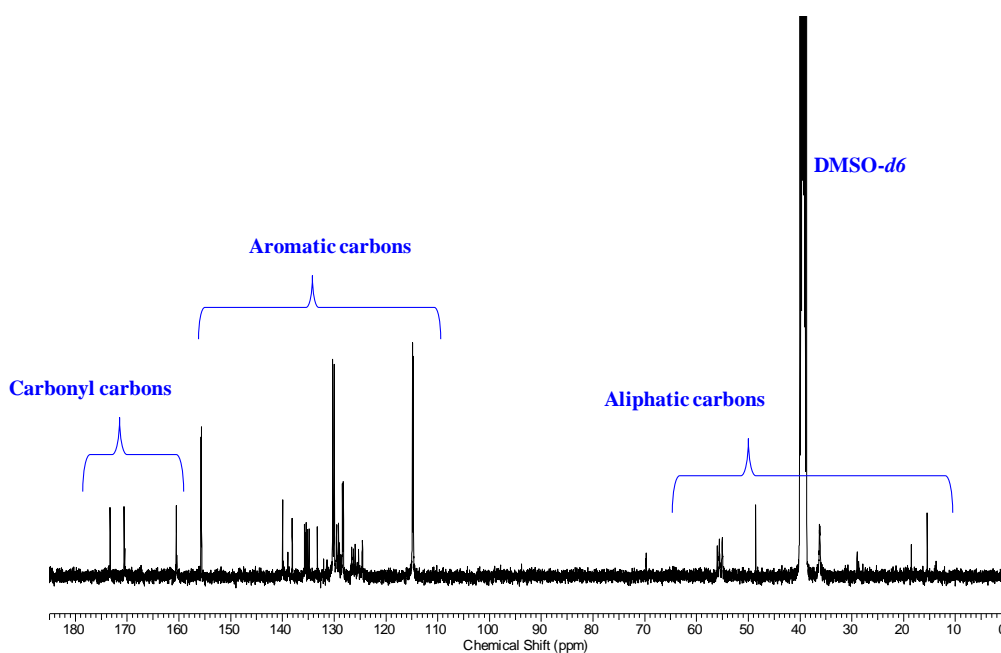


Figure 4.15. ^{13}C NMR spectrum (100 MHz, $\text{DMSO-}d_6$) of HO-Tyr-Tyr-5T-Tyr-Tyr-OH (5).

4.3 General characterization

All NMR characterizations were carried out on a Bruker AV 400 MHz spectrometer at 300 K. Compound concentrations were in the range 5-10 mmol L^{-1} in $(\text{CD}_3)_2\text{SO}$. Mass spectra were recorded on a Bruker micrOTOF-Q II by positive mode electrospray ionization.

FTIR Study: FTIR spectra of power sample and hydrogels were measured using Bruker (Tensor 27) FT-IR spectrophotometer. Samples were prepared in milli-Q water and scanned from 400 to 4000 cm^{-1} .

Circular Dichroism (CD) Spectrometer: Secondary structure of peptide-quinuethiophene conjugate **4** was analyzed with Jasco J-815 circular dichroism spectrometer. peptide-quinuethiophene conjugate **4** (20 mmol L^{-1}) was diluted to a final concentration of 200 μM in milli-Q water for experiment and measured from 600 nm to 195 nm with 0.1 data pitch, 20 nm min^{-1} scanning speed, 1 nm bandwidth and 4 s D.I.T.

UV-Vis Spectroscopy: UV-Vis absorption spectrums of the hydrogels were recorded using a Varian Cary100 Bio UV-Vis spectrophotometer. Samples were diluted to 50 μM as concentration and then the experiments were conducted.

Fluorescence Spectroscopy: Fluorescence emission spectra for hydrogel (20 mmol L^{-1}) were recorded on a Horiba Scientific Fluoromax-4 spectrophotometer with 1 cm path length quartz cell at room temperature. The slit width for the excitation and emission was set at 2 nm and a 1 nm data pitch. Excitation of gel sample was performed at absorption maxima of each molecule recorded from UV-Vis spectroscopy.

Microscopic Study: Transmission electron microscopic images were taken using a PHILIPS electron microscope (model: CM 200) operated at an accelerating voltage of 200kV. Hydrogel (20 mmol L^{-1}) solution was diluted to 1 mmol L^{-1} in milli-Q water and dried on carbon-coated copper grids (300 mesh) by slow evaporation in air, then allowed to dry separately in a vacuum at room temperature.

Rheology: Oscillating rheology was used to quantify the mechanical properties of the hydrogel **1**. Hydrogel **1** (20 mmol L^{-1}) was prepared in milli-Q water. The experiment was done on a Paar Physica Modular Compact Rheometer (MCR 301, Austria). A 25 mm cone plate with 1° angle configuration was used and the temperature was set to be constant at 25 $^\circ\text{C}$. Storage (G') and loss (G'') moduli were measured at 0.1% strain with a true gap of 0.05 mm.

Electrochemical measurements: Cyclic voltammetry (CV) was performed using an AUTOLAB /PG STAT302N and a three-electrode cell equipped with

platinum working, platinum counter and an Ag/AgCl reference electrode. The supporting electrolyte was $\text{Bu}_4\text{NClO}_4/\text{CH}_2\text{Cl}_2$ (0.1 M). For the electrochromic test, a thin film of peptide-quinquethiophene hydrogel was prepared onto an ITO coated glass and used as working electrode. Pt and Ag/AgCl were used as counter electrode and reference electrode respectively.



Figure 4.16. (a) Molecular structures of the peptide-quinquethiophene conjugates **4** (LL5TLL) and, **5** (YY5TYY); (b) Digital images of the solution of compounds **4** and **5** at basic pH and (c) hydrogel **1** and **2**.

4.4 Results and Discussion

The general synthetic design of two peptide-quinquethiophene conjugates **4** and **5** consists of a symmetric bolaamphiphile that has two segments: a redox active π -conjugated quinquethiophene core for electrochromism and peptide motifs for self-assembly. The molecular structure of peptide-quinquethiophene conjugates namely LL5TLL (compound **4**) and YY5TYY (compound **5**) is given in Figure 4.16. Compound **4** and **5** were synthesized by solution phase methodology and synthetic steps involved have been shown in Scheme 1 and, Scheme 2. To functionalize dipeptide symmetrically in both side of 5TmDCA, selected amino acids are coupled with 5TmDCA by standard peptide coupling process. Compounds **4** and **5** are

mainly different in the amino acid residue present symmetrically at the two terminal positions of quinquethiophene core. Polar functional end groups (carboxylic acid) are adopted as controlling units for self-assembly of π -conjugated cores in the aqueous phase. Solubility and gel formation ability are checked in the aqueous medium. The self-assembly and electrochromism of peptide-5T derivative are studied in aqueous phase through hydrogel formation. The peptide-quinquethiophene conjugates **4** and **5** form pH-responsive self-supporting red hydrogel **1** and **2** respectively. Hydrogel **1** is highly stable than hydrogel **2** owing to the distinction in their amino acid residue attached with the 5T. The minimum gelation concentration of compound **4** and **5** is 10 and 20 mmol L⁻¹ respectively. The spectroscopic, optical and microscopic techniques have been performed with hydrogel of compound **4** and **5** in the aqueous medium to investigate the self-assembly behavior.

4.4.1 UV-Visible absorption study

The UV-Visible study was carried out with hydrogel **1** and **2** in aqueous solution. In UV-Visible spectra of hydrogel **1**, the main absorption band at $\lambda_{\text{max}} = 430$ nm is observed (Figure 4.17a). This band originates due to π - π^* transition of π -conjugated quinquethiophene backbone. The broad absorption band at lower energy state suggests the aggregation behavior of peptide-5T hybrids. In the case of hydrogel **2**, multiple absorption peaks are observed at 222 nm, 275 nm, 349 nm and 430 nm.

4.4.2 Fluorescence study

Fluorescence properties of compound **4** was measured in gel state as well as in solution state. In solution state, bolaamphiphile **4** shows fluorescence emission at 590 nm with a shoulder at 550 nm whereas it gives only a broad peak centered at 590 nm in the gel state. The self-assembly nature of peptide-quinquethiophene conjugates **4** is confirmed by comparing the fluorescence emission of **4** in solution state with that of gel state. A fluorescence quenching is observed in gel state with that of solution state (Figure 4.17b). The fluorescence quenching suggests the stacking of molecules by the π - π interaction of quinquethiophene cores as a driving force in self-assembly. In the aqueous solution, fluorescence spectra of compound **4**

a shoulder appeared at 550 nm as a nature of molecularly dissolved peptide-5T but which disappeared in the gel state. In the fluorescence emission spectra of hydrogel **2**, an emission maximum is shifted from 592 nm (solution state) to 652 nm (gel state).

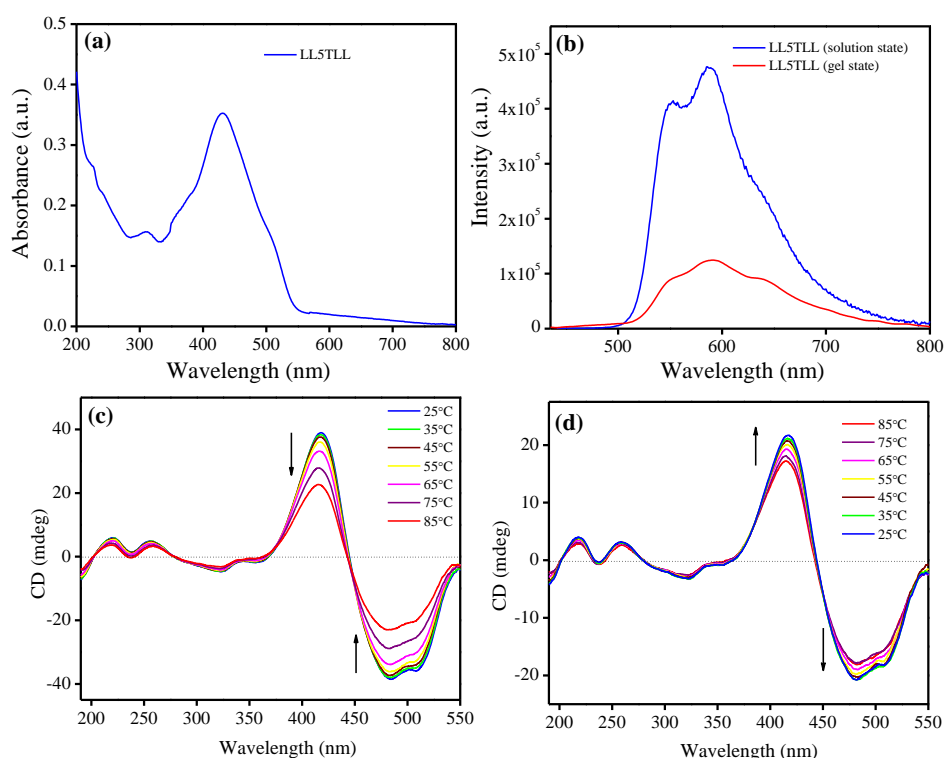


Figure 4.17. (a) UV-vis absorbance, (b) fluorescence spectra compound **4**. Excitation wavelength ($\lambda_{\text{max}} = 430$ nm) in aqueous medium. Temperature dependent CD spectra in water (c) upon heating, and (d) upon cooling. CD Spectra recorded at 200 μM .

4.4.3 Circular dichroism (CD) study

Circular dichroism (CD) spectroscopy has been used to investigate the supramolecular aggregation of peptide-quinquethiophene conjugates **4** and **5** in the aqueous medium. In water, hydrogel **1** shows a strong absorption in CD spectroscopy. This strong absorption arises from quinquethiophene core of the molecule **4**. A remarkable bisignate Cotton effect are observed in the peptide-quinquethiophene conjugates **4**. The Cotton effects are observed first at 480 nm in the negative direction and second at 416 nm in the positive direction with a zero-crossing of the CD signal located at the absorption maximum of the chromophore. It suggests the chiral aggregation of molecules by π - π stacking interaction. Further, to evaluate stacking interaction and corresponding aggregation of molecules, temperature variable CD

spectroscopy was also performed. The CD peak intensity is responsible for oligothiophene cores which gradually decrease with increasing temperature from 20 °C to 80 °C (Figure 4.17c). This suggests the decrease of π - π stacking interaction and disassembly of molecules. The retention of CD intensity and corresponding π - π stacking interaction is somehow quite less when the temperature is cooled down to the starting temperature 20 °C from 80 °C (Figure 4.17d). Therefore, π - π stacking interaction acts as a driving force for supramolecular assembly of peptide-5T hybrid.

3.4.4 Rheological Study

Hydrogel formation is also a clear evidence in favor of molecular self-assembly. Therefore a rheological experiment has been used to characterize gel phase material. Rheological measurement demonstrates the viscoelastic properties of hydrogel **1**. The values of the storage moduli (G') exceeds those of the loss moduli (G'') by an order of magnitude, which indicates the formation of strong and solid like gels (Figure 4.18a).

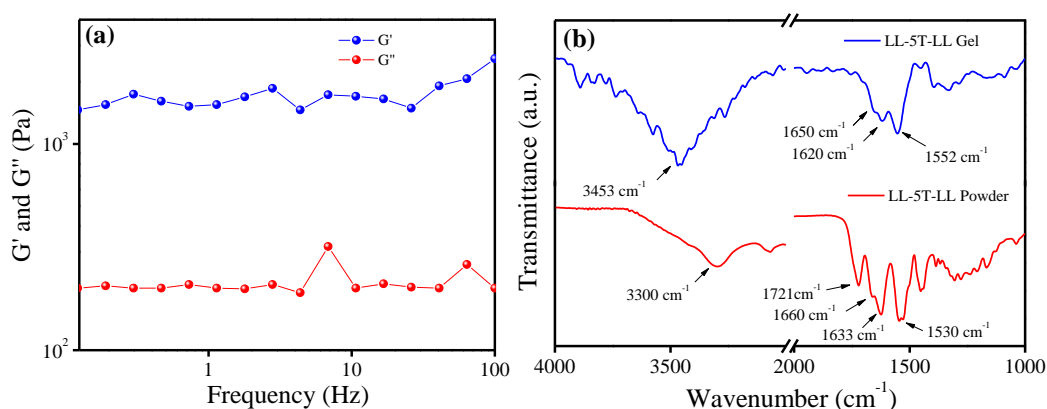


Figure 4.18. (a) Dynamic rheology (frequency sweep) of compound **4** (LL5TLL) hydrogel ($c = 20 \text{ mmol L}^{-1}$), and (b) ATR-FTIR spectra of compound **4** in powder form (red curve) and gel state (blue curve).

3.4.5 FTIR Study

FTIR analysis of powdered compound **4** sample exhibits N-H stretching (Amide A) at 3300 cm^{-1} , a carbonyl stretching (Amide I) frequency at 1633 cm^{-1} with a shoulder at 1660 cm^{-1} and N-H bending (Amide II) at 1530 cm^{-1} (Figure 4.18b). These absorptions clearly indicate that the peptide segments are in α helix conformation (secondary structure) in the powder

state.²⁰¹ The carbonyl stretching (Amide I) frequency at 1633 cm^{-1} is red shifted to 1620 cm^{-1} in the gel phase, which suggests the loss of α -helix structure. Although, the new absorption pattern in the gel state can not be explained by any known secondary structure but the presence of intermolecular H-bonding among peptide segments to drive self-assembly can be supported.

3.4.6 Microscopic study

Transmission electron microscopy (TEM) of gel sample reveals the morphology of self-assembled nanostructures. In TEM micrograph, compound **4** shows fine nanofibrillar structure (Figure 4.19a,b) created by trapping of water molecules. With the help of spectroscopic results, a possible aggregation pattern of peptide-5T bolaamphiphiles is presented schematically in Scheme 4.3.

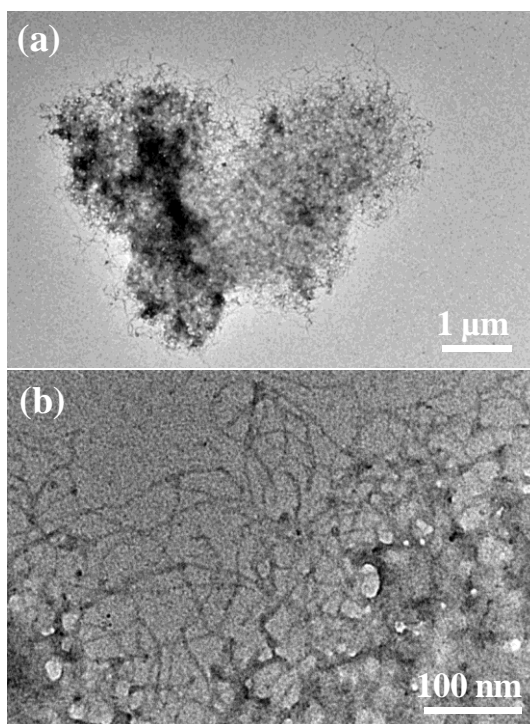


Figure 4.19. (a)-(b) TEM micrograph of compound **4** (LL5TLL) showing nanostructures in high and low magnification.

3.4.7 Cyclic voltammetry

The redox properties of oligothiophenes conjugated peptide are characterized by cyclic voltammetry (CV). The cyclic voltammogram of compound **4** (LL5TLL) in $0.1\text{ M Bu}_4\text{NClO}_4/\text{CH}_2\text{Cl}_2$ electrolyte is shown in

Figure 4.20a. Two consecutive reversible one-electron oxidations take place at the half-wave potentials ($E_{1/2}$) of 0.69 V and 1.0 V versus Ag/AgCl, which correspond to the successive formation of the cation radical and the dication of **4**, respectively (Figure 4.21). These species affect the optical properties of the molecule and resulting coloration. These oxidation potentials are comparable to those reported for oligothiophene derivatives.^[41-42] Redox processes are reproducible through repeated scanning because the extended π -conjugation of the oligothiophene core can stabilize the oxidized forms (Figure 4.20b). In the case of compound **5** (YY5TTY), redox property can not be studied due to insolubility in the electrolyte.

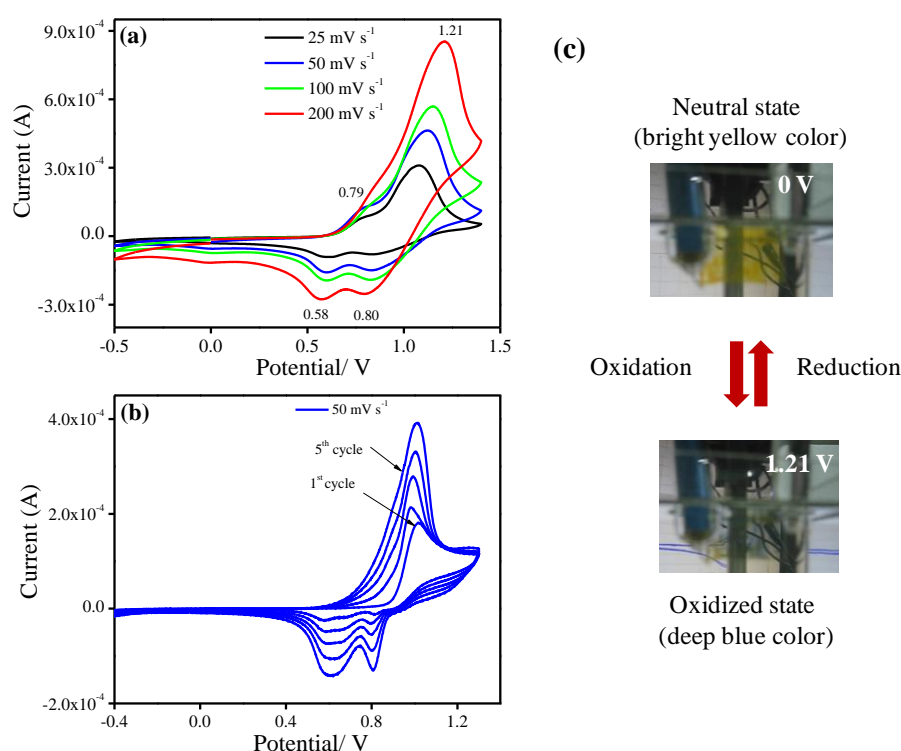


Figure 4.20. Cyclic voltammogram of compound **4** in 0.10 M Bu₄NClO₄/CH₂Cl₂ electrolyte with (a) scan rate of 25, 50, 100 and 200 mVs⁻¹ and (b) at continuous scanning. (c) Reversible colour change in hydrogel **1** (LL5TLL) coated ITO glass at operating voltage 0 V (bright yellow) and 1.21 V (deep blue).

The electrochromic response can be observed in the hydrogel film of compound **4** coated on an ITO glass electrode (Figure 4.20c). The colors of the hydrogel film change from bright yellow (neutral form) to deep blue (oxidized form) by electrochemical reaction. The reversible color change of

solid hydrogel film of compound **4** when scanning from -0.4 V to 1.4 V in CV was shot on video which is shown in the Movie A1 (Annexure 1).

The reversible color change of the hydrogel film, from bright yellow to deep blue and vice versa, together with in situ cyclic voltammogram curve at a scan rate of 50 mVs^{-1} has been beautifully captured in Movie A1. The colors corresponding to redox intermediates involved during the electrochemical oxidation of hydrogel **1** is very stable with fast and controlled switching speed.

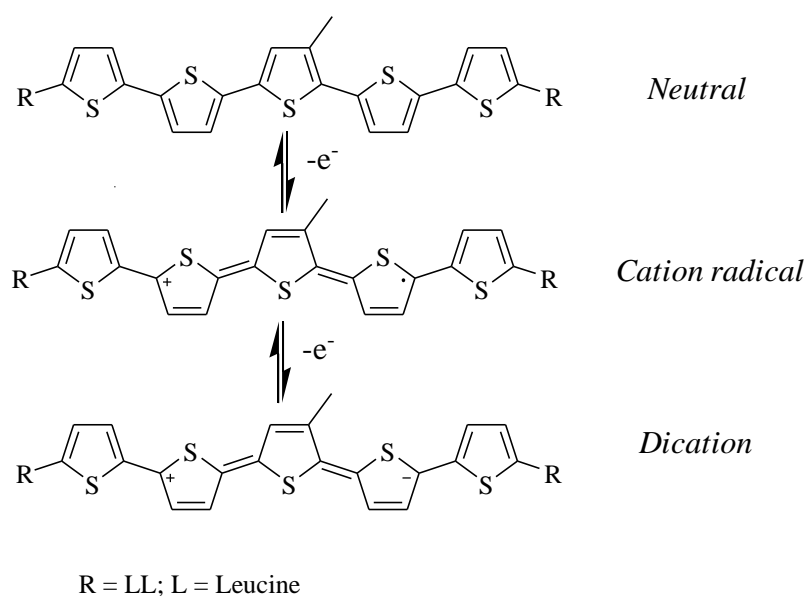
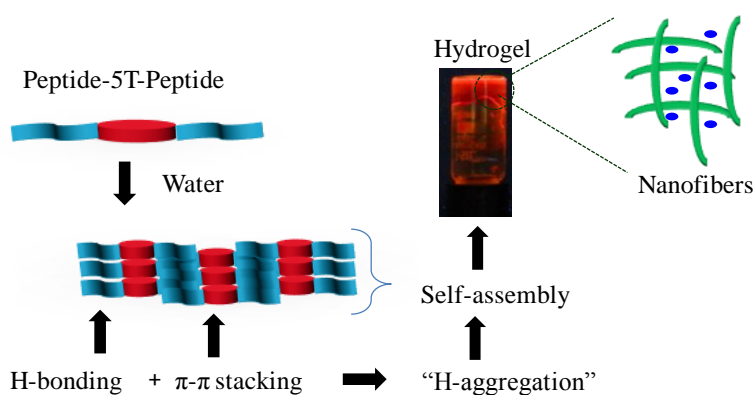


Figure 4.21. The redox mechanism of compound **4** (LL5TLL) ($\text{R}_1 = \text{R}_2 = \text{Leu}$) during electrochemical reaction.



Scheme 4.3. Self-assembly model for peptide-quinquethiophenes in the aqueous medium.

4.5 Conclusion

To conclude, this chapter makes an attempt to focus on self-assembling behavior and electrochromic property of quinquethiophene conjugated peptide. Hydrogel based on peptide-quinquethiophene exhibits electrochromism due to the presence of a redox active quinquethiophene (5T) moiety in compound **4**. Self-assembly and electrochromic properties of quinquethiophene conjugated peptide are strongly dependent on the nature of peptide motifs functionalized with quinquethiophene core. Non-covalent interactions (hydrogen bonding and π - π stacking interactions) are the driving forces for the formation of nano-fibrillar structures. Conjugated quinquethiophenes facilitate charge conduction efficiently through overlapping π -orbitals within adjacent molecules. Furthermore, colours of hydrogel film are very stable with fast and controlled switching speed at room temperature.

4.6 References

- [1] Guo Z., Song Y., Gong R., Mu Y., Jiang Y., Li M. Wan X. (2014), Assembly of peptide-thiophene conjugates: the influence of peptide content and location, *Supramolecular Chemistry*, 26, 383-391 (DOI: 10.1080/10610278.2013.844810).
- [2] Gus'kovaa O. A., Schillinger E., Khalatur P. G., Bäuerle P., Khokhlov A. R. (2009), Bioinspired hybrid systems based on oligothiophenes and peptides (ALA-GLY)_n: computer aided simulation of adsorption layers, *Polymer Science*, 51, 430-445 (DOI: 10.1134/S0965545X09040099).
- [3] Schmid S., Osteritz E. M., Kopyshev A., Bauerle P. (2009), Self-assembling carbohydrate-functionalized oligothiophenes, *Org. Lett.*, 11, 5098-5101 (DOI: 10.1021/ol9022694).
- [4] Schmid S., Mishra A., Bauerle P. (2011), Carbohydrate-functionalized oligothiophenes for concanavalin a recognition, *Chem. Commun.*, 47, 1324-1326 (DOI: 10.1039/c0cc03908j).
- [5] Zerdan R. B., Cohn P., Puodziukynaite E., Baker M. B., Voisin M., Sarun C., Castellano R. K. (2015), Synthesis, optical properties, and

- electronic structures of nucleobase-containing π -conjugated oligomers, *J. Org. Chem.*, 80, 1828-1840 (DOI: 10.1021/jo502773g).
- [6] Spada G. P., Lena S., Masiero S., Pieraccini S., Surin M., Samorì P. (2008), Guanosine-based hydrogen-bonded scaffolds: controlling the assembly of oligothiophenes, *Adv. Mater.*, 20, 2433–2438 (DOI: 10.1002/adma.200703177).
- [7] Iwaura R., Hoeben F., Masuda M., Schenning A. P. H. J., Meijer E. W., Shimizu T. (2006), Molecular-level helical stack of a nucleotide-appended oligo(p-phenylenevinylene) directed by supramolecular self-assembly with a complementary oligonucleotide as a template, *J. Am. Chem. Soc.*, 128, 13298-13304 (DOI: 10.1021/ja064560v).
- [8] Tovar J. D. (2013), Supramolecular construction of optoelectronic biomaterials, *Acc. Chem. Res.*, 46, 1527–1537 (DOI: 10.1021/ar3002969).
- [9] Jatsch A., Schillinger E.-K., Schmid S., Bauerle P. (2010), Biomolecule assisted self-assembly of π -conjugated oligomers, *J. Mater. Chem.*, 20, 3563–3578 (DOI: 10.1039/b926594e).
- [10] Ardoñ H., Ann M., Tovar J. D. (2015), Peptide π -electron conjugates: organic electronics for biology? *Bioconjugate Chem.*, 26, 2290-2302 (DOI: 10.1021/acs.bioconjchem.5b00497).
- [11] Tian L., Szilluweit R., Marty R., Bertschi L., Zerson M., Spitzner E.-C., Magerle R., Frauenrath H. (2012), Development of a robust supramolecular method to prepare well-defined nanofibrils from conjugated molecule, *Chem. Sci.*, 3, 1512-1521 (DOI: 10.1039/c2sc00977c).
- [12] Wall B. D., Diegelmann S. R., Zhang S., Dawidczyk T. J., Wilson W. L., Katz H. E., Mao H.-Q., Tovar J. D. (2011), Aligned macroscopic domains of optoelectronic nanostructures prepared via shear-flow assembly of peptide hydrogels, *Adv. Mater.*, 23, 5009–5014 (DOI: 10.1002/adma.201102963).
- [13] Tsai W.-W., Li L.-S., Cui H., Jiang H., Stupp S. I. (2008), Self-assembly of amphiphiles with terthiophene and tripeptide segments into helical nanostructures, *Tetrahedron*, 64, 8504-8514 (DOI: 10.1016/j.tet.2008.06.033).

- [14] Gus'kova O. A., Khalatur P. G., Bäuerle P., Khokhlov A. R. (2008), silk-inspired 'molecular chimeras': atomistic simulation of nanoarchitectures based on thiophene-peptide copolymers, *Chemical Physics Letters*, 461, 64-70 (DOI: 10.1016/j.cplett.2008.06.058).
- [15] Kumar R. J., MacDonald J. M., Singh Th. B., Waddington L. J., Holmes A. B. (2011), Hierarchical self-assembly of semiconductor functionalized peptide α -helices and optoelectronic properties, *J. Am. Chem. Soc.*, 133, 8564–8573 (DOI: 10.1021/ja110858k).
- [16] Lehrman J. A., Cui H., Tsai W.-W., Moyer T. J., Stupp S. I. (2012), Supramolecular control of self-assembling terthiophene-peptide conjugates through the amino acid side chain, *Chem. Commun.*, 48, 9711-9713 (DOI: 10.1039/c2cc34375d).
- [17] Sanders A. M., Dawidczyk T. J., Katz H. E., Tovar J. D. (2012), Peptide-based supramolecular semiconductor nanomaterials via Pd catalyzed solid-phase "dimerizations", *ACS Macro Lett.*, 1, 1326-1329 (DOI: 10.1021/mz3004665).
- [18] Matmour R., Cat I. De., George S. J., Adriaens W., Leclerc P., Bomans P. H. H., Sommerdijk N. A. J. M., Gielen J. C., Christianen P. C. M., Heldens J. T., van Hest J. C. M., Lo'wik D. W. P. M., Feyter S. De., Meijer E. W., Schenning A. P. H. J. (2008), Oligo(*p*-phenylenevinylene)-peptide conjugates: synthesis and self-assembly in solution and at the solid-liquid Interface, *J. Am. Chem. Soc.*, 130, 14576-14583 (DOI: 10.1021/ja803026j).
- [19] Diegelmann S. R., Hartman N., Markovic N., Tovar J. D. (2012), Synthesis and alignment of discrete polydiacetylene-peptide nanostructures, *J. Am. Chem. Soc.*, 134, 2028-2031 (DOI: 10.1021/ja211539j).
- [20] Manna M. K., Rasale D. B., Das A. K. (2015), Supramolecular assembly of dipeptide functionalized benzo[ghi]perylene monoimide directs white light emission via donor-acceptor interactions, *RSC Adv.*, 5, 90158-90167 (DOI: 10.1039/c5ra11804b).
- [21] Liu Yu-Hao, Hsu S.-M., Wu F.-Y., Cheng H., Yeh M.-Y., Lin H.-C. (2014), Electroactive organic dye incorporating dipeptides in the

- formation of self-assembled nanofibrous hydrogels, *Bioconjugate Chem.*, 25, 1794-1800 (DOI: 10.1021/bc500299c).
- [22] Eakins G. L., Gallaher J. K., Keyzers R. A., Falber A., Webb J. E. A., Laos A., Tidhar Y., Weissman H., Rybtchinski B., Thordarson P., Hodgkiss J. M. (2014), Thermodynamic factors impacting the peptide-driven self-assembly of perylene diimide nanofibers, *J. Phys. Chem. B*, 118, 8642-8651 (DOI: 10.1021/jp504564s).
- [23] Bai S., Debnath S., Javid N., Frederix Pim W. J. M., Fleming S., Pappas C., Ulijn R. V. (2014), Differential self-assembly and tunable emission of aromatic peptide bolaamphiphiles containing perylene bisimide in polar solvents including water, *Langmuir*, 30, 7576-7584 (DOI:10.1021/la501335e).
- [24] Klok H.-A., Rosler A., Gotz G., Osteritz E. M., Bauerle P. (2004), Synthesis of a silk-inspired peptide-oligothiophene conjugate, *Org. Biomol. Chem.*, 2, 3541-3544 (DOI: 10.1039/b415454a).
- [25] Diegelmann S. R., Gorham J. M., Tovar J. D. (2008), One-dimensional optoelectronic nanostructures derived from the aqueous self-assembly of π -conjugated oligopeptides, *J. Am. Chem. Soc.*, 130, 13840-13841 (DOI: 10.1021/ja805491d).
- [26] Stone D. A., Hsu L., Stupp S. I. (2009), Self-assembling quinuethiophene oligopeptide hydrogelators, *Soft Matter*, 5, 1990-1993 (DOI: 10.1039/b904326h).
- [27] Mortimer R. J. (2011), Electrochromic Materials, *Annu. Rev. Mater. Res.*, 41, 241-268 (DOI: 10.1146/annurev-matsci-062910-100344).
- [28] Chen B.-H., Kao S.-Y., Hu C.-W., Higuchi M., Ho K.-C., Liao Y.-C. (2015), Printed multicolor high-contrast electrochromic devices, *ACS Appl. Mater. Interface*, 7, 25069-25076 (DOI: 10.1021/acsami.5b08061).
- [29] Beverina L., Pagani G. A., Sassi M. (2014), Multichromophoric electrochromic polymers: colour tuning of conjugated polymers through the side chain functionalization approach, *Chem. Commun.* 50, 5413-5430 (DOI: 10.1039/C4CC00163J).
- [30] Shaplov A. S., Ponkratov D. O., Aubert P.-H., Lozinskaya E. I., Plesse C., V ygodskii F. V. Y. S. (2014), A first truly all-solid state organic

- electrochromic device based on polymeric ionic liquids, *Chem. Commun.*, 50, 3191-3193 (DOI: 10.1039/c3cc49876j).
- [31] Beaujuge P. M., Reynolds J. R. (2010), Color control in π -conjugated organic polymers for use in electrochromic devices, *Chem. Rev.*, 110, 268-320 (DOI: 10.1021/cr900129a).
- [32] Ma C., Taya M., Xu C. (2008), Smart sunglasses based on electrochromic polymers, *Polymer engineering and science*, 48, 2224-2228 (DOI: 10.1002/pen.21169).
- [33] Kim M., Park K. J., Seok S., Ok J. M., Jung H.-T., Choe J., Kim D. H. (2015), Fabrication of microcapsules for dye-doped polymer-dispersed liquid crystal-based smart windows, *ACS Appl. Mater. Interfaces*, 7, 17904-17909 (DOI: 10.1021/acsami.5b04496).
- [34] Österholm A. M., Shen D. E., Kerszulis J. A., Bulloch R. H., Kuepfert M., Dyer A. L., Reynolds J. R. (2015), Four shades of brown: tuning of electrochromic polymer blends toward high-contrast eyewear, *ACS Appl. Mater. Interfaces*, 7, 1413–1421 (DOI: 10.1021/am507063d).
- [35] Jelle B. P. (2013), Solar radiation glazing factors for window panes, glass structures and electrochromic windows in buildings measurement and calculation, *Sol. Energy Mater. Sol. Cells*, 116, 291-323 (DOI: org/10.1016/j.solmat.2013.04.032).
- [36] Niklasson G. A., Granqvist C. G. (2007), Electrochromics for smart windows: thin films of tungsten oxide and nickel oxide, and devices based on these, *J. Mater. Chem.*, 17, 127-156 (DOI: 10.1039/B612174H).
- [37] Chou Ho-Hsiu, Nguyen A., Chortos A., To J. W.F., Lu C., Mei J., Kurosawa T., Bae W.-G., Tok J. B.-H., Bao Z. (2015), A chameleon-inspired stretchable electronic skin with interactive colour changing controlled by tactile sensing, *Nat. Commun.*, 6, 8011 (DOI: 10.1038/ncomms9011).
- [38] Balan A., Baran D., Toppare L. (2010), Processable donor-acceptor type electrochromes switching between multicolored and highly transmissive states towards single component RGB-based display devices, *J. Mater. Chem.*, 20, 9861-9866 (DOI: 10.1039/C0JM01815E).

- [39] Zhao-Yang Z., Yi-Jie T., Xiao-Qian X., Yong-Jiang Z., Hai-Feng C., Wen-Wei Z. (2013), Multicolor electrochromism of low-bandgap copolymers based on pyrrole and 3,4-ethylenedioxythiophene: fine-tuning colors through feed ratio, *J. Appl. Polym. Sci.*, 129, 1506-1512 (DOI: 10.1002/app.38777).
- [40] Lee K.-R., Sotzing G. A. (2013), Green and blue electrochromic polymers from processable siloxane precursors, *Chem. Mater.*, 25, 2898-2904 (DOI: 10.1021/cm401498f).
- [41] Schillinger E.-K., Kűmin M., Digennaro A., Mena-Osteritz E., Schmid S., Wennemers H., Bűuerle P., Guiding suprastructure chirality of an oligothiophene by a single amino acid, *Chem. Mater.*, 25, 4511-4521 (DOI: 10.1021/cm4020767).
- [42] Yasuda T., Ooi H., Morita J., Akama Y., Minoura K., Funahashi M., Shimomura T., Kato T. (2009), π -conjugated oligothiophene-based polycatenar liquid crystals: self-organization and photoconductive, luminescent, and redox properties, *Adv. Funct. Mater.*, 19, 411-419 (DOI: 10.1002/adfm.200801268).

Chapter 5

**Lamellar Peptide-Cadmium-Doped Zinc Oxide
Nanohybrids That Emit White Light**

5. 1 Introduction

A variety of nanostructured materials has been investigated for the development of white light emitting devices.^[1] GaN, ZnO, Si and several nanocrystals were widely fabricated for light emitting diode (LED) applications.^[2-8] Organic based materials were also preferred for white light luminescence due to low cost, ease of fine-tuning, solution processability, low toxicity and sufficient flexibility for device fabrication.^[9-10] Small organic molecules, as well as polymers, are the key components for the development of white light emitting materials.^[11-17] Nowadays, organic light emitting diodes (OLEDs) are used due to their better performance.^[18-21] Park *et al.* described white-light-emitting single molecular dyad consisting of two non-interacting chromophores through excited-state intramolecular proton transfer (ESIPT).^[22] Ajayaghosh *et al.* designed bis- and mono cholesterol-appended OPV derivatives and the donor organogel emit white light in the presence of an acceptor.^[23] Recently, Nandi *et al.* reported white-light-emitting hydrogel of co-assembled melamine, 6,7-dimethoxy-2,4[1H, 3H]-quinazolinone (Q), with riboflavin (R) by mixing with a dye rhodamine B (RhB) in a requisite proportion.^[24] White light emitting hydrogen-bonded supramolecular copolymers based on π -conjugated oligomers were also demonstrated by Schenning *et al.*^[25]

Of late, organic-inorganic based hybrid materials gained enormous popularity to realize flexible, low-cost, and environment-friendly white luminous devices. Recently, white light emission was achieved from hybrid ZnO-graphene quantum dots.^[26] Radovanovic *et al.* reported ZnO-ATTO fluorophore nanoconjugate for efficient and sustainable white light generation by controlling Förster resonance energy transfer (FRET) process.^[27-28] Li *et al.* developed a group of hybrid semiconductor phosphors to avoid the risk of rare earth metal based lighting source.^[29] Li *et al.* also described high-performance metal-organic frameworks encapsulated iridium-complex composite for bright white light emission.^[30] Organic molecule embedded quantum dot materials were implemented to fabricate white LED.^[31] Sui *et al.* constructed polyvinyl alcohol/ZnO hybrid nanofibers by electrospinning method for intense white light emission.^[32] Bano *et al.* fabricated ZnO-organic hybrid

white light emitting diodes grown on flexible plastic using the low-temperature aqueous chemical method.^[33]

In one reports, we have developed lamellar peptide-ZnO nanohybrids exhibiting superior photo conducting behavior.^[34] In this chapter, our objective is to develop luminescent electrodeposited lamellar peptide/Cd-doped ZnO-based hybrid materials. Here, we report the synthesis of an organic molecule. The synthetic compound BPI-FF-OH (BPI: benzo[*ghi*]perylene monoimide, F: D-Phenylalanine) is used to fabricate BPI-FF-OH/Cd-doped ZnO lamellar hybrid. Cd-doped ZnO facilitates to form nanosheets and BPI-FF-OH/Cd-doped ZnO forms lamellar nanoflakes. These Cd-doped ZnO and BPI-FF-OH/Cd-doped ZnO nanohybrids emit white light.

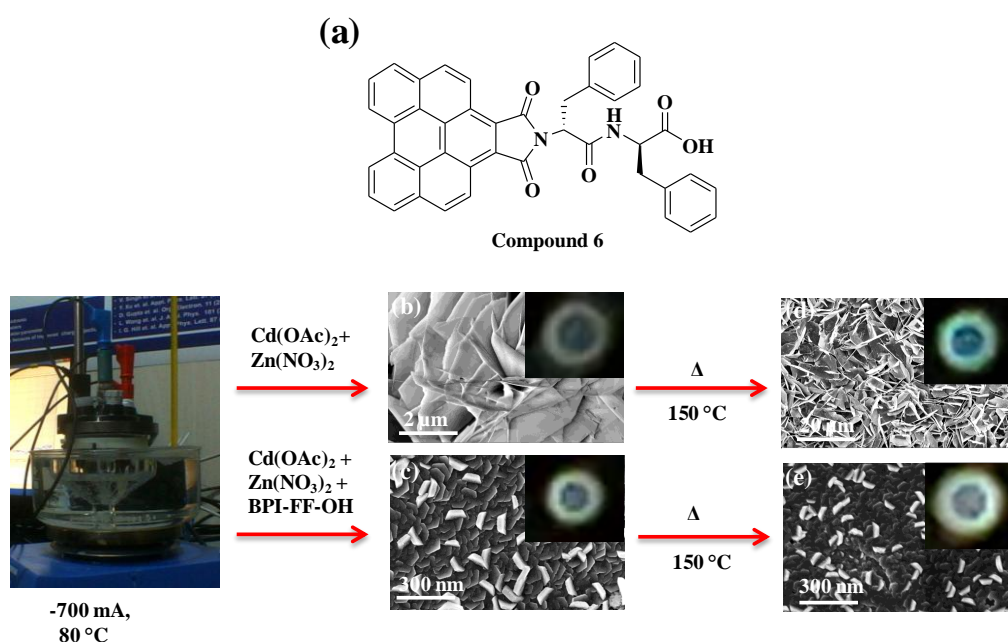


Figure 5.1. (a) The Molecular structure of compound **6** (BPI-FF-OH); Electrochemical synthesis of (b) unannealed cadmium-doped ZnO NSs and (c) unannealed BPI-FF-OH/cadmium-doped ZnO NFs at a constant applied potential of -700 mV at 80°C bath temperature. Synthesis of annealed (d) cadmium-doped ZnO NSs and (e) BPI-FF-OH/cadmium-doped ZnO NFs on heating at 150°C . Insets are digital photographs of whitish light emission from the corresponding hybrids.

5.2 Experimental

Synthesis of Boc-D-Phe-OH (25):

A solution of D-phenylalanine (3.3 g, 20 mmol) in a mixture of 1, 4 dioxane (40 mL), 1 N sodium hydroxide (20 mL) was stirred and cooled in an ice-water bath. Boc anhydride (4.8 mL, 21 mmol) was added and stirring was continued at room temperature for 12 hrs. Reaction mixture was diluted with 200 mL of water and dioxane was evaporated under vacuum. The aqueous layer was washed with diethyl ether and the pH of aqueous layer was adjusted to 2 with 2 M HCl. The aqueous phase was extracted with ethyl acetate (3 x 50 mL) and dried over Na₂SO₄ and concentrated in vacuo to obtain product **25** as colorless oil. Yield= 5.105 g (19.2 mmol, 96 %) ¹H NMR (400 MHz, DMSO-*d*₆): δ = 7.28 (m, 5H), 7.11 (d, 1H, NH), 4.09 (q, 1H, C^αH of Phe), 3.00 (d, 2H, C^βH of Phe), 1.32 (s, 9H, CH₃), 12.66 (s, 1H) ppm. HRMS (ESI) *m/z* for C₁₄H₁₉NO₄ (*M*+Na)⁺ calcd.: 288.1212, found: 288.1223.

Synthesis of Boc-D-Phe(1)-D-Phe(2)-OMe (26):

A solution of Boc-D-Phe-OH (1.32 g, 5 mmol) and HOBt (5 mmol, 0.677 g) was stirred in 2 mL of DMF. A neutralized solution of phenylalanine methyl ester was extracted from its corresponding hydrochloride salt and concentrated on adding to the reaction mixture followed by DCC (5.1 mmol, 1.052 g) at 0 °C. The mixture is allowed to stir at room temperature for 12 hrs. The mixture was diluted with ethyl acetate and the organic layer was washed with 1 M HCl (2 x 30 ml), brine solution, 1 M Na₂CO₃ (3 x 30 ml) and brine solution. The ethyl acetate layer was dried over Na₂SO₄ and evaporated under vacuum to yield white solid product **26**. Purification was done by silica gel column (100-200 mesh) using ethyl acetate- toluene as eluent. Yield= 1.85g, (4.6 mmol, 92 %). ¹H NMR (400 MHz, CDCl₃): δ = 7.54 (m, 10H), 7.00 (d, 1H, NH of Phe(1), 6.28 (d, 1H, NH of Phe(2), 4.81(q, 1H, C^α H of Phe(1), 4.34 (q, 1H, C^αH of Phe(2), 3.12 (d, 4H, CH₂), 1.47 (s, 9H, CH₃) ppm. HRMS (ESI) *m/z* for C₂₄H₃₀N₂O₅ (*M*+Na)⁺ calcd.: 449.2052, found: 449.2086.

Synthesis of NH₂-D-Phe(1)-D-Phe(2)-OMe (27):

A solution of Boc-D-Phe(1)-D-Phe(2)-OMe (**26**) (1.6 g, 3.7 mmol) in TFA stirred for 12 hrs under argon at room temperature. The excess TFA removed under vacuum oily residue was taken in 100 ml of water and washed

with diethyl ether (2 × 20 ml) white product **27** was obtained after lypholization and used further for the reactions. Yield = 1.18 g (3.6 mmol, 97.29 %). ¹H NMR (400 MHz, DMSO-*d*₆): δ = 9.03 (d, 1H, NH of Phe(2), 7.35 (m, 10H), 4.60 (q, 1H, C α H of Phe(2), 4.03 (q, 1H, C α H of Phe(1), 3.66 (s, 3H, OCH₃), 3.12 (d, 2H, C β H of Phe(2), 3.05 (d, 2H, C β H of Phe(1) ppm. HRMS (ESI) *m/z* for C₁₉H₂₃N₂O₃ (*M*+H)⁺ calcd.: 327.1709, found: 327.1717.

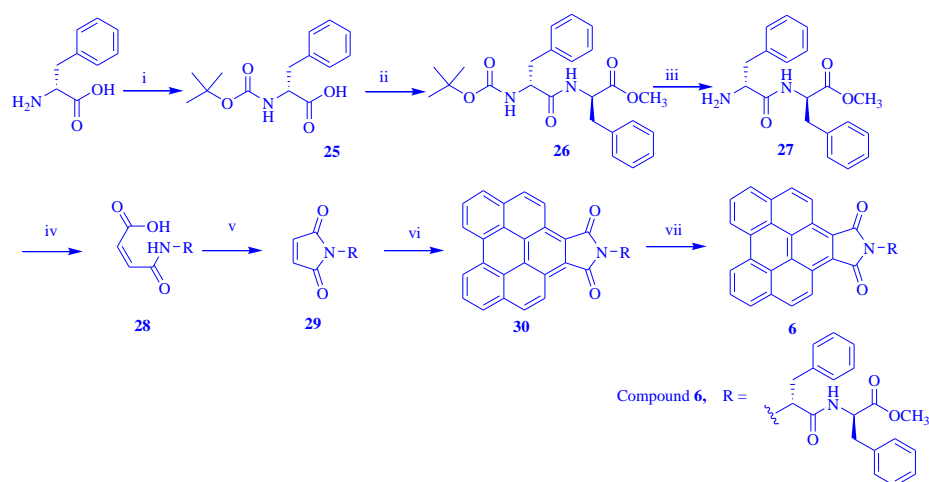
Synthesis of N-substituted benzo[ghi]perylene monoimide:

1.63 g (5 mmol) of H₂N-D-Phe-D-Phe-OMe **27** was taken in 8 mL ethyl acetate. Maleic anhydride (0.735 g, 7.5 mmol) was dissolved in the ethyl acetate and added to the reaction mixture at room temperature. After stirred over 24 hrs, the mixture was fully washed with H₂O, saturated brine and dried over Na₂SO₄. The above solution was concentrated by rotary evaporator to obtain the product *N*-maleyl-D-Phe-D-Phe-OMe **28** as a white powder. 1.50 g (3.5 mmol) of *N*-maleyl-D-Phe-D-Phe-OMe **28** was dissolved in benzene and put into a double-neck flask. The solution was heated to 50 °C and 0.48 g (3.5 mmol) ZnCl₂ was added. Then, the solution of 0.85 g (5.25 mmol) 1,1,1,3,3,3-hexamethyldisilazane (HMDS) in benzene was added dropwise into the reaction mixture at 80 °C, and kept 12 hrs with stirring. Then, the mixture was poured into 600 mL 0.5 M HCl and stirred until the clear solution was obtained. The organic layer was separated; the aqueous phase was extracted with 300 mL EtOAc. The combined organic layer was washed with 3 × 100 mL NaHCO₃ and brine solution and dried over Na₂SO₄. The organic layer was evaporated under vacuum to obtain the product *N*-maleoyl-D-Phe-D-Phe-OMe **29**. Perylene (0.504 g, 2 mmol), *N*-maleoyl-D-Phe-D-Phe-OMe **29** (1.2192 g, 3 mmol) and *p*-chloranil (1.0326 g, 4.2 mmol) were thoroughly mixed and heated at 240 °C with stirring for 3 hrs. The mixture solidified after cooling at room temperature. Chloroform was added to dissolve the solidified mass. The mixture was purified using a silica gel column with chloroform/ether (1:1) as eluent. The compound benzo[ghi]perylene-1,2-dicarboxylic(D-Phe-D-Phe-OMe)imide **30** was collected as an orange solid. A solution of benzo[ghi]perylene-1,2-dicarboxylic(D-Phe-D-Phe-OMe)imide **30** in 100 mL of dry THF was allowed to react with a solution of 2 N LiOH. The progress of the reaction was monitored by thin layer chromatography (TLC). The reaction mixture was stirred up for 3 hrs. Then, THF was removed under vacuum. The

residue was taken in 100 mL of water and washed with diethyl ether (2×20 mL). Then, the pH of aqueous layer was adjusted to 2 using 2 M HCl and it was extracted with ethyl acetate (3×30 mL). The ethyl acetate layer was dried over anhydrous sodium sulfate and evaporated under vacuum to yield **6** as an orange solid.

***N,N'*-Maleyl-D-Phe(1)-D-Phe(2)-OMe (28):**

Yield 3.0 g (7.07 mmol, 94.33%) ^1H NMR (400 MHz, DMSO- d_6): δ = 9.23 (d, 1H, J = 8.52 Hz), 8.68 (d, 1H, J = 7.52 Hz), 7.19-7.25 (m, 10H, aromatic protons), 6.36 (d, 1H, J = 12.52 Hz), 6.22 (d, 1H, J = 12.56 Hz), 4.63 (m, 1H, C^αH of Phe(2)), 4.49 (m, 1H, C^αH of Phe(1)), 3.57 (s, 3H, $-\text{OCH}_3$), 3.03 (m, 2H, C^βH s of Phe), 2.95 (m, 1H, C^βH of Phe), 2.75 (m, 1H, C^βH of Phe). MS (ESI) m/z for $\text{C}_{23}\text{H}_{24}\text{N}_2\text{O}_6\text{Na}$ ($M + \text{Na}$) $^+$ calcd: 447.1532, found: 447.1576.



Scheme 5.1. Synthesis of *N*-dipeptide functionalized benzo[ghi]perylene-1,2-dicarboxylic monoimide. (i) Boc-anhydride, 1,4 dioxane, Na_2CO_3 ; (ii) phenylalanine methyl ester, HOBt/DIPC, DMF; (iii) TFA; (iv) maleic anhydride, EtOAc; (v) $\text{ZnCl}_2/\text{HMDS}$, benzene, $80\text{ }^\circ\text{C}$; (vi) perylene, *p*-chloranil, $240\text{ }^\circ\text{C}$, 3h; (vii) LiOH/THF.

***N,N'*-Maleoyl-D-Phe(1)-D-Phe(2)-OMe (29):**

Yield = 1.3912 g (3.42 mmol, 96.86%). ^1H NMR (400 MHz, CDCl_3): δ = 6.98-7.22 (m, 10H, aromatic protons), 6.49 (s, 2H), 6.34 (d, 1H, J = 7.28 Hz, NH), 4.76-4.83 (m, 2H, C^αH s of Phe(1) and Phe(2)), 3.65 (s, 3H, $-\text{OMe}$), 3.28-3.30 (m, 2H, C^βH s), 3.07-3.12 (m, 1H, C^βH), 2.97-3.02 (m, 1H, C^βH). MS (ESI) m/z for $\text{C}_{23}\text{H}_{22}\text{N}_2\text{O}_5\text{Na}$ ($M + \text{Na}$) $^+$ calcd: 429.1426, found: 429.1565.

Benzo[ghi]perylene-1,2-dicarboxylic(D-Phe-D-Phe-OMe)imide (30):

Yield = 1.26 g (1.93 mmol, 96.92%). ^1H NMR (400 MHz, CDCl_3) δ = 8.85 (d, 2H, J = 8 Hz), 8.72 (d, 2H, J = 8 Hz), 7.86–7.98 (m, 6H), 7.08 (d, ^1H , NH), 6.76–7.06 (m, 10H, aromatic protons of phenyl rings), 5.25 (m, 1H, C^αH of Phe), 4.95 (m, 1H, C^αH of Phe), 3.67 (s, 3H, $-\text{OCH}_3$), 3.15–3.2 (m, 2H, C^βH s of Phe), 3.0–3.06 (m, 2H, C^βH of Phe). MS (ESI) m/z for $\text{C}_{43}\text{H}_{30}\text{N}_2\text{O}_5\text{Na}$ ($M + \text{Na}$) $^+$ calcd: 677.2052, found: 677.6064.

Benzo[ghi]perylene-1,2-dicarboxylic(D-Phe-D-Phe-OMe)imide (6):

Yield = 0.04 g (0.06 mmol, 80%). ^1H NMR (400 MHz, $\text{DMSO}-d_6$) δ = 9.26–9.30 (m, 2H), 9.10 (d, 1H, J = 8.28 Hz), 8.32–8.43 (m, 5H), 8.18 (t, 2H, J = 7.76, 5.00 Hz), 8.00 (d, 1H, J = 8.76 Hz), 7.18–7.38 (m, 10H, aromatic protons of phenyl rings), 5.07 (m, 1H, C^αH of Phe), 4.56 (m, 1H, C^αH of Phe), 3.15–3.16 (m, 2H, C^βH s of Phe), 3.09–3.12 (m, 2H, C^βH s of Phe). ^{13}C NMR (400 MHz, $\text{DMSO}-d_6$) δ 173.1, 171.5, 160.5, 155.6, 140.0, 138.1, 136.0, 135.7, 135.6, 135.4, 135.2, 134.9, 133.3, 130.1, 129.5, 129.2, 129.1, 128.2, 127.2, 126.8, 126.4, 126.0, 125.4, 125.3, 124.7, 124.6, 123.6, 123.5, 120.9, 118.4, 118.1, 114.8, 111.3, 109.6, 59.7, 54.9, 53.0, 36.4 ppm. HRMS (ESI): m/z calcd for $\text{C}_{42}\text{H}_{27}\text{N}_2\text{O}_5$ [$M-\text{H}$] $^-$: 639.1920; found: 639.1894.

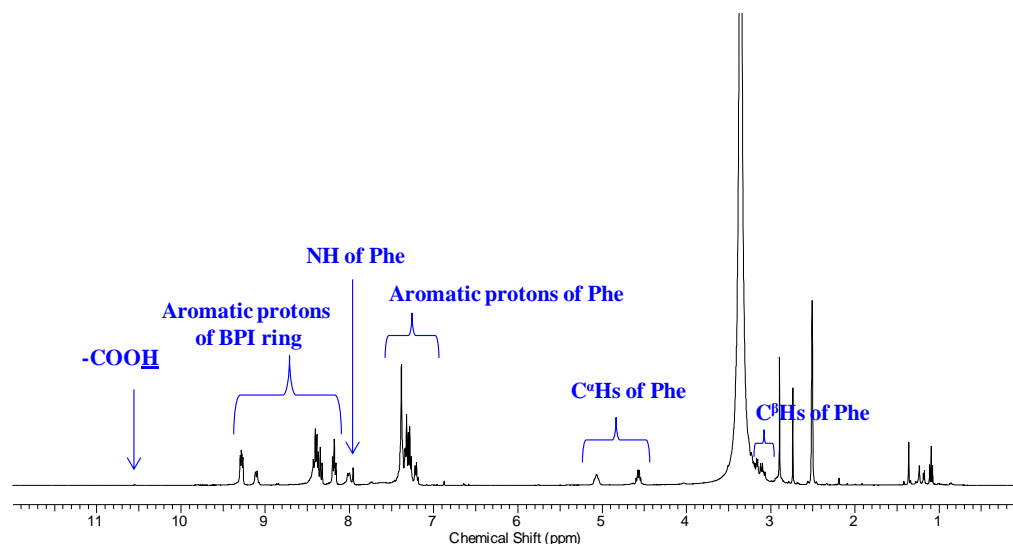


Figure 5.2. ^1H NMR spectrum (400 MHz, $\text{DMSO}-d_6$) of BPI-FF-OH (6).

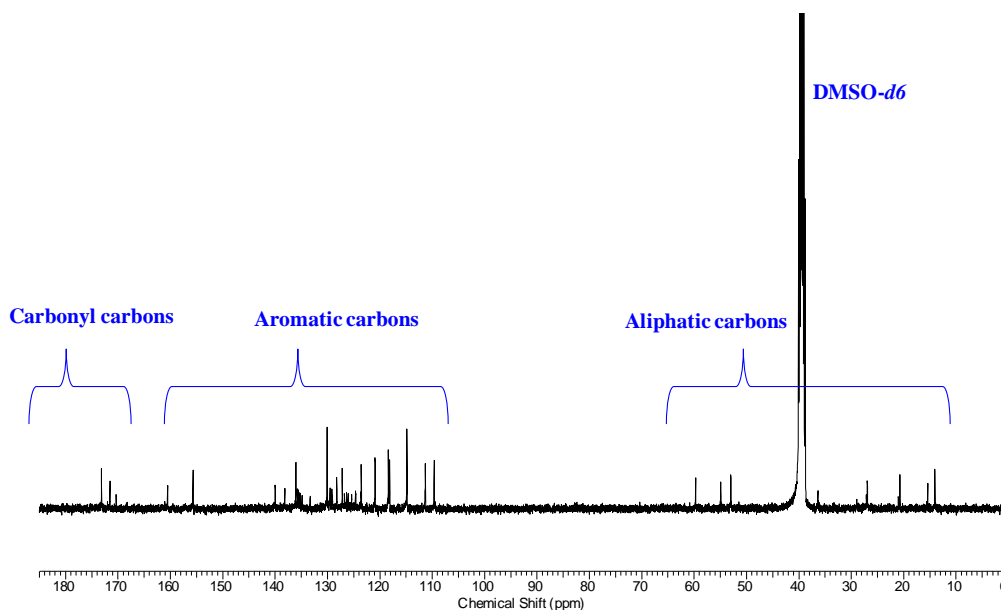


Figure 5.3. ^{13}C NMR spectrum (100 MHz, $\text{DMSO}-d_6$) of BPI-FF-OH (**6**).

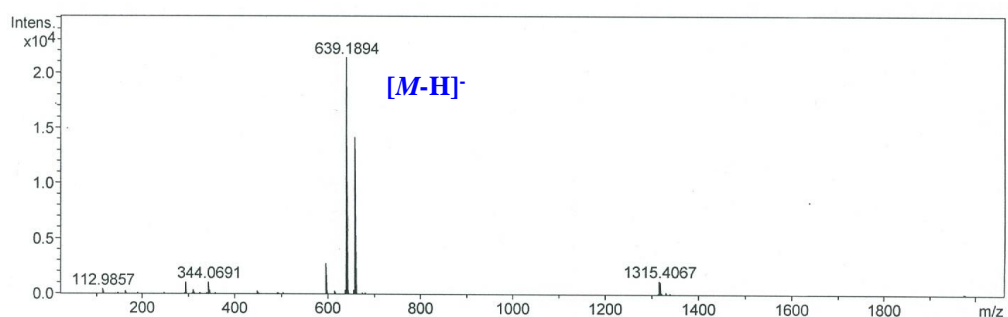


Figure 5.4. ESI-MS spectrum of BPI-FF-OH (**6**).

The growth of GZO/n-Si (100) Electrode: Working electrode Ga-doped ZnO (GZO) with a thickness of 150 nm on p-Si(111) was generated by dual ion beam sputtering deposition (DIBSD) technique. The detailed growth procedure by DIBSD system was described in chapter 2.^[36-39]

Electrochemical synthesis: Electrochemical synthesis was carried out in an aqueous solution of 0.02 M $\text{Zn}(\text{NO}_3)_2 \cdot 6\text{H}_2\text{O}$ and 0.02 M $\text{Cd}(\text{CH}_3\text{COO})_2 \cdot 6\text{H}_2\text{O}$ in a 100 mL cell vial using three electrode setup (AUTOLAB /PG STAT302N) with Pt counter electrode and an Ag/AgCl reference electrode (Autolab 6.0726.107). 0.02 M $\text{Zn}(\text{NO}_3)_2 \cdot 6\text{H}_2\text{O}$, 0.02 M $\text{Cd}(\text{CH}_3\text{COO})_2 \cdot 6\text{H}_2\text{O}$ with 1 mg of N-substituted benzo[ghi]perylene monoimide in 24 mL DMSO/water (1:1 v/v) solution was used for the deposition of BPI-FF-OH/Cd-doped ZnO hybrid thin film keeping all other parameters same. Water was required for the reduction of NO_3^- to generate OH^- and DMSO was added

to soluble the dipeptide functionalized benzo[*ghi*]perylene monoimide (BPI). Working electrode GZO/p-Si (111) was placed upright in cell and deposition was achieved potentiostatically at -700 mV (vs Ag/AgCl) for 2 hours under constant stirring at 80 °C in water bath. Deposited films were rinsed with de-ionized water and dried with nitrogen (N₂) gas. Required samples were annealed at 150 °C for 6 hours.

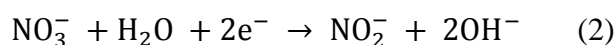
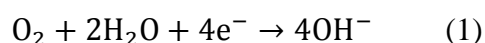
5.3 General characterization

Zeiss Supra 55 field emission scanning electron microscopy (FE-SEM) and Rigaku X-ray diffractometer with monochromatized Cu K α radiation ($\alpha = 1.54 \text{ \AA}$) were used for materials characterization. SAXS experiments were carried out on electrodeposited thin films using Cu K α ($\lambda = 1.54 \text{ \AA}$) radiation from a source (GeniX 3D, Xenocs) operating at 50 kV and 0.6 mA. The diffraction patterns were collected on a two module Pilatus detector. Absorption coefficient (α) was measured by M-2000 J. A. Woollam spectroscopic ellipsometry. Secondary mass ion spectrometry (SIMS, Hiden) equipped with oxygen ion gun of energy up to 3.5 KeV, was used to characterize the depth profile of Cd-doped ZnO films. Photoluminescence (PL) spectra were recorded using a 20 mW continuous wave He-Cd laser ($\lambda = 325 \text{ nm}$) as an excitation source.

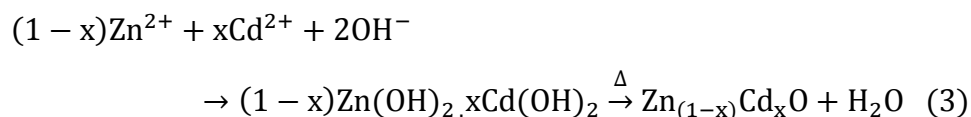
5.4 Results and Discussion

Electrodeposition is one of the simple and cost-effective techniques to grow lamellar organic-inorganic hybrid nano-architectures.^[40-42] To develop luminescent hybrid films, a simple electrochemical technique was used to synthesize Cd-doped ZnO and BPI-FF-OH/Cd-doped ZnO nanostructured lamellar hybrids (Figure 5.1). The electrochemical technique was used to dope Cd in ZnO lattice and in the ZnO of the aromatic based peptide amphiphile anchored with ZnO lamellar sheets. Furthermore, the solution based bottom-up approach is a fairly reasonable method for homogeneous mixing of metal ions in atomic level and chemical growth of hybrid nanostructure on the top of the cathode surface. In the electrochemical synthesis of BPI-FF-OH/Cd-doped ZnO nanohybrid, aromatic benzo[*ghi*]perylene moiety of BPI-FF-OH is a large aromatic surface linked with an aromatic dipeptide Phe-Phe. Aromatic faces favor intermolecular π - π stacking interactions to construct

supramolecular organic galleries and provide structural stability in nanohybrid architecture.^[43-45] Dipeptide linked with BPI enhances solubility and C-terminal acid functional group interacts with Cd-doped ZnO by covalent bonding to give structural stability of nanohybrid architecture.^[46] Cd-doped ZnO and BPI-FF-OH/Cd-doped ZnO nanostructures were grown at a potential -700 mV (vs Ag/AgCl) at 80 °C bath temperature. The chemical reactions involved in the formation of Cd-doped ZnO and BPI-FF-OH/Cd-doped ZnO hybrids are shown in equations 1-3. The electro-generation of base OH⁻ can be achieved *via* equations 1 and 2. Electrochemical reduction of O₂ and nitrate (NO₃⁻) ions give a base OH⁻. Electrochemically generated OH⁻ ions react with zinc and cadmium ions to give corresponding metal hydroxides. After annealing at 150 °C in ambient condition, the metal hydroxides form semiconductor metal oxide.



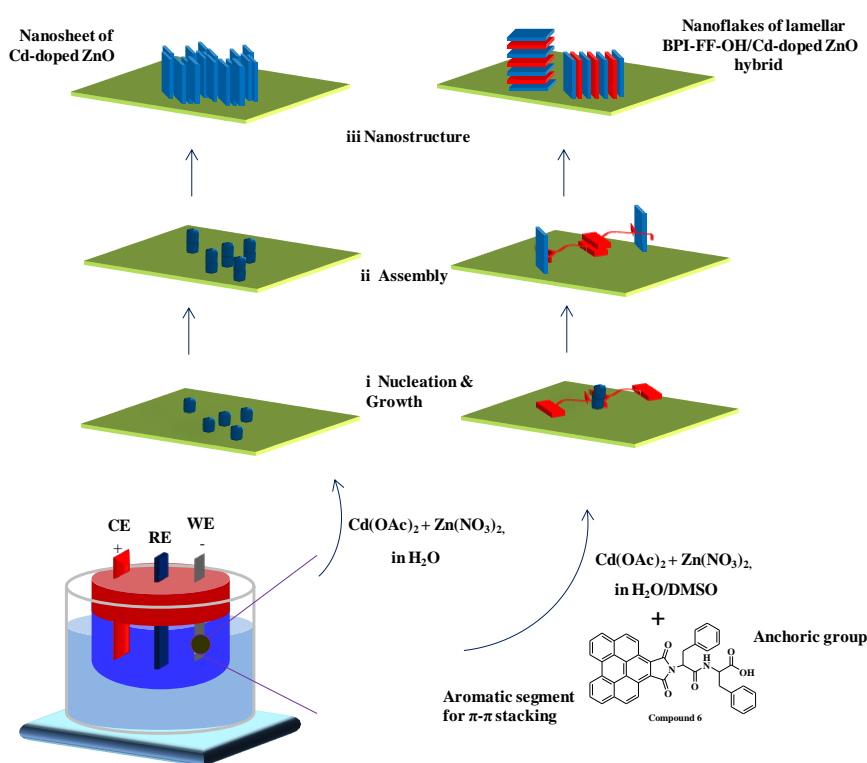
The formation of Zn_(1-x)Cd_xO is governed by equation 3 as follows:



The electrochemical thin film growth of Cd-doped ZnO and hybrids is monitored by chronoamperometry. In the electrochemical growth of Cd-doped ZnO films, only Cd-doped ZnO is formed even if the concentration of Cd and Zn precursors are kept same or varied. The Cd doping occurs in ZnO structure and only Cd-doped ZnO phase is formed. This is because zinc has larger chemical reactivity than cadmium and it can easily form crystal frames. To evaluate the physical effect of Cd doping on the fabrication and luminescence properties of Cd-doped ZnO and hybrid materials, electrodeposition is carried out in different bath concentration of Cd precursor. The various parameters obtained from the Cd-doped ZnO and hybrid thin films are summarized in Table 5.1. Cd-doped ZnO and BPI-FF-OH directed BPI-FF-OH/Cd-doped ZnO hybrids are annealed at 150 °C to understand the material behavior upon annealing. Electrodeposited inorganic hydroxide phases in lamellar BPI-FF-

OH/Cd-doped ZnO hybrids converted to oxide phases upon annealing and crystalline order are developed in the Cd-doped ZnO phase. The dipeptide functionalized benzo[*ghi*]perylene monoimide is used as a structure directing agent to grow lamellar organic/Cd-doped ZnO. The lamellar ordering of supramolecular peptide galleries and Cd-doped ZnO phase is driven by self-assembly process on the solid-liquid interface.^[46] CdO is grown under the same electrochemical parameters and bath temperature to show the effect of BPI-FF-OH in BPI-FF-OH/Cd-doped ZnO nanohybrid morphology. In the electrochemical deposition, CdO is grown as nanorod bundles where BPI-FF-OH/Cd-doped ZnO is grown as nanoflakes (Figure 5.1). The mechanism of Cd-doped ZnO nanosheets (NSs) and lamellar BPI-FF-OH/Cd-doped ZnO nanoflakes (NFs) formation is shown schematically in Scheme 5.1.

5.4.1 Field-Emission Scanning Electron Microscope (FE-SEM)



Scheme 5.1. Schematic of possible growth mechanisms for cadmium-doped ZnO and BPI-FF OH/cadmium-doped ZnO nanostructures on the Ga-doped ZnO (GZO)/n-Si(100) electrode.

The surface morphologies of the electrodeposited nanostructures are investigated using field-emission scanning electron microscope (FE-SEM). A highly dense, randomly oriented nanosheet (NS) type morphology is observed in Cd-doped ZnO. No significant difference is observed in the morphology of annealed and unannealed films of Cd-doped ZnO NSs (Figure 5.5a and 5.5b). In the case of BPI-FF-OH/Cd-doped ZnO hybrid, nanoflake type morphology is found. The lamellar hybrid nanoflakes are oriented horizontally as well as vertically with respect to the cathode surface (Figure 5.5c and 5.5d). Morphology of lamellar BPI-FF-OH/Cd-doped ZnO is also not altering even after annealing.

Table 5.1. Parameters obtained from spectroscopic ellipsometry and PL measurements.

SL. No	Sample (As-grown)	Electrochemical bath composition (deposited at 80 °C, -0.7 V)			Thickness (nm)	MSE	Roughness (nm)	Band gap	
		Zn(NO ₃) ₂ ·6H ₂ O (M)	Cd(OAc) ₂ ·6H ₂ O (M)	Organic				SE (eV)	PL (eV)
1	Cd-doped ZnO	0.04	0.04	-	205	22.06	17	2.7	2.7
2	Cd-doped ZnO	0.04	0.02	-	206	20.91	20	2.8	2.9
3	Cd-doped ZnO	0.04	0.01	-	225	20.47	30	3.06	3.27
4	BPI-FF-OH/Cd-doped ZnO	0.04	0.04	BPI-FF-OH	248	20.8	7.29	3.09	3.1
5	BPI-FF-OH/Cd-doped ZnO	0.04	0.02	BPI-FF-OH	245	16.74	7.34	3.20	3.03
6	BPI-FF-OH/Cd-doped ZnO	0.04	0.01	BPI-FF-OH	250	20.8	6.33	3.27	3.02

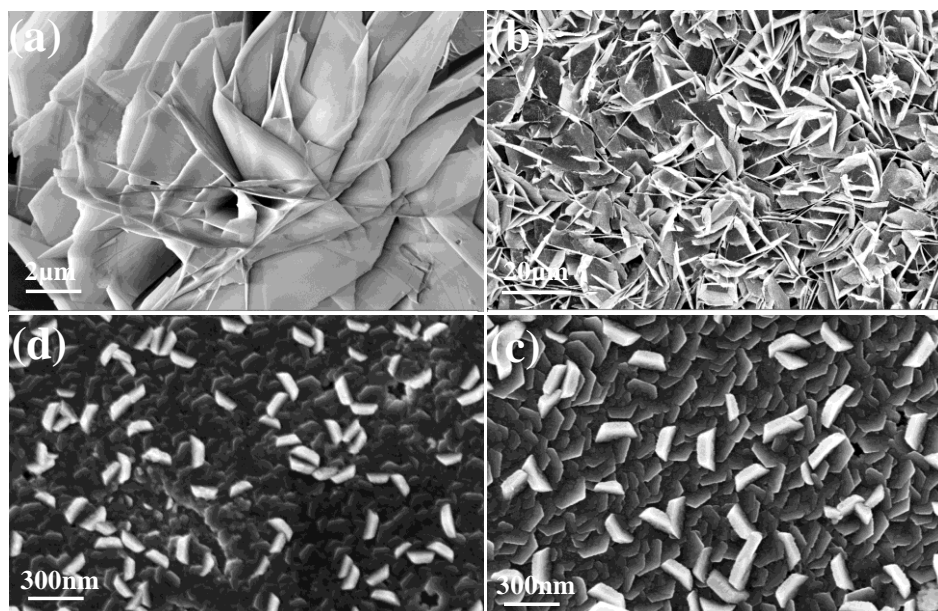


Figure 5.5. FE-SEM images of (a) unannealed cadmium-doped ZnO, (b) annealed cadmium-doped ZnO NS, (c) unannealed BPI-FF-OH/cadmium-doped ZnO, and (d) annealed BPI-FF-OH/cadmium-doped ZnO NF architectures.

5.4.2 Energy-Dispersive X-ray Spectroscopy (EDS)

Primarily, the elemental composition of nanostructured Cd-doped ZnO and BPI-FF-OH/Cd-doped ZnO hybrid is determined by energy-dispersive X-ray spectroscopy (EDS). The EDS analysis confirmed the presence of zinc (Zn), cadmium (Cd), carbon (C) and oxygen (O) elements in the deposited films. Figure 5.6 shows EDS spectrum of Cd-doped ZnO and BPI-FF-OH/Cd-doped ZnO hybrid films.

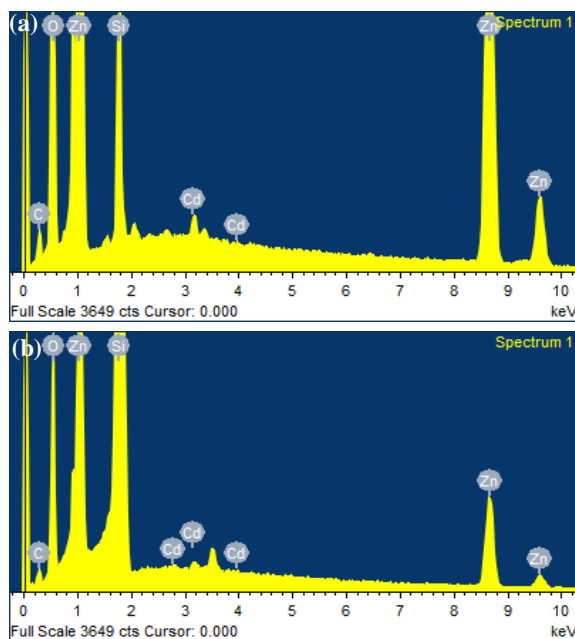


Figure 5.6. EDS spectra of annealed (a) cadmium-doped ZnO and (b) BPI-FFOH/cadmium-doped ZnO films.

5.4.3 X-ray diffraction (XRD) study

Wide angle X-ray diffraction (XRD) [$2\theta = 20^\circ$ - 60°] was employed to describe the internal structure of Cd-doped ZnO and BPI-FF-OH/Cd-doped ZnO nanohybrid. XRD analysis reveals the nature and orientation of the crystal structure of electrodeposited Cd-doped ZnO and BPI-FF-OH/Cd-doped ZnO nanostructures. A polycrystalline hexagonal wurtzite structure with a preferred *c*-axis (002) orientation along with (100), (101) is found (Figure 5.7a). No diffraction peak corresponding to Cd metal or cubic CdO phase in both Cd-doped ZnO and BPI-FF-OH/Cd-doped ZnO nanohybrids are observed. The XRD pattern of Cd-doped ZnO is similar to that of ZnO because Zn has higher chemical reactivity than Cd to form Cd-doped ZnO

lattice network. Formation of Cd-doped ZnO is also confirmed from lattice parameter (c) and crystalline size. The conventional pure ZnO exhibits (002) Bragg diffraction peak with the lattice constant $c = 5.20661 \text{ \AA}$ but the value of c is 5.2217 \AA for Cd-doped ZnO.^[47-48] The incorporation of Cd in ZnO matrix tends to expand c -axis lattice parameter because the ionic radius of Cd (0.97 \AA) is larger than that of Zn (0.74 \AA). Therefore, a substitution of Zn by Cd induces a lattice-volume expansion.^[49-51] Only single Cd-doped ZnO phase is found and there is no formation of Cd or CdO phase individually. Lattice parameter and full-width at half-maximum (FWHM) of (002) peaks obtained from Cd-doped ZnO and BPI-FF-OH/Cd-doped ZnO are listed in Table 5.2. The lattice plane (002) of wurtzite Cd-doped ZnO peak becomes sharp upon annealing at $150 \text{ }^\circ\text{C}$ indicating preferential growth along c -axis (Figure 5.7b). FWHM of unannealed and annealed Cd-doped ZnO films are 0.2168 and 0.2013 , respectively. The Crystalline quality of nanostructured Cd-doped ZnO and BPI-FF-OH/Cd-doped ZnO are enhanced due to annealing at $150 \text{ }^\circ\text{C}$, as demonstrated in Figure 5.7b and 5.7d. The results in Figure 5.7c-d also confirm preferred c -axis growth in case of BPI-FF-OH/Cd-doped ZnO material.

5.4.4 Two-Dimensional Grazing-Incidence Small Angle X-ray Scattering (2D-giSAXS)

The lamellar assembly of organic BPI-FF-OH/Cd-doped ZnO in the hybrid thin film is described by two-dimensional grazing-incidence small angle X-ray scattering (2D-giSAXS). The broad arc in the Figure 5.8a suggests a randomness of stacking direction. X-ray scattering pattern of hybrid films shows peaks at 159.19 \AA (001) and 82.20 \AA (002), 18.40 \AA (004). The former peak position corroborates well with repeated distance of lamellar ordered nanostructure. The d spacing suggests a long-range ordering of hybrid films. These peaks indicate the presence of a lamellar structure.

5.4.5 SIMS analysis

SIMS profile is used to determine the incorporation of Cd atoms in ZnO structure qualitative and quantitatively. Figure 5.8b presents the profile of detected Cd and Zn element in the nanostructure thin films. From the SIMS plot, flat Cd profile indicates that Cd-doping is uniform throughout the film

thickness and hence resulting a homogeneous Cd-doped ZnO film. The relative Cd concentrations of the electrodeposited Cd-doped ZnO thin films, on an average, are 19%, 17% and 11% fabricated from 0.04 M, 0.02 M and 0.01 M Cd salt precursor respectively. Cd concentration in BPI-FF-OH/Cd-doped ZnO film hybrid is around 8 % fabricated from 0.01 M Cd, and 0.04 M Zn precursor.

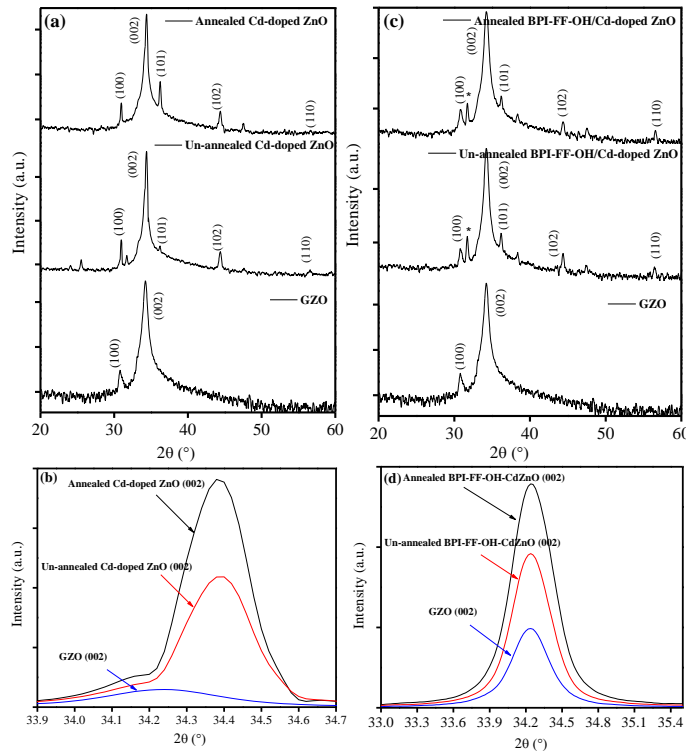


Figure 5.7. XRD patterns of GZO and annealed, and unannealed cadmium-doped ZnO (a and b) and GZO, annealed and unannealed BPI-FF-OH/cadmium-doped ZnO films (c and d). The peaks marked with asterisks are associated with silicon.

Table 5.2. Lattice parameters and FWHM parameters of Cd-doped ZnO, BPI-FF-OH/Cd-doped ZnO hybrids.

#	Substrates	2θ (°)	(h k l) plane	d-spacing, $d(hkl)$	Lattice constant (c)	FWHM
1	GZO/n-Si(100)	34.2	002	-	-	-
2	Un-annealed Cd-doped ZnO	34.4	002	2.6196 Å	5.2217 Å	0.2168
3	Annealed Cd-doped ZnO	34.4	002	2.6196 Å	5.2217 Å	0.2013
4	Un-annealed BPI-FF-OH/Cd-doped ZnO	34.4	002	2.6196 Å	5.2217 Å	0.2168
5	Annealed BPI-FF-OH/Cd-doped ZnO	34.4	002	2.6196 Å	5.2217 Å	0.2013

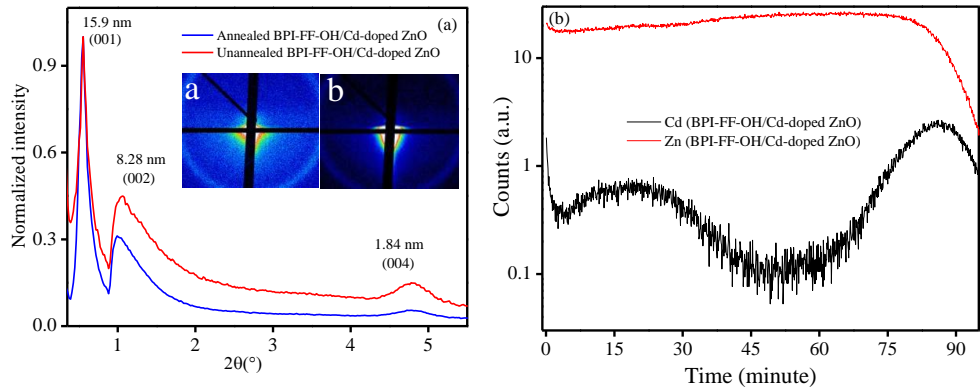


Figure 5.8. (a) SAXS of lamellar BPI-FF-OH/cadmium-doped ZnO hybrid films. Insets show the corresponding 2D giSAXS images of annealed BPI-FF-OH/cadmium-doped ZnO and unannealed BPI-FF-OH/cadmium-doped ZnO nanohybrids, (b) SIMS profile of Cd-doped ZnO and hybrid thin films deposited from 0.01 M $\text{Cd}(\text{OAc})_2 \cdot 6\text{H}_2\text{O}$; 0.04 M $\text{Zn}(\text{NO}_3)_2 \cdot 6\text{H}_2\text{O}$, BPI-FF-OH.

5.4.6 UV-Visible absorption

The optical band gap energy of Cd-doped ZnO and BPI-FF-OH/Cd-doped ZnO is obtained from absorption coefficient (α) using the Tauc's equation as follows:

$$(\alpha h\nu)^2 = C (h\nu - E_g)^n \quad (4)$$

α is the absorption coefficient, $h\nu$ is photon energy, C is the constant and E_g is energy band gap. Tauc's plot $[(\alpha h\nu)^2 \text{ vs } h\nu]$ is shown as insets in Figure 5.9. The calculated optical band gap energy is 2.7 and 3.4 eV, for unannealed and annealed Cd-doped ZnO, respectively measured at room temperature. Optical band gap energy of BPI-FF-OH/Cd-doped ZnO is 2.9 eV (un-annealed) and 3.2 eV (annealed) (Figure 5.9b). The band gap energy is lower in Cd-doped ZnO than the band gap energy of ZnO.^[52] The reduction of band gap energy is due to the Cd doping in ZnO lattice.^[53-54] Band gap energy is increased upon annealing for both the samples Cd-doped ZnO and BPI-FF-OH/Cd-doped ZnO hybrid.^[55] The band gap energy of Cd-doped ZnO fabricated from three different concentration of Cd precursor, decreases with increase in Cd-doping percent (Figure 5.10).

The Cd-doped ZnO films were grown for a fixed duration of 120 minutes at 80 °C with -0.7 Volt. Spectroscopic ellipsometry was carried out to determine the thickness of all the samples and the measured data was fitted

using various model (cauch, GenOsc) for which data is presented in Table 5.1. The approximate thicknesses of the samples varied in ranges from 220 nm-250 nm.

5.4.7 Photoluminescence Study

Photoluminescence (PL) measurements exhibit unique white luminescence from Cd-doped ZnO and hybrid BPI-FF-OH/Cd-doped ZnO under the excitation of 325 nm He-Cd laser source. Room temperature and temperature dependent PL studies were performed to have an insight to whitish luminescence from Cd-doped ZnO system (Figure 5.9c). Some observations may be cited from the PL measurements: firstly, appearance of luminescence from Cd-doped ZnO NSs generally witnessed in compound semiconductors possibly due to (a) Cd content fluctuation – possible overlapping of the emission lines, which correspond to excitonic recombination in the wavelength range from 395 to 540 nm, with different Cd content, (b) bound states corresponding to defects in crystals, and (c) strain-induced band gap modification.^[56] The emission spectra stretch from ultraviolet (UV) to cover most of the visible spectrum range. These spectra from Cd-doped ZnO make it an ideal candidate for white light emitter applications. Secondly, all obtained spectra are characterized by the presence of a higher energy band emission in the ultraviolet (UV) region centered at 367 nm (3.37 eV) and relatively wide band emission covering a wide band of electromagnetic spectra spanning from 418 to 700 nm. The peak at 367 nm around UV region is due to free exciton composite caused by radiative recombination of electron-hole pairs from the top of the valence band and electronic states at the bottom of the conduction band in Cd-doped ZnO NSs. The deep level emission (DLE) usually accompanies the presence of native defects and impurities,^[57] these can be oxygen vacancies (O_V) centered at ~ 485 nm,^[46] oxygen interstitials (O_I) at ~ 610 nm,^[58] zinc vacancies (Zn_V) at ~527 nm,^[59] zinc interstitials (Zn_I) at ~ 680 nm^[60-61] and oxygen antisites (O_{Zn}).

The PL spectrum of BPI-FF-OH shows two wide peaks centered at 394 nm and 613 nm corresponding to bluish and red emissions, respectively (Figure 5.9d). In lamellar BPI-FF-OH/Cd-doped ZnO, a weak intense

emission peak in the UV region centered at 379 nm (3.27 eV) and a broad band in the visible region ranging from 421 to 700 nm corresponding to NBE of Cd-doped ZnO and blue and red emissions of BPI-FF-OH and various defect related emission of BPI-FF-OH/Cd-doped ZnO nanohybrid, respectively are observed. Benzo[*ghi*]perylene monoimide (BPI) functionalized with a dipeptide diphenylalanine moiety in BPI-FF-OH/Cd-doped ZnO nanohybrid system contributes to the PL emission. The emission at 613 nm is due to the presence of large aromatic BPI core of BPI-FF-OH. Bluish emission is associated with Phe-Phe moiety in the assembled state.^[62] Recently Li *et al.* reported self-assembled micro and nanostructured morphology of a diphenylalanine dipeptide which acts as an optical waveguide material.^[63-66] Phe-Phe dipeptide is a well known candidate for the evolution of various self-assembled nanostructure.^[67] Recently, our previous report Phe-Phe appended BPI system is described as a new component for the white light generation when combined with an aromatic donor.^[68] White luminescence from annealed and un-annealed BPI-FF-OH/Cd-doped ZnO nanohybrid materials is shown as insets in Figure 5.9d. The DLE of BPI-FF-OH/cadmium-doped ZnO nanohybrid materials, relative to that of cadmium-doped ZnO, apparently decreases owing to the assembly of organic molecules within the inorganic phases. The BPI-FF OH-based molecules in the lamellar nanohybrids are highly stacked through π - π stacking and intermolecular hydrogen bonding interactions. The emission also decreases at higher wavelengths through the compact assembly of organic molecules in the nanohybrids, compared with BPI-FF-OH itself.

To evaluate the physical effect of Cd doping in the illumination properties Cd-doped ZnO and hybrids, we have electrodeposited Cd-doped ZnO and hybrid thin films at three different concentrations (0.04 M, 0.02 M, and 0.01 M) of Cd precursor. Cd content increases in Cd-doped ZnO as well as BPI-FF-OH/Cd-doped ZnO with the increase of Cd salt concentration. The physical effects of Cd doping in the luminescence properties of Cd-Doped ZnO and BPI-FF-OH/Cd-doped ZnO are evaluated by photoluminescence spectroscopy. The PL emission was red shifted with increasing Cd content in Cd-doped ZnO and in the hybrid thin films (Figure 5.11).

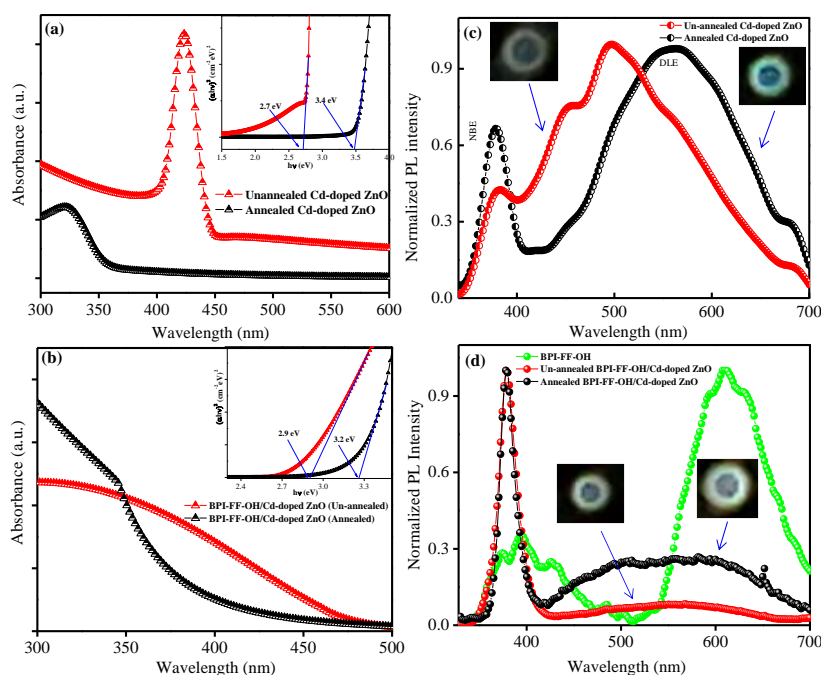


Figure 5.9. Optical absorption spectra of (a) Cd-doped ZnO and (b) lamellar BPI-FF-OH/ cadmium-doped ZnO films. Insets show the corresponding Tauc plots to evaluate the band gap energy. Room-temperature PL spectra of (c) cadmium-doped ZnO before and after annealing. The inset shows the whitish luminescence from unannealed and annealed cadmium-doped ZnO NSs. (d) PL spectra of the organic dye BPI-FF-OH and the lamellar BPI-FF-OH/cadmium-doped ZnO nanohybrid. The inset shows white-light emission from unannealed and annealed BPI-FFOH/cadmium-doped ZnO nanohybrids.

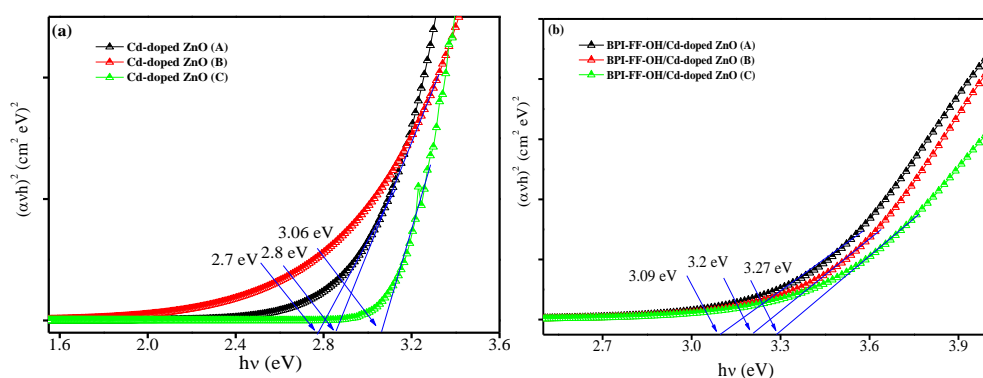


Figure 5.10. Tauc's plots to evaluate band gap energy of (a) Cd-doped ZnO and (b) BPI-FFOH/ Cd-doped ZnO hybrid deposited from different Cd precursor bath concentration. Bath compositions are (A) 0.04 M $\text{Cd}(\text{OAc})_2 \cdot 6\text{H}_2\text{O}$; 0.04 M

Zn(NO₃)₂.6H₂O, (B) 0.02 M Cd(OAc)₂.6H₂O; 0.04 M Zn(NO₃)₂.6H₂O and (C) 0.01 M Cd(OAc)₂.6H₂O; 0.04 M Zn(NO₃)₂.6H₂O.

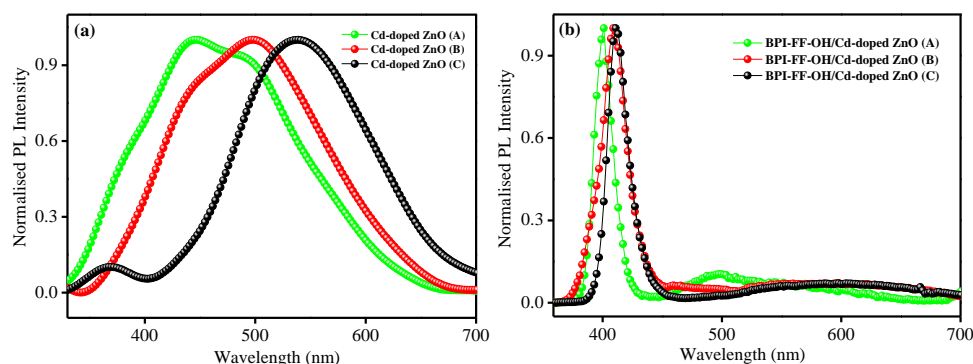


Figure 5.11. PL spectra of (a) Cd-doped ZnO and (b) BPI-FF-OH/Cd-doped ZnO hybrids. Bath compositions are (A) 0.01 M Cd(OAc)₂.6H₂O; 0.04 M Zn(NO₃)₂.6H₂O, (B) 0.02 M Cd(OAc)₂.6H₂O; 0.04 M Zn(NO₃)₂.6H₂O and (C) 0.04 M Cd(OAc)₂.6H₂O; 0.04 M Zn(NO₃)₂.6H₂O.

5.4.8 CIE (Commission Internationale d’Eclairage, 1931)

The calculation of CIE (Commission Internationale d’Eclairage, 1931) coordinates is performed using the photoluminescence data. The CIE chromaticity diagram of white luminescent nanostructured thin films is shown in Figure 7. The unannealed and annealed Cd-doped ZnO thin films show white light emission with the CIE coordinates ($x = 0.27$, $y = 0.35$) and ($x = 0.38$, $y = 0.45$) respectively. The un-annealed and annealed BPI-FF-OH/Cd-doped ZnO hybrid thin films emit white light with CIE coordinates ($x = 0.34$, $y = 0.39$) and ($x = 0.35$, $y = 0.39$) respectively, and these values are quite close to those of pure white luminescent materials ($x = 0.33$, $y = 0.33$). The observation clearly indicates the functional role of luminescent organic molecules in the lamellar organic/Cd-doped ZnO nanohybrid which is significant in the tuning of CIE coordinates of corresponding white light emission.

Here, the nanohybrids are successfully fabricated from the simple precursor Zn(NO₃)₂.6H₂O, Cd(CH₃COO)₂.6H₂O and an aromatic π -conjugated molecule BPI-FF-OH. The well-ordered nanostructures of BPI-FF-OH/Cd-doped ZnO are fabricated using a low-cost electrodeposition technique on GZO substrate. The combined organic and inorganic components emit white

light. The CIE (1931) index arising from BPI-FF-OH/Cd-doped ZnO hybrid is very close to the CIE coordinates of ideal white light emission.

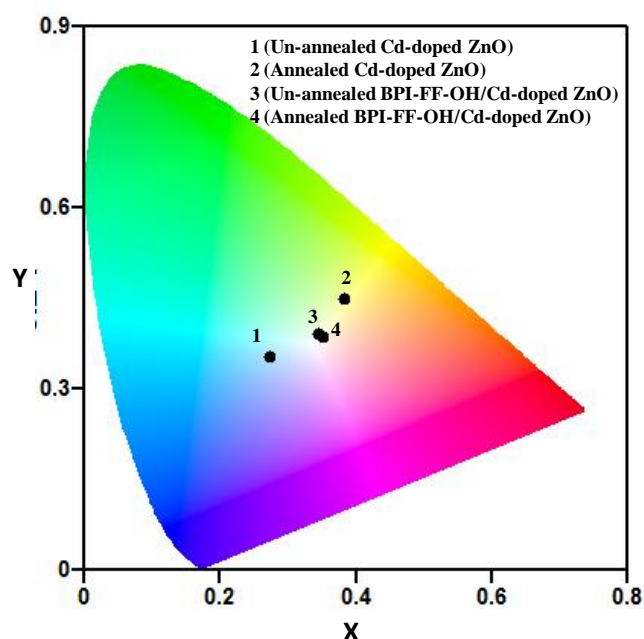


Figure 5.12. The CIE (1931) chromaticity diagram for white-light-emitting (1) unannealed cadmium-doped ZnO, (2) annealed cadmium-doped ZnO, (3) unannealed BPI-FF-OH/cadmium-doped ZnO, and (4) annealed BPI-FF-OH/cadmium-doped ZnO. The plot was obtained by using the gocie.exe program.

5.5 Conclusion

In conclusion, we have demonstrated cadmium doping in ZnO lattice in presence and absence of aromatic-capped dipeptide by electrodeposition technique and the formation of Cd-doped ZnO and BPI-FF-OH/Cd-doped ZnO hybrid nanostructures. Cd-doped ZnO reveals nanosheet and BPI-FF-OH/Cd-doped ZnO exhibits lamellar nanoflake architectures. Cd doping in ZnO is supported by band gap energy evaluated from Tauc's plot as well as in PL measurement. Cd-doped ZnO and BPI-FF-OH/Cd-doped ZnO exhibit white light emission under the excitation of 325 nm He-Cd laser source. The detailed analysis of novel growth and white light emission from Cd-doped ZnO NSs and BPI-FF-OH/Cd-doped ZnO contribute significantly towards its possible usage in the diverse cost-effective white-light-emitting material.

5.6 References

- [1] Zhang Q., Wang C.-F., Ling L.-T., Chen S. (2014), Fluorescent nanomaterial-derived white light emitting diodes: what's going on, *J. Mater. Chem. C*, 2, 4358-4373 (DOI: 10.1039/c4tc00048j).
- [2] Lin Y., Zhou S., Wang W., Yang W., Qian H., Wang H., Lin Z., Liu Z., Zhu Y., Li G. (2015), Performance improvement of GaN-based light-emitting diodes grown on Si(111) substrates by controlling the reactor pressure for the GaN nucleation layer growth, *J. Mater. Chem. C*, 3, 1484-1490 (DOI: 10.1039/c4tc02220c).
- [3] Nguyen X. L., Nguyen T. N. N., Chau V. T., Dang M. C. (2010), The fabrication of GaN-based light emitting diodes (LEDs), *Adv. Nat. Sci.: Nanosci. Nanotechnol.*, 1, 1-5 (DOI: 10.1088/2043-6254/1/2/02501).
- [4] Lin H.-W., Lu Y.-J., Chen H.-Y., Lee H.-M., Gwo S. (2010), InGaN/GaN nanorod array white light-emitting diode, *Appl. Phys. Lett.*, 97, 073101 (DOI: 10.1063/1.3478515).
- [5] Guo H., Lin Z., Feng Z., Lin L., Zhou J. (2009), White-light-emitting diode based on ZnO nanotubes, *J. Phys. Chem. C*, 113, 12546-12550 (DOI: 10.1021/jp902607c).
- [6] Rogach A. L., Gaponik N., Lupton J., Bertoni M. C., Gallardo D. E., Dunn S., Pira N. L., Paderi M., Repetto P., Romanov S. G., Dwyer C. O, Torres C. M. S., Eychmüller A. (2008), Light-emitting diodes with semiconductor nanocrystals, *Angew. Chem. Int. Ed.*, 47, 6538- 6549 (DOI: 10.1002/anie.200705109).
- [7] Dai Q., Duty C. E., Hu M. Z. (2010), Semiconductor-nanocrystals-based white light-emitting diodes, *Small*, 6, 1577-1588 (DOI: 10.1002/sml.201000144).
- [8] Puzzo D. P., Henderson E. J., Helander M. G., Wang Z., Ozin G. A., Lu Z. (2011), Visible colloidal nanocrystal silicon light-emitting diode, *Nano Lett.*, 11, 1585-1590 (DOI: 10.1021/nl1044583).
- [9] Klauk H. (2006), Organic Electronics: Materials, Manufacturing, and Applications, Wiley-VCH.
- [10] Tsujimura T. (2012), OLED Display Fundamentals and Applications (Wiley series in display technology), Wiley-VCH.

- [11] Giansante C., Schäfer C., Raffy G., Guerzo A. D. (2012), Exploiting direct and cascade energy transfer for color-tunable and white-light emission in three-component self-assembled nanofibers, *J. Phys. Chem. C*, 116, 21706-21716 (DOI: 10.1021/jp3073188).
- [12] Babu S. S., Aimi J., Ozawa H., Shirahata N., Saeki A., Seki S., Ajayaghosh A., Mçhwald H., Nakanishi T. (2012), Solvent-free luminescent organic liquids, *Angew. Chem. Int. Ed.*, 51, 3391-3395 (DOI: 10.1002/anie.201108853).
- [13] Yeh H.-C., Meng H.-F., Lin H.-W., Chao T.-C., Tseng M.-R., Zan H.-W. (2012), All-small-molecule efficient white organic light-emitting diodes by multi-layer blade coating, *Organic Electronics*, 13, 914-918 (DOI: 10.1016/j.orgel.2012.02.001).
- [14] Mukherjee S., Thilagar P. (2014), Organic white-light emitting materials, *Dyes and Pigments*, 110, 2-27 (DOI: 10.1016/j.dyepig.2014.05.031).
- [15] Sonawane S. L., Asha S. K. (2014), Blue, green, and orange-red emission from polystyrene microbeads for solid-state white-light and multicolor emission, *J. Phys. Chem. B*, 118, 9467-9475 (DOI: 10.1021/jp504718m).
- [16] Gong X., Wang S., Moses D., Bazan G. C., Heeger A. J. (2005), Multilayer polymer light-emitting diodes: white light emission with high efficiency, *Adv. Mater.*, 17, 2053-2058 (DOI: 10.1002/adma.200500727).
- [17] Wang R., Peng J., Qiu F., Yang Y., Xie Z. (2009), Simultaneous blue, green, and red emission from diblock copolymer micellar films: a new approach to white-light emission, *Chem. Commun.*, 6723-6725 (DOI: 10.1039/b915378k).
- [18] Service R. F., *Science*, 2005, 310, 1762-1763.
- [19] D'Andrade B. W., Thompson M. E., Forrest S. R. (2002), Controlling exciton diffusion in multilayer white phosphorescent organic light emitting devices, *Adv. Mater.*, 14, 147-151 (DOI: 10.1002/1521-4095(20020116)14:2).
- [20] D'Andrade B.W., Holmmes R. J., Forrest S. R. (2004), Efficient organic electrophosphorescent white-light-emitting device with triple

- doped emissive layer, *Adv. Mater.*, 16, 624-628 (DOI: 10.1002/adma.200306670).
- [21] Chang Y.-T., Chang J.-K., Lee Y.-T., Wang P.-S., Wu J.-L., Hsu C.-C., Wu I.-W., Tseng W.-H., Pi T.-W., Chen C.-T., Wu C.-I (2013), High-efficiency small-molecule-based organic light emitting devices with solution processes and oxadiazole-based electron transport materials, *ACS Appl. Mater. Interfaces*, 5, 10614-10622 (DOI: 10.1021/am402504g).
- [22] Park S., Kwon J. E., Kim S. H., Seo J., Chung K., Park S.-Y., Jang D.-J., Medina B. M., Gierschner J., Park S. Y. (2009), A white-light-emitting molecule: frustrated energy transfer between constituent emitting centers, *J. Am. Chem. Soc.*, 131, 14043-14049 (DOI: 10.1021/ja902533f).
- [23] Vijayakumar C., Praveen V. K., Ajayaghosh A. (2009), RGB emission through controlled donor self-assembly and modulation of excitation energy transfer: a novel strategy to white-light-emitting organogels, *Adv. Mater.*, 21, 2059-2063 (DOI: 10.1002/adma.200802932).
- [24] Bairi P., Roy B., Chakraborty P., Nandi A. K. (2013), Co-assembled white-light-emitting hydrogel of melamine, *ACS Appl. Mater. Interfaces*, 5, 5478-5485 (DOI: 10.1021/am4013566).
- [25] Abbel R., Grenier C., Pouderoijen M. J., Stouwdam J. W., Leclerc P. E. L. G., Sijbesma R. P., Meijer E. W., Schenning A. P. H. J. (2009), White-light-emitting hydrogen-bonded supramolecular copolymers based on π -conjugated oligomers, *J. Am. Chem. Soc.*, 131, 833-843 (DOI: 10.1021/ja807996y).
- [26] Son D. I., Kwon B. W., Park D. H., Seo W.-S., Yi Y., Angadi B., Lee C.-L., Choi W. K. (2012), *Nature Nanotechnology*, 7, 465-471 (DOI: 10.1038/NNANO.2012.71).
- [27] Layek A., Stanish P. C., Chirmanov V., Radovanovic P.V. (2015), Hybrid ZnO-based nanoconjugate for efficient and sustainable white light generation, *Chem. Mater.*, 27, 1021-1030 (DOI: 10.1021/cm504330k).
- [28] Wang T., Chirmanov V., Chiu W. H. M., Radovanovic P. V. (2013), Generating tunable white light by resonance energy transfer in

- transparent dye-conjugated metal oxide nanocrystals, *J. Am. Chem. Soc.*, 135, 14520-14523 (DOI: 10.1021/ja407013z).
- [29] Zhang X., Liu W., Wei G. Z., Banerjee D., Hu Z., Li J. (2014), Systematic approach in designing rare-earth-free hybrid semiconductor phosphors for general lighting applications, *J. Am. Chem. Soc.*, 136, 14230-14236 (DOI: 10.1021/ja507927a).
- [30] Sun C.-Y., Wang X.-L., Zhang X., Qin C., Li P., Su Z.-M., Zhu D.-X., Shan G.-G., Shao K.-Z., Wu H., Li J. (2013), Efficient and tunable white-light emission of metal-organic frameworks by iridium-complex encapsulation, *Nat. Comm.*, 4, 1-8 (DOI: 10.1038/ncomms3717).
- [31] Kim N., Lee J., An H., Pang C., Cho S. M., Chae H. (2014), Color temperature control of quantum dot white light emitting diodes by grafting organic fluorescent molecules, *J. Mater. Chem. C*, 2, 9800-9804 (DOI: 10.1039/c4tc01780c).
- [32] Sui X. M., Shao C. L., Liu Y. C. (2005), White-light emission of polyvinyl alcohol/ZnO hybrid nanofibers prepared by electrospinning, *Appl. Phys. Lett.*, 87, 113115 (DOI: 10.1063/1.2048808).
- [33] Bano N., Zaman S., Zainelabdin A., Hussain S., Hussain I., Nur O., Willander M. (2010), ZnO-organic hybrid white light emitting diodes grown on flexible plastic using low-temperature aqueous chemical method, *J. Appl. Phys.*, 108, 043103 (DOI: 10.1063/1.3475473).
- [34] Manna M. K., Pandey S. K., Maity I., Mukherjee S., Das A. K. (2014), Electrodeposited lamellar photoconductor nanohybrids driven by peptide self-assembly, *ChemPlusChem*, 80, 583-590 (DOI: 10.1002/cplu.201402348).
- [35] Rasale D. B., Maity I., Das A. K. (2012), Emerging π -stacked dynamic nanostructured library, *RSC Adv.*, 2, 9791-9794 (DOI: 10.1039/c2ra21334f).
- [36] Pandey S. K., Awasthi V., Verma S., Mukherjee S. (2014), Blue electroluminescence from Sb-ZnO/Cd-ZnO/Ga-ZnO heterojunction diode fabricated by dual ion beam sputtering, *Opt. Express*, 22, 30983-30991 (DOI:10.1364/OE.22.030983).

- [37] Verma S., Pandey S. K., Gupta M., Mukherjee S. (2014), Influence of ion-beam sputtering deposition parameters on highly photosensitive and transparent CdZnO thin film, *J. Mater. Sci.*, 49, 6917-6929 (DOI: 10.1007/s10853-014-8396-8).
- [38] Pandey Sa. K., Pandey Su. K., Awathi V., Deshpande U. P., Gupta M., Mukherjee S. (2013), Influence of in-situ annealing ambient on p-type conduction in dual ion beam sputtered Sb-doped ZnO thin films, *J. Appl. Phys.* 114, 163107 (DOI: 10.1063/1.4818819).
- [39] Pandey S. K., Pandey S. K., Deshpande U. P., Awathi V., Kumar A., Gupta M., Mukherjee S. (2013), Effect of oxygen partial pressure on the behavior of dual ion beam sputtered ZnO thin films, *Semicond. Sci. and Technol.*, 28, 085014 (DOI: 10.1088/0268-1242/28/8/085014).
- [40] Sofos M., Goldberger J., Stone D. A., Allen J. E., Ma Q., Herman D. J., Tsai W.-W., Lauhon L. J., Stupp S. I. (2009), A synergistic assembly of nanoscale lamellar photoconductor hybrids, *Nat. Mater.*, 8, 68–75 (DOI: 10.1038/NMAT2336).
- [41] Steinmiller E. M. P., Choi K.-S. (2007), Anodic construction of lamellar structured ZnO films using basic media via interfacial surfactant templating, *Langmuir*, 23, 12710-12715 (DOI: 10.1021/la702066w).
- [42] Pichon B. P., Leuvrey C., Ihiawakrim D., Tichit D., Geradin C. (2011), Films of tunable ZnO nanostructures prepared by a surfactant-mediated soft synthesis route, *J. Phys. Chem. C*, 115, 23695-23703 (DOI: 10.1021/jp2072149).
- [43] Liu K., Xing R., Chen C., Shen G., Yan L., Zou Q., Ma G., Möhwald H., Yan X. (2015), Simple peptide-tuned self-assembly of photosensitizers towards anticancer photodynamic therapy, *Angew. Chem. Int. Ed.*, 54, 500-505 (10.1002/ange.201509810).
- [44] Jeong W.-j., Choi S.-j., Choi J. S., Lim Y.-b. (2013), Chameleon-like self-assembling peptides for adaptable biorecognition nanohybrids, *ACS Nano*, 7, 6850-6857 (DOI: 10.1021/nn402025r).
- [45] Draper E. R., Walsh J. J., McDonald T. O., Zwijnenburg M. A., Cameron P. J., Cowan A. J., Adams D. J. (2014), Air-stable

- photoconductive films formed from perylene bisimide gelators, *J. Mater. Chem. C*, 2, 5570-5575 (DOI: 10.1039/c4tc00744ar).
- [46] Verma S., Manna M. K., Pandey S. K., Das A. K., Mukherjee S. (2014), Benzo[ghi]perylene monoimide based photosensitive lamellar Cd-doped ZnO nanohybrids, *RSC Advances*, 4, 62603-62614 (DOI: 10.1039/c4ra13712d).
- [47] Mahmoud W. E., Al-Ghamdi A. A. (2010), Synthesis of CdZnO thin film as a potential candidate for optical switches, *Optics & Laser Technology*, 42, 1134-1138 (DOI: 10.1016/j.optlastec.2010.02.009).
- [48] Lupan O., Pauporte T., Bahers T. L., I. Ciofini, B. Viana (2011), High aspect ratio ternary $\text{Zn}_{1-x}\text{Cd}_x\text{O}$ nanowires by electrodeposition for light-emitting diode applications, *J. Phys. Chem. C*, 115, 14548–14558 (DOI: 10.1021/jp202608e).
- [49] Li G.-R., Zhao W.-X., Bu Q. Tong Y.-X. (2009), A novel electrochemical deposition route for the preparation of $\text{Zn}_{1-x}\text{Cd}_x\text{O}$ nanorods with controllable optical properties, *Electrochemistry Communications*, 11, 282-285 (DOI: 10.1016/j.elecom.2008.11.024).
- [50] G.-R. Li, Bu Q., Zheng F.-L., Su C.-Y., Tong Y.-X. (2009), Electrochemically controllable growth and tunable optical properties of $\text{Zn}_{1-x}\text{Cd}_x\text{O}$ alloy nanostructures, *Crystal Growth and Design*, 9, 1538-1545 (DOI: 10.1021/cg800496d).
- [51] Ye Z., Ma D., He J., Huang J., Zhao B., Luo X., Xu Z. (2003), Structural and photoluminescent properties of ternary $\text{Zn}_{1-x}\text{Cd}_x\text{O}$ crystal films grown on Si(111) substrates, *J. Cryst. Growth*, 256, 78-82 (DOI: 10.1016/S0022-0248(03)01314-9).
- [52] Srikant V., Clarke D. R. (1998), On the optical band gap of zinc oxide, *Journal of Applied Physics*, 83, 5447-5451 (DOI: 10.1063/1.367375).
- [53] Li L., Yang Z., Zuo Z., Lim J. H., Liu J. L. (2010), Thermal stability of CdZnO thin films grown by molecular-beam epitaxy, *Applied Surface Science*, 256, 4734-4737 (DOI: 10.1016/j.apsusc.2010.02.083).
- [54] Sonawane B. K., Shelke V., Bhole M. P., Patil D. S. (2011), Structural, optical and electrical properties of cadmium zinc oxide films for light

- emitting devices, *Journal of Physics and Chemistry of Solids*, 72, 1442-1446 (DOI: 10.1016/j.jpcs.2011.08.022).
- [55] Singh A., Kumar D., Khannan P. K., Joshi B. C., Kumar M. (2011), Effect of post-annealing temperature on structural and optical properties of ZnCdO thin films deposited by sol-gel method, *Applied Surface Science*, 258, 1881-1887 (DOI: 10.1016/j.apsusc.2011.10.096).
- [56] Ohtomo A., Kawasaki M., Ohkubo I., Koinuma H., Yasuda T., Segawa Y. (1999), Structure and optical properties of ZnO/Mg_{0.2}Zn_{0.8}O superlattices., *Appl Phys Lett.*, 75, 980-982 (DOI :10.1063/1.124573).
- [57] Jeong S.-H., Kim B.-S., Lee B.-T. (2003), Photoluminescence dependence of ZnO films grown on Si(100) by radio-frequency magnetron sputtering on the growth ambient, *Appl. Phys. Lett.*, 82, 2625-2627 (DOI: 10.1063/1.1568543).
- [58] Asbrink S., Waskowska A., Gerward L., Olsen J. S., Talik E. (1999), High-pressure transition and properties of spinel ZnMn₂O₄, *Phys. Rev.*, 60, 12651–12656 (DOI: 10.1103/PhysRevB.60.12651).
- [59] Studentikin S. A., Golego N., Concivera M. (1998), Fabrication of green and orange photoluminescent, undoped ZnO films using spray Pyrolysis, *J. Appl. Phys.*, 84, 2287-2294 (DOI: 10.1063/1.368295).
- [60] Djurisic A. B., Leung Y. H., Tam K. H., Hsu Y. F., Ding L., Ge W. K., Zhong Y. C., Wong K. S., Chan W. K., Tam H. L., Cheah K. W., Kwok W. M., Phillips D. L. (2007), Defect emissions in ZnO nanostructures, *Nanotechnology*, 18, 095702 (DOI: 10.1088/0957-4484/18/9/095702).
- [61] Willander M., Nur O., Sadaf J. R., Qadir M. I., Zaman S., Zainelabdin A., Bano N., Hussain I. (2010), Luminescence from Zinc Oxide Nanostructures and Polymers and their Hybrid Devices, *Materials*, 3, 2643-2667 (DOI: 10.3390/ma3042643).
- [62] Handelman A., Natan A., Rosenman G. (2014), Structural and optical properties of short peptides: nanotubes-to-nanofibers phase transformation, *J. Pept. Sci.*, 20, 487-493 (DOI: 10.1002/psc.2661)
- [63] Li Q., Jia Y., Dai L., Yang Y., Li J. (2015), Controlled rod nanostructured assembly of diphenylalanine and their optical

- waveguide properties, *ACS Nano*, 9, 2689-2695 (DOI: 10.1021/acsnano.5b00623).
- [64] Yan X., Su Y., Li J., Fruh J., Möhwald H. (2011), Uniaxially oriented peptide crystals for active optical waveguiding, *Angew. Chem. Int. Ed.*, 50, 11186-11191 (DOI: 10.1002/anie.201103941).
- [65] Yan X., Li J., Möhwald H. (2011), Self-assembly of hexagonal peptide microtubes and their optical waveguiding, *Adv. Mater.*, 23, 2796-2801 (DOI: 10.1002/adma.201100353).
- [66] Li Q., Ma H., Wang A., Jia Y., Dai L., Li J. (2015), Self-assembly of cationic dipeptides forming rectangular microtubes and microrods with optical waveguiding properties, *Adv. Opt. Mater.*, 3, 194-198 (DOI: 10.1002/adom.201400308).
- [67] Reches M., Gazit E. (2003), Casting metal nanowires within discrete self-assembled peptide nanotubes, *Science*, 300, 625-627 (DOI: 10.1126/science.1082387).
- [68] Manna M. K., Rasale D. B., Das A. K. (2015), Supramolecular assembly of dipeptide functionalized benzo[ghi]perylene monoimide directs white light emission via donor-acceptor interactions, *RSC Advances*, 4, 62603-62614 (DOI: 10.1039/c5ra11804b).

Chapter 6

**Electrodeposited Lamellar Photoconductor
Nanohybrids Driven by Peptide Self-Assembly**

6. 1 Introduction

Supramolecular chromophoric π -conjugated aromatic systems^[1] are envisioned to serve as active materials in photoelectronic devices, in particular, for photovoltaics.^[2-5] Intrinsic optical and electronic properties of organic molecules are more important for exploitation in device applications.^[6-8] Controlling self-assembly of π -conjugated aromatic molecules is important as it provides optical, electronic and optoelectronic behaviors. Aromatic capped self-assembly of small organic molecules has drawn great attention in the field of supramolecular electronics.^[9] In general, crystalline silicon, Cd, Pd, Hg and As based materials are widely used as conducting materials but these are hazardous, toxic and harmful in nature.^[10] Therefore, design and synthesis of biocompatible and eco-friendly materials with desirable properties are crucial for the development of photovoltaics. The on-going research on organic materials enriches the area of organo-electronics in the context of photoconducting devices. The molecular arrangement in nano level controls the properties of self-assembled materials and directs its application in a specific field. Self-assembly of aromatic organic systems with ordered aromatic π - π stacking interactions can enhance the hole conduction or optical properties.^[11] Furthermore, the π - π stacking of aromatic chromophoric organic system depends on the state of matter and aggregation. Thus, our research is focused on to the synthesis organic-inorganic hybrid materials with improved optoelectronic behavior for the application of photovoltaics.

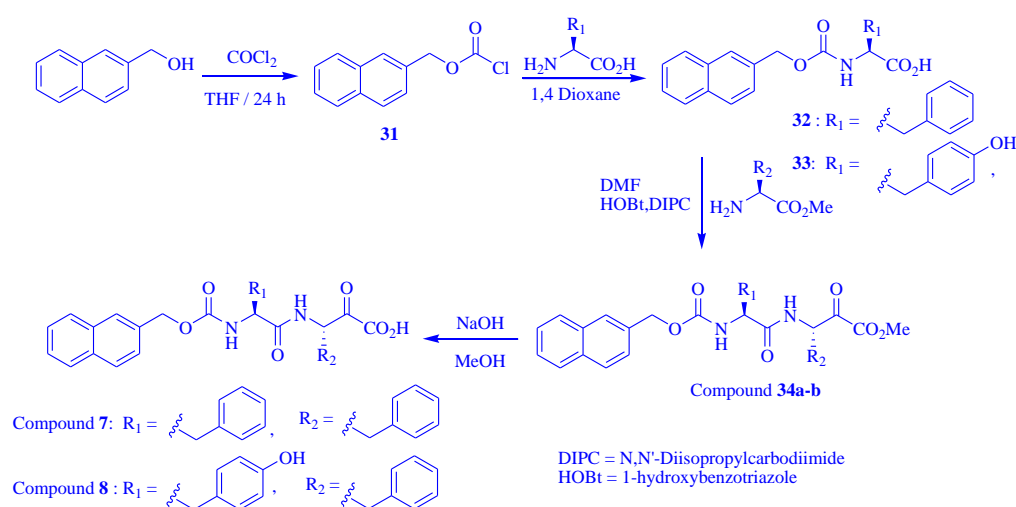
Recently, various hybrid nanostructures have been synthesized by several chemical methods including aqua chemical,^[12] sol-gel process^[13] and hydrothermal techniques.^[14] Some advanced gas-phase technologies are also used to fabricate inorganic-organic hybrid materials such as vacuum evaporation,^[15] sputtering,^[16] chemical vapor deposition (CVD) techniques.^[17-18] These techniques provide structural purity and homogeneity of materials but it needs expensive facilities and high energy provider. Electrochemical deposition is a economically cheap powerful bottom-up approach to produce highly ordered lamellar organic-inorganic hybrid nanostructured films.^[19-22] The nanostructural morphology of electrodeposited films are strongly influenced by the electrochemical parameters such as

solution concentration,^[23] bath temperature,^[24] electrode potential^[25] and the chemical structure of the surfactants. Anionic surfactant sodium dodecyl sulfate (SDS)^[26-28] has been widely used as a template for the electrodeposition of ZnO. Now, various ionic surfactants containing conjugated aromatic segment^[29-30] (dyes) are also used for further development of organo-electronic materials. Recently, Xiujuan Qin *et al.* described the effect of surfactant on the structures and properties of ZnO films which were prepared by electrodeposition technique.^[31] Stupp *et al.* reported highly ordered nanostructured organic/inorganic lamellar photoconductor hybrids.^[29] Stupp *et al.* also designed various organic surfactants for the development of electronically active materials. While, considerable work has been carried out on hybrid nanostructures comprised of organic π -conjugated systems,^[32,33] electrochemical deposition of peptide-based hybrid materials was not explored. Peptides are well known in the construction of various self-assembled nano-architectures.^[34,35] Lim *et al.* developed self-assembling peptide/inorganic hybrid materials with specific molecular recognition capabilities.^[36,37] Peptide/metal nanoparticles as efficient catalysts were also reported for the removal of N-terminus protecting groups^[38] and C-C coupling reactions in aerobic conditions.^[39] Peptide self-assembly can be influenced by various non-covalent interactions such as hydrogen bonding, hydrophobic, π - π stacking and electrostatic interactions.^[40-42]

In this chapter, we report a strategy for the synthesis of nanoscale lamellar peptide-ZnO hybrid nanostructures for the development of active electronic materials. We have synthesized aromatic Nmoc-capped small peptides (Nmoc = naphthalene-2-methoxy carbonyl) containing conjugated naphthalene moiety as organic component in the hybrid materials. The self-assembled organic-inorganic hybrid composite system can modify the conduction mechanism of current carriers and thereby influence optoelectronic behavior through extent π - π stacking interactions. The electrons can jump from excited state aromatic naphthalene moieties of peptides to the ZnO semiconductors.^[43]

6.2 Experimental

Materials and Characterization: All reagents and chemicals were obtained commercially. Reagents were distilled from appropriate drying agents prior to use. Naphthalene-2-methyloxichloroformate **31**, Nmoc-Phe-OH **32**, Nmoc-Tyr-OH **33** were prepared according to the following procedure.^[44-46] The synthetic procedure for the preparation of Nmoc-Phe-Phe-OMe **34**, Nmoc-Tyr-Phe-OMe **35**, Nmoc-Phe-Phe-OH **7** and Nmoc-Tyr-Phe-OH **8** were described below.



Scheme 6.1. Solution-phase synthetic procedure of preparation for peptides Nmoc-Phe-Phe-OH (**7**) and Nmoc-Tyr-Phe-OH (**8**).

Synthesis of Naphthalene-2-methyloxichloroformate (**31**):

To a stirred solution of naphthalene methanol (10 g, 63.2 mmol) in dry THF (287.2 mL), phosgene (78.5 mL, 20 mmol) was added at 0 °C. The stirring was continued at ambient temperature for 24 hrs. The reaction was monitored by thin layer chromatography (TLC). After completion of the reaction, excess phosgene was removed under low vacuum and trapped with aqueous NaOH. The reaction mixture was concentrated and oily product was obtained. Then it was dissolved in hot hexane and kept overnight to yield crystalline product **31**. Yield = 13 g, (58.9 mmol, 93.19 %). FTIR (KBr): $\tilde{\nu} =$

3066 (m), 1777 (s), 1601 (m), 1168 (s) cm^{-1} ; ^1H NMR (400 MHz, CDCl_3 , δ_{ppm}): 7.89 (m, 4H), 7.56 (m, 3H), 5.48 (s, 2H); ^{13}C NMR (100 MHz, CDCl_3) δ 71.82, 125.7, 126.1, 126.6, 126.8, 127.8, 128.1, 128.6, 130.6, 133.0, 133.5, 140.9, 147.9, 150.7.

Synthesis of Nmoc-Phe-OH (32):

A solution of Phenylalanine (0.83 g, 5 mmol) in a mixture of 1,4 dioxane (10 mL) and 2 (N) sodium carbonate (13 mL) was stirred and cooled in an ice-water bath. Napthalene-2-methyloxichloroformate (1.102 g, 5 mmol) was added and stirring was continued at room temperature for 12 hrs. Reaction mixture was diluted with 200 mL of water and dioxane was evaporated under vacuum. The aqueous layer was washed with diethyl ether and the pH of aqueous layer was adjusted to 2 with 2 (N) hydrochloric acid. The aqueous phase was extracted with ethyl acetate (3×50 mL) and dried over anhydrous Na_2SO_4 and concentrated in vacuo to give product **32** as a colorless oil. Yield = 1.568 (4.4 mmol, 88 %), ^1H NMR (400 MHz, $\text{DMSO}-d_6$, δ_{ppm}): 12.8 (s, 1H), 7.76 (d, 2H, $J = 8$ Hz), 7.53 (t, 2H), 7.41 (d, 1H, $J = 8$ Hz), 7.23 (m, 5H), 6.39 (d, 1H, NH), 5.15 (s, 2H), 4.19 (t, 1H, C^α H of Phe), 3.07 (d, 2H, C^β H of Phe) ppm. MS (ESI) m/z for $\text{C}_{21}\text{H}_{19}\text{NO}_4\text{Na}$ ($M+\text{Na}$) $^+$ calcd.: 372.1212, found: 372.1206.

Synthesis of Nmoc-Tyr-OH (33):

A solution of Tyrosine (0.83 g, 5 mmol) in a mixture of 1,4 dioxane (10 mL) and 2 (N) sodium hydroxide (13 mL) was stirred and cooled in an ice-water bath. Napthalene-2- methyloxichloroformate (1.102 g, 5 mmol) was added and stirring was continued at room temperature for 12 hrs. Reaction mixture was diluted with 200 mL of water and dioxane was evaporated under vacuum. The aqueous layer was washed with diethyl ether and the pH of aqueous layer was adjusted to 2 with 2(N) hydrochloric acid. The aqueous phase was extracted with ethyl acetate (3×50 mL) and dried over Na_2SO_4 and concentrated in vacuo to give product **33** as a colorless oil. Yield = 1.568 (4.4 mmol, 88 %) ^1H NMR (400 MHz, $\text{DMSO}-d_6$): δ 7.73 (d, 4H), 7.38 (d, 2H), 7.18 (s, 1H), 6.86 (d, 2H, $J = 8.04$ Hz), 6.57 (d, 2H, $J = 8.04$ Hz), 5.26 (d, 1H,

NH, $J = 7.76$ Hz), 5.17 (q, 2H, CH_2), 4.57 (m, 1H, C^αH of Tyr), 2.95 (d, 2H, C^βH s of Tyr) ppm.

The general procedures used for peptide coupling are as follows:

A solution of Nmoc-Phe-OH **32** (1.29 g, 3.69 mmol) and HOBt (0.56 g, 3.7 mmol) was stirred in 2 mL of DMF. A neutralized solution of $\text{H}_2\text{N-Phe-OMe}$ was extracted from its corresponding hydrochloride salt and concentrated to add to the reaction mixture followed by DIPC (0.5126 g, 3.7 mmol) at 0 °C. The mixture was allowed to stir at room temperature for 12 hrs. The reaction mixture was diluted with ethyl acetate and organic layer was washed with 1(N) HCl (2×30 mL), brine solution, 1(N) Na_2CO_3 (3×30 mL) and brine solution. The organic layer was dried over Na_2SO_4 and evaporated under vacuum to yield white solid product. Purification of Nmoc-Phe-Phe-OMe **34a** was done by silica gel column (100-200 mesh) using ethyl acetate-toluene (1:1) as eluent. A solution Nmoc-Phe-Phe-OMe **34a** (1.70g, 3.42 mmol) in 100 mL of dry MeOH was allowed to react with a solution of 2(N) NaOH. The progress of the reaction was monitored by thin layer chromatography (TLC). The reaction mixture was stirred up to 6 hrs. Then, methanol was removed under vacuum. The residue was taken in 100 mL of water and washed with diethyl ether (2×20 mL). Then, the pH of aqueous layer was adjusted to 2 using 2(N) HCl and it was extracted with ethyl acetate (3×30 mL). The ethyl acetate layer was dried over anhydrous sodium sulfate and evaporated under vacuum to yield Nmoc-Phe-Phe-OH **7** as white solid and used further without purification. Nmoc-Tyr-Phe-OMe **34b** and Nmoc-Tyr-Phe-OH **8** were also synthesized accordingly.

Nmoc-Phe¹-Phe²-OMe (34a):

Yield = 1.7122 g (3.47 mmol, 90.82%); ^1H NMR (400 MHz, CDCl_3 , δ_{ppm}): 7.77 (d, 2H, $J = 8.72$ Hz), 7.71 (s, 1H), 7.43 (dd, 2H, $J = 3.38, 3.48$ Hz), 7.40 (d, 2H, $J = 8.52$ Hz), 7.19 (m, 5H, Phe^1), 7.12 (m, 5H, Phe^2), 6.89 (d, $J = 5.52$ Hz, 1H, NH of Phe^1), 6.12 (d, $J = 7.28$ Hz, 1H, NH of Phe^2), 5.17 (s, 2H), 4.60 (m, C^αH of Phe^1), 4.34 (m, C^αH of Phe^2), 3.59 (s, 3H, $-\text{OCH}_3$), 3.01 (d, 1H, C^βH of Phe^1), 2.98 (d, 1H, $J = 5.76$ Hz, C^βH of Phe^1), 2.94 (d, 1H, $J = 6.04$ Hz, C^βH of Phe^2), 2.91 (d, 1H, $J = 6.04$ Hz, C^βH of Phe^2). MS (ESI) m/z for $\text{C}_{31}\text{H}_{30}\text{N}_2\text{O}_5\text{Na}$ ($M+\text{Na}$)⁺ calcd.: 533.2052, found: 533.1974.

Nmoc-Tyr-Phe-OMe (34b):

Yield = 0.50 g (0.95 mmol, 63.29%); ^1H NMR (400 MHz, CDCl_3 , δ_{ppm}): 7.84 (d, 2H, $J = 4.2$ Hz), 7.79 (s, 1H), 7.49 (dd, $J = 3.84, 3.52$ Hz), 7.43 (d, 1H, $J = 8.04$ Hz, NH of Tyr), 7.21 (t, 3H), 7.01 (d, 2H, $J = 9.28$ Hz), 6.98 (d, 2H, $J = 6.76$ Hz, Tyr), 6.68 (d, 2H, $J = 8.28$ Hz, Tyr), 6.20 (d, 1H, $J = 7.52$ Hz, NH of Phe), 5.24 (s, 2H), 4.75 (m, 1H C^αH of Tyr), 4.33 (m, 1H C^αH of Phe), 3.66 (s, 3H), 3.05 (dd, 2H, $J = 5.52, 6$ Hz, C^βH of Tyr), 2.96 (d, 2H, $J = 6.76$ Hz, C^βH of Phe). MS (ESI) m/z for $\text{C}_{31}\text{H}_{30}\text{N}_2\text{O}_6\text{Na}$ ($M+\text{Na}$) $^+$ calcd.: 549.2002, found: 549.18564.

Nmoc-Phe¹-Phe²-OH (7):

Yield = 1.50 g (3.02 mmol, 90.91%); ^1H NMR (400 MHz, $\text{DMSO}-d_6$, δ_{ppm}): 8.30 (d, $J = 7.52$, 1H, NH of Phe¹), 7.37 (d, $J = 8.28$ Hz, 1H, NH of Phe²), 7.89 (t, 4H), 7.77 (s, 1H), 7.51 (d, 2H), 7.24 (m, 10H), 5.09 (s, 2H), 4.47 (m, C^αH of Phe¹), 4.30 (m, C^αH of Phe²), 3.10 (dd, 2H, $J = 4.52$ Hz, C^βH of Phe¹), 2.94 (d, 2H, C^βH of Phe²); ^{13}C NMR (100 MHz, $\text{DMSO}-d_6$, δ_{ppm}): 177.98, 176.81, 160.99, 143.28, 142.58, 139.84, 137.90, 137.65, 134.40, 133.40, 133.23, 133.12, 132.90, 132.79, 131.66, 131.51, 131.44, 131.28, 131.20, 130.75, 70.52, 61.20, 58.68, 42.60, 41.90 ppm. MS (ESI) m/z for $\text{C}_{30}\text{H}_{28}\text{N}_2\text{O}_5\text{Na}$ ($M+\text{Na}$) $^+$ calcd.: 519.1896, found: 519.3244.

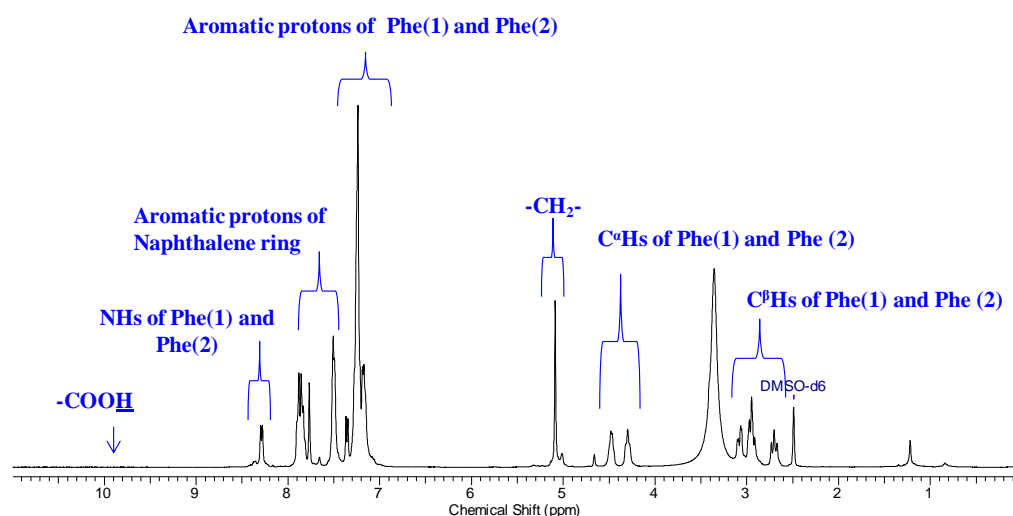


Figure 6.1. ^1H NMR spectrum (400 MHz, $\text{DMSO-}d_6$) of Nmoc-FF-OH (**7**).

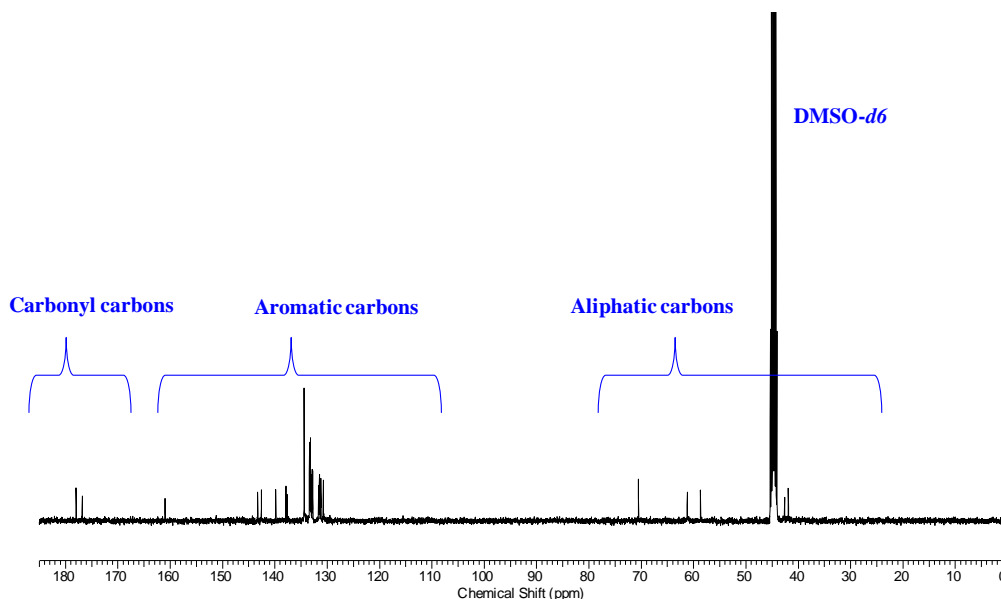


Figure 6.2. ^{13}C NMR spectrum (100 MHz, $\text{DMSO-}d_6$) of Nmoc-FF-OH (**7**).

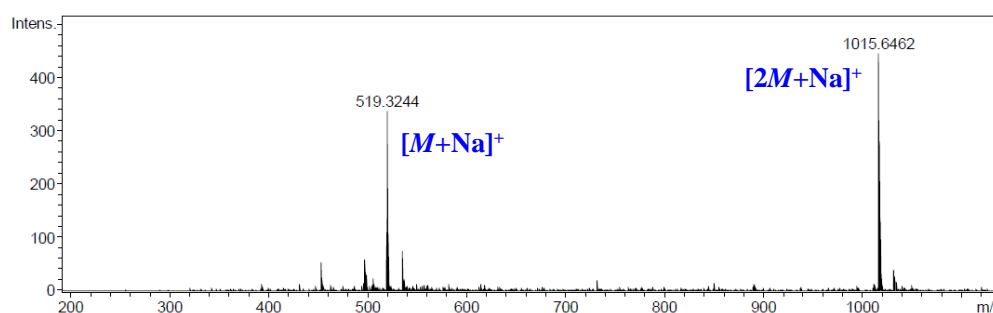


Figure 6.3. ESI-MS spectrum of Nmoc-FF-OH (**7**).

Nmoc-Tyr-Phe-OH (8**):**

Yield = 0.40 g (0.78 mmol, 81.63%); ^1H NMR (400 MHz, $\text{DMSO-}d_6$, δ_{ppm}): 12.77 (s, 1H, $-\text{COOH}$), 9.19 (d, 1H, NH of Phe), 8.24 (1H, NH of Tyr), 7.89 (dd, 2H, $J = 2.76, 5.52$ Hz), 7.79 (s, 1H), 7.52 (d, 2 H), 7.42 (d, 2H) 7.26 (m, 5H), 7.06 (d, 2H, Tyr), 6.65 (d, 2H, Tyr), 5.12 (s, 2H), 4.47 (m, 1H C^αH of Tyr), 4.22 (m, 1H, C^αH of Phe), 3.34 (s, 3H), 3.10 (d, 1H, $J = 14.04$ Hz, C^βH of Tyr), 2.96 (d, 1H, $J = 5.52$ Hz, C^βH of Phe), 2.87(d, 1H, $J = 13.8$ Hz, C^βH of Tyr), 2.60 (d, 1H, C^βH of Phe). ^{13}C NMR (100 MHz, $\text{DMSO-}d_6$, δ_{ppm}): 172.74, 171.67, 155.73, 137.35, 134.62, 132.66, 132.38, 130.08, 129.14, 128.13, 127.87, 127.67, 127.53, 126.38, 126.27, 126.02, 125.83, 125.44,

114.80, 65.23, 56.23, 53.47, 53.43, 36.66 ppm. MS (ESI) m/z for $C_{30}H_{28}N_2O_6Na$ ($M+Na$)⁺ calcd.: 535.1845, found: 535.0381.

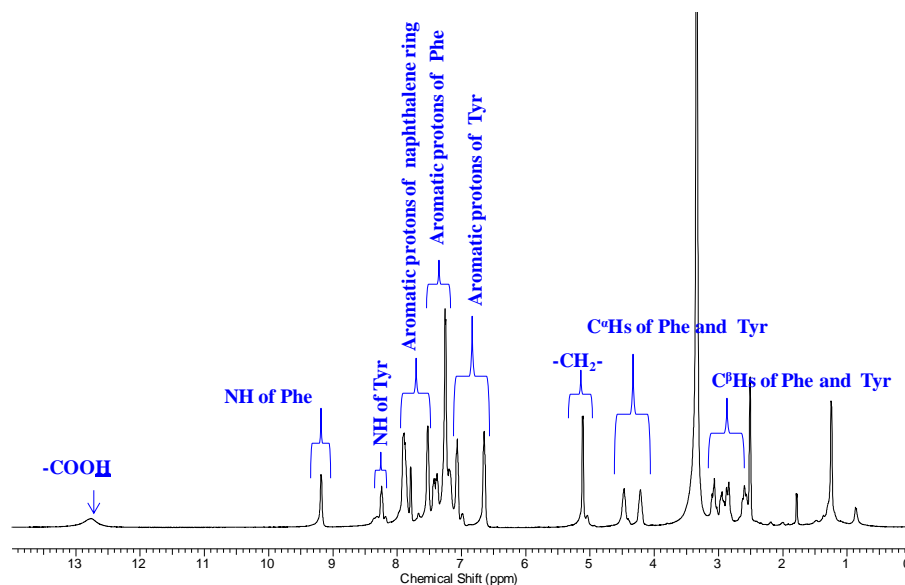


Figure 6.4. 1H NMR spectrum (400 MHz, $DMSO-d_6$) of Nmoc-YF-OH (**8**).

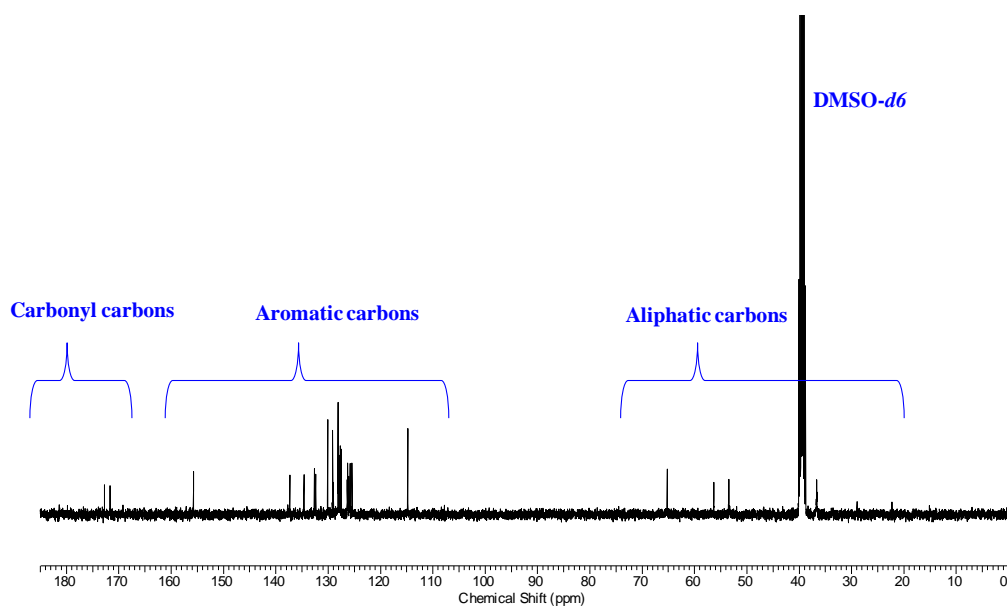


Figure 6.5. ^{13}C NMR spectrum (100 MHz, $DMSO-d_6$) of Nmoc-YF-OH (**8**).

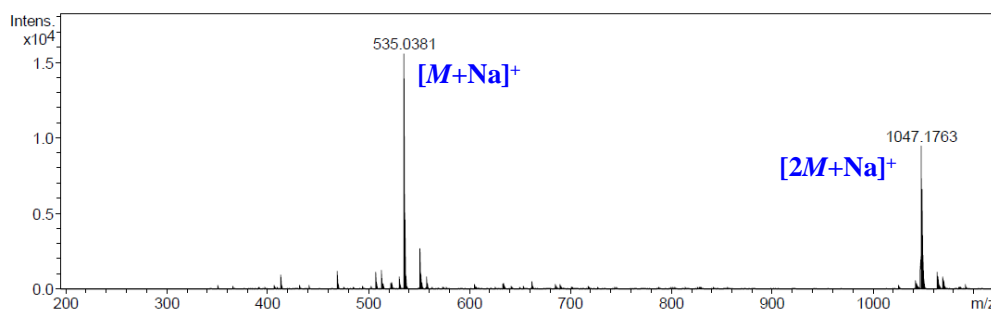


Figure 6.6. ESI-MS spectrum of Nmoc-YF-OH (**8**).

Dual Ion Beam Sputtering Deposition (DIBSD):

Electrorava DIBSD system was deployed to deposit ITO thin films (200 nm) on quartz glass substrates. The angle between the sputtering beam and sputtering target was fixed at 45° off normal while the angle between the assist ion beam and the substrate was maintained at 60°. Before inserting into DIBSD growth chamber, quartz glass substrates were rinsed thoroughly with trichloroethylene, acetone, iso-propanol and de-ionized (DI) water and subsequently purged by nitrogen gas (purity 99.999%) in order to remove dust particles and various organic contaminants. Prior to actual film deposition, assist source was turned on for 10 minutes to perform substrate pre-cleaning by Ar ion bombardment. During material growth, assist ion beam, consisting of plasma of Ar ions, helped in the reduction of columnar growth and thereby enhancing growth uniformity and film adhesion to the substrate. The discharge voltage and current of the assist ion source was kept constant at 70 volt and 600 mA respectively, during ITO thin film deposition, using a 4N (99.99%) pure 4-in-diameter ITO target mounted on a water-cooled target holder inside the DIBSD system chamber. The background pressure inside the process chamber was maintained at around 1×10^{-8} mbar, while the working pressure during film growth was kept at 3.26×10^{-4} mbar.

Electrochemical Synthesis:

Electrochemical synthesis was carried out in 24 mL solution (1:1 (v/v) DMSO/water) of 0.04 M $\text{Zn}(\text{NO}_3)_2$ with 10-12 mg peptide amphiphile in a 100 mL cell vial using three electrode set up (Autolab PG STAT302N) with a Zn counter electrode (Alfa Aesar 99.9997%) and a Silver/Silver chloride reference electrode (KCl Autolab 6.0726.107). Water was required for

reduction of NO_3^- to generate OH^- and DMSO was added for surfactant solubility. Working electrode indium tin oxide substrates (ITO) were placed upright in cell and deposition was achieved potentiostatically at -0.9 volts for 16 to 24 hours depending on growth time under constant stirring at 80 °C in water bath. Deposited films were rinsed with de-ionized water and ethanol and dried with dry nitrogen. Finally, thin films were annealed at 150 °C.

6.3 General characterization

All NMR spectra were recorded on a Bruker AV 400 MHz spectrometer. Compound concentrations were in the range of 5-10 mmol L⁻¹ in $(\text{CD}_3)_2\text{SO}$ and CDCl_3 . Mass spectra were recorded on Bruker micrOTOF-Q II by positive mode electrospray ionization. All reported FT-IR spectra were taken using Bruker (Tensor 27) FT-IR spectrophotometer. Specific rotations of the synthesized compounds were measured on an Autopol^R V automatic polarimeter (Rudolph research analytical). The cell (length = 100 mm, capacity = 2 mL) was used for this study at 25 °C. For SEM study, electrodeposited films were coated with gold. Then, the micrographs were recorded on a Field- gun scanning electron microscope (Jeol Scanning Microscope-JSM-7600F). The XRD measurements were carried out using a Bruker D8 Advance X-ray diffractometer. The X-rays were produced using a sealed tube and the wavelength of the X-ray was 0.154 nm (Cu K-alpha). The X-rays were detected using a fast counting detector based on Silicon strip technology (Bruker LynxEye detector).

Photoluminescence and I-V Measurement: DongWoo Optron PL set-up, affixed with a 20 mW continuous wave (CW) He-Cd laser (excitation wavelength = 325 nm, TEM00 mode), 320 mm and 150 mm focal length monochromators, chopper, lock-in amplifier, and a photomultiplier tube (PMT) detector, was deployed to conduct optical studies of annealed and un-annealed hybrid films. The UV light He-Cd laser (excitation wavelength = 325 nm, TEM00 mode) was used to measure photosensitivity of the hybrid materials. The current between the two contacts were measured using a Keithley source meter (Model 2612A).

6.4 Results and Discussion

Prior to electrochemical deposition of organic-inorganic hybrid materials, we have synthesized two aromatic Nmoc-capped dipeptides Nmoc-FF-OH **7** (F: phenylalanine) and Nmoc-YF-OH **8** (Y: tyrosine) (Scheme 6.1). All the synthetic aromatic capped peptides used in here are shown in Figure 6.7. The peptides having carboxylic acid groups at the end can bind with zinc ions with the inorganic segment and the backbone amide bonds can strongly interact through hydrogen bonds.

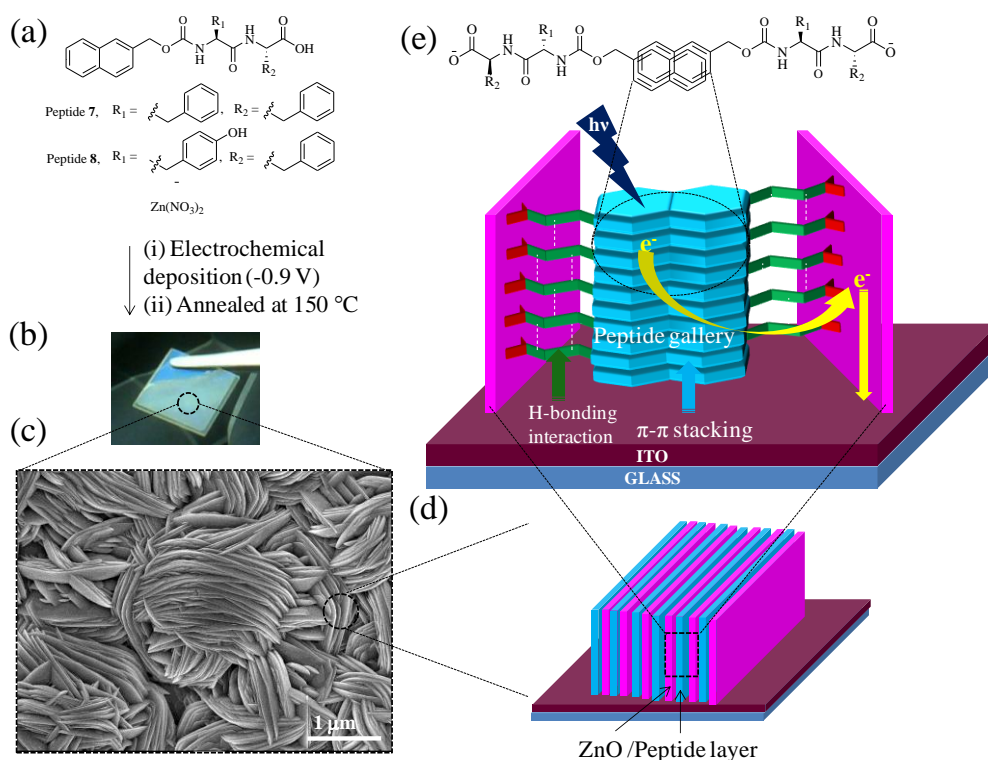
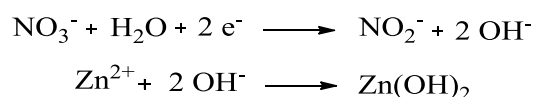


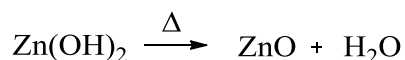
Figure 6.7. (a) The molecular structure of the designed peptide amphiphiles and Zn(NO₃)₂ precursor used for electrochemical deposition. (b) Digital photograph of the electrodeposited annealed hybrid thin film on an indium tin oxide (ITO)-coated quartz glass substrate. (c) Field-emission scanning electron microscopy (FESEM) image of the electrodeposited hybrid film with peptide **8**. (d) Schematic illustration of alternate ZnO and peptide layers in the lamellar network structures. (e) Schematic presentation of the peptide assembly within the ZnO inorganic phases. The aromatic π-π stacking interactions among the aromatic Nmoc moieties and hydrogen bonding of the peptide amphiphiles are the driving force for the evolution of lamellar nanostructures. Upon excitation with light, excited electrons move through the

aromatic Nmoc groups of the peptide amphiphiles into inorganic ZnO lattices and the flow of current produces a photocurrent.

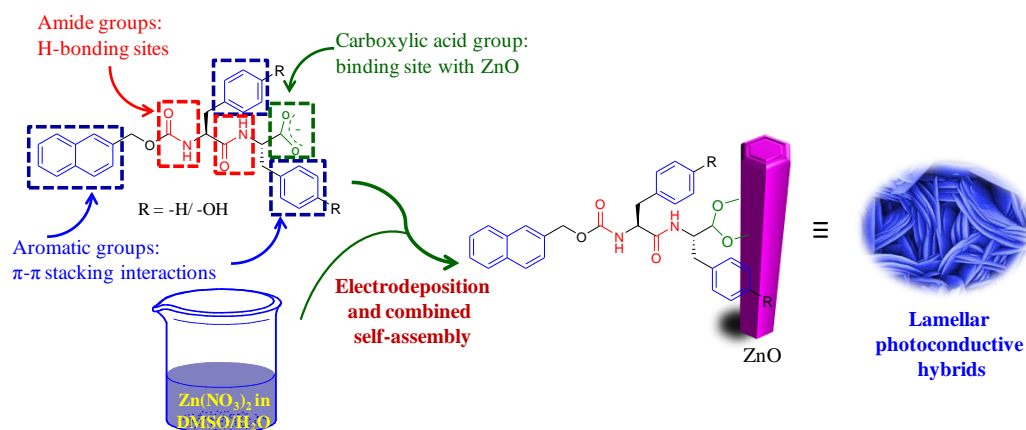
Here, we utilize the self-assembly process of peptide molecules to synthesize lamellar hybrids where N-capped naphthalene moieties are strongly interacting through π - π stacking interactions (Scheme 6.2). Electrochemical deposition is an effective technique to design organic-inorganic hybrid materials. Lamellar thin films were grown on the surface of electrodes enabling their direct integration into functional photoconductor devices. The organic-inorganic hybrid nanostructures were grown on the working electrodes through cathodic deposition from a mixture of H₂O-dimethylsulphoxide (1:1) solution of Zn(NO₃)₂ and peptides as self-assembling architectures. The experimental temperature was set at 80 °C, which is compatible with organic molecules. The electrochemical deposition follows the following electrochemical reaction.^[47]



The increase concentration of OH⁻ at the working electrode increases the local pH and facilitated the cathodic deposition of Zn(OH)₂ which is insulator in nature. On annealing at 150 °C, the insulator Zn(OH)₂ turns to a semiconductor material ZnO as per the following reaction.



Two semiconducting organic-inorganic lamellar thin films were constructed using electrochemical deposition technique by exploiting supramolecular ordering of two different dipeptides containing optoelectronic functionality. Peptide based thin films with semiconducting ZnO hybrids were prepared on annealing at 150 °C of electrodeposited peptide/Zn(OH)₂ thin films.



Scheme 6.2. Peptide design for the fabrication of photoconductor nanohybrids.

6.4.1 FTIR Study

Fourier Transform Infrared spectroscopy (FTIR) is used to understand the structural information and the interactions between the organic and inorganic phases in the hybrid materials. In FTIR spectroscopy, the broad region of $3690\text{--}3000\text{ cm}^{-1}$ is very important to understand the hydrogen bonding interactions of amide and hydroxyl groups of acid and alcohol. FTIR spectroscopy (Figure 6.8a-b) shows a relatively narrow peak at 3306 cm^{-1} , which is appeared for peptide Nmoc-FF-OH **7** whereas the significant peak appeared at 3425 cm^{-1} in its ZnO/Nmoc-FF-OH (hybrid **1**) thin film. This peak is broadened and shifted in the organic-inorganic hybrid thin film, which reveals the extensive hydrogen bonding interactions between the peptide and the inorganic layer.^[48] Furthermore, the carbonyl stretching frequency of carboxylic acid at 1716 cm^{-1} in native peptide Nmoc-FF-OH **7** has disappeared in its ZnO hybrid material due to the strong covalent bonding between organic and inorganic layers.^[49] For native peptide Nmoc-YF-OH **8**, the hydroxyl group of acid appears at 3412 cm^{-1} with a characteristic carbonyl stretching peak at 1694 cm^{-1} . The band of hydroxyl groups of acid functionality is broadening and shifted to 3437 cm^{-1} for ZnO/Nmoc-YF-OH (hybrid **2**) thin film, which is the evidence of hydrogen bonding interactions between the peptide amphiphiles and the inorganic ZnO layer.^[50-51]

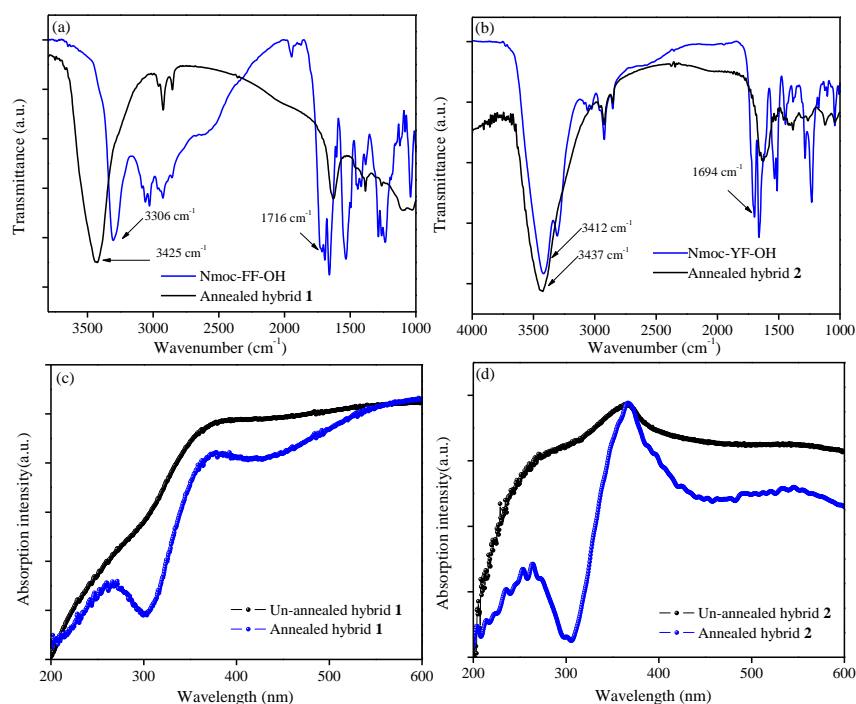


Figure 6.8. FTIR spectra of (a) annealed hybrid **1** and peptide **7**, and (b) annealed hybrid **2** with peptide **8**. Absorption spectra of (c) unannealed hybrid **1** and (d) annealed hybrid **2**.

6.4.2 Scanning electron microscope (SEM)

Scanning electron microscope (SEM) was used to characterize self-assembled nanostructured Nmoc capped peptide surfactants and ZnO thin films. The morphology of ZnO thin film without the peptide scaffold as a control sample was also investigated to understand the structural effect of peptides in organic-inorganic hybrid materials. The SEM image shows hexagonal microrods like structure (Figure 6.11a). The diameter of the hexagonal ZnO microrods is in the range of 0.7 to 1.6 nm. Interestingly, the interaction of peptides with ZnO completely changes the morphology of the organic-inorganic hybrid thin films. The SEM images show lamellar nanostructures (Figure 6.9) all over the thin films for hybrid samples **1** and **2**.^[20] The SEM image for Nmoc-FF-OH **7** based ZnO hybrid thin film **1** shows that the lamellar sheets are deposited across the substrate. The nanostructured sheets are oriented vertically and laterally by random fashion. The 2D sheets are randomly stacked with each other. The cross sectional SEM image shows the homogeneous thickness of deposited peptide film having the average thickness of 1.25 μm . The Nmoc-YF-OH **8** based hybrid ZnO thin film **2**

shows plate-like morphology, which was grown homogeneously by electrochemical deposition across the entire substrate. The cross sectional SEM image reveals that the plate-like nanostructures are stacked through layer by layer deposition and form lamellar thin film with average thickness of 1.82 nm.

6.4.3 Energy-dispersive X-ray spectroscopy (EDS)

Energy-dispersive X-ray spectroscopy (EDS) analytical technique is used for the elemental composition analysis of the electrodeposited hybrid materials (Figure 6.10). The presence of Zn, oxygen, and carbon elements corresponds to the organic-inorganic hybrid films.

6.4.4 UV-Vis study

Peptide/ZnO hybrid thin films were characterized by using UV-Vis spectroscopy before and after annealing (Figure 6.8c-d). The UV-Vis spectra clearly indicate the existence of both organic and inorganic phases in the electrodeposited thin films. The UV-Vis spectroscopy shows an absorbance peak at 370 nm for $\text{Zn}(\text{OH})_2/\text{Nmoc-FF-OH}$ hybrid film before thermal treatment.

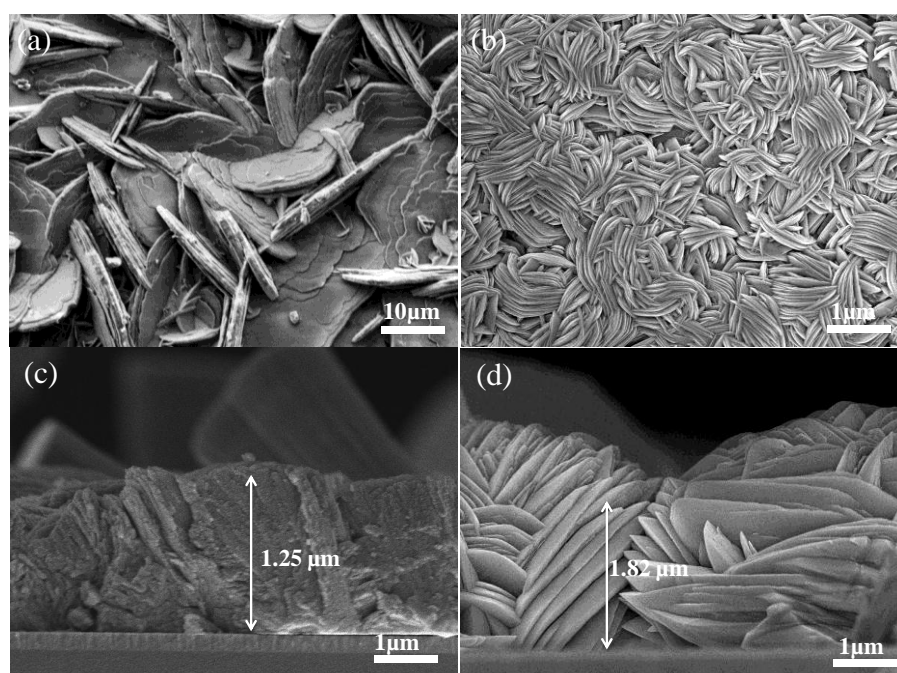


Figure 6.9. FESEM images of the top view of annealed hybrids **1** (a) and **2** (b), as well as cross-sectional images of hybrids **1** (c) and **2** (d).

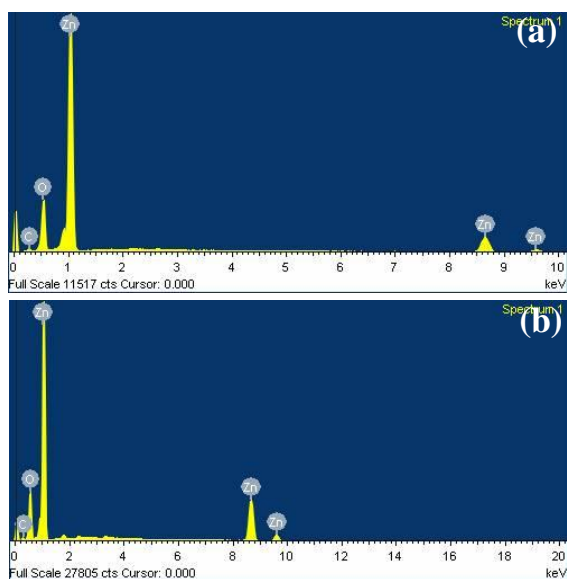


Figure 6.10. Energy-dispersive X-ray spectroscopy (EDS) of electrodeposited hybrid films in the presence of (a) peptide Nmoc-FF-OH **7**, (b) peptide Nmoc-YF-OH **8**.

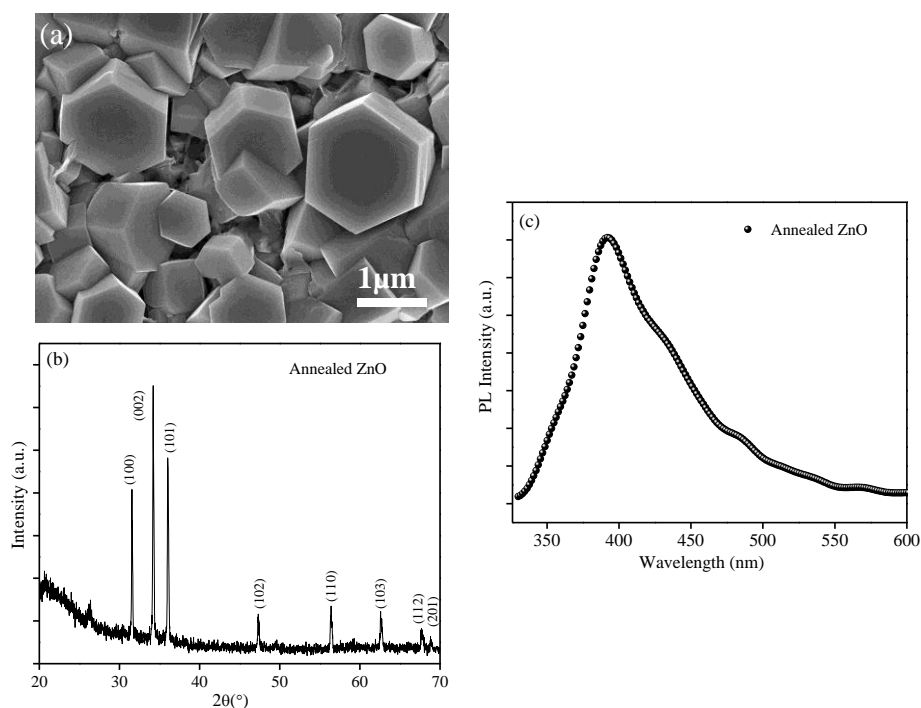


Figure 6.11. (a) FESEM image showing the wurtzite hexagonal ZnO grown without any peptide Amphiphile. (b) PL spectra of annealed electrodeposited ZnO thin film. (c) Powder XRD of annealed electrodeposited ZnO thin film.

The $\text{Zn(OH)}_2/\text{Nmoc-FF-OH}$ hybrid film turns to $\text{ZnO}/\text{Nmoc-FF-OH}$ film upon thermal annealing at 150 °C in atmosphere. For the annealed film, the UV-Vis spectroscopy displays a well-defined absorbance peak at 266 nm and a characteristic absorbance maxima band at 380 nm. The appearance of the absorbance peak at 266 nm is the characteristics of naphthalene double ring, which clearly signifies the organic phase in the hybrid material.^[44] The other absorbance band at 380 nm has resulted from the electronic transition between the ZnO band-gap for the hybrid material of $\text{ZnO}/\text{Nmoc-FF-OH}$ film. The un-annealed hybrid thin film of $\text{Zn(OH)}_2/\text{Nmoc-YF-OH}$ shows an absorbance band at 365 nm whereas the annealed hybrid thin film of $\text{ZnO}/\text{Nmoc-YF-OH}$ demonstrates the characteristic band at 265 nm and a broad band from 310 to 440 nm having absorbance maxima at 370 nm. The results clearly indicate co-existence of both ZnO and peptides in the thin film for hybrid materials. The hybrid films that consist in nanostructures grown from the peptides present some differences in absorption at higher wavelengths, which can be related to the grown nanostructures with different peptide sequences.

6.4.5 Photoluminescence (PL) Study

In addition, tuning of Nmoc-capped peptide sequence influences the lamellar structure of hybrid materials. The peptide/ZnO hybrid films were characterized by photoluminescence (PL) spectroscopy to understand the functional role of peptides in the lamellar architectures for photodetection (Figure 6.12a-b). The PL spectrum for un-annealed $\text{Zn(OH)}_2/\text{Nmoc-FF-OH}$ thin film showed a sharp peak at 367 nm and a broad peak at 420 nm. These peaks exhibited from the binding of the peptides with Zn^{2+} . Photoluminescence spectra of hybrids clearly distinguishes ZnO (3.16 eV) nanowire arrays fabricated from $\text{Zn(NO}_3)_2$ solution by electrodeposition (Figure 6.11c). After annealing, the insulator Zn(OH)_2 phase turns into conducting ZnO phase and the PL shows a huge change in the optical property for the same film. For the annealed $\text{ZnO}/\text{Nmoc-FF-OH}$ thin film, the PL spectrum shows a photoluminescence quenching is due to the transfer of electrons from excited state Nmoc-FF-OH **7** into the ZnO lattice. Un-annealed $\text{Zn(OH)}_2/\text{Nmoc-YF-OH}$ thin film exhibited a broad peak in the range of 370-

460 nm in the PL spectrum due to the strong binding of the peptides and Zn^{2+} . Photoluminescence quenching is also observed in case of ZnO/Nmoc-YF-OH hybrid represented in Figure 6.12b.^[29]

6.4.6 X-ray diffraction (XRD) Study

X-ray diffraction (XRD) study is a fundamental technique to achieve structural information about the lamellar architectures of hybrid films and crystal lattices of inorganic material. ZnO thin film without peptide support shows several characteristic peaks for the crystal lattices of ZnO hexagonal structures. A series of peaks corresponding to 2θ of 31.60° , 34.19° and 36.13° are attributed from (100), (002) and (101) planes of ZnO nanocrystal (Figure 6.11b). The formation of the lamellar structure is also supported by XRD study. The presence of four characteristics d-spacing indicates four distinct stable bilayer arrangements of Nmoc-FF-OH **7** based thin film. X-ray scattering study (Figure 6.12c-d) confirms the ordered lamellar arrangement with the d-spacing of 2.3 nm and 1.65 nm corresponding to (001) and (001)* reflections. Two types of lamellar arrangement are attributed from the bilayer of peptides in lamellar hybrid **1**.

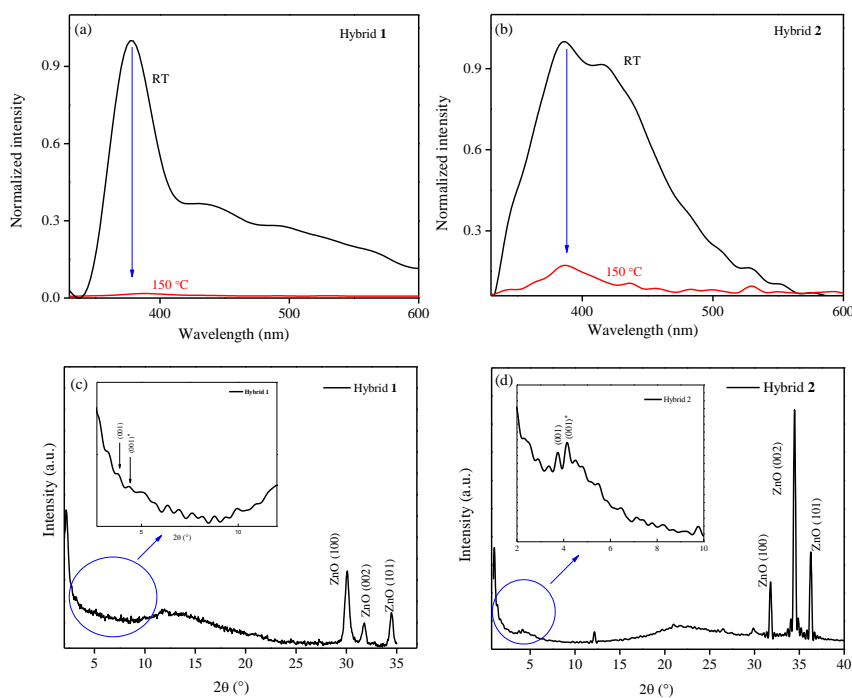


Figure 6.12. PL spectra of hybrids **1** (a) and **2** (b) before and after annealing recorded with $\lambda = 325$ nm laser excitation. Powder XRD patterns of hybrid thin films a) ZnO/7

and b) ZnO/8. Powder XRD peak patterns (001) and (001)* refer to lamellar ordering in the hybrid material; (100), (002), (101) indicate lattice planes of the wurtzite ZnO crystal.

Moreover, two distinct peaks corresponding to 2θ of 31.80° and 34.49° are attributed from (100) and (002) planes of ZnO hexagonal structure of nanoplates. In the case of lamellar hybrid **2**, an XRD peak 2θ at 3.7 corresponds to d-spacing of 2.3 nm, which is close to the bilayer of peptide **8**. For peptide supported hybrid thin film, crystal planes of ZnO are slightly shifted from the thin film without peptide support, which is resulted from the interactions of peptide molecules with the ZnO planes.^[52-54]

6.4.7 Current-voltage (I-V) measurements

The organic-inorganic lamellar hybrids are subjected to investigate its optoelectronic property. Current-voltage (I-V) measurements of the un-annealed Zn(OH)₂/Nmoc-FF-OH film showed no significant current (Figure 6.12a). The electro-deposited hybrid film acts as an insulator before annealing at 150°C . After annealing, the insulator Zn(OH)₂ is converted into semiconductor ZnO. The conductivity is observed for ZnO/Nmoc-FF-OH film even under dark condition. I-V curve shows that the hybrid material can act as photoconductor upon excitation 325 nm laser in continuous wave mode. The widely understood mechanism of photocarrier generation process in organic-inorganic hybrid is exciton formation of organic under irradiation of photon and subsequent dissociation for transfer the electrons into region of ZnO. The current of the hybrid material increases due to the presence of aromatic stacked peptide gallery under ultraviolet light. The dark current and photocurrent of annealed hybrids ZnO/Nmoc-FF-OH and ZnO/Nmoc-YF-OH is measured under UV light exposure of 20 mW/cm^2 . Photosensitive nature of such nanohybrid structure can be quantified as:

$$P = (I_{\text{light}} - I_{\text{dark}})/I_{\text{dark}}$$

where I_{light} is the photocurrent, I_{dark} is the dark current. The photosensitivity of hybrid ZnO/Nmoc-FF-OH is 0.12 at 2 V, measured at room temperature. For ZnO/Nmoc-YF-OH based thin film, the measured photosensitivity is comparatively less than hybrid ZnO/Nmoc-FF-OH. The photosensitivity for

annealed ZnO/Nmoc-YF-OH film is 0.06 at 2 V. At room temperature, the unannealed Zn(OH)₂/Nmoc-YF-OH thin film behaves as an insulator (Figure 6.13). The change in voltage does not allow passing the current throughout the circuit. After annealing at 150 °C, the insulator Zn(OH)₂/Nmoc-YF-OH thin film turns to semiconductor ZnO/Nmoc-YF-OH thin film and shows its optoelectronic property by changing the optical condition from dark to UV light (Figure 6.13b). I-V measurement study of such peptide based hybrid material shows that such types of material can be efficiently used as an optoelectronic photoconducting material.

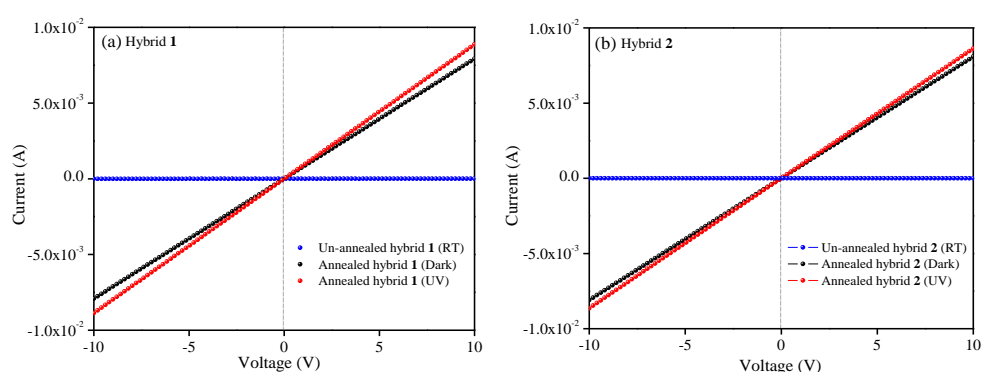


Figure 6.13. I–V characteristics of deposited (a) hybrid films of peptide **7**: unannealed hybrid (blue), the annealed hybrid under dark conditions (black), and the annealed hybrid under UV light (red) irradiation at $\lambda = 325$ nm; and (b) hybrid films of peptide **8**: unannealed hybrid (blue), annealed hybrid under dark conditions (black), and the annealed hybrid under UV light (red) irradiation at $\lambda = 325$ nm.

6.5 Conclusion

We have developed peptide-ZnO based semiconductor lamellar nanostructures through electrochemical deposition. All the electrochemical deposited Nmoc-capped aromatic dipeptide-ZnO based hybrid lamellar nanostructures show optoelectronic behavior. FTIR data clearly suggests the interaction of peptide motifs with the ZnO inorganic phase. The acid functionalities of aromatic dipeptides anchor with inorganic ZnO layers. UV-Vis and photoluminescence spectroscopy reveal the optoelectronic properties of peptide-based ZnO thin films. Aromatic dipeptides are self-assembled through hydrogen bonding as well as π - π stacking interactions inside the

lamellar nanostructures. The introduction of peptide self-assembly successfully established the hybrid materials as good conducting materials. The PL and UV-Vis measurement studies show good optoelectronic property of these materials. I-V characteristics of these hybrids both in dark and light illumination indicate that the conductivity of these hybrid nanostructure materials is increased due to the presence of photon absorbing active self-assembled peptide gallery. This investigation can play a pioneer role to inspire for further development of peptide-based hybrid optoelectronic materials.

6.6 References

- [1] Babu S. S., Praveen V. K., Ajayaghosh A. (2014), Functional π -gelators and their applications, *Chem. Rev.*, 114, 1973-2129 (DOI: 10.1021/cr400195e).
- [2] Herrmann D., Niesar S., Scharsich C., Kohler A., Stutzmann M., Riedle E. (2011), Role of structural order and excess energy on ultrafast free charge generation in hybrid polythiophene/Si photovoltaics probed in real time by near-infrared broadband transient absorption, *J. Am. Chem. Soc.*, 133, 18220-18233 (DOI: 10.1021/ja207887q).
- [3] Huang J., Yin Z., Zheng Q. (2011), Applications of ZnO in organic and hybrid solar cells, *Energy Environ. Sci.*, 4, 3861-3877 (DOI: 10.1039/C1EE01873F).
- [4] Dong H., Zhu H., Meng Q., Gong X., Hu W. (2012), Organic photoresponse materials and devices, *Chem. Soc. Rev.*, 41, 1754-1808 (DOI: 10.1039/C1CS15205J).
- [5] He M., Qiu F., Lin Z. (2013), Toward high-performance organic-inorganic hybrid solar cells: bringing conjugated polymers and inorganic nanocrystals in close contact, *J. Phys. Chem. Lett.*, 4, 1788-1796 (DOI: 10.1021/jz400381x).
- [6] Wu S., Tai Q., Yan F. (2010), Hybrid photovoltaic devices based on poly (3-hexylthiophene) and ordered electrospun ZnO nanofibers, *J. Phys. Chem. C*, 114, 6197-6200 (DOI: 10.1021/jp910921a).
- [7] Kim C.-H., Cha S.-H., Kim S. C., Song M., Lee J., Shin W. S., Moon S.-J., Bahng J. H., Kotov N. A., Jin S.-H. (2011), Silver nanowire

- embedded in P3HT: PCBM for high-efficiency hybrid photovoltaic device applications, *ACS Nano*, 5, 3319-3325 (DOI: 10.1021/nn200469d).
- [8] Lin C.-L., Yeh M.-Y., Chen C.-H., Sudhakar S., Luo S.-J., Hsu Y.-C., Huang C.-Y., Ho K.-C., Luh T.-Y. (2006), Silica-titania-based organic-inorganic hybrid materials for photovoltaic applications, *Chem. Mater.*, 18, 4157-4162 (DOI: 10.1021/cm0602693).
- [9] Xu H., Das A. K., Horie M., Shaik M. S., Smith A. M., Luo Y., Lu X., Collins R., Liem S. Y., Song A., Popelier P. L. A., Turner M. L., Xiao P., Kinloch I. A., Ulijn R. V. (2010), An investigation of the conductivity of peptide nanotube networks prepared by enzyme-triggered self-assembly, *Nanoscale*, 2, 960-966 (DOI: 10.1039/B9NR00233B).
- [10] Fayette M., Robinson R. D. (2014), Chemical transformations of nanomaterials for energy applications, *J. Mater. Chem. A*, 2, 5965-5978 (DOI: 10.1039/C3TA13982D).
- [11] Schenning A. P. H. J., Meijer E. W. (2005), Supramolecular electronics; nanowires from self-assembled π -conjugated Systems, *Chem. Commun.*, 3245-3258 (DOI: 10.1039/b501804h).
- [12] Bano N., Zaman S., Zainelabdin A., Hussain S., Hussain I., Nur O., Willander M. (2010), ZnO-organic hybrid white light emitting diodes grown on flexible plastic using low-temperature aqueous chemical method, *J. Appl. Phys.*, 108, 043103 (DOI: 10.1063/1.3475473).
- [13] Liu J., Berg J. C. (2007), An aqueous sol-gel route to prepare organic-inorganic hybrid materials, *J. Mater. Chem.*, 17, 4430-4435 (DOI: 10.1039/B709078A).
- [14] Yan H., Yu Z., Lu K., Zhang Y., Wei Z. (2011), Self-assembly of graphene like ZnO superstructured nanosheets and their application in hybrid photoconductors, *Small*, 7, 3472-3478 (DOI: 10.1002/sml.201101732).
- [15] Wang L., Yoon M.-H., Facchetti A., Marks T. J. (2007), Flexible inorganic/organic hybrid thin-film transistors using all-transparent component materials, *Adv. Mater.*, 19, 3252-3256 (DOI: 10.1002/adma.200700393).

- [16] Sessolo M., Bolink H. J. (2011), Hybrid organic-inorganic light-emitting diodes, *Adv. Mater.*, 23, 1829-1845 (DOI: 10.1002/adma.201004324).
- [17] Yoon K.-H., Han K.-S., Sung M.-M. (2012), Fabrication of a new type of organic-inorganic hybrid superlattice films combined with titanium oxide and polydiacetylene, *Nanoscale Res. Lett.*, 7, 71 (DOI: 10.1186/1556-276X-7-71).
- [18] Karaman M., Kooi S. E., Gleason K. K. (2008), Vapor deposition of hybrid organic-inorganic dielectric bragg mirrors having rapid and reversibly tunable optical reflectance, *Chem. Mater.*, 20, 2262-2267 (DOI: 10.1021/cm703107d).
- [19] Bruns C. J., Herman D. J., Minuzzo J. B., Lehrman J. A., Stupp S. I. (2013), Rationalizing molecular design in the electrodeposition of anisotropic lamellar nanostructures, *Chem. Mater.* 25, 4330-4339 (DOI: 10.1021/cm402505p).
- [20] Herman D. J., Goldberger J. E., Chao S., Martin D. T., Stupp S. I. (2011), Orienting periodic organic-inorganic nanoscale domains through one-step electrodeposition, *ACS Nano*, 5, 565-573 (DOI: 10.1021/nn102697r).
- [21] Pichon B. P., Mezy A., Tedenac J.-C., Tichit D., Gerardin C. A (2009), Soft chemistry route to prepare hybrid ZnO nanostructured films with a lamellar structure, *New J. Chem.*, 33, 2350-2354 (DOI: 10.1039/B9NJ00365G).
- [22] Tan Y., Srinivasan S., Choi K.-S. (2005), Electrochemical deposition of mesoporous nickel hydroxide films from dilute surfactant solutions, *J. Am. Chem. Soc.*, 127, 3596-3604 (DOI: 10.1021/ja0434329).
- [23] Xu L., Guo Y., Liao Q., Zhang J., Xu D. (2005), Morphological control of ZnO nanostructures by electrodeposition, *J. Phys. Chem. B*, 109, 13519-13522 (DOI: 10.1021/jp051007b).
- [24] Otani S., Katayama J., Umemoto H., Matsuoka M. (2006), Effect of bath temperature on the electrodeposition mechanism of zinc oxide film from zinc nitrate solution, *J. Electrochem. Soc.*, 153, 551-566 (DOI: 10.1149/1.2205187b).

- [25] Izaki M., Omi T. (1996), Transparent zinc oxide films prepared by electrochemical reaction, *Appl. Phys. Lett.*, 68, 2439-2440 (DOI: 10.1063/1.116160).
- [26] Choi K.-S., Lichtenegger H. C., Stucky G. D. (2002), Electrochemical synthesis of nanostructured ZnO films utilizing self assembly of surfactant molecules at solid-liquid interfaces, *J. Am. Chem. Soc.*, 124, 12402-12403 (DOI:10.1021/ja0275562).
- [27] Jing H.-Y., Li X.-L., Lu Y., Mai Z.-H., Li M. (2005), Electrochemical self-assembly of highly oriented ZnO-surfactant hybrid multilayers, *J. Phys. Chem. B*, 109, 2881-2884 (DOI: 10.1021/jp0458351).
- [28] Tan Y, Steinmillar E. M. P., Choi K.-S. (2005), Electrochemical tailoring of lamellar-structured ZnO films by interfacial surfactant templating, *Langmuir*, 21, 9618-9624 (DOI: 10.1021/la050789x).
- [29] Sofos M., Goldberger J., Stone D. A., Allen J. E., Ma Q., Herman D. J., Tsai W.-W., Lauhon L. J., Stupp S. I. (2009), A synergistic assembly of nanoscale lamellar photoconductor hybrids, *Nat. Mater.*, 8, 68-75 (DOI: 10.1038/NMAT2336).
- [30] Yoshida T., Zhang J., Komatsu D., Sawatani S., Minoura H., Pauporte T., Linkot D., Oekermann T., Schlettwein D., Tada H., Wohrle D., Funabiki K., Matsui M., Miura H., Yanagi H. (2009), Electrodeposition of inorganic/organic hybrid thin films, *Adv. Funct. Mater.*, 19, 17-43 (DOI: 10.1002/adfm.200700188).
- [31] Qin X., Shao G., Zhao L. (2012), The effect of surfactant on the structure and properties of ZnO films prepared by electrodeposition, *Mater. Sci. Eng. B*, 177, 1678-1681 (DOI: 10.1016/j.mseb.2012.08.012).
- [32] Stupp S. I., Palmer L. C. (2014), Supramolecular chemistry and self-assembly in organic materials design, *Chem. Mater.*, 26, 507-518 (DOI: 10.1021/cm403028b).
- [33] Beaujuge P. M., Frechet J. M. J. (2011), Molecular design and ordering effects in π -functional materials for transistor and solar cell applications, *J. Am. Chem. Soc.*, 133, 20009-20029 (DOI: 10.1021/ja2073643).

- [34] Briggs B. D., Knecht M. R. (2012), Nanotechnology meets: peptide-based methods for the fabrication of functional materials, *J. Phys. Chem. Lett.*, 3, 405-418 (DOI: 10.1021/jz2016473).
- [35] Huang R., Qi W., Su R., Zhao J., He Z. (2011), Solvent and surface controlled self-assembly of diphenylalanine peptide: from microtubes to nanofibers, *Soft Matter*, 7, 6418-6421 (DOI: 10.1039/C1SM05752A).
- [36] Yan X., Cui Y., He Q., Wang K., Li J. (2008), Organogels based on self-assembly of diphenylalanine peptide and their application to immobilize quantum dots, *Chem. Mater.*, 20, 1522-1526 (DOI: 10.1021/cm702931b).
- [37] Chen L., Revel S., Morris K., Serpell L. C., Adams D. J. (2010), Effect of molecular structure on the properties of naphthalene-dipeptide hydrogelators, *Langmuir*, 26, 13466-13471 (DOI: 10.1021/la102059x).
- [38] I. Maity, M. K. Manna, D. B. Rasale, A. K. Das, (2014), Peptide-nanofiber-supported palladium nanoparticles as an efficient catalyst for the removal of N-terminus protecting groups, *ChemPlusChem*, 79, 413-420 (DOI: 10.1002/cplu.201300348).
- [39] Maity I., Rasale D. B., Das A.K. (2014), Peptide nanofibers decorated with Pd nanoparticles to enhance the catalytic activity for C–C coupling reactions in aerobic conditions, *RSC Adv.*, 4, 2984-2988 (DOI: 10.1039/C3RA44787A).
- [40] Yan X., Cui Y., He Q., Wang K., Li J. (2008), Organogels based on self-assembly of diphenylalanine peptide and their application to immobilize quantum dots, *Chem. Mater.*, 20, 1522-1526 (DOI: 10.1021/cm702931b).
- [41] Chen L., Revel S., Morris K., Serpell L. C., Adams D. J. (2010), Effect of molecular structure on the properties of naphthalene-dipeptide hydrogelators, *Langmuir*, 26, 13466-13471 (DOI: 10.1021/la102059x).
- [42] Maity I., Rasale D. B., Das A. K. (2012), Sonication induced peptide-appended bolaamphiphile hydrogels for in situ generation and catalytic activity of Pt nanoparticles, *Soft Matter*, 8, 5301-5308 (DOI: 10.1039/c2sm25126d).

- [43] Saunders B. R., Turner M. L. (2008), Nanoparticle-polymer photovoltaic cells, *Adv. Col. Inter. Sci.*, 138, 1-23 (DOI:10.1016/j.cis.2007.09.001).
- [44] Rasale D. B., Maity I., Das A. K. (2014), Lipase catalyzed inclusion of gastrodigenin for the evolution of blue light emitting peptide nanofibers, *Chem. Commun.*, 50, 8685-8688 (DOI: 10.1039/c4cc02484b).
- [45] Rasale D. B., Maity I., Konda M., Das A. K. (2013), Peptide self-assembly driven by oxo-ester mediated native chemical ligation, *Chem. Commun.*, 49, 4815-4817 (DOI: 10.1039/c3cc41475b).
- [46] Rasale D. B., Maity I., Das A. K., (2014), In situ generation of redox active peptides driven by selenoester mediated native chemical ligation, *Chem. Commun.* 50, 11397-11400 (DOI: 10.1039/C4CC03835E).
- [47] Lee J., Tak Y. (2001), Electrodeposition of ZnO on ITO electrode by potential modulation method, *Electrochem. Solid-State Lett.*, 4, 63-65 (DOI: 10.1149/1.1388179).
- [48] Rouhi J., Mahmud S., Naderi N., Ooi C. R., Mahmood M. R. (2013), Physical properties of fish gelatin-based bio-nanocomposite films incorporated with ZnO nanorods, *Nanoscale Res. Lett.* 2013, 8, 364 (DOI: 10.1186/1556-276X-8-364).
- [49] Mathew S., Yella A., Gao P., Humphry-Baker R., Curchod B. F. E., Ashari-Astani N., Tavernelli I., Rothlisberger U., Nazeeruddin M. K., Gratzel M. (2014), Dye-sensitized solar cells with 13% efficiency achieved through the molecular engineering of porphyrin sensitizers, *Nat. Chem.*, 6, 242-247 (DOI: 10.1038/nchem.1861).
- [50] Ogata S., Tagaya H., Karasu M., Kadokawa J.-I. (2000), New preparation method for organic-inorganic layered compounds by organo derivatization reaction of Zn(OH)₂ with carboxylic acids, *J. Mater. Chem.*, 10, 321-327 (DOI: 10.1039/A905859A).
- [51] Inoue S., Fujihara S. (2011), Liquid-liquid biphasic synthesis of layered zinc hydroxides intercalated with long-chain carboxylate ions and their conversion into ZnO nanostructures, *Inorg. Chem.*, 50, 3605-3612 (DOI: 10.1021/ic1025729).

- [52] Pichon B. P., Leuvrey C., Ihiawakrim D., Tichit D., Geradin C. (2011), Films of tunable ZnO nanostructures prepared by a surfactant-mediated soft synthesis route, *J. Phys. Chem. C*, 115, 23695-23703 (DOI: 10.1021/jp2072149).
- [53] Cruickshank A. C., Tay S. E. R., Illy B. N., Campo R. D., Schumann S., Jones T. S., Heutz S., McLachlan M. A., McComb D. W., Riley D. J., Ryan M. P. (2011), Electrodeposition of ZnO nanostructures on molecular thin films, *Chem. Mater.*, 23, 3863-3870 (DOI: 10.1021/cm200764h).
- [54] Tan Y., Steinmiller E. M. P., Choi K.-S. (2005), Electrochemical tailoring of lamellar-structured ZnO films by interfacial surfactant templating, *Langmuir*, 21, 9618-9624 (DOI: 10.1021/la050789x).

Chapter 7

Synergistic Assembly of Peptide-metal Hydroxide Hybrid Nanostructures for Electrochemical Capacitors

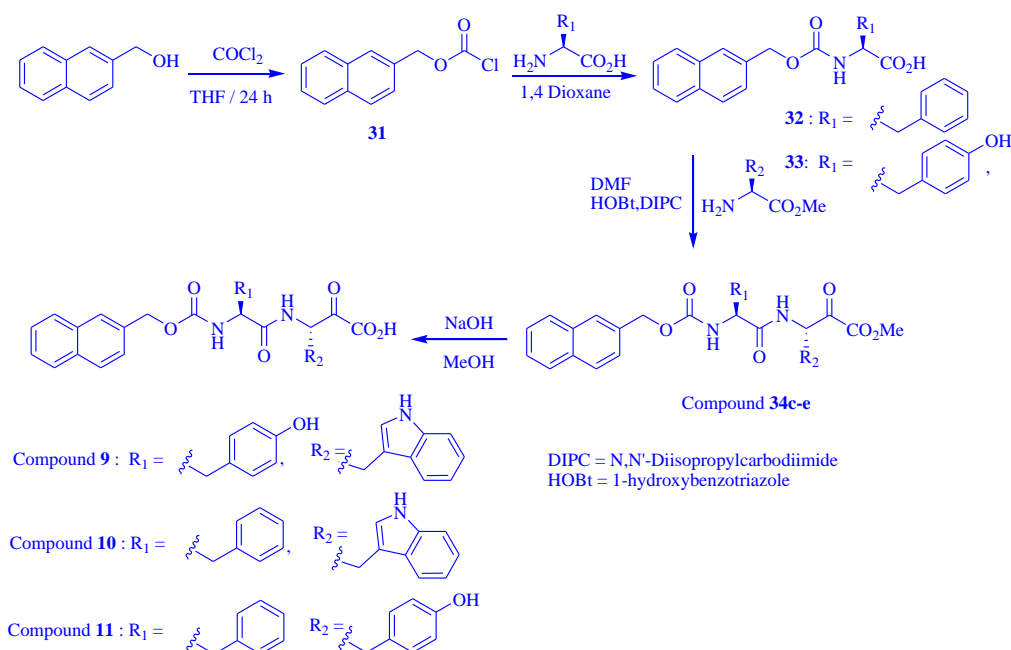
7. 1 Introduction

Rational nanostructures design to improve material's performance is an exciting goal for the researchers worldwide. In recent years, nanostructured metal hydroxides ($M(OH)_2$) have drawn a great deal of attention due to their wide range of applications in electrochemical and electronic devices such as electrochemical capacitance storage,^[1-3] supercapacitors,^[4-6] battery,^[7-9] electrochromic devices^[10,11] and water splitting.^[12-14] However, their fabrication, cost, stability and safety issues are the main obstacles which have prevented the application of metal hydroxides in commercial appliances. Therefore, inexpensive, ecofriendly and nontoxic electrode materials with good capacitive characteristics are highly desired to resolve these issues.

Recently, self-assembled organic nanostructures are of great interest for applications in several optoelectronic materials.^[15,16] The organic biomolecules are environment friendly, easily available, low cost, flexible and disposable but degrade with time when used alone. Therefore, it becomes beneficial to work towards hybrid organic/inorganic nanostructures to enhance device/material functionality. The development of hybrid organic/inorganic material makes it possible to utilize advantages associated with organic as well as inorganic counterpart. Various synthetic strategies have been developed to construct such nanoscale hybrid materials such as sol-gel chemistry,^[17] immiscible liquid-liquid biphasic system,^[18] chemical methods^[19,20] and electrochemical methods.^[21-23] In the electrochemical method, several small organic molecules have been designed to develop assembly of organic-inorganic hybrids. Sodium dodecyl sulfate (SDS) is the mostly used surfactant for the electrodeposition of metal hydroxides.^[24-30] Stupp *et al.* have reported aromatic based π -conjugated oligothiophenes to grow lamellar hybrid nanostructures.^[31-33] Several organic dyes are also used as organic components in the electrochemical self-assembly of organic-inorganic hybrids for dye-sensitized solar cells applications.^[34-36] In addition, among these variety of molecules, small peptides^[37-41] are considered to be excellent biomolecule to produce wide variety of nanostructured materials.^[42-51] In the previous chapter 6, we have shown aromatic peptide based surfactant to construct lamellar

organic-inorganic hybrid materials for applications in optoelectronic materials.^[52-54]

This chapter demonstrates the novel strategy for the preparation of a set of peptide-metal hydroxide nanoscale hybrids by using electrochemical deposition and peptide self-assembly. The main purpose of this chapter is to identify the peptide molecular variables that affect the morphology of different metal hydroxide nanostructures which is very important in energy storage applications. The target has achieved through synthesis of a series of peptides which are used for growing peptide-metal hydroxides nanohybrids. Naphthalene-2-methoxy carbonyl (Nm) is choosed as a π -conjugated moiety to connect with peptide molecule and modified it synthetically to produce a range of peptides with different amino acids. Then, a set of nine peptide/metal hydroxide hybrids have been synthesized by using electrochemical deposition where we found that peptides play a significant role in the morphology of hybrid nanomaterials. The different nanostructures with ordered morphology are formed and characterization of peptide-metal hydroxide hybrid nanostructures by using SEM, FTIR, XRD, energy dispersive X-ray spectroscopy (EDS) and cyclic voltammetry (CV) has been illuminated here.



Scheme 7.1. Synthetic route of peptides **9**, **10** and **11**.

7.2 Experimental

Synthesis of peptides

Peptides were synthesized in laboratory by employing solution phase procedure. Peptides NmYW (**9**), NmFW (**10**) and NmFY (**11**) were synthesized according to following procedure.

The general procedures used for peptide coupling are as follows: A solution of **33** (1.35 g, 3.69 mmol) and HOBt (0.50 g, 3.7 mmol) were stirred in DMF (2 mL). A neutralized solution of H₂N-Trp-OMe was extracted from its corresponding hydrochloride salt (1.88 g, 7.38 mmol) and concentrated to add to the reaction mixture followed by DIPC (0.47 g, 3.7 mmol) at 0°C. The mixture was stirred at room temperature for 12 hrs. The reaction mixture was diluted with ethyl acetate and the organic layer was washed with 1 M HCl (2 × 30 mL), brine, 1 M Na₂CO₃ (3 × 30 mL) and again with brine. The organic layer was dried over Na₂SO₄ and evaporated under vacuum to yield a white solid. Purification of **34c** was performed by column chromatography on silica gel (100–200 mesh) with ethyl acetate/toluene (1:1) as eluent. A solution of **34c** (1.93 g, 3.42 mmol) was taken in dry MeOH (100 mL) and allowed to react with 2 M solution of NaOH. The reaction progress was monitored by thin-layer chromatography (TLC). The reaction mixture was stirred up to 6 hrs. Then, methanol was removed under vacuum. The residue was dissolved in water (100 mL) and washed with diethyl ether (2 × 20 mL). Then, the pH of the aqueous layer was adjusted to 2 by using 2 M HCl and extracted with ethyl acetate (3 × 30 mL). The ethyl acetate layer was dried over anhydrous sodium sulfate and evaporated under vacuum to yield **9** as a white solid and used for the next step without purification. The intermediates naphthalene-2-methyloxichloroformate (**31**), NmF (**32**) and NmY (**33**) were prepared according to the procedure described in chapter 6. Compounds **34d**, **34e**, **10** and **11** were also synthesized according to the procedure described above.

Nm-YW-OMe (**34c**):

¹H NMR (400 MHz, CDCl₃, δ_{ppm}): 8.50 (d, 1H, ring -NH- of Trp), 8.22 (d, 1H, NH of Tyr), 8.10 (d, 1H, NH of Trp), 7.81 (d, 2H, $J = 4.2$ Hz), 7.72 (s, 1 H), 7.47 (dd, $J = 3.8, 3.5$ Hz), 7.35 (d, 2H, ring protons of Trp), 7.25 (s, 1H), 7.20 (d, 2H, ring protons of Trp), 7.01 (dd, $J = 9.3$ Hz, 2H), 6.90 (d, $J = 6.8$ Hz, 2H,

Tyr), 6.60 (d, $J = 7.3$ Hz, 2H, Tyr), 5.15 (s, 2 H), 4.36 (m, 1H, C ^{α} H of Tyr), 4.14 (m, 1H, C ^{α} H of Trp), 3.57 (s, 3H), 3.18 (m, 2H, C ^{β} H of Tyr), 2.89 (m, 2H, C ^{β} H of Trp); HRMS (ESI) m/z for C₃₀H₃₁N₃O₆Na (M +Na)⁺ calcd.: 588.2111, found: 588.2132

NmFW-OMe (34d):

¹H NMR (400 MHz, CDCl₃, δ_{ppm}): 8.50 (d, 1H, ring -NH- of Trp), 8.15 (d, 1H, NH of Phe), 7.90 (d, 1H, NH of Trp), 7.82 (d, 2H, $J = 4.2$ Hz), 7.75 (s, 1 H), 7.48 (dd, 2H, $J = 3.2, 3.4$ Hz), 7.37 (d, 2H, ring protons of Trp), 7.27 (s, 1H), 7.22 (d, 2H, ring protons of Trp), 7.20 (d, 2H), 7.15-7.09 (m, 5H, aromatic protons of Phe), 5.17 (s, 2 H), 4.83 (m, 1H, C ^{α} H of Phe), 4.41 (m, 1H, C ^{α} H of Trp), 3.61 (s, 3H), 3.22 (d, 2H, $J = 5.0$ Hz, C ^{β} H of Phe), 3.02 (d, 2H, $J = 6.2$ Hz, C ^{β} H of Trp); MS (ESI) m/z for C₃₃H₃₁N₂O₅Na (M +Na)⁺ calcd.: 572.2161, found: 572.5412.

NmFY-OMe (34e):

¹H NMR (400 MHz, CDCl₃, δ_{ppm}): 7.83 (d, 2H, $J = 8$ Hz), 7.78 (s, 1H), 7.49 (dd, 2H, $J = 3.9$ Hz, 3Hz), 7.42 (d, $J = 7.5$ Hz, 1H NH of Phe), 7.16 (d, 2H, $J = 6.0$ Hz), 7.26 (m, 5H), 6.81 (d, $J = 7.04$, 2H, ring protons of Tyr), 6.64 (d, $J = 8.3$ Hz, 2H, ring protons of Tyr), 6.62 (d, 1H, $J = 5.0$ Hz, NH of Tyr), 5.23 (s, 2H), 4.74 (m, C ^{α} H of Phe), 4.42 (m, C ^{α} H of Tyr), 3.05 (d, 2H, $J = 6.3$ Hz, C ^{β} H of Phe), 2.97 (d, 1H, $J = 5.5$ Hz, C ^{β} H of Tyr), 2.93 (d, 1H, $J = 5.8$ Hz, C ^{β} H of Tyr). MS (ESI) m/z for C₃₁H₃₀N₂O₆Na (M +Na)⁺ calcd.: 549.2002, found: 549.5042.

NmYW (9):

Yield = 0.80 g (1.45 mmol, 82.47 %, ¹H NMR (400 MHz, DMSO-*d*₆, δ_{ppm}): $\delta = 11.98$ (s, 1H, -COOH), 11.38 (s, 1H, -NH- proton of heterocyclic ring), 9.69 (s, 1H, -OH- of Tyr), 8.75 (d, 1H, $J = 7.5$ Hz), 8.40-8.34 (m, 4H), 8.29 (s, 1H), 8.06 (d, 1H, $J = 7.8$ Hz), 8.01 (t, 2H), 7.94 (d, 1H, $J = 8.5$ Hz), 7.87 (d, 1H, $J = 9.0$ Hz), 7.84 (d, 1H, $J = 7.8$ Hz), 7.70 (s, 1H), 7.58 (m, 1H), 7.57 (d, 2H), 7.50 (d, 1H, $J = 7.5$ Hz), 7.14 (d, 2H, $J = 8.3$ Hz), 5.62 (s, 2H), 5.04 (m, 1H, C ^{α} H of Tyr), 4.75 (m, 1H, C ^{α} H of Trp), 3.70 (m, 1H, C ^{β} H of Tyr), 3.61 (m, 1H, C ^{β} H of Tyr), 3.38 (m, 1H, C ^{β} H of Trp), 3.12 (m, 1H, C ^{β} H of Trp); ¹³C NMR (100 MHz, DMSO-*d*₆, δ_{ppm}): 178.44, 176.99, 161.07, 141.28, 139.87, 137.91, 137.63, 135.36, 133.36, 133.13, 132.92, 132.78, 132.45, 131.53, 131.13, 130.73, 128.89, 126.15, 123.62, 123.42, 120.05, 116.57, 114.81,

70.53, 61.62, 58.13, 32.26, 19.29; MS (ESI) m/z for $C_{32}H_{29}N_3O_6Na$ ($M+Na$)⁺ calcd.: 574.1954, found: 574.5638.

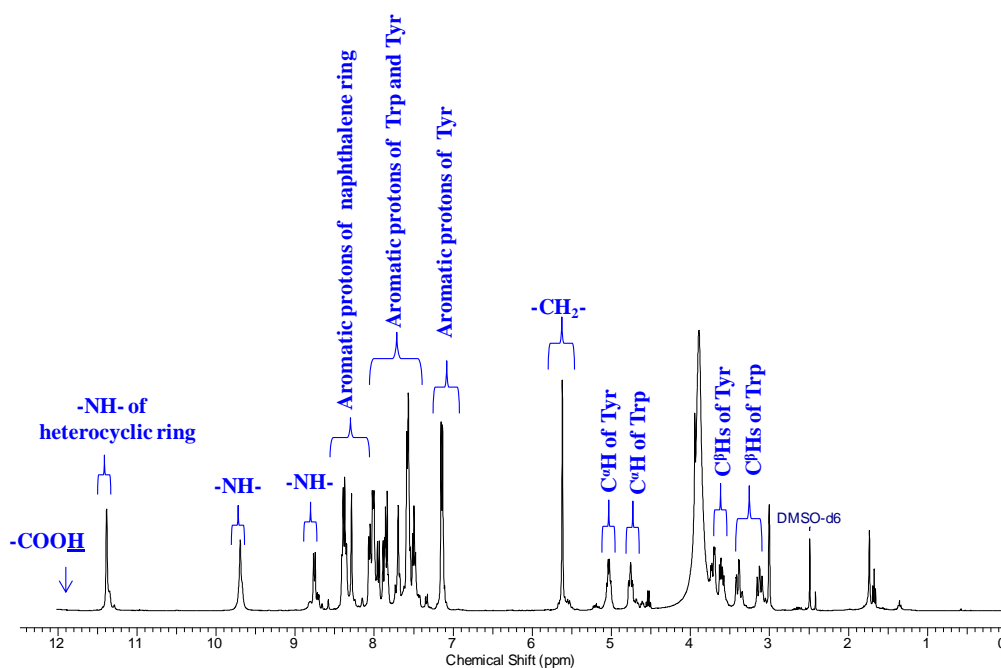


Figure 7.1. 1H NMR spectrum (400 MHz, $DMSO-d_6$) of NmYW (**9**).

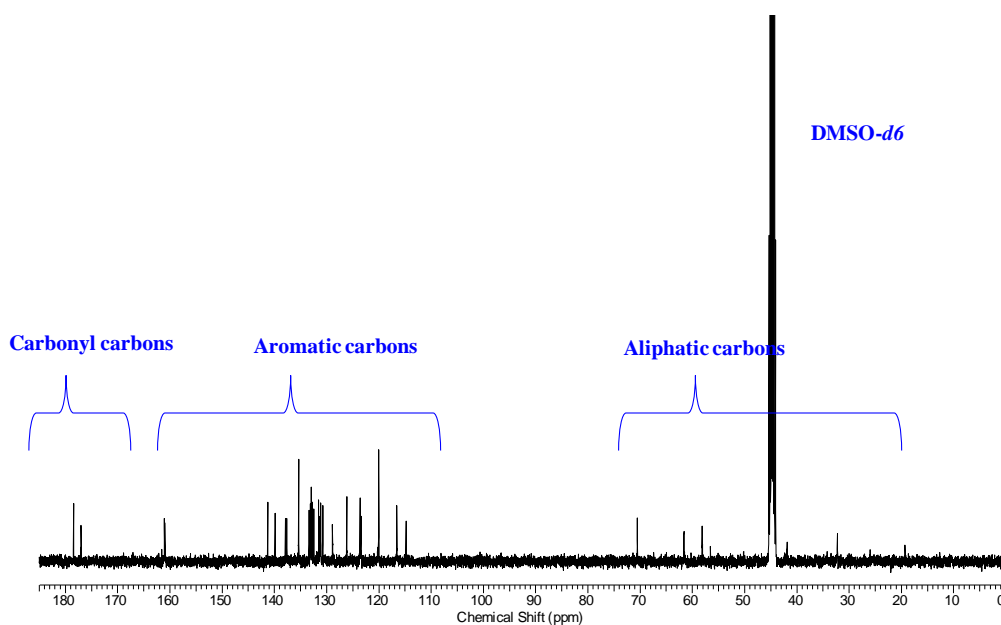


Figure 7.2. ^{13}C NMR spectrum (100 MHz, $DMSO-d_6$) of NmYW (**9**).

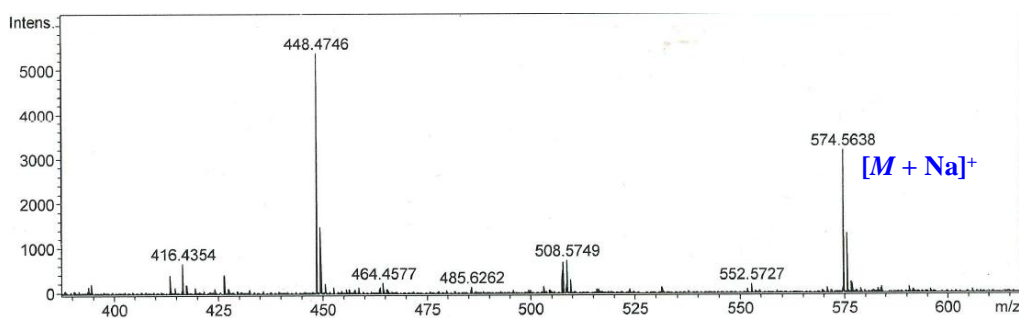


Figure 7.3. ESI-MS spectrum of NmYW (**9**).

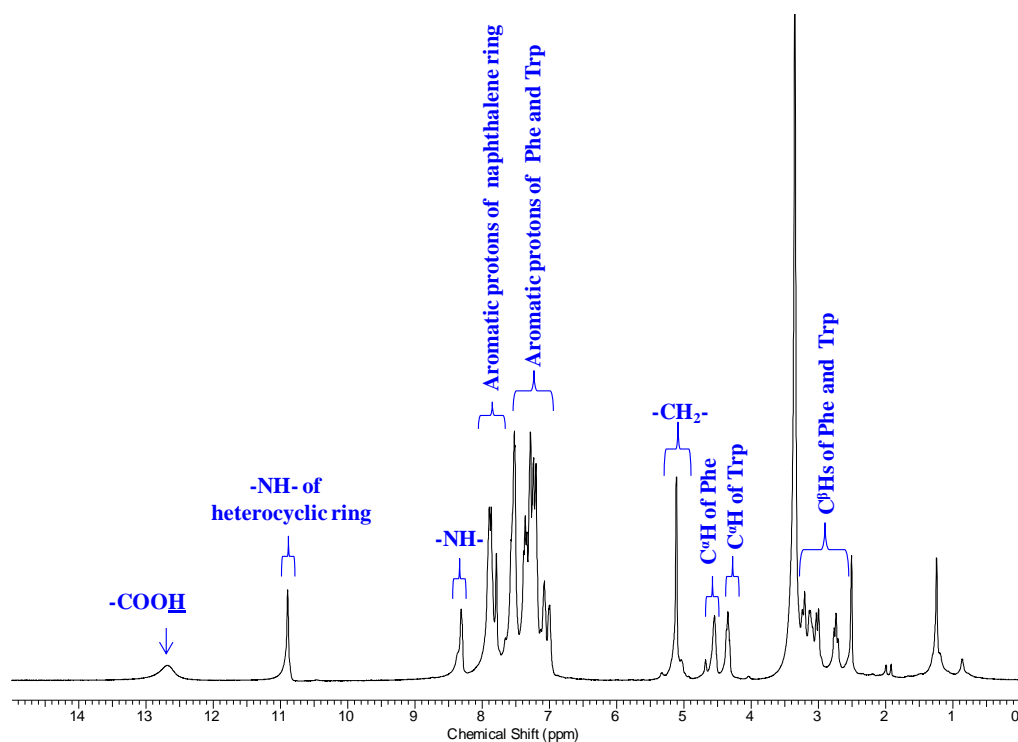


Figure 7.4. ^1H NMR spectrum (400 MHz, $\text{DMSO}-d_6$) of NmFW (**10**).

NmFW (10**):**

Yield = 0.45 g (0.84 mmol, 77.59 %, ^1H NMR (400 MHz, $\text{DMSO}-d_6$, δ_{ppm}): 12.67 (s, 1H, $-\text{COOH}$), 10.89 (s, 1H, $-\text{NH}-$ proton of heterocyclic ring), 8.31 (m, 1H), 7.90 (m, 4H), 7.79 (s, 1H), 7.52 (m, 5H), 7.36 (d, 3H), 7.23 (t, 2H), 7.07 (d, 2H), 5.11 (s, 2H), 4.55 (m, 1H, C^αH of Trp), 4.34 (m, 1H, C^αH of Phe), 3.24 (m, 1H, C^βH of Trp), 3.12 (m, 1H, C^βH of Trp), 3.00 (m, 1H, C^βH of Phe), 2.74 (m, 1H, C^βH of Phe); ^{13}C NMR (100 MHz, $\text{DMSO}-d_6$, δ_{ppm}): 173.17, 171.60, 155.82, 138.05, 136.03, 134.57, 132.64, 132.39, 129.17, 127.96, 127.88, 127.65, 127.53, 127.21, 126.26, 126.18, 126.03, 125.98,

125.52, 123.64, 120.90, 118.37, 118.17, 111.32, 109.54, 65.32, 56.00, 52.93, 37.37, 27.00; MS (ESI) m/z for $C_{32}H_{29}N_3O_5Na$ ($M+Na$)⁺ calcd.: 558.2005, found: 558.0850.

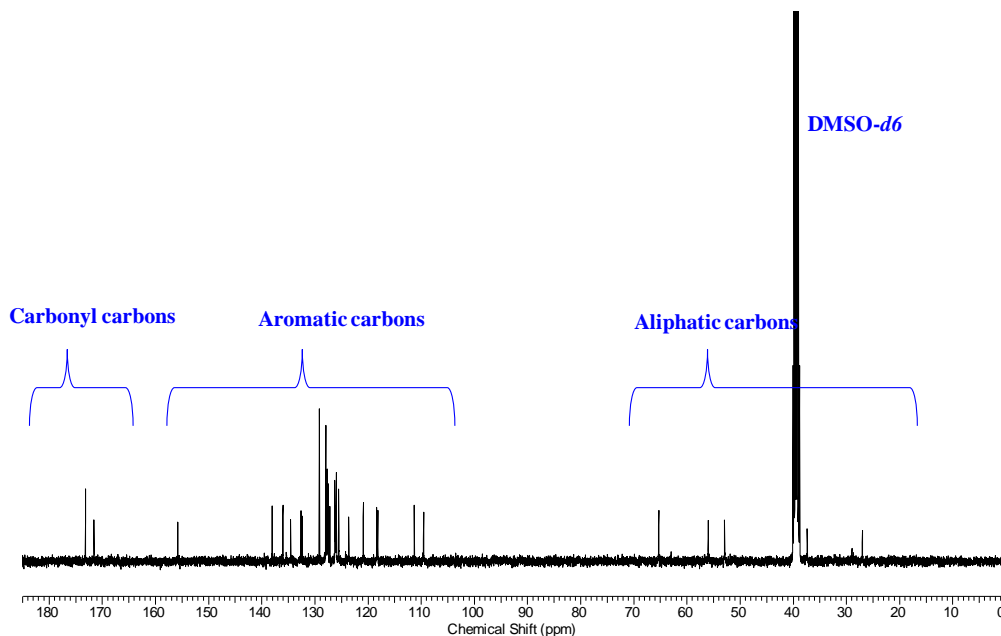


Figure 7.5. ^{13}C NMR spectrum (100 MHz, DMSO- d_6) of NmFW (10).

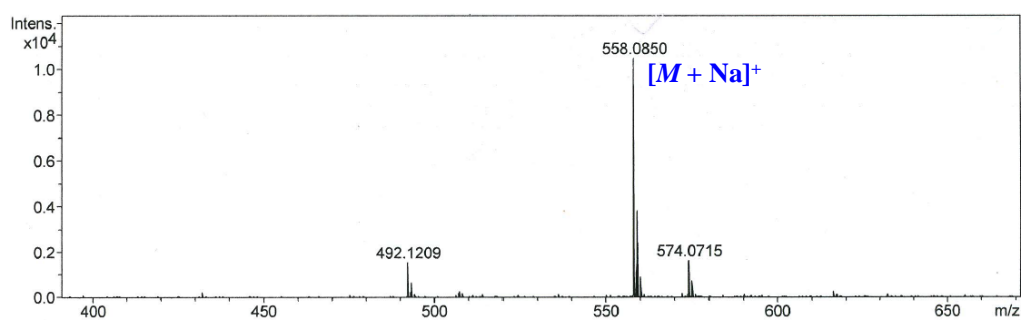


Figure 7.6. ESI-MS spectrum of NmFW (10).

NmFY (11):

Yield = 0.50 g (0.98 mmol, 86.20 %; 1H NMR (400 MHz, DMSO- d_6 , δ_{ppm}): δ = 12.67 (s, 1H, -COOH), 9.22 (s, 1H, -NH- of Tyr), 8.21 (d, 1H, J = 7.8 Hz, -NH- of Phe), 7.92-7.85 (m, 4H), 7.78 (s, 1H), 7.53-7.50 (m, 2H), 7.37 (d, 1H, J = 8.5 Hz), 7.29-7.22 (m, 5H), 7.19 (d, 1H), 7.04 (d, 2H, J = 8.3 Hz), 6.67 (d, 2H, J = 8.3 Hz), 5.10 (s, 2H), 4.40 (m, 1H, C^α H of Phe), 4.30 (m, 1H, C^α H of Tyr), 3.00 (m, 1H, C^β H of Phe), 2.96 (m, 1H, C^β H of Phe), 2.85 (m, 1H, C^β H

of Tyr), 2.72 (m, 1H, C^β H of Tyr); ¹³C NMR (100 MHz, DMSO-*d*₆, δ_{ppm}): 172.85, 171.51, 156.82, 155.93, 155.77, 138.04, 134.55, 132.65, 132.40, 130.08, 129.16, 127.98, 127.88, 127.66, 127.54, 127.30, 126.26, 126.04, 125.97, 125.51, 114.98, 65.31, 55.98, 53.79, 37.34, 35.93; MS (ESI) *m/z* for C₃₀H₂₈N₂O₆H (*M*+H)⁺ calcd.: 513.2026, found: 513.0594.

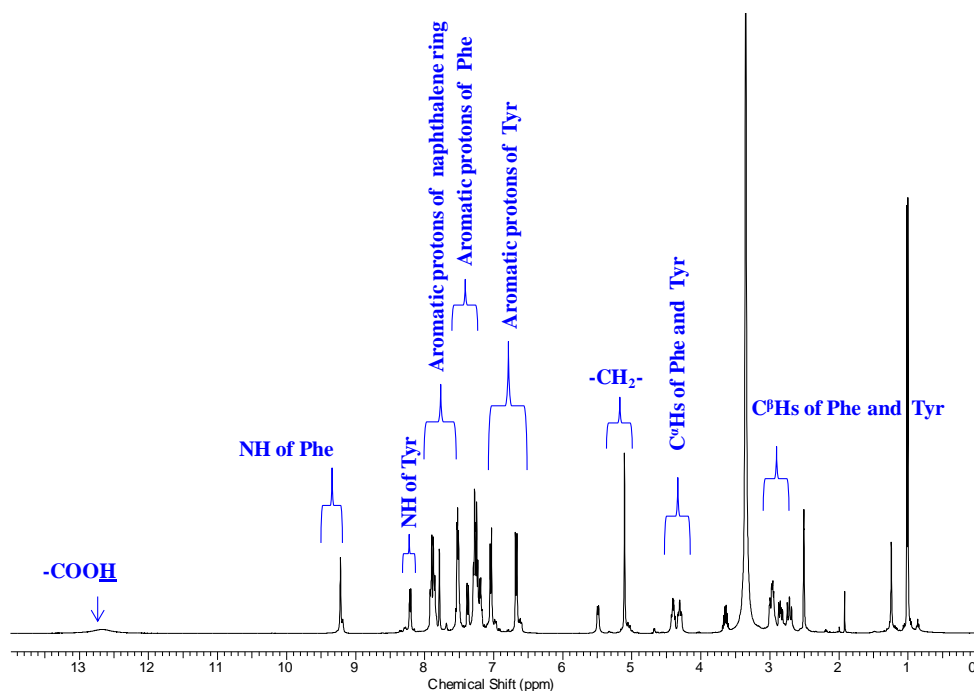


Figure 7.7. ¹H NMR spectrum (400 MHz, DMSO-*d*₆, δ_{ppm}) for NmFY (**11**).

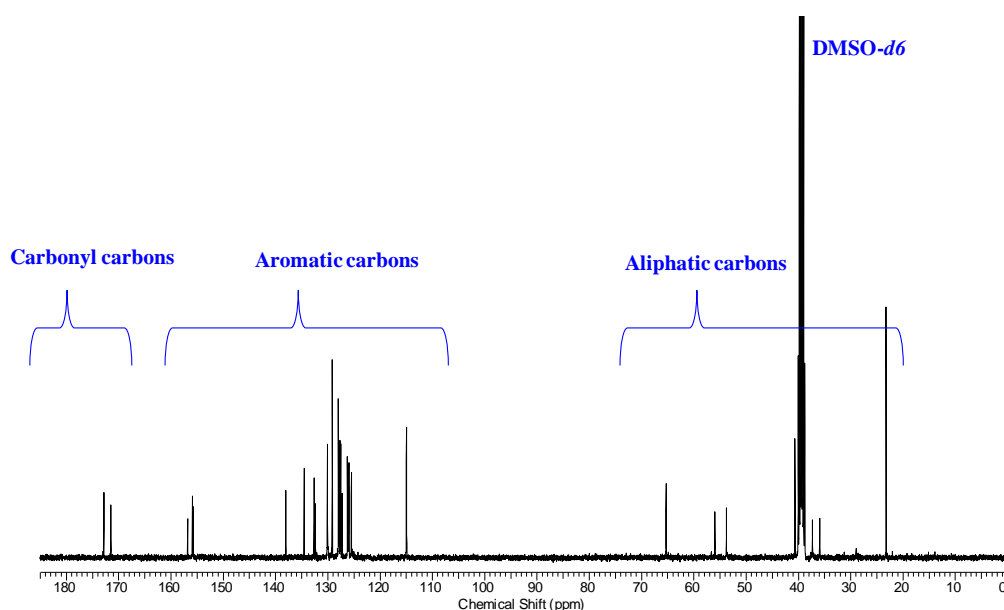


Figure 7.8. ¹³C NMR spectrum (100 MHz, DMSO-*d*₆) of NmFY (**11**).

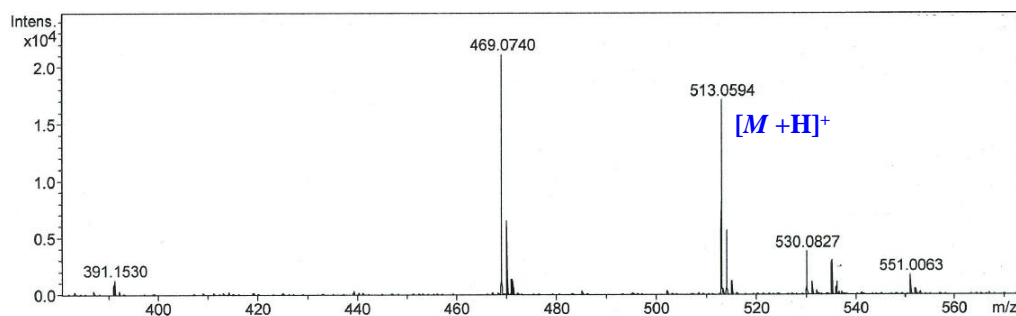


Figure 7.9. ESI-MS spectrum of NmFY (**11**).

Electrochemical synthesis of nanoscale hybrids

ITO coated glass substrate was cleaned by scrubbing with soap water and then sonicated in baths of water, ethanol and water. Electrochemical deposition was carried out in 24 mL solution (1:1 v/v) DMSO/water of 0.04 M of each $\text{Co}(\text{NO}_3)_2 \cdot 6\text{H}_2\text{O}$, $\text{Ni}(\text{NO}_3)_2 \cdot 6\text{H}_2\text{O}$ and $\text{Zn}(\text{NO}_3)_2 \cdot 6\text{H}_2\text{O}$ with 6.0-12.0 mg of each peptide (**9-11**). Working electrode (ITO) was placed upright in cell and deposition was performed potentiodynamically at -0.9 V for 1-3 hours depending upon the growth time under constant stirring at 80°C in water bath. After deposition, films were rinsed with de-ionized water and dried under a flow of nitrogen gas.

7.3 General characterization

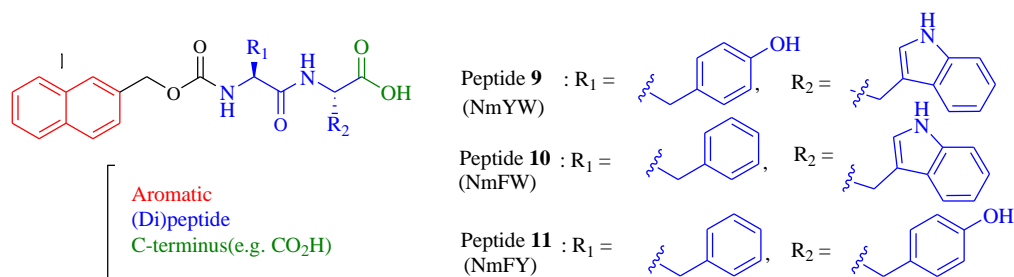
NMR characterizations were recorded on a Bruker AV spectrometer with working frequencies of 400 MHz for ^1H NMR. Compound concentrations were in the range of 5-10 mmolL^{-1} in $(\text{CD}_3)_2\text{SO}$ and CDCl_3 . Mass characterizations were recorded on a Bruker microTOF-Q II mass spectrometer by positive and negative mode electrospray ionization. FTIR characterizations were recorded using Bruker (Tensor 27) FTIR spectrophotometer. For SEM measurements, the images were recorded on a field-gun scanning electron microscope (Jeol Scanning Microscope-JSM-7600F). Hybrid thin films were investigated using Rigaku SmartLab, Automated Multipurpose X-ray Diffractometer ($\text{Cu K}\alpha$, $\lambda = 0.1541 \text{ nm}$). The electrodepositions were performed using an AUTOLAB potentiostat (Model PG STAT302N). Cyclic voltammograms and chronopotentiometry were recorded on AUTOLAB potentiostat (Model PG STAT302N). A conventional three-electrode cell assembly consisting of Ag/AgCl electrode (Model

6.0726.107) as reference electrode, platinum wire as counter electrode and peptide/metal hydroxide deposited ITO as working electrode, was used for carrying out electrochemical measurements.

7.4 Results and Discussion

7.4.1 Designing of peptides

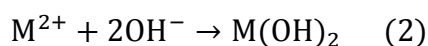
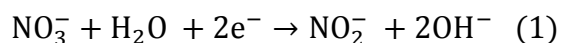
Structurally, peptide molecules contain three fundamental units. N-capped aromatic rings, dipeptide backbone and a carboxylic acid functional group as depicted in Scheme 7.2. Aromatic rings contribute in self-assembling of peptide domain through π - π stacking interactions whereas carboxylic acid functional group binds with inorganic component covalently for providing structural stability to the nanohybrid architecture.^[42] Moreover, amide bonds of peptide help in the formation of peptide self-assembly within the inorganic phases through intermolecular H-bonding interactions.^[52] Peptide serves several functions during electrochemical self-assembly of nanohybrids. Peptides (i) are used in the electrochemical growth of inorganic-organic hybrid nanostructures similar to conventional surfactants sodium dodecyl sulphate (SDS), cetyltrimethylammonium bromide (CTAB) and decanoic acid, (ii) interact with the inorganic component during electrochemical growth at the solid-liquid interfaces (*i.e.* the working electrode surface) due to surface forces (electrostatic interaction between the carboxylic functional group and surface charges) at a definite concentration, (iii) act as a capping agent on the nucleated crystal surface to give a definite size and shape to the inorganic component, (iv) prevent the aggregation of early formed nucleated inorganic particles and (v) forms self-assembly on the electrode surface due to interfacial tension.^[55,56] It is indicated that owing to the biocompatibility, structure stability and excellent properties, peptides have several advantages over conventional surfactants. Therefore, the efforts have been made to synthesize different peptide molecules for constructing beneficial nanostructures. In this study we have synthesized three peptide molecules namely NmYW (**1**), NmFW (**2**) and NmFY (**3**) by altering the amino acid sequences. Synthetic route of peptides has been shown in Scheme 7.1.



Scheme 7.2. Molecular structure of peptides **9** (NmYW), **10** (NmFW) and, **11** (NmFY).

7.4.2 Electrodeposition of peptide/M(OH)₂

The synthesized peptides are used in electrodeposition of three different metal hydroxides Co(OH)₂, Ni(OH)₂ and Zn(OH)₂ to show the efficient role of peptides as nanostructure directing agent towards transition metal hydroxides. Here we have constructed nine (3-11) peptide/metal hydroxides hybrids from all possible combinations of each three different peptides with each three different metal hydroxides. The electrochemical reactions involved during the formation of peptide/M(OH)₂ are shown in equation 1-2.



M = transition metal [Co, Ni, Zn]

The formation of OH⁻ ions near the substrate causes M(OH)₂ to nucleate and coassemble with peptides on the top of electrode surface.

7.4.3 Characterization of nanoscale hybrid thin films

We have used SEM to visualize the external surface feature of the electrodeposited peptide/metal hydroxide hybrid thin films as shown in Figure 7.10. We observed that the nanoscale morphologies of the hybrid thin films have dependence on the types of peptide and M(OH)₂ used for electrodeposition. Peptides NmYW, NmFW and NmFY direct sea sponge like soft, porous nanoarchitecture with Co(OH)₂ (Figure 7.10 a-c) whereas with Ni(OH)₂, peptides do not exhibit porous nanostructure (Figure 7.10 d-f). The

vertically oriented and closely packed nanosheets are found in SEM characterization of peptides NmYW, NmFW and NmFY with $\text{Zn}(\text{OH})_2$ (Figure 7.10 g-i). The supramolecular organization of peptide/ $\text{Co}(\text{OH})_2$ and peptide/ $\text{Ni}(\text{OH})_2$ shows spherical shaped nanoarchitecture.

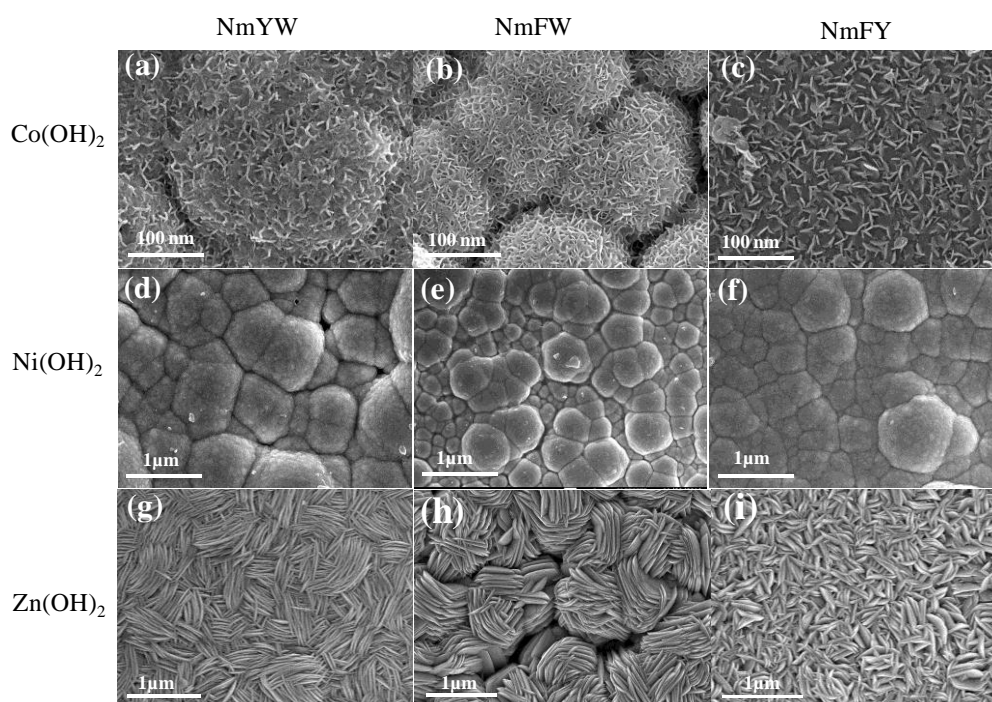


Figure 7.10. FE-SEM images of peptide/ $\text{M}(\text{OH})_2$: $\text{Co}(\text{OH})_2$ nanostructure hybrid films with three peptides (top row), (a) hybrid 3: Compound 9/ $\text{Co}(\text{OH})_2$, (b) hybrid 4: Compound 10/ $\text{Co}(\text{OH})_2$ and (c) hybrid 5: Compound 11/ $\text{Co}(\text{OH})_2$; $\text{Ni}(\text{OH})_2$ nanostructure hybrid films with three different peptides (middle row), (d) hybrid 6: Compound 9/ $\text{Ni}(\text{OH})_2$, (e) hybrid 7: Compound 10/ $\text{Ni}(\text{OH})_2$ and (f) hybrid 8: Compound 11/ $\text{Ni}(\text{OH})_2$; $\text{Zn}(\text{OH})_2$ nanostructure hybrids films with three different peptides (bottom row), (g) hybrid 9: Compound 9/ $\text{Zn}(\text{OH})_2$, (h) hybrid 10: Compound 10/ $\text{Zn}(\text{OH})_2$ and (i) hybrid 11: Compound 11/ $\text{Zn}(\text{OH})_2$.

The energy dispersive X-ray spectroscopy was used for elemental analysis of carbon, nitrogen, oxygen and transition metals in three peptide/ $\text{M}(\text{OH})_2$ hybrids (hybrid 3, 6 and 9) as presented in Figure 7.11. The spectra of the hybrid thin films indicates that the peaks can be identified as arising from the films due to the presence of C, N, O and Co in NmYW/ $\text{Co}(\text{OH})_2$, C, N, O and Ni in NmYW/ $\text{Ni}(\text{OH})_2$ and C, N, O and Zn in NmYW/ $\text{Zn}(\text{OH})_2$. Peptide NmFW and NmFY containing hybrids (4-5, 7-8

and 10-11) also indicate the presence of both the components, *i.e.* peptide and metal hydroxide (Figure 7.12).

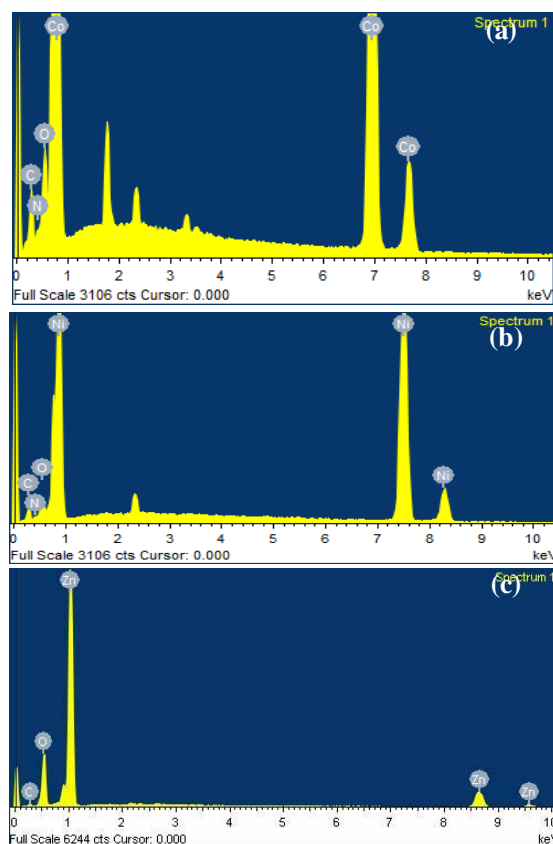
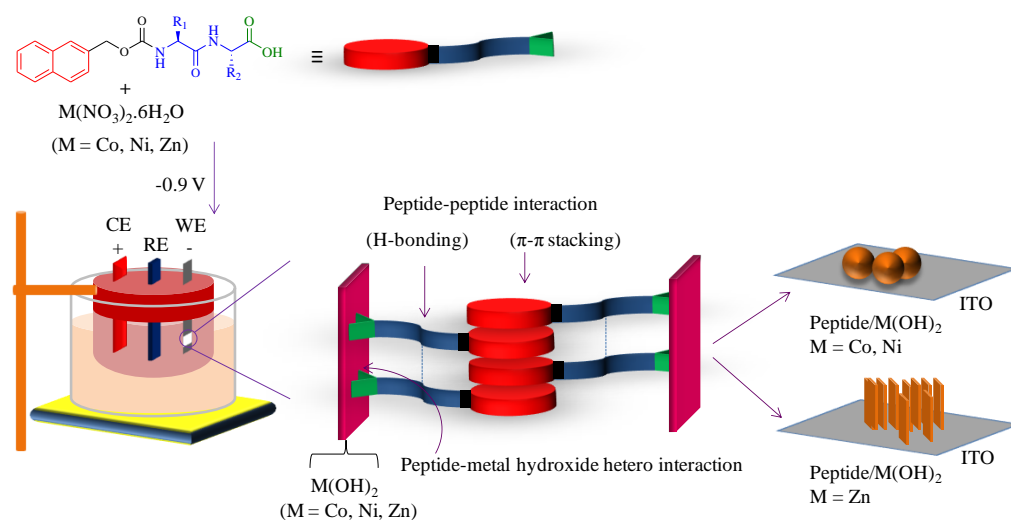


Figure 7.11. EDS spectra of peptide/metal hydroxide hybrid films; (a) hybrid **3**: NmYW/Co(OH)₂, (b) hybrid **6**: NmYW/Ni(OH)₂ and (c) hybrid **9**: NmYW/ Zn(OH)₂.



Scheme 7.3. Schematic illustration of two major interactions during the electrochemical growth of peptide-metal hydroxide nanospheres and nanosheets.

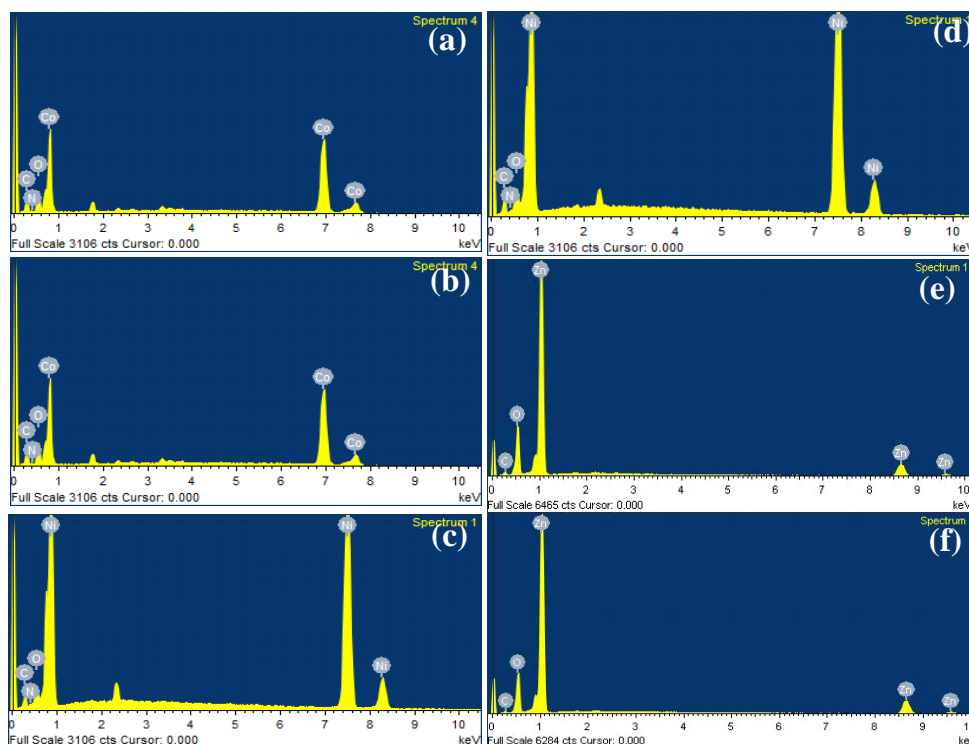


Figure 7.12. EDS spectra of peptide/M(OH)₂: (a) hybrid **4**: NmFW/Co(OH)₂, (b) hybrid **5**: NmFY/Co(OH)₂, (c) hybrid **7**: NmFW/Ni(OH)₂, (d) hybrid **8**: NmFY/Ni(OH)₂, (e) hybrid **10**: NmFW/Zn(OH)₂ and (f) hybrid **11**: NmFY/Zn(OH)₂.

Fourier transform infrared spectroscopy is an important analytical technique which was employed to detect the interactions among peptides and peptides-metal hydroxides in different nanoscale hybrids as shown in Figure 7.13a. The IR characteristic absorption band in peptide NmYW corresponding to --C=O (--COOH) stretching vibration was observed at 1703 cm^{-1} . The peak due to --C=O str. (--COOH) is found absent in IR spectra of hybrids NmYW/Co(OH)₂, NmYW/Ni(OH)₂ and NmYW/Zn(OH)₂.^[57] It reveals that there is a covalent bonding between carboxylic group of dipeptide amphiphile and metal hydroxide suggesting the peptide-metal hydroxide hetero interactions. The characteristic vibrational mode near 3303 cm^{-1} corresponds to --OH (--COOH) stretching vibration for peptide NmYW. It is found that the IR band due to --OH str. (--COOH) is disappeared in IR spectra of hybrids NmYW/Co(OH)₂, NmYW/Ni(OH)₂ and NmYW/Zn(OH)₂, confirming the occurrence of covalent bonding between peptide and metal hydroxides. In addition, in peptide/metal hydroxide hybrid materials a new sharp peak due to --OH stretching of metal hydroxide is found to be noticed. For the

NmYW/Co(OH)₂ hybrid the –OH frequency was shifted from 3628 cm⁻¹ (for pure Co(OH)₂) to 3437 cm⁻¹ suggesting a chemical interaction between peptide NmYW and Co(OH)₂.^[58] For NmYW/Ni(OH)₂ hybrid an intense band at 3437 cm⁻¹ is attributed to –OH stretching, which is observed at 3462 cm⁻¹ in pure Ni(OH)₂.^[57] Similarly in case of NmYW/Zn(OH)₂ hybrid an IR band near 3435 cm⁻¹ is observed resulting from stretching vibration mode of hydroxyl group (-OH) of zinc hydroxide.^[59] Moreover, the amide I band in peptide NmYW is noticed at 1652 cm⁻¹ being mainly associated with the –C=O stretching vibrations and directly related to backbone conformation. This band is shifted to low wave number in the range from 1638 cm⁻¹ to 1627 cm⁻¹ for NmYW/Co(OH)₂, NmYW/Ni(OH)₂ and NmYW/Zn(OH)₂ hybrids due to the supramolecular organization of peptides confirming the intermolecular β -sheet conformation.^[60-62] In addition vibrational modes due to –C=O str. (–COOH), –OH str. (–COOH) and –C=O str. (amide I) for peptides NmFW, NmFY and other vibrations (–OH str.) related to hybrid materials (4-5, 7-8 and 10-11) have been shown in Figure 7.14. IR data obtained using different hybrid material shows that the interactions among peptides and peptides-metal hydroxides give significant contribution in construction of hybrid nanoarchitectures. These interactions are shown in Scheme 7.3.

The X-ray diffraction patterns of NmYW, NmYW/Co(OH)₂, NmYW/Ni(OH)₂ and NmYW Zn(OH)₂ are depicted in the Figure 7.13b. The diffraction peaks represent organic-inorganic hybrid formation and metal hydroxide phases. Peptide NmYW shows a broad peak at 2 θ of 19.60°. The broad peak is attributed to the amorphous nature of peptide. XRD pattern of hybrid NmYW/Co(OH)₂ displays two distinct kind of peak profile. The strong and broad diffraction peak around 20° (001) is a result of peptide-metal hydroxide hybrid formation.^[63, 64] The sharp diffraction peaks of (100), (101) and (110) indicate β -Co(OH)₂ phases.^[65] Similar trends are also found in case of hybrids NmFW/Co(OH)₂ and NmFY/Co(OH)₂ (Figure 7.15). In case of hybrid NmYW/Ni(OH)₂, broad peak corresponding to (001) is found responsible for the formation of peptide-Ni(OH)₂ hybrid.^[63, 64] The sharp diffraction peaks of (101) and (102) represent hexagonal phases of Ni(OH)₂, assembling into flower like Ni(OH)₂ microspheres^[63] which is also supported by SEM images as shown in Figure 7.10. NmFW and NmFY containing

Ni(OH)₂ hybrids show similar XRD patterns (Figure 7.15). In the XRD pattern of NmYW/Zn(OH)₂, a broad diffraction peak at 2θ of 20° (001) arises due to the NmYW/Zn(OH)₂ organic–inorganic hybrid network.^[63, 64] The sharp diffraction peaks of (100), (002), (101), (102), (110), (103), (201) and (112) indicate the hexagonal phases of Zn(OH)₂.^[66] Hybrid NmFW/ Zn(OH)₂ and NmFY/Zn(OH)₂ also display the similar trend shown in Figure 7.15.

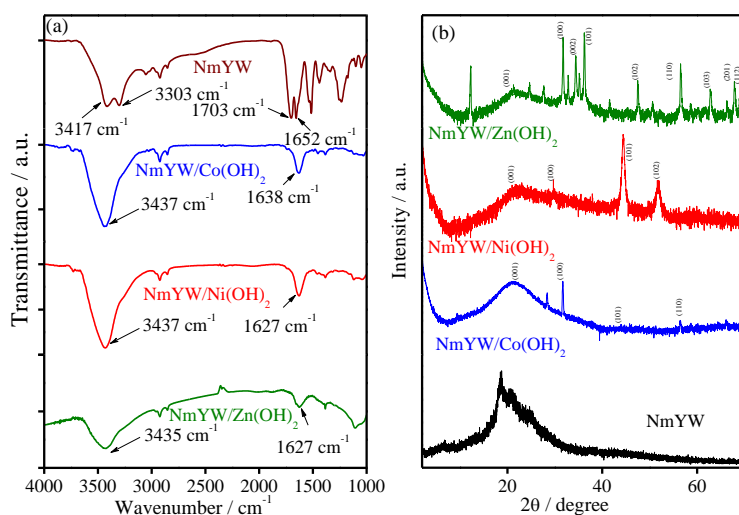


Figure 7.13. FTIR and XRD spectra of NmYW (peptide **9**), NmYW/Co(OH)₂ (hybrid **3**), NmYW/Ni(OH)₂ (hybrid **6**) and NmYW/Zn(OH)₂ (hybrid **9**).

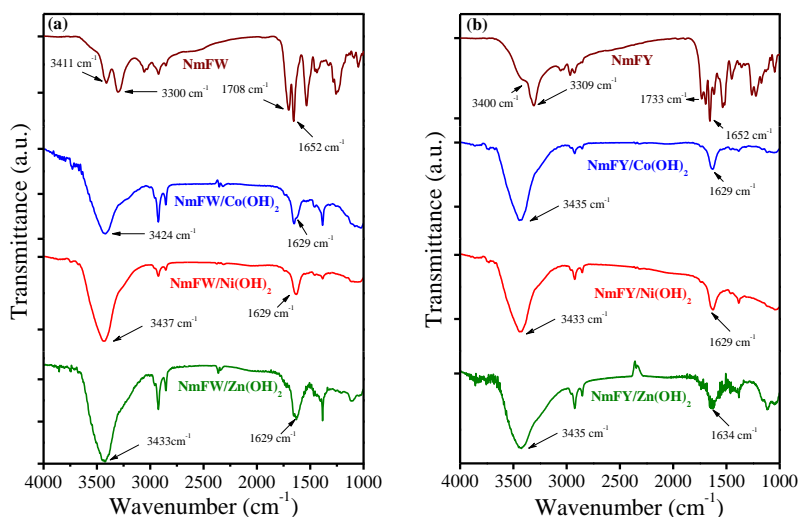


Figure 7.14. FTIR spectra of (a) NmFW (peptide **10**), NmFW/Co(OH)₂ (hybrid **4**), NmFW/Ni(OH)₂ (hybrid **7**), NmFW/Zn(OH)₂ (hybrid **10**) and (b) NmFY (peptide **11**), NmFY/CO(OH)₂ (hybrid **5**), NmFY/Ni(OH)₂ (hybrid **8**) and NmFY/Zn(OH)₂ (hybrid **11**).

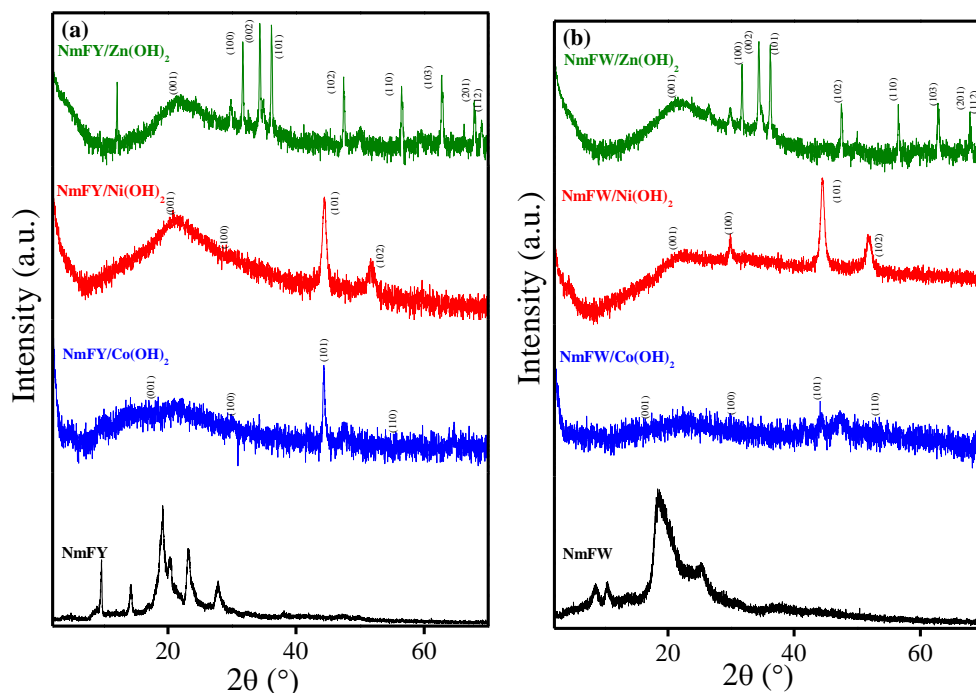
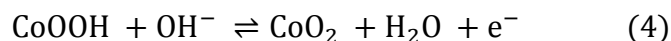
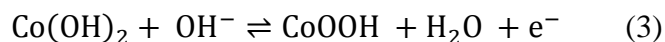


Figure 7.15. XRD spectra of (a) NmFW (peptide **10**), NmFW/Co(OH)₂ (hybrid **4**), NmFW/Ni(OH)₂ (hybrid **7**), NmFW/Zn(OH)₂ (hybrid **10**) and (b) NmFY (peptide **11**), NmFY/Co(OH)₂ (hybrid **5**), NmFY/Ni(OH)₂ (hybrid **8**) and NmFY/Zn(OH)₂ (hybrid **11**).

3.4 Electrochemical behavior of hybrid thin films

Cyclic voltammetry and chronopotentiometry are considered to be ideal analytical tools to indicate the capacitive behaviour of any material. Figure 7.16a shows the typical cyclic voltammograms recorded for pure peptide (NmYW) and hybrid thin film of NmYW/Co(OH)₂. The CV curves were obtained by scanning the potential between -0.3 V to 0.5 V in presence of 4 M of KOH electrolyte at a scan rate of 20 mV s⁻¹. Four strong redox peaks arise in the cyclic voltammogram of NmYW/Co(OH)₂. Anodic peak P₁ is attributed to the oxidation of Co(OH)₂ to cobalt oxyhydroxide (CoOOH) and cathodic peak P₂ is observed for reverse process. Another oxidation peak P₃ is attributed due to the oxidation of CoOOH to CoO₂ and peak P₄ corresponds to the reverse reaction of CoO₂ to CoOOH. The potential difference between anodic and cathodic peaks (P₁ and P₂) is 0.06 V which is very close to theoretical ΔE_p value 0.058 V, suggesting the reversible nature of redox couple. Another redox couple (P₃/P₄) shows potential difference 0.1 V, which

is higher than the theoretical ΔE_p value 0.058 V of reversible process, stating that the reaction occurs in quasi-reversible manner.^[58,67-69] The complete redox process for NmYW/Co(OH)₂ is described as following.



The charge-discharge measurements is used to calculate the specific capacitance of NmYW/Co(OH)₂ nano hybrid thin film (Fig. 7.16b). The specific capacitance of NmYW/Co(OH)₂ is found to be 3070 Fg⁻¹. The high specific capacitance results from sponge like porous nanoarhiteture associated with the synergistic effect of peptide and metal hydroxide which regulates the fast faradic reaction on Co(OH)₂ phase within the electrolyte solution. Furthermore, cyclic voltammogram of pure peptide indicates that peptide does not provide any contribution in specific capacitance of peptide/Co(OH)₂. We also recorded cyclic voltammograms of different scan rates at 20, 50 and 100 mV s⁻¹ and observed that as the scan rate increases, the overall shape of CV curves is still maintained, indicating high performance as shown in Figure 7.17a. These redox processes are reproducible through repeated scanning and are depicted in Figure 7.17b.

The cyclic voltammogram of NmYW/Ni(OH)₂ indicates that anodic peak is appeared due to oxidation of Ni(OH)₂ to Nickel oxyhydroxide (NiOOH) and cathodic peak is observed for reverse process (Figure 7.16c). Electrochemical redox reaction for peptide/Ni(OH)₂ is stated as below.



The specific capacitance of peptide/Ni(OH)₂ is found to be 250 Fg⁻¹ using charge-discharge curve (Figure 7.16d). There is no contribution of peptide found in specific capacitance of peptide/ Ni(OH)₂. The specific capacitance of peptide/Ni(OH)₂ is dramatically lower than usual,^[70] which can be correlated with the SEM observations (Figure 7.10, hybrid 6-8), exhibiting non porous structure of peptide/Ni(OH)₂. The cyclic voltammograms recorded at different scan rates and repetitive cycles exhibit high performance and long term stability of hybrid thin film as shown in Figure 7.17c, and 7.17d. For the

peptide/ $\text{Zn}(\text{OH})_2$ hybrid marix in which metal cation (Zn^{2+}) is electrochemically silent, no peak is observed in cyclic voltammetric experiments.^[71]

In summary, the present results describe that peptide/metal hydroxide hybrid films are successfully deposited using potentiodynamically mode of electrodeposition which is further confirmed by excellent electrochemical capacitive behaviour of nanostructured hybrid thin films.

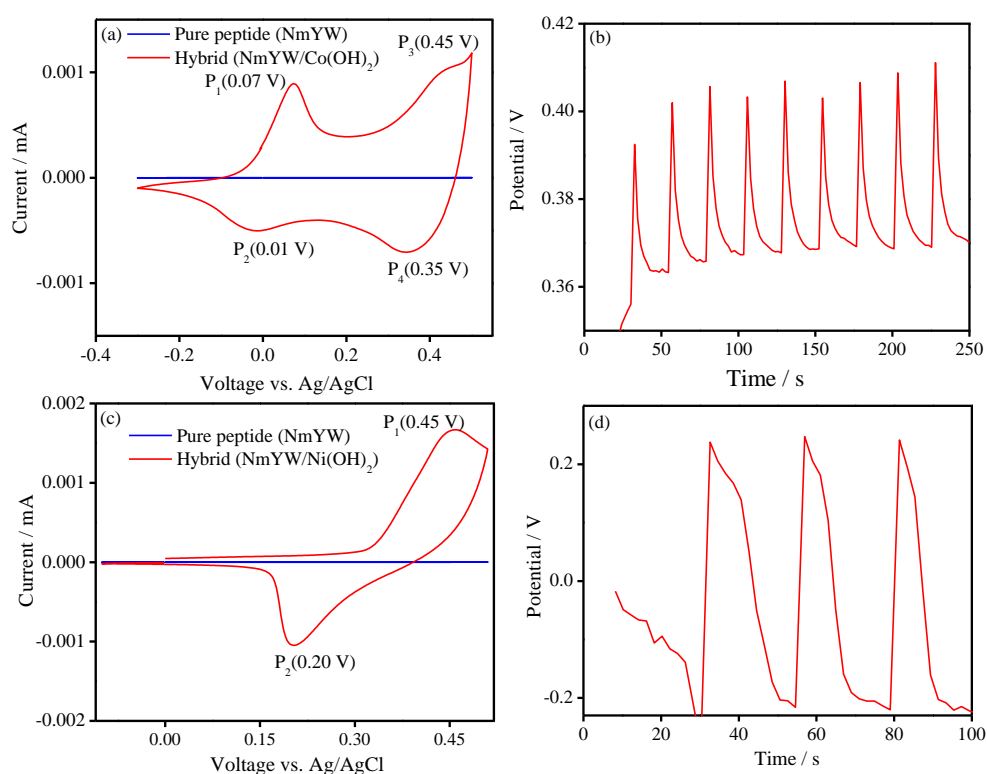


Figure 7.16. (a) Cyclic voltammograms of NmYW and NmYW/Co(OH)₂ recorded by scanning the potential from -0.3 to 0.5 V at scan rate of 20 mV s⁻¹, (b) charging–discharging curve of NmYW/Co(OH)₂ in 4 m KOH with a potential window of -0.2 to 0.6 V vs. Ag/AgCl, discharging curve obtained at 5 mA. (c) Cyclic voltammograms of NmYW and NmYW/Ni(OH)₂ recorded by scanning the potential from -0.3 to 0.6 V at a scan rate of 20 mV s⁻¹ and (d) charging–discharging curve of NmYW/Ni(OH)₂ in 4 m KOH with a potential window of -0.2 to 0.6 V vs. Ag/AgCl, discharging curve obtained at 6 mA.

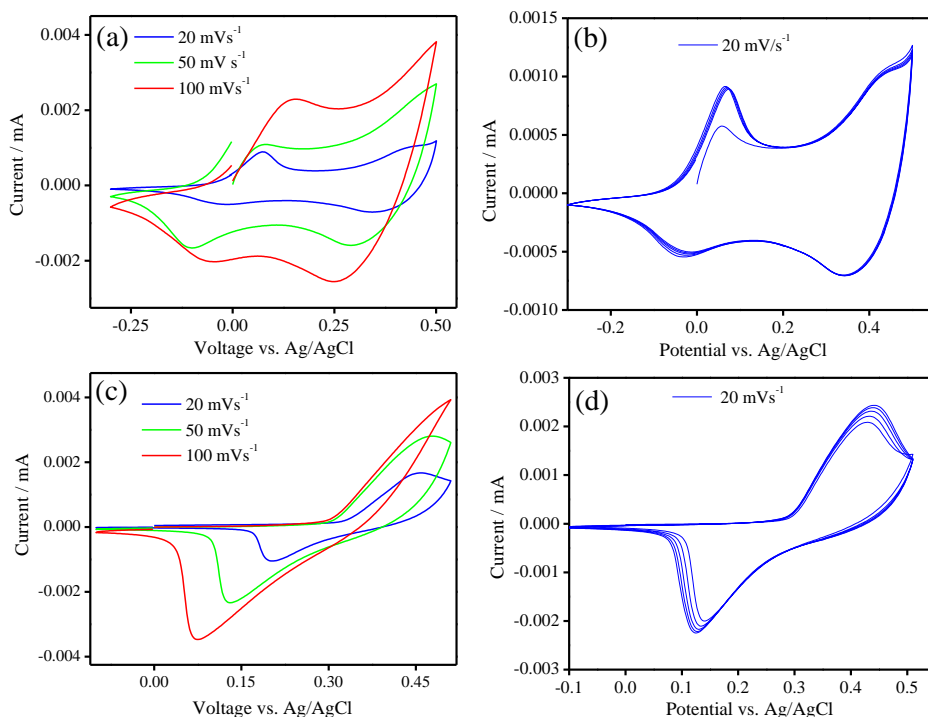


Figure 7.17. (a)-(b) Cyclic voltammogram of NmYW/Co(OH)₂ at different scan rates and repetitive 5 cycles at scan rate of 20 mVs⁻¹ respectively. (c)-(d) Cyclic voltammogram of NmYW/Ni(OH)₂ at different scan rates and repetitive 5 cycles at scan rate of 20 mVs⁻¹ respectively. Experiments performed in 4 M aqueous KOH solution.

7.5 Conclusion

In conclusion, a strategy of self-assembly of peptide and metal hydroxide is designed to prepare hybrid nanostructures for the purpose developing electrochemically active materials. Small peptides with carboxylic acid functional group may become a new class of surfactants in electrochemical growth of variety of metal hydroxide nanostructure. Role of peptide on the hybrid is to act as a structure directing agent as well as to stabilize the nano architecture by peptide-peptide and peptide-metal hydroxide hetero interaction. The unique peptide/Co(OH)₂ hybrid nanoarchitecture with flat discharge plateau and triangular shape plot is found to exhibit capacitive electrochemical performance in energy storage applications. We also state that specific capacitance of peptide/Ni(OH)₂ hybrid films gets drop due to the non porous surface morphology. The studies described here point to the possibility of creating novel peptide/metal hydroxide supramolecular

arrangement with desired structural and electrochemical properties. This method could be extended to other performed nanostructures and it could also promote the development of other functional peptide/metal hydroxide nanohybrids. The detail of peptide effect on growth of such hybrids and the applications in various electrical components is ongoing in our laboratory.

7.6 References

- [1] Cao L., Kong L.-B., Liang Y.-Y., Li H.-L. (2004), Preparation of novel nano-composite $\text{Ni}(\text{OH})_2/\text{USY}$ material and its application for electrochemical capacitance storage, *Chem. Commun.*, 1646-1647 (DOI: 10.1039/B401922A).
- [2] Cheng J. P., Zhang J., Liu F. (2014), Recent development of metal hydroxides as electrode material of electrochemical capacitors, *RSC Adv.*, 4, 38893-38917 (DOI: 10.1039/C4RA06738J).
- [3] Ryu J., Kim S.-W., Kang K., Park C. B. (2010), Synthesis of diphenylalanine/cobalt oxide hybrid nanowires and their application to energy storage, *ACS Nano*, 4, 159-164 (DOI: 10.1021/nn901156w).
- [4] Simon P., Gogotsi Y. (2008), Materials for electrochemical capacitor, *Nat. Mater.*, 7, 845-854 (DOI:10.1038/nmat2297).
- [5] Cao L., Xu F., Liang Y.-Y., Li H.-L. (2004), Preparation of novel nanocomposite $\text{Co}(\text{OH})_2/\text{ultra-stable Y zeolite}$ and its application as a supercapacitor with high energy density, *Adv. Mater.*, 16, 1853-1857 (DOI: 10.1002/adma.200400183).
- [6] Li Z., Han J., Fan L., Wang M., Taoc S., Guo R. (2015), The anion exchange strategy towards mesoporous $\alpha\text{-Ni}(\text{OH})_2$ nanowires with multinanocavities for high-performance supercapacitors, *Chem. Commun.*, 51, 3053-3056 (DOI: 10.1039/C4CC09225B).
- [7] Gao X.-P., Yao S.-M., Yan T.-Y., Zhou Z. (2009), Alkaline rechargeable Ni/Co batteries: cobalt hydroxides as negative electrode materials, *Energy Environ. Sci.*, 2, 502-505 (DOI: 10.1039/B901934K).
- [8] Zhao W., Zhang C., Geng F., Zhuo S., Zhang B. (2014), Cobalt hydroxide/oxide hexagonal ring-graphene hybrids through chemical

- etching of metal hydroxide platelets by graphene oxide: energy storage applications, *ACS Nano*, 8, 2755-2765(DOI: 10.1021/nn406480g).
- [9] Zhou J., Li J., Liu K., Lan L., Song H., Chen X. (2014), Free-standing cobalt hydroxide nanoplatelet array formed by growth of preferential-orientation on graphene nanosheets as anode material for lithium-ion batteries. *J. Mater. Chem. A*, 2, 20706-20713 (DOI: 10.1039/C4TA05073H).
- [10] Vidotti M., Greco C. V., Ponzio E. A., Torresi S. I. C. D. (2006), Sonochemically synthesized Ni(OH)₂ and Co(OH)₂ nanoparticles and their application in electrochromic electrodes, *Electrochem. Commun.*, 8, 554-560 (DOI: 10.1016/j.elecom.2006.01.024).
- [11] Chia-Chingn L. (2012), Lithium-driven electrochromic properties of electrodeposited nickel hydroxide electrodes, *Solar Energy Materials & Solar Cells*, 99, 26-30 (DOI: 10.1016/j.solmat.2011.12.001).
- [12] Gao M., Sheng W., Zhuang Z., Fang Q., Gu S., Jiang J., Yan Y. (2014), Efficient water oxidation using nanostructured α -nickel-hydroxide as an electrocatalyst, *J. Am. Chem. Soc.*, 136, 7077-7084 (DOI: 10.1021/ja502128j).
- [13] Zhang Y., Cui B., Derr O., Yao Z., Qin Z., Deng X., Li J., Lin H. (2014), Hierarchical cobalt-based hydroxide microspheres for water oxidation, *Nanoscale*, 6, 3376-3383 (DOI: 10.1039/C3NR05193E).
- [14] Deng X., Tuysuz H. (2014), Cobalt-oxide-based materials as water oxidation catalyst: recent progress and challenges, *ACS Catal*, 4, 3701-3714 (DOI: 10.1021/cs500713d).
- [15] Schenning A. P. H. J., Meijer E. W. (2005), Supramolecular electronics; nanowires from self-assembled π -conjugated Systems, *Chem. Commun.*, 3245–3258 (DOI: 10.1039/b501804h).
- [16] Babu S. S., Praveen V. K., Ajayaghosh A. (2014), Functional π -gelators and their applications, *Chem. Rev.*, 114, 1973–2129 (DOI: 10.1021/cr400195e).
- [17] Sanchez C., Soler-Illia G. J. D. A. A., Ribot F., Grosso D. (2003), Design of functional nano-structured materials through the use of controlled hybrid organic-inorganic interfaces, *C. R. Chimie*, 6, 1131-1151 (DOI: 10.1016/j.crci.2003.06.001).

- [18] Inoue S., Fujihara S. (2010), Synthesis of inorganic-organic layered compounds using immiscible liquid-liquid systems under the distribution law. *Langmuir*, 26, 15938-15944 (DOI: 10.1021/la1028542).
- [19] Briseno A. L., Holcombe T. W., Boukai A. I., Garnett E. C., Shelton S. W., Frechet J. J. M., Yang P. (2010), Oligo- and polythiophene/ZnO hybrid nanowire solar cells, *Nano Lett.*, 10, 334-340 (DOI: 10.1021/nl9036752).
- [20] Li L.-L., Fu X.-F., Ren Z., Zhao Y.-G., Feng W., Yan C.-H. (2010), Hierarchical self-assembly of superlattice hybrids consisting of periodic and alternating cores of porphyrin molecules separated by nanoscale silica walls, *Langmuir*, 26, 15730-15733 (DOI: 10.1039/C4CC05192K).
- [21] Raeburn J., Alston B., Kroeger J., McDonald T. O., Howse J. R., Cameron P. J., Adams D. J. (2014), Electrochemically-triggered spatially and temporally resolved multi-component gels, *Mater. Horiz.*, 1, 241-246 (DOI: 10.1021/la1034036).
- [22] Peng L., Feng A., Huo M., Yuan J. (2014), Ferrocene-based supramolecular structures and their applications in electrochemical responsive systems, *Chem. Commun.*, 50, 13005-13014 (DOI: 10.1039/C3MH00150D).
- [23] Li M., Ishihara S., Akada M., Liao M., Sang L., Hill J. P., Krishnan V., Ma Y., Ariga K. (2011), Electrochemical-coupling layer-by-layer (ECCLbL) assembly, *J. Am. Chem. Soc.*, 133, 7348-7351 (DOI: 10.1021/ja202768k).
- [24] Choi K.-S., Lichtenegger H. C., Stucky G. D. (2002), Electrochemical synthesis of nanostructured ZnO films utilizing self assembly of surfactant molecules at solid-liquid interfaces, *J. Am. Chem. Soc.*, 124, 12402-12403 (DOI:10.1021/ja0275562).
- [25] Tan Y., Srinivasan S., Choi K.-S. (2005), Electrochemical deposition of mesoporous nickel hydroxide films from dilute surfactant solutions, *J. Am. Chem. Soc.*, 127, 3596-3604 (DOI: 10.1021/ja0434329).

- [26] Yarger S. M., Steinmillar E. M. P., Choi K.-S. (2007), Electrochemical synthesis of cobalt hydroxide films with tunable interlayer spacings, *Chem. Commun.*, 159-161(DOI: 10.1039/B609621B).
- [27] Steinmiller E. M. P., Choi K.-S. (2007), Anodic construction of lamellar structured ZnO films using basic media via interfacial surfactant templating, *Langmuir*, 23, 12710-12715 (DOI: 10.1021/la702066w).
- [28] Pichon B. P., Mezy A., Tedenac J.-C., Tichit D., Gerardin C. (2009), A soft chemistry route to prepare hybrid ZnO nanostructured films with a lamellar structure, *New J. Chem.*, 33, 2350-2354 (DOI: 10.1039/B9NJ00365G).
- [29] Pichon B. P., Leuvrey C., Ihiawakrim D., Tichit D., Geradin C. (2011), Films of tunable ZnO nanostructures prepared by a surfactant-mediated soft synthesis route, *J. Phys. Chem. C*, 115, 23695-23703 (DOI: 10.1021/jp2072149).
- [30] Boeckler C., Oekermann T., Feldhoff A., Wark M. (2006), Role of the critical micelle concentration in the electrochemical deposition of nanostructured ZnO films under utilization of amphiphilic molecules, *Langmuir*, 22, 9427-9430 (DOI: 10.1021/la0615544).
- [31] Herman D. J., Goldberger J. E., Chao S., Martin D. T., Stupp S. I. (2011), Orienting periodic organic-inorganic nanoscale domains through one-step electrodeposition, *ACS Nano*, 5, 565-573 (DOI: 10.1021/nn102697r).
- [32] Bruns C. J., Herman D. J., Minuzzo J. B., Lehrman J. A., Stupp S. I. (2013), Rationalizing molecular design in the electrodeposition of anisotropic lamellar nanostructures, *Chem. Mater.* 25, 4330-4339 (DOI: 10.1021/cm402505p).
- [33] Sofos M., Goldberger J., Stone D. A., Allen J. E., Ma Q., Herman D. J., Tsai W.-W., Lauhon L. J., Stupp S. I. (2009), A synergistic assembly of nanoscale lamellar photoconductor hybrids, *Nat. Mater.*, 8, 68-75 (DOI: 10.1038/NMAT2336).
- [34] Yoshida T., Zhang J., Komatsu D., Sawatani S., Minoura H., Pauporte T., Linkot D., Oekermann T., Schlettwein D., Tada H., Wohrle D., Funabiki K., Matsui M., Miura H., Yanagi H. (2009),

- Electrodeposition of inorganic/organic hybrid thin films, *Adv. Funct. Mater.*, 19, 17-43 (DOI: 10.1002/adfm.200700188).
- [35] Goux A., Pauporte T., Yoshida T., Lincot D. (2006), Mechanistic study of the electrodeposition of nanoporous self-assembled ZnO/eosin Y hybrid thin films: effect of eosin concentration, *Langmuir*, 22, 10545-10553 (DOI: 10.1021/la061199h).
- [36] Zhang J., Sun L., Ichinose K., Funabiki K., Yoshida T. (2010), Effect of anchoring groups on electrochemical self-assembly of ZnO/xanthene dye hybrid thin films, *Phys. Chem. Chem. Phys.*, 12, 10494-10502 (DOI: 10.1039/c002831b).
- [37] Rasale D. B., Das A. K. (2015), Chemical reactions directed peptide self-assembly, *Int. J. Mol. Sci.* 16, 10797-10820 (DOI: 10.3390/ijms160510797).
- [38] Rasale D. B., Maity I., Das A. K. (2014), In situ generation of redox active peptides driven by selenoester mediated native chemical ligation, *Chem. Commun.* 2014, 50, 11397-11400 (DOI: 10.1039/C4CC03835E).
- [39] Rasale D. B., Maity I., Das A. K. (2014), Lipase catalyzed inclusion of gastrodiginin for the evolution of blue light emitting peptide nanofibers, *Chem. Commun.* 50, 8685-8688 (DOI: 10.1039/C4CC02484B).
- [40] Rasale D. B., Maity I., Konda M., Das A. K. (2013), Peptide self-assembly driven by oxo-ester mediated native chemical ligation, *Chem. Commun.*, 49, 4815-4817 (DOI: 10.1039/C3CC41475B).
- [41] Rasale D. B., Konda M., Biswas S., Das A. K. (2016), Controlling peptide self-assembly through a native chemical ligation/desulfurization strategy, *Chem. - An Asian Journal*, 11, 926-935 (DOI: 10.1002/asia.201501458).
- [42] Fleming S., Ulijn R. V. (2014), Design of nanostructures based on aromatic peptide amphiphiles, *Chem. Soc. Rev.*, 43, 8150-8177 (DOI: 10.1039/c4cs00247d).
- [43] Gazit E. (2007), Self-assembled peptide nanostructures: the design of molecular building blocks and their technological utilization, *Chem. Soc. Rev.*, 36, 1263-1269 (DOI: 10.1039/b605536m).

- [44] Yan X., Zhu P., Li J. (2010), Self-assembly and application of diphenylalanine-based nanostructures, *Chem. Soc. Rev.*, 39, 1877-1890 (DOI: 10.1039/B915765B).
- [45] Ryu J., Kim S.-W., Kang K., Park C. B. (2010), Mineralization of self-assembled peptide nanofibers for rechargeable lithium ion batteries, *Adv. Mater.*, 22, 5537-5541 (DOI: 10.1002/adma.201000669).
- [46] Johnson E. K., Adams D. J., Cameron P. J. (2010), Directed self-assembly of dipeptides to form ultrathin hydrogel membranes, *J. Am. Chem. Soc.*, 132, 5130-5136 (DOI: 10.1021/ja909579p).
- [47] Chen L., Revel S., Morris K., Serpell L. C., Adams D. J. (2010), Effect of molecular structure on the properties of naphthalene-dipeptide hydrogelators, *Langmuir*, 26, 13466-13471 (DOI: 10.1021/la102059x).
- [48] Briggs B. D., Knecht M. R. (2012), Nanotechnology meets: peptide-based methods for the fabrication of functional materials, *J. Phys. Chem. Lett.*, 3, 405-418 (DOI: 10.1021/jz2016473).
- [49] Huang R., Qi W., Su R., Zhao J., He Z. (2011), Solvent and surface controlled self-assembly of diphenylalanine peptide: from microtubes to nanofibers, *Soft Matter*, 7, 6418-6421 (DOI: 10.1039/C1SM05752A).
- [50] Santis E. D., Ryadnov M. G. (2015), Peptide self-assembly for nanomaterials: the old new kid on the block, *Chem. Soc. Rev.*, 44, 8288-8300 (DOI: 10.1039/C5CS00470E).
- [51] Guo X., Matsui H. (2005), Peptide-based nanotube and their applications in bionanotechnology, *Adv. Mater.*, 17, 2037-2050 (DOI: 10.1002/adma.200401849).
- [52] Manna M. K., Pandey S. K., Maity I., Mukherjee S., Das A. K. (2015), Electrodeposited lamellar photoconductor nanohybrids driven by peptide self-assembly, *ChemPlusChem*, 80, 583-590 (DOI: 10.1002/cplu.201402348).
- [53] Verma S., Manna M. K., Das A. K., Mukherjee S. (2014), Benzo[ghi]perylene monoimide based photosensitive lamellar Cd-doped ZnO nanohybrids, *RSC Advances*, 4, 62603-62614 (DOI: 10.1039/c4ra13712d).

- [54] Manna M. K., Aaryashree, Verma S, Mukherjee S., Das A. K. (2016), Lamellar peptide-cadmium-doped zinc oxide nanohybrids that emit white light, *ChemPlusChem*, 81, 329-337 (DOI: 10.1002/cplu.201500402).
- [55] Steinmiller E. M. P., Choi K.-S. (2007), Anodic construction of lamellar structured ZnO films using basic media via interfacial surfactant templating, *Langmuir*, 23, 12710-12715 (DOI: 10.1021/la702066w).
- [56] Spray R. L., Choi K.-S. (2007), Electrochemical synthesis of SnO₂ films containing three-dimensionally organized uniform mesopores via interfacial surfactant templating, *Chem. Commun.*, 655-3657 (DOI: 10.1039/B704428C).
- [57] Inoue S., Fujihara S. (2011), Liquid-liquid biphasic synthesis of layered zinc hydroxides intercalated with long-chain carboxylate ions and their conversion into ZnO nanostructures, *Inorg. Chem.*, 50, 3605-3612 (DOI: 10.1021/ic1025729).
- [58] Liang Y.-Y., Cao Lin., Kong L.-B., Li H.-L. (2004), Synthesis of Co(OH)₂/USY composite and its application for electrochemical supercapacitors, *Journal of Power Sources*, 136, 197-200 (DOI: 10.1016/j.jpowsour.2004.05.009).
- [59] Giarola D. A., Catarini da Silva P. R., Urbano A., Midori de Oliveira F., Tarley C. R. T., Dall'Antonia L. H. (2014), Surfactant effect on electrochemical-induced synthesis of α -Ni(OH)₂, *J. Solid State Electrochem.*, 18, 497-504 (DOI: 10.1007/s10008-013-2280-3).
- [60] Lamm M. S., Rajagopal K., Schneider J. P., Pochan D. J. (2005), Laminated morphology of nontwisting beta-sheet fibrils constructed via peptide self-assembly, *J. Am. Chem. Soc.*, 127, 16692-16700 (DOI: 10.1021/ja054721f).
- [61] Roytman R., Adler-Abramovich L., Ajish Kumar K. S., Kuan T.-C., Lin C.-C., Gazit E., Brik A. (2011), Exploring the self-assembly of glycopeptides using a diphenylalanine scaffold, *Org. Biomol. Chem.*, 9, 5755-5761 (DOI: 10.1039/C1OB05071K).
- [62] Orbach R., Adler-Abramovich L., Zigerson S., Mironi-Harpaz I., Seliktar D., Gazit E. (2009), Self-assembled Fmoc-peptides as a

- platform for the formation of nanostructures and hydrogels, *Biomacromolecules*, 10, 2646-2651 (DOI: 10.1021/bm900584m).
- [63] Chakroune N., Viau G., Ammar S., Jouini N., Gredin P., Vaulaya M. J., Veta F. F. (2005), Synthesis, characterization and magnetic properties of disk-shaped particles of a cobalt alkoxide: $\text{CoII}(\text{C}_2\text{H}_4\text{O}_2)$, *New J. Chem.*, 29, 355-361 (DOI: 10.1039/B411117F).
- [64] Zhang Y., Liang W., Wang B., Wang G., Guo Z. (2015), Green solvothermal synthesis of micro-/nano-structured porous $\beta\text{-Ni}(\text{OH})_2$ microspheres with enhanced electrochemical performance, *Materials Research Bulletin*, 64, 386-394 (DOI: 0.1016/j.materresbull.2014.11.035).
- [65] Rahbani J., Khashab N. M., Patra D., Al-Ghoul M. (2012), Kinetics and mechanism of ionic intercalation/de-intercalation during the formation of α -cobalt hydroxide and its polymorphic transition to β -cobalt hydroxide: reaction–diffusion framework, *J. Mater. Chem.*, 22, 16361-16369 (DOI: 10.1039/C2JM31694C).
- [66] Liang C., Shimizu Y., Masuda M., Sasaki T., Koshizaki N. (2004), preparation of layered zinc hydroxide/surfactant nanocomposite by pulsed-laser ablation in a liquid medium, *Chem. Mater.*, 16, 963-965 (DOI: 10.1021/cm034706e).
- [67] Nicholson R. S. (1965), Theory and application of cyclic voltammetry for measurement of electrode reaction kinetics, *Anal. Chem.*, 37, 1351-1355 (DOI: 10.1021/ac60230a016).
- [68] Mabbott G. A. (1983), An introduction to cyclic voltammetry, *J. Chem. Educ.*, 60, 697-702 (DOI: 10.1021/ed060p697).
- [69] Evans D. H., Kathleen M. O., Petersen R. A., Kelly M. J. (1983), Cyclic voltammetry, *J. Chem. Educ.*, 60, 290-293 (DOI: 10.1021/ed060p290).
- [70] Yang G.-W., Xu C.-L., Li H.-L. (2008), Electrodeposited nickel hydroxide on nickel foam with ultrahigh capacitance, *Chem. Commun.*, 6537-6539 (DOI: 10.1039/B815647F).
- [71] Eyele-Mezui S., Vialat P., Higy C., Bourzami R., Leuvrey C., Parizel N., Turek P., Rabu P., Rogez G., Mousty C. (2015), Electrocatalytic properties of metal phthalocyanine tetrasulfonate intercalated in metal

layered simple hydroxides (metal: Co, Cu, and Zn), *J. Phys. Chem. C.*, 119, 13335-13342 (DOI: 10.1021/acs.jpcc.5b02985).

Chapter 8

Conclusions and Scope for Future Work

8.1 Conclusions

This thesis reports two significant studies: Supramolecular construction of π -conjugated peptides and electrochemical assembly of peptide-inorganic hybrid nanostructured materials.

Self-assembled soft nanostructured materials are significant due to their potential applications in the fields of nanoscience and supramolecular electronics. The design of the self-assembled structures is based on π -conjugated peptides, yielding interesting optical as well as electronic properties. Potential applications lie in organic, opto-electronic and energy storage devices like light emitting diodes, photoconductor, electrochemical capacitor and electrochromism.

Chapter 1 gives an overview of current status regarding the assembly of π -conjugated peptides. Small organic molecules for the construction of functional organic-inorganic nanoscale hybrid materials and their applications in diverse fields have been discussed.

Chapter 2 summarizes synthetic methodology and characterization techniques used in the thesis.

Chapter 3 describes the synthesis and self-assembly study of a dipeptide diphenylalanine (Phe-Phe) functionalized benzo[ghi]perylene monoimide (BPI). Solvent dependent photophysical behavior of newly synthesized compound **2** (BPI-FF-OMe) has been described in detail. Compound **2** exhibits positive solvatochromic emission as a function of solvent polarity with higher lifetimes and quantum yields. Compound **2** self-assembles into nanospheres in methanol and toluene solvents. Intermolecular hydrogen bonding and aromatic π - π stacking interactions play an important role in the formation of the nanospherical architecture of compound **2**. Temperature dependent ^1H -NMR studies support the involvement of intermolecular interactions in solution-phase self-assembly of compound **2**. The microscopic techniques including SEM, TEM and AFM elucidate the nanostructural morphology of compound **2**. White light emission is observed when compound **2** co-assembles with 1-pyrenebutyric acid (PyBA) (compound **1**) through donor-acceptor interaction in methanol solution. White

light emission is attributed to the energy transfer from donor to acceptor molecules.

Chapter 4 makes an attempt to describe an electrochromic hydrogel based on a self-assembled quinquethiophene functionalized peptide (compound **4**). In this study, pH-responsive hydrogel exhibits electrochromism due to the presence of a redox active quinquethiophene (5T) moiety in compound **4**. Self-assembly and electrochromic properties of compound **4** are strongly dependent on the nature of peptide motifs functionalized with quinquethiophene core. Non-covalent interactions (hydrogen bonding and π - π stacking interactions) are the driving forces for the formation of nano-fibrillar structures. Conjugated quinquethiophenes facilitate charge conduction efficiently through overlapped self-assembled π -orbitals within adjacent molecules. Furthermore, colours of hydrogel film are very stable with fast and controlled switching speed at room temperature.

Chapter 5 studies the fabrication of peptide/Cd-doped ZnO nanohybrid for the development of a white light emitting system. An electrochemical method is employed to synthesize cadmium-doped Zinc oxide nanosheets and lamellar organic/cadmium-doped Zinc oxide nanoflakes on a gallium-doped ZnO/p-Si(111) substrate. White-light luminescence is attributed to cadmium doping in the zinc oxide crystal and the presence of a dipeptide-functionalized BPI fluorophore in the lamellar nanohybrid.

Chapter 6 attempts to describe electrochemical construction of hybrid nanostructures utilizing small peptides as an organic component with ZnO. Hydrogen bonding and π - π stacking interactions of aromatic peptide amphiphiles are the driving forces for the formation of self-assembled lamellar nanostructures. UV-Vis and PL spectroscopy reveal the optoelectronic properties of peptide-based ZnO thin films. I-V characteristics of these hybrids under dark and light illuminations indicate that the conductivity of these nanostructure materials increases owing to the presence of photon-absorbing active self-assembled peptides.

Chapter 7 finally describes electrochemical deposition of peptide/metal hydroxide hybrids for the purpose of developing electrochemically active materials. Scanning electron microscope (SEM) is used to visualize the surface morphology of peptide/metal hydroxide thin film. The interactions

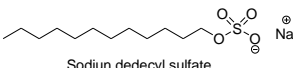
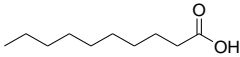
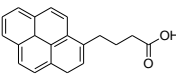
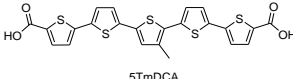
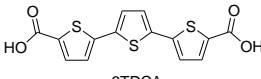
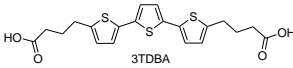
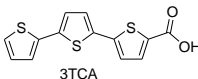
among peptides and peptide-metal hydroxides are exhibited using FTIR spectroscopy and X-ray diffraction studies. Peptide/Co(OH)₂ nanostructured hybrid films exhibit capacitive electrochemical performance in energy storage applications. Porous nanostructure of compound **9**/Co(OH)₂ hybrid shows high capacitance of 3070 Fg⁻¹ through electron transfer mechanism in the potential range -0.2 to 0.6 V at a discharge current of 5 mA. Porous and soft nanostructure facilitates electrochemical accessibilities of electrolyte OH⁻ ions to Co(OH)₂ thin film and fast diffusion rate within the redox phase.

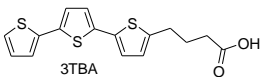
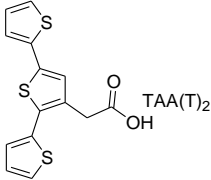
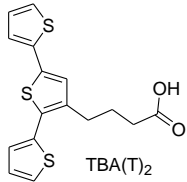
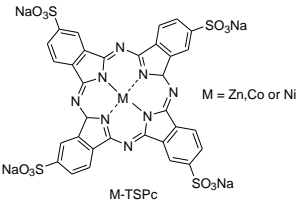
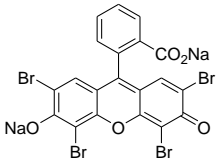
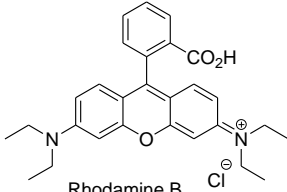
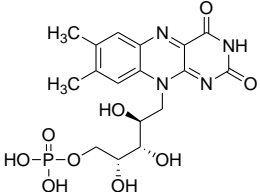
8.2 Future prospects

The structural diversity of oligopeptide sequence and the π -electron system modulates intermolecular interactions for a self-assembled system and hence produces engineered nanostructures with distinct morphologies which provide alteration in photophysical, electrical and mechanical properties. Therefore, self-assembly of the π -conjugated peptides achieves supramolecular nano-architectures which are the most promising functional materials in the variety of flexible bioelectronics such as sensing/signaling as well as for encouraging cell growth, migration, and differentiation. These are affordable and biocompatible materials. Moreover, self-assembling peptide-based π -electron molecules (and their resulting nanomaterials) are efficient to realize the photonic creation of charge-separated states. Therefore, with the appropriate design of π -conjugated peptides (and their resulting supramolecular nanostructure), they could be useful materials for solar energy conversion. On the other hand, a wide range of functional nanomaterials with enhanced performance can be achieved by developing peptide-inorganic hybrids with varying π -conjugated peptides as an organic with different kind of inorganic components.

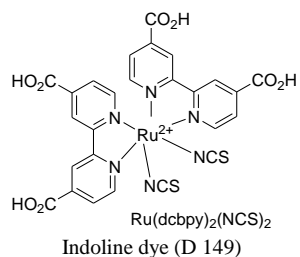
Annexure I

Table A1. A list of small organic molecules used in the electrochemical self-assembly of organic/inorganic hybrids

#	Molecular structure	Nature	Inorganic component	Morphology and structural ordering	References
1	 Sodium decyl sulfate	Hydrophobic segment: alkyl group, Hydrophilic group: sulphate Flexible	ZnO Pt Ni(OH) ₂ Cu ₂ O SnO ₂ Co(OH) ₂	lamellar Hexagonally ordered porous structure lamellar - Worm-like structure lamellar	<i>J. Am.Chem.Soc.</i> , 2002 , 124, 12402-12403 <i>Adv.Mater.</i> 2003 , 15, 2018-2021 <i>J. Am.Chem.Soc.</i> , 2005 , 127, 3596-3604 <i>Chem. Commun.</i> 2006 , 3311-3313 <i>Chem. Commun.</i> 2007 , 3655-3657 <i>Chem. Commun.</i> 2007 , 159-161
2	 Decanoic acid	Hydrophobic segment: alkyl group Hydrophilic group: Carboxyl group Flexible		flat, flake-like lamellae perpendicular on PEDOT:PSS and parallel on ITO	<i>Chem. Mater.</i> 2013 , 25, 4330-4339
3	 1-pyrenebutyric acid	Hydrophobic segment conjugate moiety (pyrene), Hydrophilic group: Carboxyl group Flexible		platelet structures with lamellar morphology	<i>Nat. Mater.</i> 2009 , 8, 68-75
4	 5TmDCA	Hydrophobic segment conjugate moiety (pentathiophene), Hydrophilic group: Carboxyl group		fibre-like morphology	<i>Nat. Mater.</i> 2009 , 8, 68-75
	 3TDCA	Hydrophobic segment conjugate moiety (pentathiophene), Hydrophilic group: Carboxyl group	ZnO	Layer double hydroxide (LDH) structure	
	 3TDBA	Hydrophobic segment conjugate moiety (pentathiophene), Hydrophilic group: Carboxyl group Flexible		Layer double hydroxide (LDH) structure	<i>Chem. Mater.</i> 2013 , 25, 4330-4339
	 3TCA	Hydrophobic segment conjugate moiety (pentathiophene), Hydrophilic group: Carboxyl group		lamellar films	

	 <p>3TBA</p>	<p>Hydrophobic segment conjugate moiety (pentathiophene), Hydrophilic group: Carboxyl group Flexible</p>	<p>lamellar films</p>
5	 <p>TAA(T)₂</p>	<p>Hydrophobic segment conjugate moiety (pentathiophene), Hydrophilic group: Carboxyl group</p>	<p>Lamellar structure absent</p>
	 <p>TBA(T)₂</p>	<p>Hydrophobic segment conjugate moiety (pentathiophene), Hydrophilic group: Carboxyl group</p>	<p>Lamellar structure absent</p>
	 <p>M-TSPc M = Zn, Co or Ni</p>	<p>Hydrophobic segment: alkyl group, Hydrophilic group: sulphate Flexible</p>	<p>Stacking "disks" <i>Chem. Mater.</i> 1999, 11, 2657-2667</p>
6	 <p>Eosin Y disodium salt</p>		<p>"cauliflower" structure <i>Adv. Mater.</i> 2000, 12, 1214-1217</p>
7	 <p>Rhodamine B</p>	<p>CuSCN</p>	<p><i>J. Phys. Chem. C</i> 2014, 118, 16581-16590</p>
8	 <p>Riboflavin 5'-phosphate</p>	<p>ZnO</p>	<p><i>Thin Solid Films</i> 2001, 397, 63-69</p>

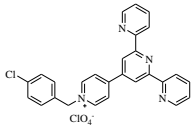
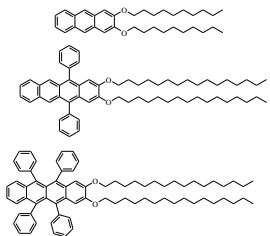
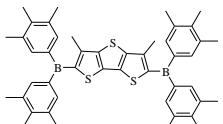
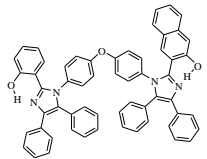
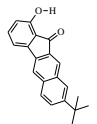
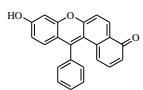
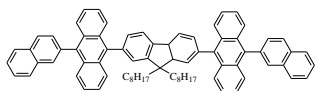
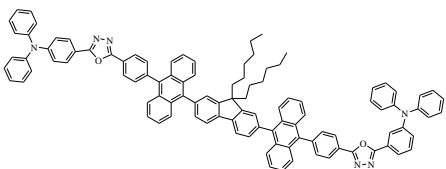
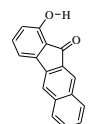
9

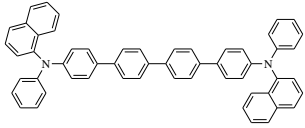
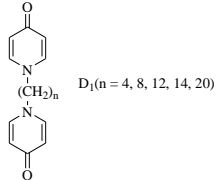
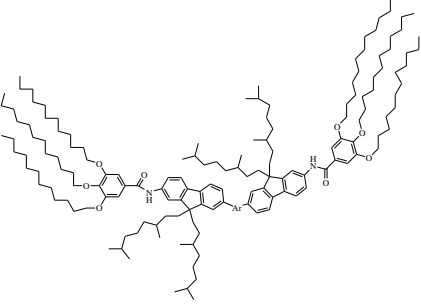
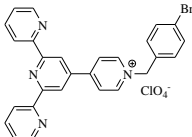
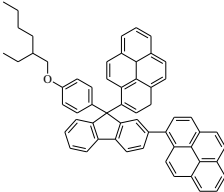
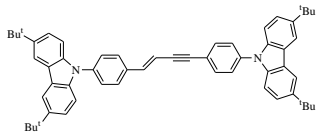
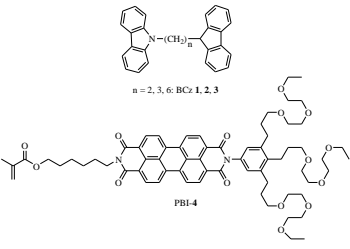


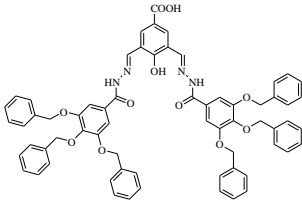
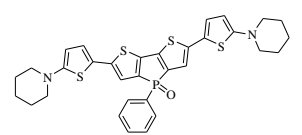
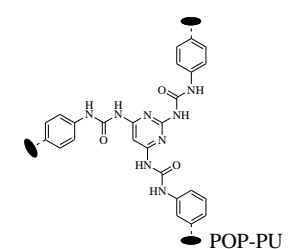
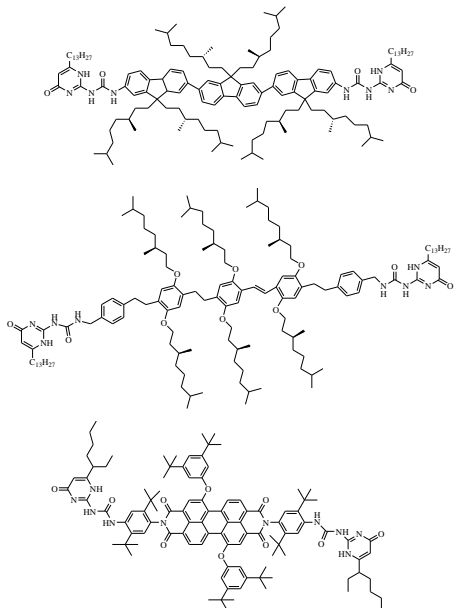
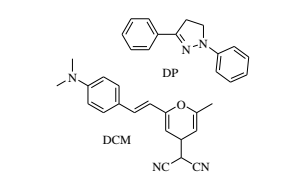
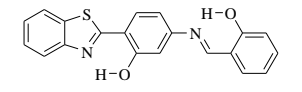
*Electrochimica
Acta* **2003**, *48*,
3071-3078

Table A2: Reports on white light emitting materials.

#	Molecular structure	Purpose	Reference
1		White light emission	<i>ACS Appl. Mater. Interfaces</i> 2013, 5 , 5478–5485
2		White light emission	<i>Adv.Mater.</i> 2009, 21 , 2059–2063.
3		White light emission	<i>Chem. Commun.</i> , 2013, 49 , 6909-6911.
4		White light emission	<i>Chem. Eur. J.</i> 2012, 18 , 1290-1294.
5		White light emission	<i>Chem. Commun.</i> , 2010, 46 , 8002–8004.
6		White light emission	<i>Adv. Mater.</i> 2008, 20 , 79-83

7		White light emission	<i>Chem. Commun.</i> , 2014, 50 , 15878-15881
8		White light emission	<i>J. Phys. Chem. C</i> 2012, 116 , 21706-21716
9		White light emission	<i>Adv. Mater.</i> , 2005, 17 , 34-39
10		White light emission	<i>J. Am. Chem. Soc.</i> 2009, 131 , 14043-14049.
11		White light emission	<i>International Journal of Photoenergy</i> , 2014
12		White light emission	<i>J. Am. Chem. Soc.</i> 2006, 128 , 14081-14092,
13		White light emission	<i>J. Mater. Chem.</i> , 2011, 21 , 12969-12976.
14		White light emission	<i>J. Phys. Chem. C</i> 2011, 115 , 17965-17972
15		White light emission	<i>J. Am. Chem. Soc.</i> 2011, 133 , 17738-17745

16		White light emission	<i>Adv. Mater.</i> 2007, 19 , 3672-3676
17	 $D_1(n = 4, 8, 12, 14, 20)$	White light emission	<i>Angew. chem.</i> 2014, 126 , 4660-4665.
18		White light emission	<i>Chem. Eur. J.</i> 2009, 15 , 9737-9746.
19		White light emission	<i>J. Mater. Chem. C</i> , 2015, 3 , 4563-4569.
20		White light emission	<i>J. Phys. Chem. C</i> 2009, 113 , 4641-4647
21	Vegetable extract	White light emission	<i>Scientific Reports</i> , 2015, 5 , 11118.
23		White light emission	<i>J. Am. Chem. Soc.</i> 2006, 128 , 5592-5593
24	 $n = 2, 3, 6$; BCz 1, 2, 3	White light emission	<i>Chem. Commun.</i> , 2013, 49 , 8178-8180.

25		White light emission	<i>Chem. Commun.</i> , 2015, 51 , 2130-2133
26		White light emission	<i>Chem. Commun.</i> , 2013, 49 , 4899-4901
27	 POP-PU	White light emission	<i>ACS Appl. Mater. Interfaces</i> 2014, 6 , 22569-22576
28		White light emission	<i>J. Am. Chem. Soc.</i> 2009, 131 , 833-843.
29	 DP DCM NC-CN	White light emission	<i>J. Am. Chem. Soc.</i> 2010, 132 , 1742-1743
30		White light emission	<i>Phys. Chem. A</i> 2009, 113 , 5888-5895

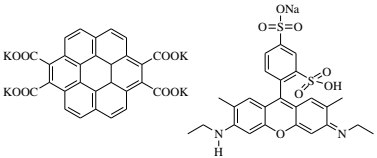
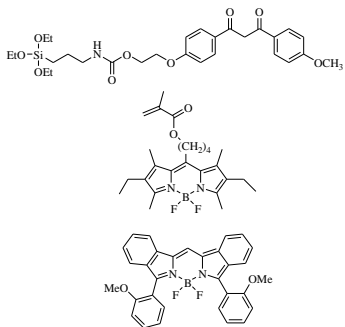
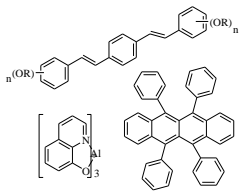
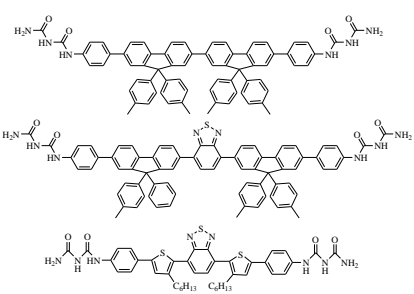
31		White light emission	<i>Adv. Mater.</i> 2013, 25 , 1713–1718
32		White light emission	<i>J. Mater. Chem. C</i> , 2013, 1 , 4437–4444
33		White light emission	<i>Angew. Chem. Int. Ed.</i> 2012, 51 , 3391–3395
34		White light emission	<i>Angew. Chem. Int. Ed.</i> 2011, 50 , 7032–7036

Table A3. DLS characterization of BPI-FF-OMe nanospheres in toluene and methanol

#	Solvent	d_h/nm^a	PD1^b	ξ/mV^c
1	Methanol	613	0.30	-17.97
2	Toluene	857	0.47	-25.89

^a d_h is the hydrodynamic diameter. ^bPDI is the polydispersity index. ^c ξ is the zeta potential.

The Lippert-Mataga Equation

Equation 2 is a simplified from equation 1.

$$\bar{\nu}_{abs} - \bar{\nu}_{em} = \frac{2}{hc} \left(\frac{\varepsilon-1}{2\varepsilon+1} - \frac{n^2-1}{2n^2+1} \right) \frac{(\mu_e - \mu_g)^2}{\rho^3} + C \quad (1)$$

$$(2) \quad \Delta\bar{\nu} = \frac{2\Delta f}{4\pi\varepsilon_0 hc\rho^3} (\mu_e - \mu_g)^2 + C$$

$\Delta\bar{\nu} = \bar{\nu}_{abs} - \bar{\nu}_{em}$ is the solvatochromic shift or Stokes shift (in cm^{-1}) between the absorbance maxima and emission maxima [$\bar{\nu}_{abs} = 1/\lambda_{abs}(\text{max})$, $\bar{\nu}_{em} = 1/\lambda_{em}(\text{max})$]. $\Delta f = [(\varepsilon - 1/2\varepsilon + 1) - (n^2 - 1/2n^2 + 1)]$ is solvent polarizability parameter, which is described by solvent's dielectric constants(ε) and refractive indices(n). ρ represents radius of solvated cavity of dipole. μ_e and μ_g are the dipole moments of a dye both in excited and ground states respectively. The Lippert - Mataga expression of Stokes shift strongly depends on the change of dipole moment of a dye upon excitation ($\Delta\mu_{ge} = \mu_e - \mu_g$) and the size of the cavity radius (ρ). ε_0 denotes dielectric constant of vacuum. h and c are Plank's constant and velocity of light respectively. C is a constant.

Movie A1. Electrochromic hydrogel